



Cite this: *Chem. Soc. Rev.*, 2021, **50**, 3889

## Atomic/molecular layer deposition for energy storage and conversion

Yang Zhao,<sup>†a</sup> Lei Zhang,<sup>†a</sup> Jian Liu,<sup>†b</sup> Keegan Adair,<sup>†c</sup> Feipeng Zhao,<sup>a</sup> Yipeng Sun,<sup>a</sup> Tianpin Wu,<sup>c</sup> Xuanxuan Bi,<sup>d</sup> Khalil Amine,<sup>†d</sup> Jun Lu<sup>†d</sup> and Xueliang Sun<sup>†\*a</sup>

Energy storage and conversion systems, including batteries, supercapacitors, fuel cells, solar cells, and photoelectrochemical water splitting, have played vital roles in the reduction of fossil fuel usage, addressing environmental issues and the development of electric vehicles. The fabrication and surface/interface engineering of electrode materials with refined structures are indispensable for achieving optimal performances for the different energy-related devices. Atomic layer deposition (ALD) and molecular layer deposition (MLD) techniques, the gas-phase thin film deposition processes with self-limiting and saturated surface reactions, have emerged as powerful techniques for surface and interface engineering in energy-related devices due to their exceptional capability of precise thickness control, excellent uniformity and conformity, tunable composition and relatively low deposition temperature. In the past few decades, ALD and MLD have been intensively studied for energy storage and conversion applications with remarkable progress. In this review, we give a comprehensive summary of the development and achievements of ALD and MLD and their applications for energy storage and conversion, including batteries, supercapacitors, fuel cells, solar cells, and photoelectrochemical water splitting. Moreover, the fundamental understanding of the mechanisms involved in different devices will be deeply reviewed. Furthermore, the large-scale potential of ALD and MLD techniques is discussed and predicted. Finally, we will provide insightful perspectives on future directions for new material design by ALD and MLD and untapped opportunities in energy storage and conversion.

Received 28th July 2020

DOI: 10.1039/d0cs00156b

[rsc.li/chem-soc-rev](https://rsc.li/chem-soc-rev)

<sup>a</sup> Department of Mechanical & Materials Engineering, University of Western Ontario, London, ON, N6A 5B9, Canada. E-mail: xsun9@uwo.ca

<sup>b</sup> School of Engineering, Faculty of Applied Science, University of British Columbia, Kelowna, BC, V1V 1V7, Canada

<sup>c</sup> X-ray Science Division, Advanced Photon Sources, Argonne National Laboratory, Lemont, IL, 60439, USA

<sup>d</sup> Chemical Sciences and Engineering Division, Argonne National Laboratory, Lemont, IL, 60439, USA. E-mail: junlu@anl.gov

<sup>†</sup> These authors contributed equally to this work.



**Yang Zhao**

*Dr Yang Zhao is an Assistant Professor in the Department of Mechanical and Materials Engineering at the University of Western Ontario, Canada. Dr Zhao received his BS and MS degrees from Northwestern Polytechnical University (Xi'an, China) in 2011 and 2014, respectively. He obtained his PhD degree under the supervision of Prof. Xueliang (Andy) Sun from the University of Western Ontario in 2018. Then, he had his postdoc training at the University*

*of Western Ontario and the Advanced Light Source of Lawrence Berkeley National Laboratory in 2019–2020. His research interests focus on atomic/molecular layer depositions, next-generation batteries, and synchrotron-based X-ray techniques.*



**Lei Zhang**

*Dr Lei Zhang received his BS degree in Chemistry (2008) and PhD degree in Nanomaterial Chemistry (2014) from Xiamen University with Prof. Zhaoxiong Xie. He was a visiting graduate student at Georgia Institute of Technology in Prof. Younan Xia's group from 2012 to 2014. From 2015 to 2016, he worked as a Postdoc at Tianjin University. He is currently a postdoctoral associate with Professor Xueliang Sun at the University*

*of Western Ontario. His research interests include the design and synthesis of metal nanomaterials and single atom catalysts for fuel cells, carbon dioxide reduction, and water splitting devices.*

## 1. Introduction

Energy storage and conversion systems have played vital roles in the development of electric vehicles (EVs), reduction of fossil fuel usage, and addressing environmental issues.<sup>1</sup> Among the various systems, Li-ion batteries (LIBs) and proton exchange membrane fuel cells (PEMFCs) are two of the most prominent technologies for powering electric vehicles due to their high energy and power density, high efficiency, room temperature operation, and zero emissions. However, the state-of-the-art LIBs and PEMFCs still need further improvement for higher energy density, longer durability, better safety, and lower cost to meet the increasing demands from automotive applications. Meanwhile, next-generation batteries, such as Li metal, Li-sulfur, and Li-O<sub>2</sub> batteries, solid-state Li batteries, Na batteries

and beyond, have been intensively studied as promising alternatives to LIBs for large-scale energy storage applications due to their lower cost compared to conventional LIBs.<sup>2–5</sup> Nevertheless, several formidable challenges inhibit the commercialization of these battery systems, including the detrimental structural changes and unfavourable side reactions at the surface and interface of the electrode materials, which need to be addressed in order to prevent rapid capacity degradation and limited battery lifetime.<sup>6–8</sup> Therefore, it is necessary to rationally engineer the surface and interface of the electrode materials to prevent parasitic side reactions and thus enhance battery performance.<sup>9–12</sup> For PEMFCs, the high cost and insufficient durability of Pt electrocatalysts is still a major barrier for their application in fuel cell vehicles. Degradation of the electrocatalytic properties of Pt could occur through the coalescence of



**Jian Liu**

*Dr Jian Liu is an Assistant Professor in the School of Engineering at the University of British Columbia (UBC) Okanagan campus, Canada. Dr Liu received his PhD in materials science (2013) from the University of Western Ontario (Canada), and worked as an NSERC Postdoctoral Fellow at Lawrence Berkeley National Laboratory and Pacific Northwest National Laboratory prior to joining UBC in January 2017. His current research interests focus on*

*advanced nanofabrication techniques, material design for Li-ion batteries and beyond, and interfacial control and understanding in energy storage systems.*



**Khalil Amine**

*Dr Khalil Amine is a Distinguished Fellow and leader of the Advanced Battery Technology programs at Argonne National Laboratory. Currently Dr Amine serves as a member of the U.S. National Research Council on battery-related technologies. Dr Amine is a 2003 recipient of Scientific America's Top Worldwide Research 50 Research Award, a 2009 recipient of the U.S. Federal Laboratory Award for Excellence in Technology*

*Transfer and a six-time recipient of the R&D 100 Award. He has filed over 207 patents and has over 632 publications. From 1998 to 2018, he was the most cited scientist in the field of batteries.*



**Jun Lu**

*Dr Jun Lu is a chemist at Argonne National Laboratory. His research interests focus on electrochemical energy storage and conversion technology, with a main focus on technology beyond Li-ion batteries. He received his bachelor's degree in chemistry physics from the University of Science and Technology of China (USTC) in 2000. He completed his PhD in materials science from the Department of Metallurgical Engineering at the University of*

*Utah in 2009. Following a DOE-EERE postdoctoral fellowship under Vehicles Technology Program, he joined the Division of Chemical Sciences and Engineering at Argonne National Laboratory as a chemist in 2015.*



**Xueliang Sun**

*Prof. Xueliang (Andy) Sun is a Canada Research Chair in Development of Nanomaterials for Clean Energy, Fellow of the Royal Society of Canada and Canadian Academy of Engineering and Full Professor at the University of Western Ontario, Canada. Dr Sun received his PhD in materials chemistry in 1999 from the University of Manchester, UK, which he followed up by working as a postdoctoral fellow at the*

*University of British Columbia, Canada and as a Research Associate at L'Institut National de la Recherche Scientifique (INRS), Canada. His current research interests are focused on advanced materials for electrochemical energy storage and conversion.*

Pt particles due to weak interactions between Pt and the support, Pt particle agglomeration, corrosion of the support material, and Ostwald ripening. Therefore, it is critical to design a strong interface between Pt and the support to preserve such structures in the harsh environment of PEMFCs while providing the three-phase boundary (catalyst, support, and reactants) required for performing multifunctional electrochemistry.<sup>13,14</sup> Moreover, renewable solar energy and solar fuels are regarded as the most promising alternative clean energy source for fossil fuels. Surface and interface engineering in a well-designed fashion are indispensable for obtaining desirable material structure and achieving optimal performance for energy storage and conversion applications. In this review, as shown in Fig. 1, we will deeply discuss the unique techniques of atomic layer deposition (ALD) and molecular layer deposition (MLD) in the applications of energy storage and conversion. In particular, we will summarize the mechanism, properties, wide applications and large scale potential of ALD and MLD.

ALD has emerged as a powerful technique for surface and interface engineering in energy-related devices, such as rechargeable batteries, supercapacitors, fuel cells, solar cells, and electrochemical water splitting, due to its exceptional capability in controlling material deposition with atomic-level precision.<sup>15–17</sup> During an ALD process, gas-phase precursors are sequentially exposed to the substrate, leading to self-limiting and saturated

surface reactions (Fig. 2a). This reaction mechanism endows ALD-deposited inorganic thin films with several advantages, including precise thickness control, excellent uniformity and conformity, and tunable composition. These thin films have been employed as surface coating layers on the anode and cathode materials of LIBs to address structural and interfacial problems. Moreover, nanoparticles can also be deposited on substrates by ALD by controlling the nucleation sites on the substrate surface through pre-planted functional groups. This is because nucleation sites, such as hydroxyl groups, defect sites, and heteroatom-doping sites, are prerequisites for ALD surface reactions to take place.<sup>18,19</sup> While ALD can traditionally deposit inorganic materials, MLD, the organic counterpart of ALD, can fabricate organic and hybrid inorganic–organic thin films (Fig. 2b). The incorporation of organic segments in the MLD process offers almost unlimited combinations for the film structure, which could lead to unique mechanical, optical, and thermal properties. These MLD thin films hold great promise for tackling surface and interfacial problems in energy storage and conversion systems.

Since the development of ALD in the late 1970's (previously referred to as atomic layer epitaxy (ALE)), this advanced thin film deposition technique has received increasing attention for multiple applications, including catalysis, microelectronics, energy storage and conversion, and sensing.<sup>20–22</sup> Various materials, including metal oxides, metal sulfides, metal fluorides, and metal phosphates can be deposited by ALD with precisely controlled

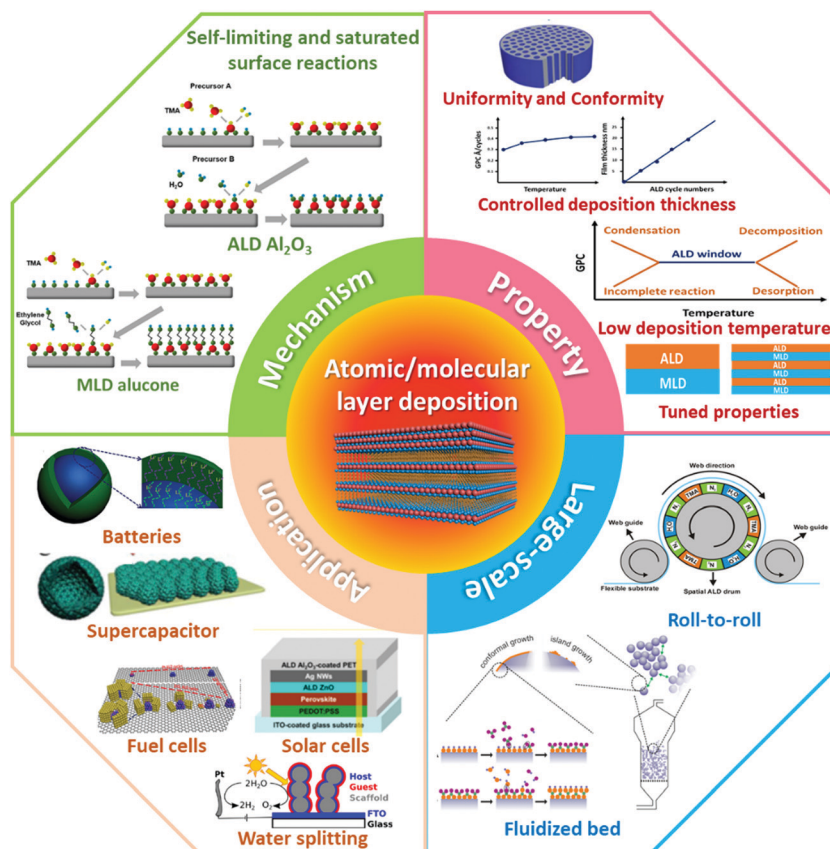


Fig. 1 The mechanism, properties, large-scale potential, and applications for energy storage and conversion of ALD/MLD techniques.

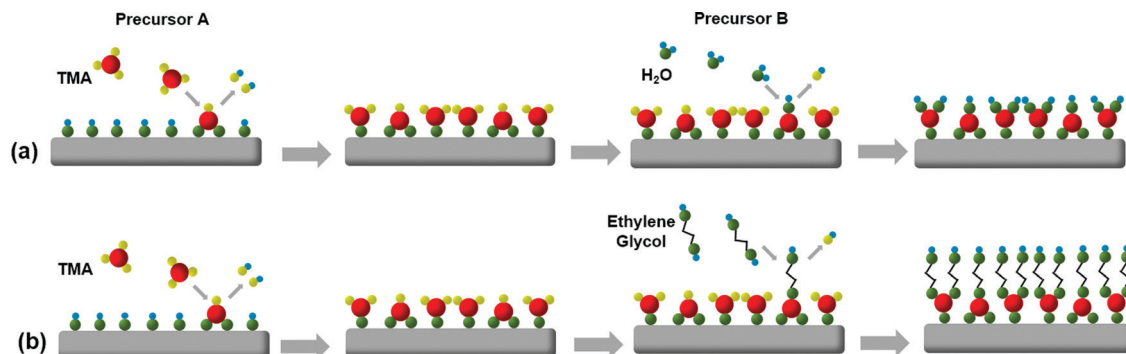


Fig. 2 Illustration of (a) ALD for inorganic films and (b) MLD for hybrid inorganic–organic films.

thicknesses, compositions and structures.<sup>23,24</sup> Particularly in the past ten years, the fields of ALD and MLD for energy storage and conversion have grown rapidly. Fig. 3(a) shows the number of publications associated with atomic layer deposition from 2009 to date, with a significant increase in recent years. As an extension of ALD, MLD was later developed as the organic molecule equivalent. Although the publication numbers on MLD are not as large as that of ALD (Fig. 3(b)), the unique properties of MLD films are still attracting attention for different applications. Among the various applications, energy storage and conversion, especially batteries and fuel cells, are one of the most attractive areas for ALD and MLD (Fig. 3(c and d)). There are several excellent review papers that

have summarized the fundamental chemistry and principles of ALD/MLD, and their application for LIBs and Li-S batteries.<sup>25–44</sup> However, there is no comprehensive review that summarizes both ALD and MLD in the applications of energy storage and conversion.

In this review, we focus on the development and achievements of ALD and MLD and their applications for energy storage and conversion. Different energy storage systems, including batteries and supercapacitors, are included in this comprehensive review. Moreover, the application of ALD/MLD for energy conversion systems including fuel cells, solar cells and photoelectrochemical water splitting, have been discussed in detail. Not only the

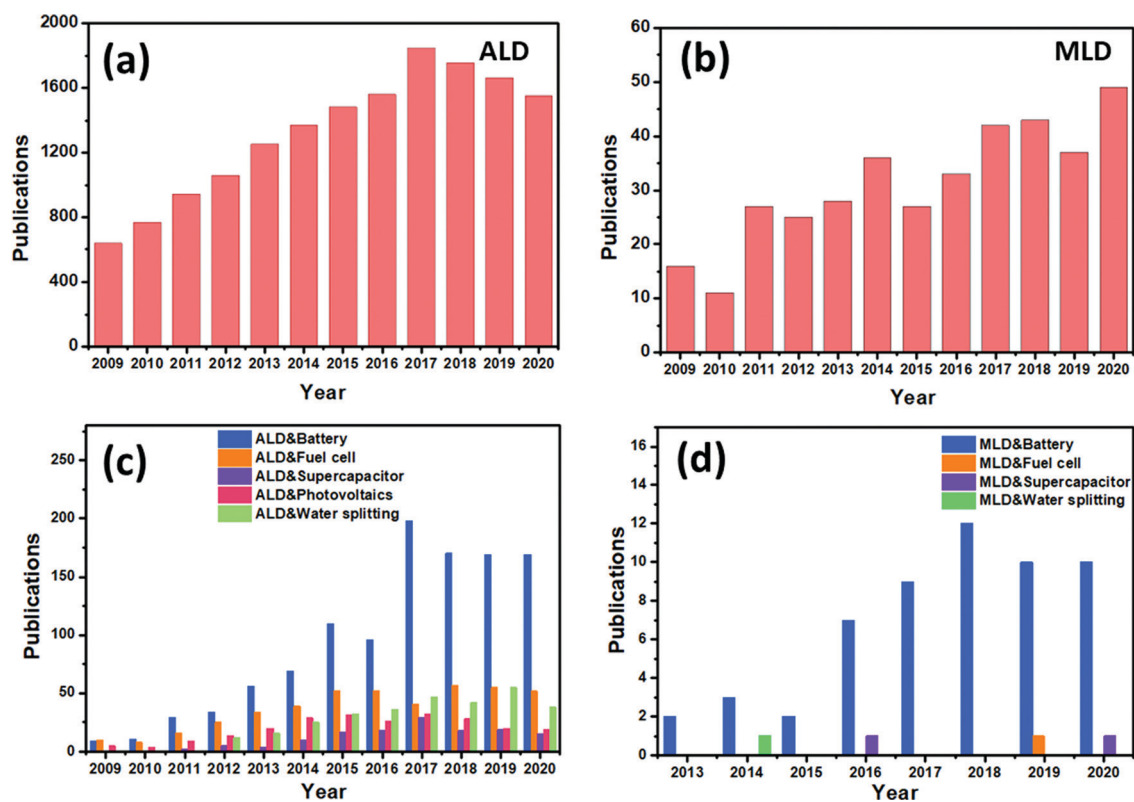


Fig. 3 Publication numbers in the past ten years with the keywords of (a) atomic layer deposition (ALD); (b) molecular layer deposition (MLD); (c) ALD & battery, ALD & fuel cell, ALD & supercapacitor, ALD & photovoltaics, ALD & water splitting; (d) MLD & battery, MLD & fuel cell, MLD & supercapacitor, MLD & photovoltaics, MLD & water splitting. (Based on Web of Science.)

significant progress has been summarized, but also a fundamental understanding of the mechanisms involved will be deeply reviewed. Finally, we will provide insightful perspectives on future directions for new material design by ALD and MLD and untapped opportunities in energy storage and conversion.

## 2. ALD/MLD for energy storage

### 2.1 ALD/MLD for batteries

#### 2.1.1 ALD/MLD for Li-ion batteries

**2.1.1.1 ALD/MLD for electrode fabrication.** Metal oxides are the most popular films deposited by ALD and are promising candidates as electrode materials for LIBs. For example, SnO<sub>2</sub> has been extensively investigated due to its high specific capacity and energy density, relative to conventional graphite anodes. ALD SnO<sub>2</sub> was first demonstrated as an anode material for LIBs when deposited on graphene nanosheets (GNS),<sup>45</sup> as shown in Fig. 4(a). Benefitting from the unique properties of ALD, the structural phases of SnO<sub>2</sub> were precisely controlled by the ALD deposition temperatures, resulting in amorphous and crystalline SnO<sub>2</sub>-GNS composites with sandwich nanostructures.

The precursors used in this study were SnCl<sub>4</sub> and H<sub>2</sub>O at two different temperatures of 200 °C and 400 °C. It is very interesting to note that the amorphous SnO<sub>2</sub>-GNS showed higher electrochemical stability and coulombic efficiency compared to the crystalline SnO<sub>2</sub>-GNS. The amorphous SnO<sub>2</sub>-GNS obtained a capacity of 793 mA h g<sup>-1</sup> after 150 cycles, which is higher than that of the crystalline SnO<sub>2</sub>-GNS (499 mA h g<sup>-1</sup> after 150 cycles). It is believed that the amorphous SnO<sub>2</sub>-GNS is more effective than the crystalline SnO<sub>2</sub>-GNS in overcoming the large volume change of SnO<sub>2</sub> nanoparticles during electrochemical cycling. Subsequently, ALD SnO<sub>2</sub> was deposited on different substrates, including stainless steel,<sup>46</sup> reduced graphene oxide,<sup>47</sup> and MXene.<sup>48</sup> The as-prepared ALD SnO<sub>2</sub> is uniform on different substrates with highly controlled structures and thicknesses.<sup>49,50</sup>

TiO<sub>2</sub> is another attractive anode material candidate for LIBs due to its chemical stability, low volume expansion during cycling, high rate capability and intrinsic safety. ALD TiO<sub>2</sub> is also a routine recipe for the ALD community, in which TiCl<sub>4</sub> and titanium(IV) isopropoxide (TTIP) are widely used as precursors for Ti-based ALD processes.<sup>51,52</sup> Ban *et al.* firstly reported ALD amorphous TiO<sub>2</sub> on high surface area graphene (reduced graphene oxide) sheets for LIBs.<sup>53</sup> The as-prepared ALD TiO<sub>2</sub> can effectively

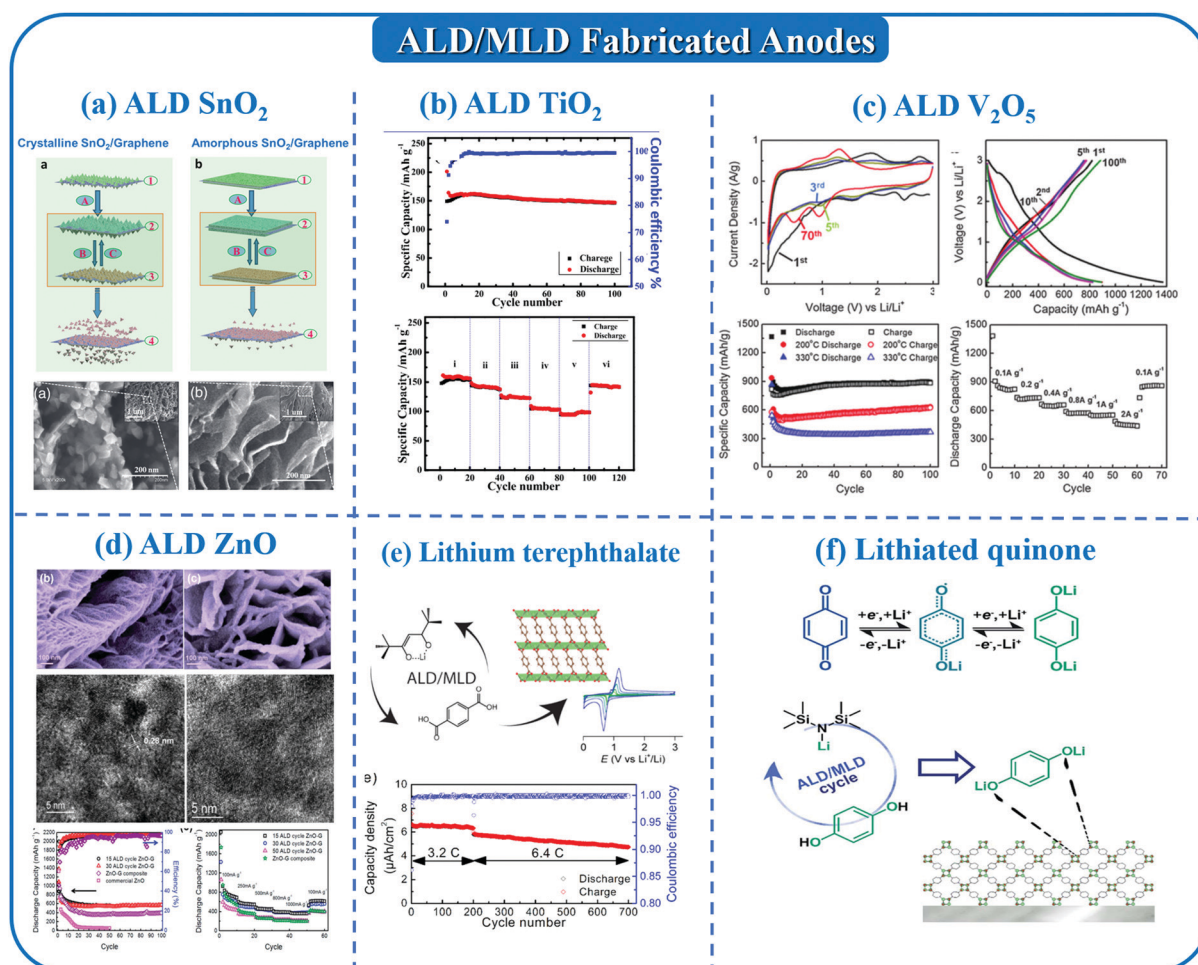


Fig. 4 ALD and MLD metal oxide anodes: (a) ALD SnO<sub>2</sub>; (b) ALD TiO<sub>2</sub>; (c) ALD V<sub>2</sub>O<sub>5</sub>; (d) ALD ZnO; (e) lithium terephthalate; (f) lithiated quinone.

minimize the Li-ion diffusion coefficient of TiO<sub>2</sub>, resulting in a stable and high capacity anode with high rate performances. Other matrices have also been used as substrates for ALD TiO<sub>2</sub>, such as graphite, graphene, carbon nanotubes, anodic aluminum oxide (AAO) templates and Ni nanotubes.<sup>54–58</sup> Sun's group also fabricated ALD TiO<sub>2</sub> on worm-like GNS with high capacity and stability, as shown in Fig. 4(b).<sup>59</sup> Another interesting work has been demonstrated by Hong *et al.*,<sup>60</sup> in which carbon black is used as a sacrificial template to create the mesoporous structure of TiO<sub>2</sub>. As a result, the mesoporous TiO<sub>2</sub> exhibits a large specific surface area, high capacity, and good coulombic efficiency.

Among the aforementioned metal oxides, ZnO shows various advantages, such as low cost, facile synthesis, chemical stability, and a high theoretical capacity of 978 mA h g<sup>-1</sup> in LIBs. ZnO has been widely deposited by ALD, in which Zn(CH<sub>3</sub>CH<sub>2</sub>)<sub>2</sub> is the most widely used precursor.<sup>61</sup> Lian *et al.* firstly reported ALD ZnO on graphene layers as an anode material for LIBs, as shown in Fig. 4(d).<sup>62</sup> In their study, the ZnO was deposited as quantum dots (QDs) on graphene with controllable sizes from 2 to 7 nm. Interestingly, the smaller ZnO QDs on graphene displayed better electrochemical performance, in which a high reversible specific capacity of 960 mA h g<sup>-1</sup> is achieved. Another work has been reported using graphene frameworks as substrates for ALD ZnO.<sup>63</sup> To achieve better electrochemical performance, another ALD Al<sub>2</sub>O<sub>3</sub> layer was deposited on the ZnO-graphene electrode as a physical protection layer and an artificial ionically conductive SEI layer. As a result, the ALD Al<sub>2</sub>O<sub>3</sub>-wrapped ALD ZnO-graphene architecture provided the electrode with superior electrochemical performance with high capacity, excellent rate capability, and good cycling stability.

Some other metal oxides have also been deposited by ALD and used as anode materials for LIBs,<sup>64–66</sup> such as MoO<sub>3</sub>, RuO<sub>2</sub>, and V<sub>2</sub>O<sub>5</sub>. For example, as shown in Fig. 4(c), V<sub>2</sub>O<sub>5</sub> was deposited on graphene using vanadyl oxytriisopropoxide and

water as precursors with a deposition temperature of 150 °C, achieving a growth per cycle (GPC) of 1 Å.<sup>64</sup> The electrochemical results reveal that a stable capacity of 892 mA h g<sup>-1</sup> can be achieved for the ALD V<sub>2</sub>O<sub>5</sub>-graphene composite with excellent cycling stability. It is believed that the highly conformal coating induced by the ALD process is the key to mitigating mechanical degradation and vanadium dissolution. Besides the popular metal oxides, other metal nitrides, metal phosphates, and metal sulfides deposited by ALD have also been reported,<sup>67–74</sup> including MoS<sub>2</sub>, MoN, W<sub>2</sub>N, WS<sub>2</sub>, VP<sub>x</sub>, AlS<sub>x</sub>, and ZnS. The detailed ALD deposition parameters and performances of these materials as anodes in LIBs are shown in Table 1.

Organic electrode materials for metal ion batteries have shown great potential due to their high theoretical capacity, flexible structure design, and environmental friendliness.<sup>75–77</sup> Generally, the redox reactions of organic electrode materials are based on the charge-state change of the electroactive groups.<sup>78</sup> With this in mind, MLD can be used to fabricate organic electrodes for LIBs. Karppinen's group firstly reported the synthesis of lithium terephthalate (LiTP) by ALD/MLD for anode applications in LIBs.<sup>79</sup> As shown in Fig. 4(e), the LiTP was deposited using the precursors of Li(thd) (thd = 2,2,6,6-tetramethyl-3,5-heptanedionate) and terephthalic acid (TPA) at 200 °C with a GPC of 3.0 Å. The ALD-LiTP presented the same layered crystal structure and high electrochemical activity. Moreover, they demonstrated *in situ* deposition of the quinone cathode in its lithiated state by ALD/MLD, using LiHMDS and hydroquinone as the precursors, as shown in Fig. 4(f).<sup>80</sup> Furthermore, organic all-solid-state cells were successfully developed and fully functional without any conductive additives. However, the MLD-fabricated anode material is still in its infancy and the electrochemical performances of the MLD anode need to be further enhanced.

Nanostructured anode materials demonstrate various structure-dependent advantages, such as high surface area to mass/volume

Table 1 The detailed parameters and performances of the ALD-fabricated anode materials for LIBs

ALD materials	Precursors	Substrate	Deposition temperature	Electrochemical performances	Ref.
SnO <sub>2</sub>	SnCl <sub>4</sub> and H <sub>2</sub> O	Graphene nanosheets	200 °C	793 mA h g <sup>-1</sup> after 150 cycles	45
			400 °C	499 mA h g <sup>-1</sup> after 150 cycles	
	Tin(IV)-butoxide and plasma O <sup>-</sup>	Stainless steel	200 °C	646 mA h g <sup>-1</sup> after 250 cycles	46
	Tetrakis(dimethylamino) tin and H <sub>2</sub> O	Reduced graphene oxide	150 °C	800 mA h g <sup>-1</sup> after 200 cycles	47
	Tetrakis(diethylamido) tin and O <sub>3</sub>	MXenes	150 °C or 200 °C	843 mA h g <sup>-1</sup> after 50 cycles	48
TiO <sub>2</sub>	Sn(C <sub>2</sub> H <sub>5</sub> ) <sub>4</sub> and O <sub>2</sub> plasma	Silicon and stainless steel	150 °C and 200 °C	650 mA h g <sup>-1</sup> after 400 cycles	50
		Reduced graphene oxide	120 °C	120 mA h g <sup>-1</sup> after 400 cycles	53
	TiCl <sub>4</sub> and H <sub>2</sub> O	Graphite	—	~230 mA h g <sup>-1</sup> after 100 cycles	54
	Titanium tetraisopropoxide and H <sub>2</sub> O	Graphene nanosheets	100 °C	140 mA h g <sup>-1</sup> after 100 cycles	59
	TiCl <sub>4</sub> and H <sub>2</sub> O	Carbon nanotubes	120 °C	120 mA h g <sup>-1</sup> after 1000 cycles	55
	TiCl <sub>4</sub> and H <sub>2</sub> O	Carbon black	200 °C	128 mA h g <sup>-1</sup> after 100 cycles	60
	TiCl <sub>4</sub> and H <sub>2</sub> O	CNTs/CFP	120 °C	178 mA h g <sup>-1</sup> after 400 cycles	56
ZnO	Diethyl zinc and H <sub>2</sub> O	Graphene nanosheets	120 °C	540 mA h g <sup>-1</sup> after 100 cycles	62
	Zn(C <sub>2</sub> H <sub>5</sub> ) <sub>2</sub> and H <sub>2</sub> O	Graphene	150 °C	490 mA h g <sup>-1</sup> after 100 cycles	63
	Diethyl zinc and H <sub>2</sub> O	Carbon black	150 °C	769 mA h g <sup>-1</sup> after 500 cycles	61
MoS <sub>2</sub>	Mo(CO) <sub>6</sub> and H <sub>2</sub> S	Carbon	170 °C	851 mA h g <sup>-1</sup> after 500 cycles	67
MoN	Mo(CO) <sub>6</sub> and NH <sub>3</sub>	Carbon	170 °C	700 mA h g <sup>-1</sup> after 100 cycles	68
MoO <sub>3</sub>	Mo(CO) <sub>6</sub> and O <sub>3</sub>	Carbon nanotube	165 °C	150 mA h g <sup>-1</sup> after 60 cycles	66
V <sub>2</sub> O <sub>5</sub>	Vanadyl oxytriisopropoxide and H <sub>2</sub> O	Graphene	150 °C	892 mA h g <sup>-1</sup> after 100 cycles	64
RuO <sub>2</sub>	Ru(C <sub>9</sub> H <sub>13</sub> ) <sub>2</sub> and O <sub>2</sub>	Carbon nanotube	210–240 °C	~600 mA h g <sup>-1</sup> after 100 cycles	65
W <sub>2</sub> N	W(CO) <sub>6</sub> and NH <sub>3</sub>	Stainless steel	180–195 °C	25 μA h cm <sup>-2</sup> after 200 cycles	69
WS <sub>2</sub>	W(CO) <sub>6</sub> and H <sub>2</sub> S	Stainless steel	180–195 °C	13 μA h cm <sup>-2</sup> after 100 cycles	70

ratios and robust hierarchical structures.<sup>81,82</sup> In the past years, nanomaterials with different dimensions and structures have been synthesized *via* different methods.<sup>83,84</sup> Among them, ALD is also a powerful tool to design nanostructured materials,<sup>85,86</sup> especially with sacrificial templates.<sup>87–93</sup> For example, Jeun *et al.* fabricated SnO<sub>2</sub>@TiO<sub>2</sub> double-shell nanotubes through a combination of electrospinning and ALD methods. As shown in the schematic diagram of Fig. 5(a), electrospun polyacrylonitrile (PAN) is chosen as a sacrificial template and two layers of SnO<sub>2</sub> (inner shell) and TiO<sub>2</sub> (outer shell) were deposited and precisely controlled by ALD.<sup>87</sup> As a result, the TiO<sub>2</sub> outer shell can encapsulate the inner SnO<sub>2</sub> nanotube, leading to a hollow structure that can effectively relieve the volume expansion of SnO<sub>2</sub> during cycling and improve the electrochemical performance. Their group further developed TiO<sub>2</sub>@SnO<sub>2</sub>@TiO<sub>2</sub> triple-shell nanotubes by a similar procedure.<sup>93</sup> The diameter of the triple-shell nanotubes is around 200 nm with a shell thickness of 10 nm. Fan's group also developed a series of anode materials by ALD with rationally designed nanostructures.<sup>56,88,90</sup> Generally, the sacrificial template materials are firstly synthesized through hydrothermal methods. Then, popular metal oxides (such as TiO<sub>2</sub>, ZnO, *etc.*) are deposited on the template materials by ALD. Finally, the templates can be removed by an ion-exchange method or acid etching method to achieve a hollow nanostructure. For example, Fig. 5(b) shows a schematic diagram of the synthesis process and morphology of the TiO<sub>2</sub>@Fe<sub>2</sub>O<sub>3</sub> nanostructured anode materials.

The cathode material is typically considered as the limiting factor in determining the energy density of LIBs. Popular cathode materials include LiCoO<sub>2</sub>, LiFePO<sub>4</sub>, LiMn<sub>2</sub>O<sub>4</sub>, LiCo<sub>x</sub>Ni<sub>y</sub>Mn<sub>z</sub>O<sub>2</sub> (NMC), LiNi<sub>0.8</sub>Co<sub>0.15</sub>Al<sub>0.05</sub>O<sub>2</sub> (NCA) *etc.* However, the fabrication of complex oxides with more than three elements by ALD is relatively challenging compared to the binary oxides. The early work using ALD to synthesize cathode materials started from binary oxides of V<sub>2</sub>O<sub>5</sub>. V<sub>2</sub>O<sub>5</sub> presents a high reversible capacity of 147 mA h g<sup>-1</sup> (at 2.6–4.0 V) and 294 mA h g<sup>-1</sup> (at 2.0–4.0 V) as well as fast lithiation and enhanced safety.<sup>94–96</sup> In the last section, we have introduced examples using ALD V<sub>2</sub>O<sub>5</sub> as anode materials within the potential range of 0–2 V. However, ALD V<sub>2</sub>O<sub>5</sub> is more often used as a cathode material for LIBs.<sup>97,98</sup> Rubloff's group firstly reported ALD V<sub>2</sub>O<sub>5</sub> as a cathode

material for LIBs,<sup>99</sup> as shown in Fig. 6(a). In their study, VO(OC<sub>3</sub>H<sub>7</sub>)<sub>3</sub> and O<sub>3</sub> are used as precursors within a deposition temperature range of 150 to 210 °C. The 30 nm thick ALD V<sub>2</sub>O<sub>5</sub> film was deposited on Au-coated stainless-steel disks and used as the cathode in coin cell configurations. The electrochemical results indicated that the initial specific discharge capacity of ALD V<sub>2</sub>O<sub>5</sub> is 142 mA h g<sup>-1</sup> at 2.6–4.0 V with outstanding rate and cycling performances. Furthermore, their group compared the ALD V<sub>2</sub>O<sub>5</sub> recipes using O<sub>3</sub> and H<sub>2</sub>O as oxidant precursors.<sup>100</sup> As a result, polycrystalline V<sub>2</sub>O<sub>5</sub> films were obtained by the O<sub>3</sub>-based process and amorphous V<sub>2</sub>O<sub>5</sub> films were synthesized from the H<sub>2</sub>O-based process. From the electrochemical performances, the polycrystalline V<sub>2</sub>O<sub>5</sub> films delivered a higher storage capacity than the amorphous films because of their ability to incorporate up to three Li per V<sub>2</sub>O<sub>5</sub> formula unit. In another study, Mattelaer *et al.* synthesized VO<sub>2</sub> using tetrakis[ethylmethylamino] vanadium and H<sub>2</sub>O or O<sub>3</sub> as precursors.<sup>101</sup> This work provided a series of stable vanadium oxide phases in the VO<sub>2</sub>–V<sub>2</sub>O<sub>5</sub> series fabricated under different oxygen partial pressures between ambient air and 3.7 Pa. It is found that the different vanadium oxide phases demonstrate different volumetric capacities in the order of V<sub>2</sub>O<sub>5</sub> < VO<sub>2</sub> (B) < V<sub>6</sub>O<sub>13</sub> < V<sub>3</sub>O<sub>7</sub> < V<sub>4</sub>O<sub>9</sub> in the 1.5–4.5 V *vs.* Li<sup>+</sup>/Li potential range.

LiCoO<sub>2</sub> is the most popular commercialized cathode material for LIBs. However, the development of complex oxides by ALD with three elements is complicated. Generally, the procedure is separated into two sub-cycles of Li compounds and Co compounds and the ratio between these two sub-cycles is controlled to achieve the desired composition. Donders *et al.* firstly reported the ALD LiCoO<sub>2</sub> process using CoCp<sub>2</sub> as the cobalt precursor, LiOtBu as the lithium precursor and O<sub>2</sub> plasma as an oxidant source with a deposition temperature of 325 °C.<sup>102</sup> The schematic diagram is shown in Fig. 6(b) and the super-cycles of LiCoO<sub>2</sub> consist of two sub-cycles of Co<sub>3</sub>O<sub>4</sub> and Li<sub>2</sub>CO<sub>3</sub>. The crystalline LiCoO<sub>2</sub> was obtained after annealing at 700 °C for 6 minutes. The ALD-deposited LiCoO<sub>2</sub> electrodes were electrochemically active, revealing good electrochemical performance. Similar to LiCoO<sub>2</sub>, LiMn<sub>2</sub>O<sub>4</sub> is also an important cathode material for LIBs, especially for high-rate performances. The first report of

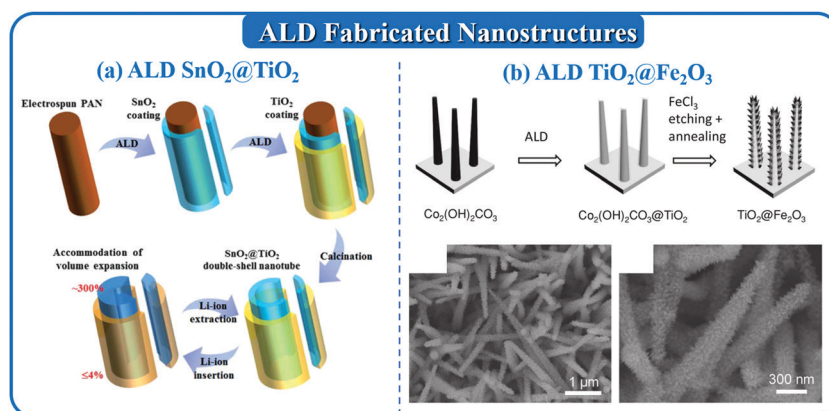


Fig. 5 Nanostructured anodes fabricated by ALD: (a) SnO<sub>2</sub>@TiO<sub>2</sub>; (b) TiO<sub>2</sub>@Fe<sub>2</sub>O<sub>3</sub>.

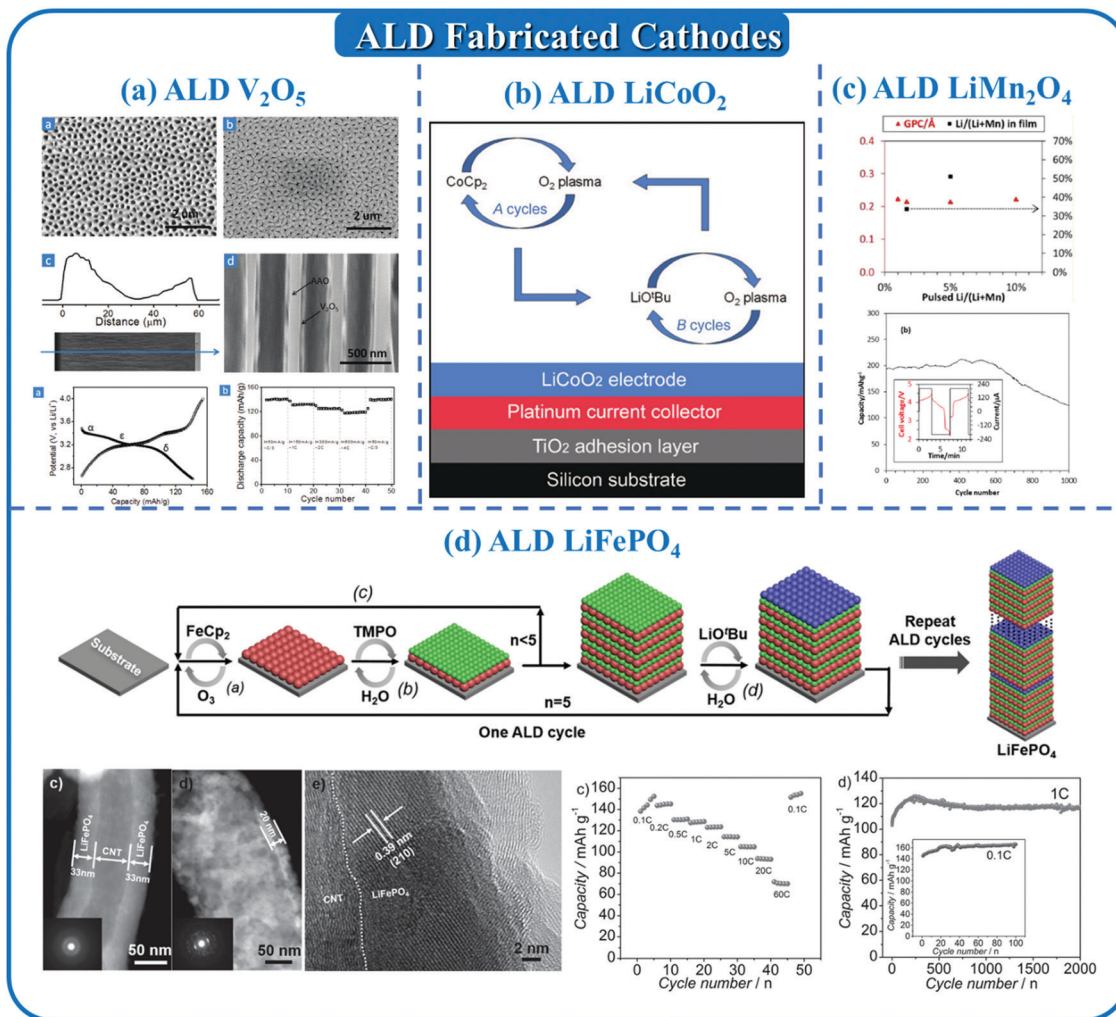


Fig. 6 ALD-fabricated cathodes: (a) V<sub>2</sub>O<sub>5</sub>; (b) LiCoO<sub>2</sub>; (c) LiMn<sub>2</sub>O<sub>4</sub>; (d) LiFePO<sub>4</sub>.

ALD LiMn<sub>2</sub>O<sub>4</sub> was from Miikkulainen *et al.* with a combination of binary ALD processes for ALD Li<sub>2</sub>O/LiOH and MnO<sub>2</sub> or MnO,<sup>103</sup> as shown in Fig. 6(c). In their study, the tris(dipivaloyl-methanato)manganese (Mn(thd)<sub>3</sub>), Li(thd), and O<sub>3</sub> were used as precursors at the deposition temperature of 240 °C. However, it is very challenging to obtain pure LiMn<sub>2</sub>O<sub>4</sub> through the supercycles. Moreover, they further developed a conversion process for using Li(thd)/O<sub>3</sub> and LiO<sup>t</sup>Bu/H<sub>2</sub>O treatment to convert ALD-MnO<sub>2</sub> into Li<sub>x</sub>Mn<sub>2</sub>O<sub>4</sub>, in which the obtained Li<sub>x</sub>Mn<sub>2</sub>O<sub>4</sub> films presented high electrochemical capacity and good cycling stability (Fig. 5(c)). There are other examples of the direct application of ALD MnO<sub>2</sub> as a cathode<sup>104</sup> or converting the MnO/MnO<sub>2</sub> into LiMn<sub>2</sub>O<sub>4</sub> through (electro)chemical methods.<sup>105,106</sup>

LiFePO<sub>4</sub> is one of the most popular cathode materials for commercialized LIBs because of its excellent cycling stability, environmental friendliness, and promising safety. Some important breakthroughs in recent years have allowed its successful commercialization.<sup>107–109</sup> The research of ALD LiFePO<sub>4</sub> started from FePO<sub>4</sub> as the base. Gandrud *et al.* synthesized FePO<sub>4</sub> for the first time by ALD, combining two sub-cycles of FeO<sub>x</sub> and PO<sub>x</sub>.<sup>110</sup> The precursors used in this recipe are trimethyl

phosphate (Me<sub>3</sub>PO<sub>4</sub>) and H<sub>2</sub>O/O<sub>3</sub> as oxygen sources for PO<sub>x</sub>, while Fe(thd)<sub>3</sub> (Hthd = 2,2,6,6-tetramethyl-3,5-heptanedionate) and O<sub>3</sub> are used for FeO<sub>x</sub>. The as-deposited films are amorphous and a post annealing treatment at 600 °C was required to obtain the crystalline trigonal FePO<sub>4</sub>. However, the amorphous FePO<sub>4</sub> was found to be electrochemically active and provide exceptional cyclability with a capacity of 178 mA h g<sup>-1</sup>. Sun *et al.* also reported ALD-deposited FePO<sub>4</sub> on carbon nanotubes and other 3D carbon nanostructures for cathode applications in LIBs.<sup>111,112</sup> PE-ALD deposited FePO<sub>4</sub> was reported by Detavernier's group using Me<sub>3</sub>PO<sub>4</sub> plasma, O<sub>2</sub> plasma, and *tert*-butylferrocene as precursors with an exceptionally high GPC of 1.1 nm per cycle.<sup>113</sup> The as-deposited films were amorphous with a composition of FeP<sub>1.5</sub>O<sub>4.7</sub> and further formed a trigonal FePO<sub>4</sub> after annealing to 700 °C in air. Furthermore, Sun *et al.* developed ALD LiFePO<sub>4</sub> by a combination of Fe<sub>2</sub>O<sub>3</sub>, PO<sub>x</sub>, and Li<sub>2</sub>O subcycles, which is the first report using ALD to fabricate complex compounds with four elements. Fig. 6(d) shows the schematic diagram of the ALD LiFePO<sub>4</sub> process, in which the ratio of the different subcycles is the key to obtaining the proper stoichiometry. Similarly, post-treatment is necessary to obtain the

crystalline  $\text{LiFePO}_4$ . The annealed  $\text{LiFePO}_4/\text{CNTs}$  exhibited exceptional battery performance with excellent rate capability, high power density, and long lifetime. Other types of phosphates, such as vanadium phosphate and titanium phosphate, have been further developed by Detavernier's group *via* plasma enhanced-ALD (PEALD) and used as cathode materials for LIBs.<sup>71,114</sup>

In this section, the recent development of ALD-fabricated electrode materials, including both cathodes and anodes, has been summarized in detail. (1) Metal oxides, including  $\text{SnO}_2$ ,  $\text{ZnO}$ ,  $\text{TiO}_2$ , *etc.*, have been deposited by ALD and used as anode materials for LIBs. The morphology, structures, and thickness of the metal oxides are precisely controlled by ALD parameters. Some other compounds, including metal nitrides, metal phosphates, and metal sulfides, have also been fabricated by ALD and used as anode materials for LIBs. (2) Organic electrode materials have been developed and deposited by MLD as anode materials for LIBs, however, the electrochemical performances of the MLD-derived organic electrodes still need to be further improved. (3) Nanostructured materials, such as hollow structures and core-shell structures, were designed and realized by ALD with sacrificial templates. (4) Several types of cathode materials, such as  $\text{V}_2\text{O}_5$ ,  $\text{LiCoO}_2$ ,  $\text{LiMn}_2\text{O}_4$ , and  $\text{LiFePO}_4$ , were synthesized by ALD. Although promising progress has been obtained and various electrode materials have been synthesized by ALD, it should be noted that there are still several drawbacks of ALD/MLD for electrode fabrication. The slow GPC of the ALD/MLD films is a major concern, which is in the Å per cycle range for most deposition processes. In the reported literature, hundreds or even thousands of ALD cycles are required to obtain electrodes with reasonable active material mass loading. However, the time-consuming process is less commercially viable for standard battery technologies, particularly when compared with composite/powder-based electrodes.

#### 2.1.1.2 ALD/MLD for cathode/electrolyte interface engineering.

Cathode materials are considered as the limiting factor for the energy density and capacity of LIBs. As discussed above, layered  $\text{LiCoO}_2$ , spinel  $\text{LiMn}_2\text{O}_4$ , and polyanion  $\text{LiFePO}_4$  are the primary groups of cathode materials.<sup>115,116</sup> The layered  $\text{LiCoO}_2$  is the first developed and most widely used cathode material for commercial LIBs. However, the high cost, toxicity, limited capacity and chemical instability in the deep charged state have prevented its further applications for transportation and stationary storage. Compared to  $\text{LiCoO}_2$ , spinel  $\text{LiMn}_2\text{O}_4$  shows the advantages of material availability and environmental compatibility. However, the Mn dissolution of  $\text{LiMn}_2\text{O}_4$  during electrochemical cycling leads to capacity fading especially when operating at temperatures above ambient.  $\text{LiFePO}_4$  is another promising cathode material with low cost, low toxicity, high safety, and excellent cycling performance. The challenges for  $\text{LiFePO}_4$  include poor rate performances and surface chemistry stability. More recently,  $\text{LiNi}_x\text{Mn}_y\text{Co}_{1-x-y}\text{O}_2$  (NMC) and  $\text{LiNi}_{0.8}\text{Co}_{0.15}\text{Al}_{0.05}\text{O}_2$  (NCA) have become popular because of their high operational voltage and specific capacities. For example, the NCA cathode possesses a high theoretical capacity of  $265 \text{ mA h g}^{-1}$

( $0.95 \text{ Li}^+$  involving (re)-insertion), which is higher than other "4 V" cathode candidates. However, the Li transition metal oxide cathode still has serious challenges, such as phase transition, mechanical cracking, electrolyte decomposition, transition metal dissolution, conductivity, and air instability.<sup>117</sup> Among these issues, the interface between cathode materials and electrolyte, which is referred to as the cathode electrolyte interphase (CEI), plays the most important role.<sup>118,119</sup> At high oxidation potentials, the electrolytes decompose to form an interface with side products on the cathode materials, which is referred to as the CEI. On one hand, a stable and dense CEI can enhance the stability of the cathode materials by preventing the interfacial reactions, HF etching and transition metal dissolution. On the other hand, an unstable CEI may aggravate the interfacial reactions and cause an increase of the interfacial impedance and result in the fast degradation of the battery performance.<sup>120</sup> To address the interfacial challenges and achieve a stable CEI, surface modification of cathode materials is the most effective approach, especially to prevent electrolyte decomposition and transition metal dissolution.<sup>121</sup> The basic requirements of the coating layers are (1) controllable thickness. On one hand, a coating that is too thick will affect Li-ion or electron transportation. On the other hand, coatings that are too thin cannot totally prevent side reactions. (2) Uniform, conformable and continuous coating on cathode materials. (3) Good mechanical properties.<sup>122,123</sup> To meet these requirements, ALD/MLD is the ideal technique due to its aforementioned attributes. Lee's group firstly reported the enhanced stability of  $\text{LiCoO}_2$  cathodes using surface coating by ALD, in which routine ALD  $\text{Al}_2\text{O}_3$  was chosen as the coating material.<sup>124</sup> From their study, only two cycles of ALD  $\text{Al}_2\text{O}_3$  with a thickness of 3–4 Å can effectively improve the electrochemical performance, exhibiting capacity retention of 89% after 120 charge–discharge cycles, as shown in Fig. 7(a). Furthermore, they compared the performances of ALD coating directly on the electrode *versus* the powder. As a result, the capacity retention for ALD  $\text{Al}_2\text{O}_3$  directly on the composite is slightly inferior to the capacity retention of ALD on powders. Several questions relating to the reaction mechanism during the ALD process on cathode materials have been raised. Elam's group used *in situ* and *ex situ* experimental characterization coupled with DFT calculations to elucidate the mechanism for ALD  $\text{Al}_2\text{O}_3$  on  $\text{LiMn}_2\text{O}_4$  cathodes (Fig. 7(d)).<sup>125</sup> *In situ* Fourier transform infrared spectroscopy (FTIR), quadrupole mass spectrometry (QMS), and quartz crystal microbalance (QCM) measurements are combined to have a comprehensive study. It is very interesting to note that the ALD  $\text{Al}_2\text{O}_3$  process on  $\text{LiMn}_2\text{O}_4$  in the early cycles was different compared to the deposition on conventional substrates. The Al heteroatom bridged several oxygen atoms at the LMO surface initially, even doping into the  $\text{LiMn}_2\text{O}_4$  surface. The initial few cycles of ALD  $\text{Al}_2\text{O}_3$  lead to a reduction in the average Mn oxidation state, with a higher ratio of  $\text{Mn}^{3+}$ , resulting in higher capacities.

In the past few years, several studies have reported the use of ALD  $\text{Al}_2\text{O}_3$  as a surface coating for different types of cathode materials, such as  $\text{LiCoO}_2$ ,  $\text{LiMn}_2\text{O}_4$ , and  $\text{LiNi}_x\text{Mn}_y\text{Co}_{1-x-y}\text{O}_2$ .<sup>126–155</sup> Leung *et al.* provided insight into the mechanism of ALD coating on

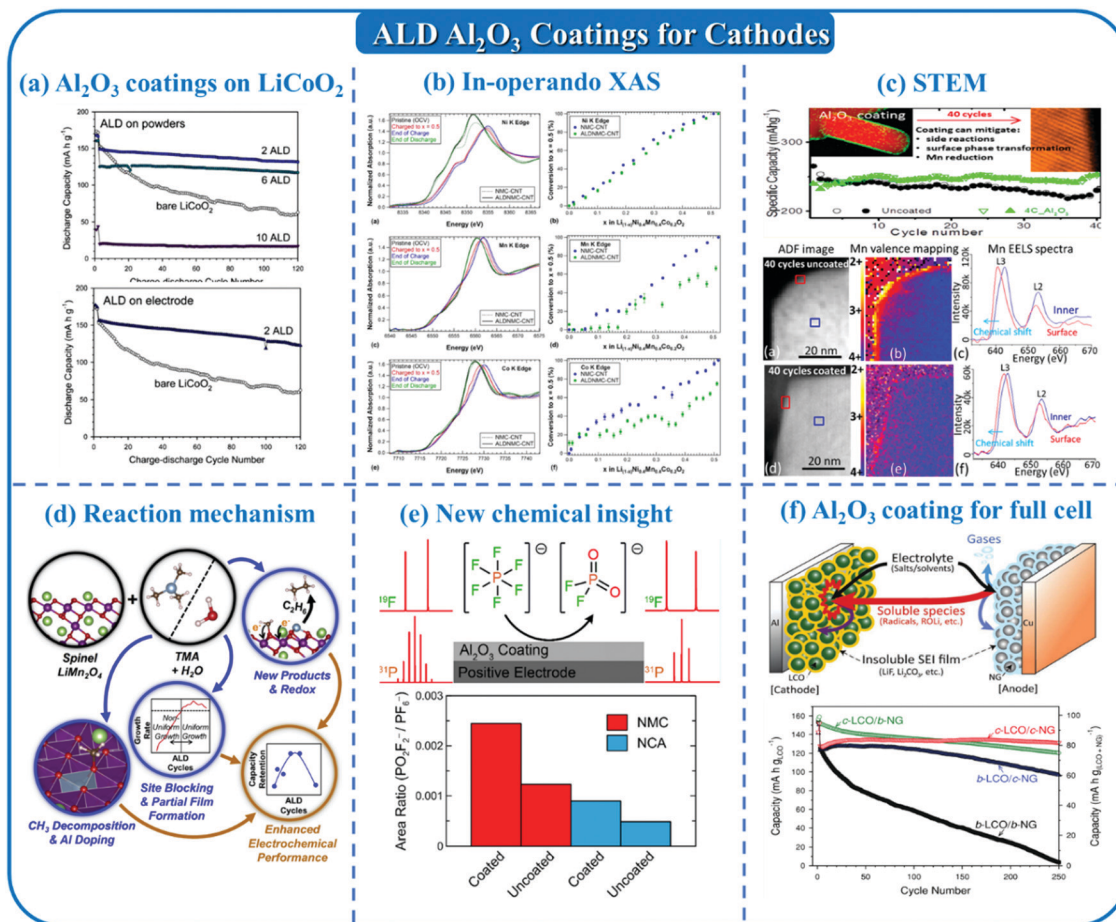


Fig. 7 Characterization and application of ALD  $\text{Al}_2\text{O}_3$  coatings for cathode materials: (a) comparison between ALD coating directly on powders and electrodes; (b) *in operando* XAS for ALD coated cathodes; (c) STEM for interface characterization; (d) reaction mechanism during an ALD process for cathode applications; (e) effects of ALD coating on chemical reactions; (f)  $\text{Al}_2\text{O}_3$  coating for full cells.

the interface of cathode materials by first-principles calculations.<sup>156</sup> The results revealed that with the oxide coating,  $e^-$  tunnelling to the adsorbed ethylene carbonate (EC) falls within the non-adiabatic regime, resulting in reduced electrolyte decomposition. To better understand the mechanism of ALD  $\text{Al}_2\text{O}_3$  coating for cathodes, *in operando* synchrotron-based X-ray diffraction (XRD) and *in operando* X-ray absorption near edge structure spectroscopy (XANES) were carried out to probe the structure and interfacial chemistry of cathode materials of  $\text{LiNi}_{0.4}\text{Mn}_{0.4}\text{Co}_{0.2}\text{O}_2$  cathodes during electrochemical cycling.<sup>157</sup> The *operando* XRD results indicated that the ALD  $\text{Al}_2\text{O}_3$ -coated electrodes displayed a higher level of reversibility in the shift of  $d$ -spacing following charge to 4.7 V. Moreover, as shown in Fig. 7(b), the *operando* XANES data revealed that the ALD coating can suppress the transformation of Co and Mn at low capacities, which was attributed to the protection of the Ni by preventing side reactions of the highly reactive oxygen at the Ni sites with the electrolyte and enabling reversible cycling.<sup>157</sup> Besides synchrotron-based X-ray techniques, electron microscopy is another powerful tool to study the structure and morphology of the coatings. Wang's group used aberration-corrected scanning transmission electron microscopy (STEM) and high-efficiency spectroscopy to characterize and

understand the functions and roles of the ALD  $\text{Al}_2\text{O}_3$  coating layer for the  $\text{Li}_{1.2}\text{Ni}_{0.2}\text{Mn}_{0.6}\text{O}_2$  cathode,<sup>158</sup> as shown in Fig. 7(c). The atomic-level imaging and nanoscale chemical composition analysis from STEM and EELS revealed that the ALD  $\text{Al}_2\text{O}_3$  coating can mitigate the side reactions between cathode and electrolyte, eliminate the surface structure transformation, and suppress the reduction of Mn at the particle surface. Most of the reported studies believe that the ALD  $\text{Al}_2\text{O}_3$  plays a role as a chemical scavenger of corrosive HF and the physical blockage of electrolyte decomposition. However, Dahn's group proposed a new mechanism recently, combining published thermochemistry data with new density functional theory calculations.<sup>159</sup> As shown in Fig. 7(e),  $^{19}\text{F}$  and  $^{31}\text{P}$  solution nuclear magnetic resonance spectroscopy were applied to understand the surface chemistry. Their results showed that the  $\text{LiPF}_6$ -containing liquid electrolyte solution can chemically react with ALD  $\text{Al}_2\text{O}_3$  cathode coatings to produce  $\text{LiPO}_2\text{F}_2$ , which is a well-known and effective electrolyte additive. Moreover, it is a universal phenomenon observed in both NMC622 and NCA cathodes with ALD  $\text{Al}_2\text{O}_3$  coating, in which  $\text{LiPO}_2\text{F}_2$  is found in electrolyte solutions stored for 14 days.

Generally, ALD  $\text{Al}_2\text{O}_3$  has been widely recognized and proven as an effective coating for various cathode materials with

enhanced electrochemical performances. Potential mechanisms were proposed to explain the functions of the ALD  $\text{Al}_2\text{O}_3$  layers. The most popular mechanism is that the ALD  $\text{Al}_2\text{O}_3$  can prevent electrolyte decomposition, HF corrosion, and transition metal dissolution. However, recent literature suggests the potential for other possibilities. In this case, the functions and roles of ALD  $\text{Al}_2\text{O}_3$  in performance enhancement are still worth further exploration.

Besides ALD  $\text{Al}_2\text{O}_3$ , other metal oxides have also been used as coatings for various cathode materials, including  $\text{ZrO}_2$ ,  $\text{ZnO}$ ,  $\text{TiO}_2$ ,  $\text{CeO}_2$ ,  $\text{Ga}_2\text{O}_3$ ,  $\text{MgO}$  and  $\text{FeO}_x$ .<sup>160–182</sup> Most of these metal oxides showed similar functions with ALD  $\text{Al}_2\text{O}_3$  and the electrochemical performances were enhanced with a few cycles of ALD metal oxide. However, the comparison between different metal oxide coatings is critical. Wang's group first studied ALD  $\text{ZnO}$ ,  $\text{ZrO}_2$ , and  $\text{Al}_2\text{O}_3$  as surface modification layers for  $\text{LiMn}_2\text{O}_4$ .<sup>183</sup> All of the ALD-coated  $\text{LiMn}_2\text{O}_4$  electrodes demonstrated improved cyclability compared to the bare electrode, in which  $\text{ZnO}$  is the most effective oxide coating. However, this conclusion is a bit different from the earlier work on ALD  $\text{ZnO}$  and  $\text{Al}_2\text{O}_3$  for  $\text{LiCoO}_2$ , in which the  $\text{Al}_2\text{O}_3$  coated  $\text{LiCoO}_2$  delivered better performances than that of  $\text{ZnO}$  coated  $\text{LiCoO}_2$ . Sun's group also compared the different metal oxides, including  $\text{Al}_2\text{O}_3$ ,  $\text{TiO}_2$ , and  $\text{ZrO}_2$  as coatings for  $\text{LiCoO}_2$  cathodes,<sup>184</sup> as shown in Fig. 8(a). From their results, the  $\text{Al}_2\text{O}_3$  coating demonstrated the best cycling stability while the  $\text{ZrO}_2$  coating contributes to the best rate capability. The reasons behind the observations can be attributed to multiple factors, including; (1)  $\text{Al}_2\text{O}_3$  possesses the highest bandgap energy ( $E_g = 9.00$  eV) and is most effective in suppressing phase transitions during electrochemical cycling; (2) the higher electrical conductivity of  $\text{ZrO}_2$  leads to higher rate performances. One of the consensuses from this area of research is that ALD  $\text{Al}_2\text{O}_3$  is the best coating among the different metal oxides in terms of cycling stability. Moreover, the electrical

conductivity of metal oxides affects the rate performances of the cathode materials.

Phosphates, including  $\text{FePO}_4$  and  $\text{AlPO}_4$ , are another family of coating material for cathodes, which have also been deposited by ALD.<sup>185–187</sup> For example, as shown in Fig. 8(b),  $\text{FePO}_4$  was developed by Sun's group as a coating for  $\text{LiNi}_{0.5}\text{Mn}_{1.5}\text{O}_4$ .<sup>185</sup> When the  $\text{LiNi}_{0.5}\text{Mn}_{1.5}\text{O}_4$  was coated with 40 cycles of ALD  $\text{FePO}_4$ , the capacity retention increased up to 100%. Compared to the regular metal oxides, ALD  $\text{FePO}_4$  can provide both electron/ion diffusion across the surface. Another candidate material,  $\text{AlPO}_4$ , presented a much higher thermal resistivity than  $\text{Al}_2\text{O}_3$ , leading to enhanced high-temperature electrochemical performances. The DSC profiles of the charged pristine high energy NMC (HEMNC),  $\text{Al}_2\text{O}_3$ -coated HENMC, and  $\text{AlPO}_4$ -coated HENMC are shown in Fig. 8(c). The DSC results show that the decomposition temperatures of pristine high energy NMC (HEMNC),  $\text{Al}_2\text{O}_3$  coated HENMC, and  $\text{AlPO}_4$  coated HENMC are 219 °C, 223 °C, and 237 °C, respectively. The thermal stability improvement induced by the  $\text{AlPO}_4$  coating can be ascribed to the high thermal stability of phosphate, leading to better electrochemical performances at high temperatures.

Metal oxide coatings are still limited by their ionic conductivity and Li-ion transport across the interface of the electrode particles. In this case, the development of surface coatings with Li-ion conductivity is necessary and solid-state electrolyte thin films are the ideal candidates. As shown in Fig. 8(d), Sun *et al.* reported for the first time the ALD solid-state electrolyte (SSE)  $\text{LiTaO}_3$  as a coating for an NMC cathode.<sup>188</sup> A 5 nm  $\text{LiTaO}_3$  coating was proved to be beneficial for preventing transition metal dissolution into the electrolyte and aided in maintaining the microstructure of NMC. As a result, the electrochemical performance of NMC was significantly improved with as low as 5 cycles of  $\text{LiTaO}_3$  coating. Meanwhile, another Li-ion conductive film,  $\text{LiAlO}_2$ , was also used as a surface modification for  $\text{LiCoO}_2$  and NCA.<sup>189–191</sup> For example, Cui's group developed a chemically inert and ionically conductive  $\text{LiAlO}_2$  interfacial

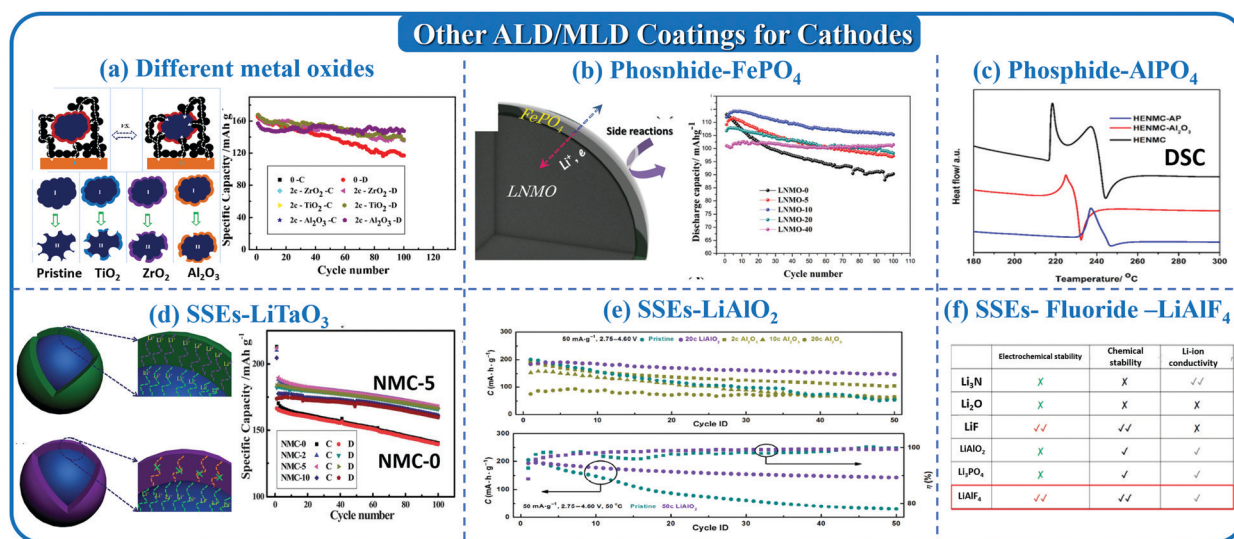


Fig. 8 Other ALD/MLD coatings for cathode applications: (a) different metal oxides; (b)  $\text{FePO}_4$ ; (c)  $\text{AlPO}_4$ ; (d)  $\text{LiTaO}_3$  solid-state electrolyte; (e)  $\text{LiAlO}_2$  solid-state electrolyte; (f)  $\text{LiAlF}_4$  solid-state electrolyte.

layer on LiCoO<sub>2</sub> by ALD. It was found that the LiAlO<sub>2</sub>-coated LiCoO<sub>2</sub> cathode was able to deliver a much higher specific capacity than that of the Al<sub>2</sub>O<sub>3</sub> coating, which can be attributed to the ionic conductivity of LiAlO<sub>2</sub>. Moreover, the stability of the LiAlO<sub>2</sub>-coated LiCoO<sub>2</sub> cathode in an extended electrochemical window of 2.75–4.60 V showed significant improvement compared to the bare LiCoO<sub>2</sub> cathode, as shown in Fig. 8(e). From these studies, it has been proven that Li-ion conductive films fabricated by ALD are more promising as a coating for cathode materials compared to metal oxide coatings. However, the currently developed ALD SSE films still present low ionic conductivity ( $10^{-6}$ – $10^{-9}$  S cm<sup>-1</sup>), which cannot meet the requirements for fast Li-ion transport across the interface. Moreover, the relationship between the ionic conductivity of the coating and the electrochemical performance is still unclear.

Based on computational simulations, fluoride materials have the widest electrochemical windows and are especially favoured for their high potential stability (up to 5 V).<sup>192,193</sup> Fluoride chemistry has been widely studied in the ALD community, for either deposition or etching. Several types of fluorides, including MgF<sub>2</sub>, AlF<sub>3</sub>, and AlW<sub>x</sub>F<sub>y</sub>, were deposited as a coating for high-voltage cathode materials, including LiNi<sub>0.5</sub>Mn<sub>1.5</sub>O<sub>4</sub> and LiCoO<sub>2</sub>.<sup>194–199</sup> AlF<sub>3</sub> is the most popular fluoride ALD coating, which uses TMA as the Al precursor and another F containing compound (HF, TaF<sub>5</sub> or hexafluoroacetylaceton) as the F precursor. As a result, the cathode materials coated with ALD fluoride materials delivered remarkable performances at high voltage. However, the poor ionic conductivity of metal fluorides such as AlF<sub>3</sub> has limited their further improvement. In this case, Cui's group designed an ALD LiAlF<sub>4</sub> process to be applied for high Ni content NMC811.<sup>200</sup> Compared to other potential coatings such as Li<sub>3</sub>N, Li<sub>2</sub>O, LiF, LiAlO<sub>2</sub>, and Li<sub>3</sub>PO<sub>4</sub>, LiAlF<sub>4</sub> demonstrates a wider electrochemical window and ideal chemical stability (Fig. 8(f)). The ionic conductivity of ALD LiAlF<sub>4</sub> is around  $3.5 \pm 0.5 \times 10^{-8}$  S cm<sup>-1</sup>, which is much higher than that of the metal fluoride of LiF and AlF<sub>3</sub>. The ALD interfacial layer is chemically and electrochemically

stable as well as Li-ion conductive, resulting in improved cycling stability and rate performances of the NMC-811 cathode.

Most ALD coatings are generally amorphous and used as deposited. The continuous ALD films will shrink and form island-like structures after high-temperature annealing.<sup>201</sup> However, recent studies have discovered that post-treatment of ALD coatings can modify the structures of the cathode material itself. As shown in Fig. 9(a), a two-step surface modification method was developed by the Sun's group to deposit ALD TiO<sub>2</sub> on spinel LiNi<sub>0.5</sub>Mn<sub>1.5</sub>O<sub>4</sub> cathode materials with a subsequent post-annealing treatment.<sup>202</sup> A TiMn<sub>2</sub>O<sub>4</sub>-like spinel phase was formed resulting from the reaction of TiO<sub>2</sub> with the surface LiNi<sub>0.5</sub>Mn<sub>1.5</sub>O<sub>4</sub>. The TiMn<sub>2</sub>O<sub>4</sub>-like spinel phase can combat the impedance growth from continuous irreversible structural transition and alleviate the electrolyte decomposition during electrochemical cycling. The electrochemical results revealed that 25 ALD TiO<sub>2</sub> cycles appeared to produce the optimal thickness that yields improved stability, coulombic efficiency, discharge capacity, and rate capability.

In addition to the degradation of the cathode surface, the permeation and penetration of liquid electrolytes along the grain boundaries and cracks in the secondary particles are another serious issue that worsens the decay of the electrochemical performance. In particular, for the Ni-rich NMC (LiNi<sub>x</sub>Mn<sub>y</sub>Co<sub>1-x-y</sub>O<sub>2</sub>) cathode, when the Ni content is above 0.8, there is a phase transition that occurs near the end of charge, causing an abrupt anisotropic shrinkage (or expansion during discharge), which is similar to LiNiO<sub>2</sub>. This phase transition has residual stress that causes internal microcracks and allows the cracks to propagate to the surface of the cathode particles, leading to the electrolyte penetration and degradation of the exposed surfaces.<sup>203</sup> To address this challenge, the ALD solid-state electrolyte Li<sub>3</sub>PO<sub>4</sub> was infused into the grain boundaries of a Ni-rich NMC cathode material,<sup>204</sup> as shown in Fig. 9(b). 10 nm of Li<sub>3</sub>PO<sub>4</sub> was firstly deposited on the surface of Ni-rich NMC by ALD. After annealing at 600 °C for two hours in the air, the Li<sub>3</sub>PO<sub>4</sub> was successfully infused along the grain boundaries of the secondary particles. The infused solid-state

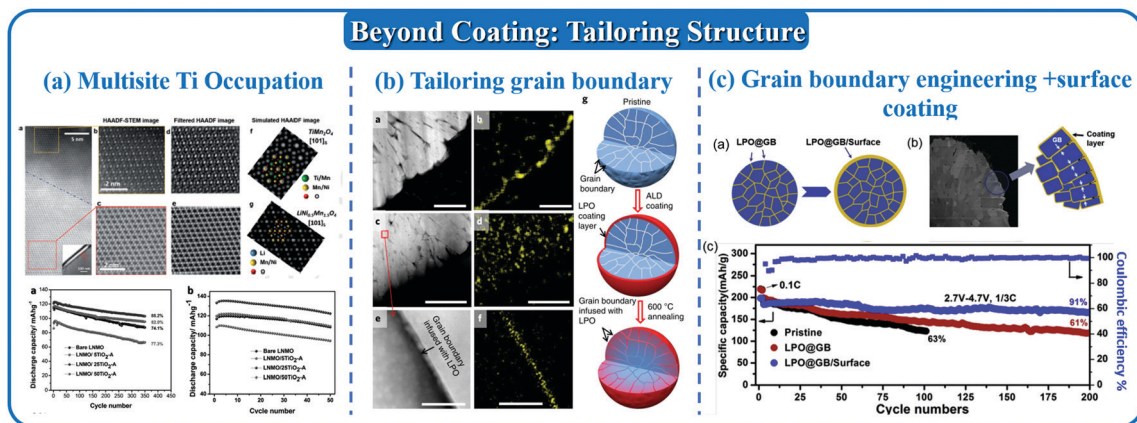


Fig. 9 Function of ALD films more than coating. (a) Multisite Ti occupation by ALD TiO<sub>2</sub>; (b) tailoring grain boundaries with ALD Li<sub>3</sub>PO<sub>4</sub>; (c) dual functions of grain boundary engineering and surface coating.

electrolyte within the grain boundaries played several roles in improving the electrochemical performances, including; (1) providing fast channels for Li-ion transport; (2) preventing the penetration of the liquid electrolyte into the boundaries; (3) eliminating intergranular cracking and layered-to-spinel phase transformation. The capacity retention and voltage stability of the cathode were significantly improved with this grain boundary modification. However, after thermal infusion, the ALD  $\text{Li}_3\text{PO}_4$  almost completely disappeared from the surface of the NMC particles, resulting in exposure of the particle surface to the electrolyte. With this in mind, based on the  $\text{Li}_3\text{PO}_4$  infused NMC cathode, another layer of ALD  $\text{Li}_3\text{PO}_4$  was further deposited on the exterior surface.<sup>205</sup> With the dual functional grain boundary engineering and surface coating, superior cycling stability was achieved even with high voltage cut-offs (91% retention after 200 cycles at 2.7–4.7 V), as shown in Fig. 9(c).

Until recently, MLD coatings have rarely been reported as coatings for cathode materials. The major concern is the high voltage stability of the organic components in the MLD films. However, it is still interesting to explore the application of MLD coatings for cathode materials due to the unique properties of MLD, such as high flexibility. To extend the applicability of MLD-type coatings, new polymers with good electronic or ionic conductivity and high voltage stability should be developed for cathode applications. Moreover, the films derived from MLD are another possibility for cathodes. For example, a uniform carbon- $\text{Al}_2\text{O}_3$  composite coating was deposited on NMC-622 by the pyrolysis of MLD alucone under argon.<sup>206</sup> The C- $\text{Al}_2\text{O}_3$  coated NCM-622 exhibited enhanced electrochemical performances with higher reversible capacity, better rate capability, and stability. In the MLD-derived composite coating, the  $\text{Al}_2\text{O}_3$  plays a role in suppressing the undesirable side reactions and stabilizing the layered structure, and the conductive carbon in the composite enhances the transport of electrons.

In this section, we have summarized the application of ALD/MLD films in addressing the interfacial issues for different cathode materials. (1) ALD  $\text{Al}_2\text{O}_3$  is the most popular coating for cathode materials and has been widely studied over the past ten years. The electrochemical performances are effectively enhanced with ultrathin  $\text{Al}_2\text{O}_3$  coatings. Furthermore, the mechanism and interface evolution have been deeply understood using advanced characterization techniques. In addition, other metal oxides have also been deposited on cathode materials, and among them, ALD  $\text{Al}_2\text{O}_3$  is generally considered as the best coating in terms of electrochemical performance. (2) Solid-state electrolytes have been deposited by ALD as coatings for cathode materials, such as  $\text{Li}_3\text{PO}_4$  and  $\text{LiAlO}_2$ . Compared to the metal oxides, even with thicker layers, solid-state electrolyte coatings enable better Li-ion conduction across the interface and enhanced performance. (3) Other ALD materials, including phosphates and fluorides are developed to modify the interface. On one hand, the metal phosphates present higher thermal resistivity, which is beneficial for high-temperature applications. On the other hand, the metal fluoride demonstrates a wide electrochemical window for high voltage cathode materials. (4) Beyond surface modification, ALD films are further designed

to tailor the structure of the cathode, such as preventing phase transition and engineering grain boundary.

The general requirements of the coatings for cathode materials are discussed above, including controllable thickness, uniformity and conformity. These requirements can be achieved with ALD/MLD techniques; however, there are extra requirements for the application of ALD materials as coating layers. (1) A wide electrochemical window. The ALD coatings for cathodes are required to be electrochemically stable at high potential, preventing the decomposition of the liquid electrolyte. (2) Chemically stable with a cathode and an electrolyte. The ALD coatings on the cathode are required to be stable when deposited on the cathode and in contact with liquid electrolytes. (3) High Li-ion conductivity. The fast Li-ion transport across the interface leads to low resistance and better rate performances. A thicker coating also can be realized with high Li-ion conductivity. (4) Good mechanical properties. The mechanical properties are also critical for maintaining the structure and volume expansion of the materials, which should be considered for the coating design.<sup>207</sup>

#### 2.1.1.3 ALD/MLD for anode/electrolyte interface engineering.

The SEI layer on the anode materials is formed due to the decomposition of the electrolyte at the low electrochemical potential. The SEI continuously grows in these electron/electrolyte-participated reactions and the thickness of the SEI layer is not homogeneous with dual-layer structure and various components. The generally recognized description of the SEI structure is the mosaic model, in which the layer close to the anode surface contains species of low oxidation states of  $\text{Li}_2\text{O}$ ,  $\text{Li}_3\text{N}$ ,  $\text{LiF}$ ,  $\text{LiOH}$ , and  $\text{Li}_2\text{CO}_3$ . The outer layer near the surface consists of high oxidation state species such as  $\text{ROCO}_2\text{Li}$ ,  $\text{ROLi}$ , and  $\text{RCOO}_2\text{Li}$ , which is related to the solvent decomposition process. It is widely regarded that the properties of the SEI layer are the key factor determining the electrochemical performances of the anode materials. Graphite is a commercialized anode material that is widely used for its low electrochemical potential, minimal volume change, and low cost. The solid electrolyte interphase (SEI) layer related to the side reactions between the anode materials and electrolyte is one of the key factors determining the overall electrochemical performance of the battery. Lee's group was the first to report ALD  $\text{Al}_2\text{O}_3$  as a coating for graphite,<sup>208</sup> as shown in Fig. 10(a). Graphite with an ALD  $\text{Al}_2\text{O}_3$  coating on both the powder and electrodes was compared at an increased temperature of 50 °C for charge-discharge cycling. The decomposition of the SEI at increased temperature is exothermic and considered to initiate thermal runaway. The electrochemical data indicated that the  $\text{Al}_2\text{O}_3$  coating on graphite electrodes presented much better cycling performance than that of  $\text{Al}_2\text{O}_3$  coating directly on the powders. The mechanism is explained in the schematic diagram in Fig. 10(a). When depositing  $\text{Al}_2\text{O}_3$  on the powders, the graphite and current collector were isolated by the insulating  $\text{Al}_2\text{O}_3$  film and the electrical conductivity was disrupted. Moreover, ALD  $\text{Al}_2\text{O}_3$  coated directly on the electrode enables electrical pathways between interconnected particles, which is necessary for electronic conductivity. Another interesting work

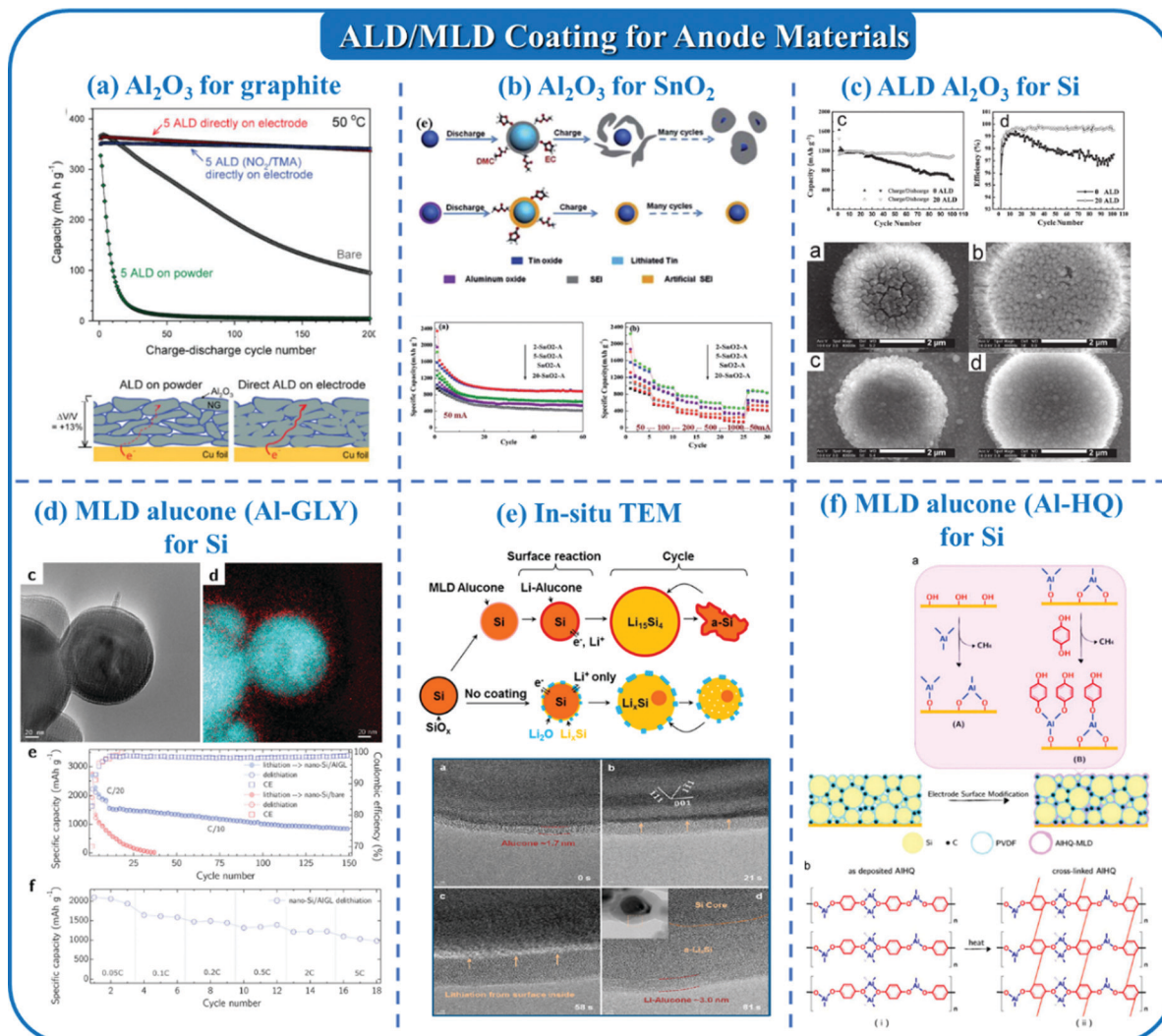


Fig. 10 ALD/MLD coatings for anodes: (a) ALD  $\text{Al}_2\text{O}_3$  for graphite; (b) ALD  $\text{Al}_2\text{O}_3$  for  $\text{SnO}_2$ ; (c) ALD  $\text{Al}_2\text{O}_3$  for Si; (d) MLD alucone (Al-GLY) for Si; (e) *in situ* TEM for MLD alucone coated Si; (f) MLD alucone (Al-HQ) for Si.

demonstrated the application of ALD  $\text{Al}_2\text{O}_3$  coatings on both  $\text{LiCoO}_2$  and graphite for full cells,<sup>209</sup> as shown in Fig. 7(f). It was observed that the full cell with coating on both the cathode and anode delivered better electrochemical performance compared to that of the bare electrodes and coating on an individual electrode. ALD and MLD coatings on other carbon anode materials, such as carbon nanotubes and carbon fibres, have also been reported to improve electrochemical performance.<sup>210–212</sup>

Sn-Based materials, including tin oxides, tin sulfides, and stannates, are attractive anode materials for LIBs with high theoretical capacity and improved safety.<sup>213–215</sup> However, the large volume fluctuation of Sn-based materials is the biggest challenge limiting their further application.<sup>216</sup> The volume change during electrochemical cycling causes the continuous consumption of electrolyte and accumulation of a thick SEI layer, leading to the performance degradation of Sn-based materials. To address these issues, Sun's group demonstrated ALD  $\text{Al}_2\text{O}_3$  coating on  $\text{SnO}_2$  based anodes<sup>217</sup> (Fig. 10(b)). It was found that the particle sizes of the  $\text{SnO}_2$  electrodes affected the

volume change of the electrodes, resulting in the need for  $\text{Al}_2\text{O}_3$  coating layers with optimized thickness. The well-defined ALD  $\text{Al}_2\text{O}_3$  layer can (1) relieve the volume expansion and mechanical failure; (2) act as an artificial interface to block the undesirable reactions and decomposition of the electrolyte, resulting in significantly enhanced cycling stability. Furthermore, other ALD films, such as  $\text{HfO}_2$  and  $\text{TiO}_2$  have also been deposited as protective coatings for Sn-based anodes, including Sn,  $\text{SnO}_2$ , and  $\text{SnS}_2$ .<sup>218–222</sup> Nevertheless, it has been proven difficult for thin ALD coatings to accommodate the large volume fluctuation of Sn-based anodes. Fan's group designed a hollow wire-in-tube structure of  $\text{SnO}_2@/\text{TiO}_2$  on a carbon cloth with a high mass loading by ALD.<sup>223</sup> This hollow  $\text{SnO}_2@/\text{TiO}_2$  structure presented radically improved rate capability and cycling stability compared to both bare  $\text{SnO}_2$  nanowires and solid electrodes. This study extends the application of ALD for anodes beyond surface coating to nanostructure engineering. Other kinds of anode materials, including  $\text{Li}_4\text{Ti}_5\text{O}_{12}$ ,  $\text{MoO}_3$ ,  $\text{MnO}_x$ ,  $\text{NiCo}_2\text{O}_4$ ,  $\text{Fe}_2\text{O}_3$ , and  $\text{Fe}_3\text{O}_4$ , *etc.*, have also been studied

as ALD coatings designed to improve the electrochemical properties of anode materials.<sup>224–238</sup>

Si is an excellent alternative for graphite due to its high theoretical capacity of 4200 mA h g<sup>-1</sup>, low discharge potential (~0.2 to 0.3 V vs. Li/Li<sup>+</sup>), natural abundance, low cost and environmental friendliness.<sup>239–243</sup> Si and its composites have attracted enormous attention in recent years for industrial applications. However, the alloying process of Si anodes leads to a large volume expansion (~400%) during cycling, low ionic conductivity, and unstable SEI.<sup>244</sup> Similar to other anode materials, the SEI is a critical factor for Si-based electrodes, and ALD/MLD displays great potential to stabilize the interface. Huang's group first reported ALD Al<sub>2</sub>O<sub>3</sub> on patterned amorphous Si anodes for LIBs.<sup>245</sup> As shown in Fig. 10(c), 20 cycles ALD alumina-coated Si electrodes presented excellent cycling performance with an initial charge capacity of 1125 mA h g<sup>-1</sup> and a retained capacity of 1100 mA h g<sup>-1</sup> after 100 cycles. From the SEM images after cycling, cracks are observed on the bare Si columns. Remarkably, with the conformal ALD Al<sub>2</sub>O<sub>3</sub> coating, the small cracks and pinholes of Si were reduced, resulting in high coulombic efficiency and good cycling performance. The reduced cracking with ALD Al<sub>2</sub>O<sub>3</sub>-coated Si was also investigated by *in situ* atomic force microscopy (AFM) in detail.<sup>246</sup> It has been proven through first-principles investigations that the intrinsic ionic conductivity of ALD Al<sub>2</sub>O<sub>3</sub> is very low, but the Li diffusion energy barrier becomes lower as lithiation proceeds and LiAlO<sub>2</sub> is formed.<sup>247</sup> To further improve the electrochemical performance, Hwang's group proposed multiple approaches combining the ALD technique with a vinylene carbonate (VC) electrolyte additive.<sup>248</sup> With the combination of these strategies, the stability of the Si anode was significantly improved due to the formation of a more stable SEI. Moreover, other ALD coatings, such as TiN, TiO<sub>2</sub>, and ZnO, were used for Si anodes and led to improved performances.<sup>249–254</sup> Mitlin's group provided a detailed comparison between Al<sub>2</sub>O<sub>3</sub>, TiN, and TiO<sub>2</sub> coatings on the inner, the outer, or both surfaces of hollow Si nanotubes.<sup>255</sup> Optimal performance was achieved for Si nanotubes with ALD TiO<sub>2</sub> on both sides, enabling a capacity retention of 1700 mA h g<sup>-1</sup> after 200 cycles at 0.2C, which is significantly improved compared to the bare Si nanotubes. The TiO<sub>2</sub> layer, which consists of amorphous TiO<sub>2</sub> and cubic LiTiO<sub>2</sub>, displayed both high ionic and electronic conductivity leading to fast lithiation kinetics. However, ALD films with only high electronic (TiN) or only ionic (Al<sub>2</sub>O<sub>3</sub>) conductivity are not nearly as effective.<sup>255</sup>

In contrast to ALD materials, MLD layers have become more attractive as coatings for Si anodes. The MLD films, including organic–inorganic hybrid layers and polymer layers, are considered to be more mechanically robust and highly flexible, which is beneficial for relieving the large volume change in the Si anode during lithiation and delithiation.<sup>256</sup> Ban's group first applied MLD alucone for Si nanoparticles, using TMA and glycerol (C<sub>3</sub>H<sub>5</sub>(OH)<sub>3</sub>) forming the Al–GL hybrid films (Fig. 10(d)).<sup>257</sup> The Al–GL coating on the Si anode provided significant improvement in cycling stability, rate, and CE. It was concluded that the Al–GL layers maintained a

mechanically robust, resilient, and highly conductive network for the Si electrodes, and are stable against liquid electrolyte, allowing for long and stable cycle life. To understand the influence of MLD alucone coatings on the performances of Si nanoparticles, *in situ* TEM analysis was carried out on both uncoated and alucone-coated Si nanoparticles, as shown in Fig. 10(e).<sup>258,259</sup> The MLD alucone coating on Si nanoparticles can reduce the formation of Li<sub>2</sub>O, resulting in fast and highly reversible lithiation kinetics. It was also clarified that the alucone coating possesses good mechanical flexibility and fast Li<sup>+</sup> conductivity.<sup>258</sup> Furthermore, the DFT calculations by Ma *et al.* revealed that the alucone film is electronically and ionically conductive after saturation with Li atoms, which is in agreement with the observed morphology and electrochemical analysis.<sup>260</sup> Rather than alucone with glycerol linkers, another type of MLD alucone (Al-dioxybenzene, Al-HQ) was developed using TMA and hydroquinone as precursors (Fig. 10(f)).<sup>261</sup> During the MLD deposition and subsequent treatment, a longitudinal crosslinking reaction occurred between the aluminum-dioxybenzene chains. The 3D cross-linked network led to improved conductivity and mechanical properties. High flexibility of the Al-HQ coating enabled the accommodation of volume expansion and maintenance of the mechanical integrity of the Si electrodes, resulting in excellent cycling performance and high rate capability with a reversible capacity of over 1500 mA h g<sup>-1</sup> after 200 cycles. More recently, Ban's group further developed a nanoscale polyamide coating by MLD on a Si anode with excellent electrochemical performance.<sup>262</sup>

In this section, we discuss the typical examples of ALD/MLD coatings for anode materials in LIBs, such as graphite, Sn-based materials, and Si anodes. The roles of ALD/MLD coatings are summarized as (1) forming a stable artificial SEI to prevent the side reactions between anodes and liquid electrolytes. (2) Relieving the volume change of alloy-based anodes (Sn and Si). ALD Al<sub>2</sub>O<sub>3</sub> is the most popular and widely developed coating for different anodes. However, due to the volume change of most anode materials, coatings with better mechanical properties are highly desired. In this case, MLD coatings with high flexibility are more promising as protective layers for anode materials, especially for Si anodes.

There is still significant room for exploring the engineering of electrode interfaces by ALD/MLD. Firstly, better mechanical properties, including flexibility and stiffness, are among the major requirements for accommodating the large volume changes. Secondly, both ionic and electronic conductivity are required to provide pathways for Li-ions and electrons across the surface of the electrodes. Thirdly, the chemical and electrochemical stabilities towards liquid electrolytes are the most basic requirements for a high-performance ALD/MLD coating.

**2.1.1.4 ALD/MLD for 2D/3D micro-batteries.** Additionally, as unique thin film deposition techniques, ALD/MLD are considered as promising approaches for the fabrication of thin-film batteries and 3D micro-batteries.<sup>35,263</sup> It is possible to deposit uniform electrodes and electrolytes on 2D flexible substrates

(such as polymers) and more complex 3D substrates with these techniques.

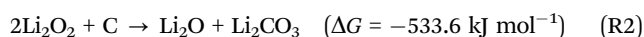
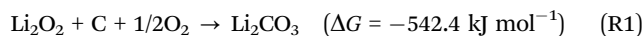
A thin film solid-state battery (SSB) was demonstrated by Stewart *et al.*, in which the tin oxynitride was deposited by ALD using tetrakisdimethylamido(tin), H<sub>2</sub>O, and N<sub>2</sub> plasma as precursors.<sup>264</sup> LiPON was deposited by ALD as SSEs and Li was deposited by e-beam evaporation. In the thin film SSBs, the SnN<sub>y</sub> anodes demonstrated more stable performances than the SnO<sub>2</sub> or SnO<sub>x</sub>N<sub>y</sub> films, which retained 75% of their capacity over 200 cycles compared to only 50% for SnO<sub>2</sub>. Another example of thin film SSBs was reported by the same group, in which LiPON was deposited by ALD as an SSE and LiCoO<sub>2</sub> and Si were deposited as the cathode and anode, respectively.

Besides the 2D configuration, the 3D electrodes of hierarchical CNTs@FePO<sub>4</sub> architecture were designed by ALD. Compared to the 2D electrodes, the 3D CNTs@FePO<sub>4</sub> nanostructure displays 16 and 33 times higher areal capacity Li and Na ion batteries, which is 64 and 33 μA h cm<sup>-2</sup> after 180 cycles, respectively.<sup>112</sup> Lethien's group reported another 3D electrode design by ALD for micro-batteries, in which an anatase TiO<sub>2</sub> negative electrode was coated on 3D tubes with Li<sub>3</sub>PO<sub>4</sub> as an electrolyte.<sup>265</sup> A high surface capacity of 0.37 mA h cm<sup>-2</sup> was achieved by this proposed approach.

Pearse *et al.* also demonstrated a 3D micro full cell by ALD, in which all the active battery components including electrodes, solid electrolyte, and current collectors were deposited by ALD onto Si wafers with arrays.<sup>266</sup> The 3D micro-battery fabricated by ALD utilized a prelithiated LiV<sub>2</sub>O<sub>5</sub> as a cathode, Li<sub>2</sub>PO<sub>2</sub>N as a solid electrolyte, SnN<sub>x</sub> as an anode and TiN and Ru as current collectors with a deposition temperature at or below 250 °C. Remarkably, the 3D micro-batteries fabricated by ALD exhibit a reversible capacity of 2.6 μA h cm<sup>-2</sup> up to 100 cycles. Moreover, by using a 3D substrate with ALD deposition, the areal discharge capacity of the cell is 9.3 times higher than the integrating planar cells. This work provided a new opportunity for the realization of long-sought 3D micro-batteries by ALD techniques.

### 2.1.2 ALD/MLD for next generation Li batteries

**2.1.2.1 ALD/MLD for Li–O<sub>2</sub> batteries.** Li–O<sub>2</sub> batteries provide high theoretical energy densities up to 3–5 times larger than LIBs and have significant potential for application in EVs and large-scale energy storage systems.<sup>267–269</sup> However, the development of Li–O<sub>2</sub> batteries has been greatly hindered by the sluggish oxygen evolution reaction (OER) process during charge, which is caused by the poor charge conductivity of the discharge product, Li<sub>2</sub>O<sub>2</sub>. In addition, the liquid electrolyte is decomposed from reactive superoxide species during discharge, and Li<sub>2</sub>O<sub>2</sub> suffers from side reactions with the defect sites on the carbon cathode.<sup>270,271</sup> A thin layer of Li<sub>2</sub>CO<sub>3</sub> could be created at the interface of Li<sub>2</sub>O<sub>2</sub> and carbon, as shown in reactions (R1) and (R2).



The insulating nature of carbonate species generates high interfacial resistance, contributing to the large voltage polarization

during discharge/charge.<sup>272</sup> Hence, surface modification of the air electrodes is critical to prevent the accumulation of side products on the carbon surface and tune the formation mechanism of the discharge products. ALD not only enables uniform surface coating on flat surfaces but can also form thin films on 3D or mesoporous structures, which is ideal for modifying the air electrode in Li–O<sub>2</sub> batteries. Amine's group demonstrated ALD deposited Al<sub>2</sub>O<sub>3</sub> on super P conductive carbon particles to cover the defect sites, preventing unwanted side reaction of the electrolyte with the carbon.<sup>273</sup> Then Pd nanoparticles were further coated on the carbon surface by ALD. Pd nanoparticles created active sites for crystalline Li<sub>2</sub>O<sub>2</sub> formation and served as the catalyst during the Li<sub>2</sub>O<sub>2</sub> decomposition (Fig. 11(a)). Compared to the charge overpotential of the bare carbon-based cathode (over 1 V), the ALD-coated material shows a much lower charge potential of 0.2 V. Density functional theory (DFT) calculations revealed that the Al<sub>2</sub>O<sub>3</sub> was inert to TEGDME solvent and could prevent the dissociation of TEGDME molecules in the electrolyte.

Detailed studies (Fig. 11(b)) on Pd/Al<sub>2</sub>O<sub>3</sub>/C materials with 1, 3 and 10 ALD cycles of Pd catalysts revealed the role of ALD in relation to the electrochemical performance of Li–O<sub>2</sub> batteries.<sup>274</sup> ALD enabled the formation of Pd nanoparticles in the range of 2–8 nm with uniform dispersion on the carbon substrate. Although with high charge overpotential, the Pd/Al<sub>2</sub>O<sub>3</sub>/C electrode with 3 ALD cycles delivers a high capacity of 6600 mA h g<sup>-1</sup>, suggesting that the full coverage of the carbon defects may prevent the decomposition of the electrolyte. For the case of the electrode with 10 ALD cycles, the cell shows a low charge overpotential of 3.3 V, which is probably due to improved electronic conductivity and more crystallization sites created by the Pd nanoparticles on the electrode surface. Similar nano-architecture by ALD could also be expanded to other catalysts such as Pd/ZnO/C.<sup>275</sup> The catalyst further lowered the charge potential to 3.0 V, supporting the synergic effect of ZnO and Pd nanoparticles. Subsequently, other ALD metal oxides, including TiO<sub>2</sub>, In<sub>2</sub>O<sub>3</sub>, Fe<sub>2</sub>O<sub>3</sub>, and ZnO, were deposited either on carbon electrodes or catalysts to prevent the corrosion and side reactions between air electrodes and electrolyte.<sup>276–281</sup> The electrode architecture achieved by ALD opened a new door for the prevention of side reactions and guided the new design of functional catalysts in Li–O<sub>2</sub> batteries.

The defect sites on the carbon could react with Li<sub>2</sub>O<sub>2</sub> compromising the electrochemical performance, which is difficult to rule out when focusing on fundamental studies. We employed ALD to cover the surface defect sites and silver clusters are further loaded to probe the different scenarios during the discharge process in Li–O<sub>2</sub> batteries.<sup>282</sup> Silver clusters with different sizes (3, 9, and 15 atoms) were deposited on ALD-modified carbon by the magnetron sputtering method.<sup>283–286</sup> It was found that the morphology of the discharge products has a high dependency on the cluster size, and the Li<sub>2</sub>O<sub>2</sub> formation is through a solution-mediated process (Fig. 11(c)). DFT results supported that superoxide species had a weaker bonding to Ag<sub>15</sub> clusters and thus LiO<sub>2</sub> reached a supersaturated solution, growing on the nucleation sites as LiO<sub>2</sub> containing

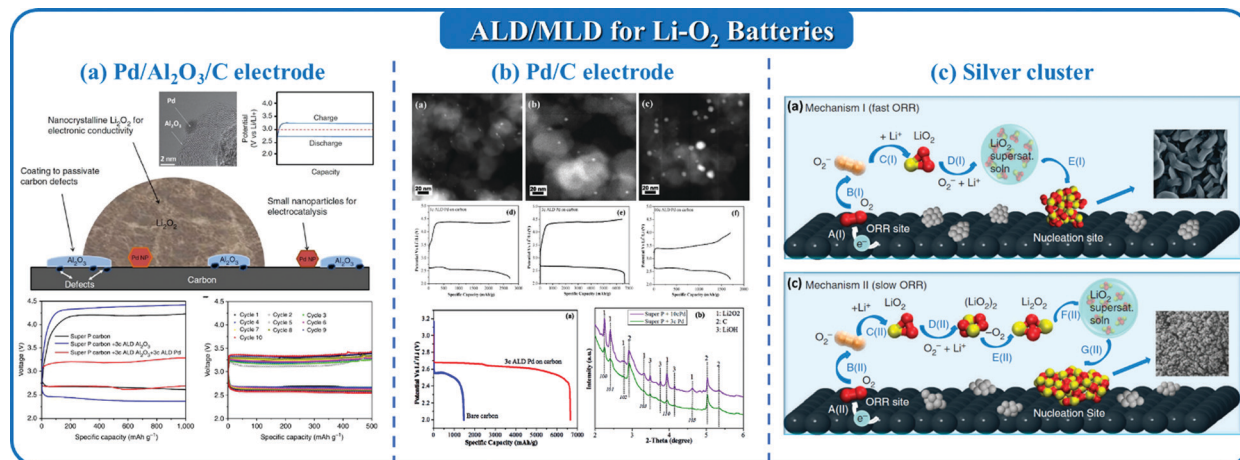


Fig. 11 ALD/MLD for Li–O<sub>2</sub> air electrode design: (a) Pd/Al<sub>2</sub>O<sub>3</sub>/C; (b) Pd/C; (c) silver cluster.

product and leading to the low charge overpotential. The form of LiO<sub>2</sub> was proved to be present in Li–O<sub>2</sub> cells and showed fast kinetics during charge.<sup>267</sup> Meanwhile, in Ag<sub>3</sub> and Ag<sub>9</sub> based electrodes, LiO<sub>2</sub> underwent a disproportionation reaction to form Li<sub>2</sub>O<sub>2</sub> in the electrolyte and then deposited on the electrode surface, resulting in high charge potential in galvanostatic mode. Another effective catalyst deposited by ALD for air electrodes for Li–O<sub>2</sub> batteries is Ru or RuO<sub>2</sub> nanoparticles.<sup>287</sup> Wang's group reported the selective deposition of Ru onto the *b* planes of TiSi<sub>2</sub> nanonets by ALD as a catalyst for Li–O<sub>2</sub> batteries.<sup>288</sup> The selective deposition was a result of different interface energetics proven by DFT calculations. As a result, extensive cyclability (>100 cycles) with confirmed Li<sub>2</sub>O<sub>2</sub> formation and decomposition was obtained. Furthermore, Sun and his group further designed a 3D nanostructure using a conductive and porous matrix of Mn<sub>3</sub>O<sub>4</sub> nanowire and carbon nanotube composite film as substrates. Then, the ALD RuO<sub>2</sub> nanoparticles with an extremely low loading (just 2.84 wt%) were uniformly deposited on the matrix to form the composite electrode.<sup>289</sup> The Mn<sub>3</sub>O<sub>4</sub>/CNTs–RuO<sub>2</sub> electrode delivered a high specific capacity, improved round-trip energy efficiency, and ultra-long cycle life.

In this section, the recent results of the application of ALD for Li–O<sub>2</sub> batteries have been summarized and discussed. Several critical challenges for Li–O<sub>2</sub> batteries were effectively addressed by ALD. Firstly, catalysis was widely used to decrease the overpotential for the oxygen reduction reaction (ORR) and oxygen evolution reaction (OER). ALD is an ideal coating technique for catalysts in Li–O<sub>2</sub> batteries, especially for noble metals such as Pd and Ru. Secondly, the corrosion and side reaction between the carbon electrodes and electrolyte is one of the major issues limiting the performance of Li–O<sub>2</sub> batteries. Benefitting from the uniform coverage of ALD, thin metal oxides were used to protect the carbon electrode and catalysis with significantly improved cycling stability.

**2.1.2.2 ALD/MLD for Li–S batteries.** Li–S batteries are highly sought after for their high theoretical energy density of 2600 W h g<sup>−1</sup> and the wide abundance of elemental sulfur.

However, several problems have plagued the development of Li–S batteries including poor electrical conductivity of sulfur, side reactions of electrode materials with electrolyte, Li dendrite formation, and dissolution of polysulfide species, leading to rapid capacity fading. ALD/MLD are promising techniques that have been shown to eliminate many of these issues through various mechanisms. For example, there have been several studies using ALD/MLD modified cathodes to prevent polysulfide dissolution.<sup>290–297</sup> Other cases have used ALD to modify the separator and trap dissolved polysulfides.<sup>298</sup> More recently, ALD has been applied to Li metal anodes to further prevent side reactions and extend the cycling lifetime of Li–S batteries significantly, which will be discussed in detail in the following section. As a result, ALD/MLD are promising coating techniques for addressing the issues of Li–S battery systems.

As one of the earliest examples of ALD for S cathodes, Elam *et al.* utilized low-temperature ALD of Al<sub>2</sub>O<sub>3</sub> on S<sub>8</sub> cathodes at 50 °C to improve the electrochemical performance of Li–S batteries (Fig. 12(a)).<sup>297</sup> The low-temperature ALD process suppressed the sublimation of S, which is important for retaining the electrode capacity. Moreover, depending on the number of ALD cycles, different morphologies ranging from Al<sub>2</sub>O<sub>3</sub> nanoparticles to thin films can be obtained. The mechanism of improved performance is postulated to differ depending on the morphology of the ALD coating. For ALD Al<sub>2</sub>O<sub>3</sub> nanoparticles, it is believed that they adsorb polysulfides, effectively eliminating the shuttling effect and improving coulombic efficiency. In contrast, ALD Al<sub>2</sub>O<sub>3</sub> thin films on the S cathode act as a physical barrier to prevent the dissolution of polysulfides into the electrolyte.

As one of the primary roles of ALD coatings for Li–S batteries, many materials have been used to adsorb polysulfide species. Pint *et al.* recently used an ALD process for V<sub>2</sub>O<sub>5</sub> on CNTs to anchor polysulfides and achieve long cycle life.<sup>295</sup> After optimization of the ALD coating thickness, a balance between polysulfide anchoring and high S confinement within the CNT channels was achieved, leading to Li–S batteries with 73% capacity retention after 450 cycles (Fig. 12(b)). Several other ALD materials have been explored for applications in Li–S

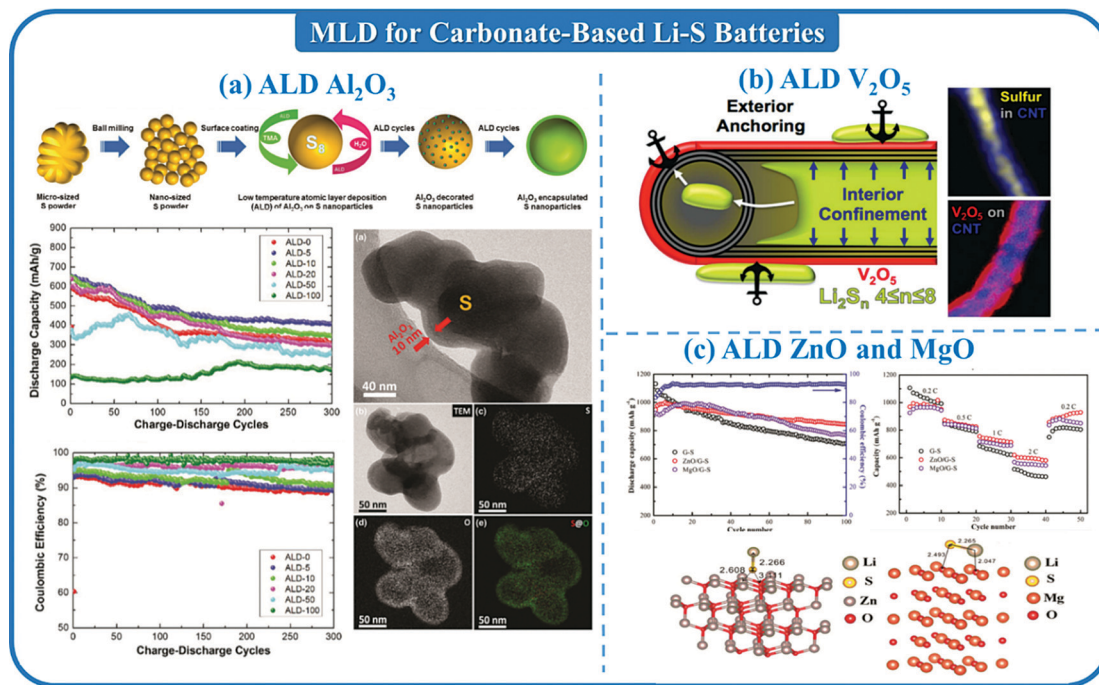


Fig. 12 ALD for Li–S batteries: (a) ALD  $\text{Al}_2\text{O}_3$  – encapsulated S cathodes for Li–S batteries. (b) ALD  $\text{V}_2\text{O}_5$  coated CNTs for S confinement and adsorption. (c) ALD MgO and ZnO-coated rGO sulfur-composite aerogels for polysulfide trapping.

batteries, such as MgO and ZnO, as exemplified by Shi *et al.*<sup>293</sup> They developed a reduced graphene oxide (rGO)–sulfur composite aerogel which was modified by ALD ZnO or MgO as an electrode for Li–S batteries (Fig. 12(c)). While batteries with both ALD coatings had enhanced electrochemical performance relative to the uncoated electrodes, it was found that ZnO was more effective than MgO. The authors carried out DFT calculations which revealed that ZnO has a significantly higher binding energy towards  $\text{Li-S}^*$  radical species (5.40 eV) compared to MgO (1.22 eV). Because of this, it is believed that ALD ZnO is more effective in inhibiting polysulfide shuttling. The ZnO-modified electrode could achieve a discharge capacity of  $998 \text{ mA h g}^{-1}$  at a current density of 0.2C with minimal capacity fading after 100 cycles.

ALD has proven to be a powerful tool for application in Li–S batteries. The wide range of ALD chemistries can be applied on either the anode, separator, or cathode to directly enhance electrochemical performance. While multiple ALD coatings have been shown to interact with polysulfide species, there is still relatively little work studying the effects of different metal centers or how they may affect the interconversion of S species during electrochemical cycling. Nevertheless, ALD chemistries often need reaction temperatures greater than  $100^\circ\text{C}$ , which may cause S sublimation and reduce the capacity of electrodes. In this case, MLD coatings with lower deposition temperatures may prove vital for future improvements.

MLD has recently been shown to be advantageous for applications in Li–S batteries. Traditionally, Li–S batteries have been cycled in ether electrolytes due to the reversible transformation between elemental S and  $\text{Li}_2\text{S}$  species through

polysulfide intermediates. Nevertheless, ether electrolytes have narrow electrochemical stability windows and have low flash points which cause severe safety concerns. In an ideal scenario, Li–S batteries may be better suited for carbonate electrolyte systems due to their better thermal stability. However, conventional Li–S batteries are unable to operate in carbonate electrolytes due to the irreversible side reactions between polysulfide intermediates and carbonate solvents.

Recently, Sun *et al.* discovered that MLD alucone coatings on carbon–S cathode composites can enable stable electrochemical cycling of Li–S cells in carbonate systems.<sup>294</sup> The alucone coating serves multiple functions including acting as a protective barrier against side reactions and plays a role in the interconversion of S species. In a typical Li–S battery with ether electrolyte, two cathodic reactions occur at around 2.3 V and 2.1 V during the lithiation of sulfur corresponding to the reduction of cyclo- $\text{S}_8$  to long-chain polysulfides and short-chain sulfide species, respectively (Fig. 13(a)). In comparison, the pristine carbon–S cathode in a carbonate electrolyte exhibits a broad CV peak at 2.5 V that is irreversible in subsequent cycles, which can be attributed to the formation of long-chain polysulfides. However, upon applying as little as 10 cycles of MLD alucone on the carbon–S cathode, the Li–S batteries show reversible cycling of S species, albeit with electrochemical activity at different potentials compared to traditional Li–S voltages, suggesting an alternative reaction route. The Li–S cells were shown to not only cycle better with alucone coated cathodes in carbonate electrolyte at increased temperatures, but also the cells actually performed better than that with conventional ether electrolytes. This work highlighted the ability of MLD to

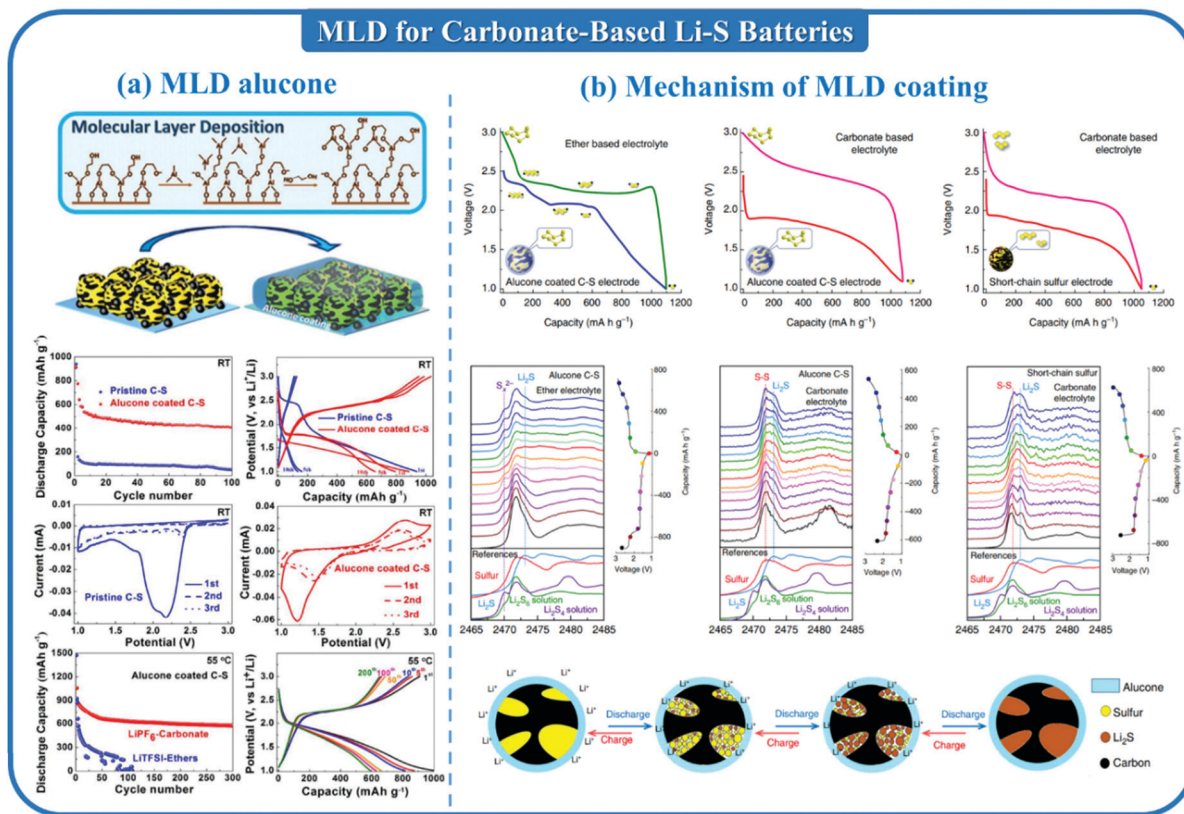


Fig. 13 MLD for Li-S batteries: (a) MLD alucone coating on a microporous S cathode can enable long cycle life in carbonate electrolytes. (b) The working mechanism of MLD coating on S cathodes in a carbonate electrolyte studied by *in situ* XANES showing solid-state interconversion between cyclo-S<sub>8</sub> and Li<sub>2</sub>S.

enable Li-S batteries with longer life in new types of electrolyte systems, which is important for their commercialization.

Shortly after, Sun's group further revealed the working mechanism of alucone coated S in Li-S batteries by *in operando* XANES studies.<sup>299</sup> S K-edge XANES of Li-S batteries with alucone-coated S cathodes revealed different reaction mechanisms found in ether *versus* carbonate electrolyte systems (Fig. 13(b)). In conventional ether electrolytes, the alucone coating does not affect the interconversion of S intermediates, following the traditional reaction scheme. However, in a carbonate electrolyte, the *in operando* S K-edge XANES reveals that the MLD coating enables cyclo-S<sub>8</sub> molecules to be directly reduced to Li<sub>2</sub>S in a solid-phase reaction without the formation of polysulfide intermediates. Moreover, high-performance Li-S pouch cells were fabricated with MLD-coated S cathodes in carbonate electrolyte for the first time. A first discharge capacity of over 1100 mA h g<sup>-1</sup> at a 0.05C rate was achieved, resulting in an energy density at the cell level of over 200 W h kg<sup>-1</sup>. This work provided important information on the reaction mechanisms of Li-S batteries in carbonate electrolytes and the role of MLD alucone coatings in achieving high electrochemical performances.

It is expected that new MLD coatings may provide alternative reaction chemistries for Li-S batteries and more work in the future should be focused on studying the effects of different MLD thin films and their interactions with S cathodes.

**2.1.2.3 ALD/MLD for solid-state Li batteries.** All-solid-state Li batteries (ASSLBs) based on solid-state electrolytes (SSEs) have attracted significant attention recently due to their capability of achieving high energy density and improved safety compared to liquid-based electrolyte systems. One of the major components of SSBs is the solid-state electrolyte (SSE), which requires a wide voltage stability window and good ionic conductivity. Until now, several types of SSEs, including oxide, sulfide, halide, and polymer electrolytes, have been developed to replace the flammable liquid electrolyte in conventional batteries.<sup>300–303</sup> The organic polymer-based SSE poly(ethylene oxide) (PEO) is one of the earliest developed SSEs for SSBs. However, the ionic conductivity of polymer SSEs at room temperature is generally in the range of 10<sup>-5</sup>–10<sup>-6</sup> S cm<sup>-1</sup>, which is still far away from practical applications. An ionic conductivity of over 10<sup>-4</sup> S cm<sup>-1</sup> can be achieved at high operation temperatures (65–80 °C). For the oxide SSEs such as perovskite (Li<sub>3.3</sub>La<sub>0.56</sub>TiO<sub>3</sub>), NASICON (LiTi<sub>2</sub>(PO<sub>4</sub>)<sub>3</sub>), and garnet (Li<sub>7</sub>La<sub>3</sub>Zr<sub>2</sub>O<sub>12</sub>), the ionic conductivities at room-temperature are around 10<sup>-5</sup>–10<sup>-3</sup> S cm<sup>-1</sup>. The sulfide-based SSEs possess the highest ionic conductivity of 10<sup>-2</sup> S cm<sup>-1</sup> (Li<sub>10</sub>GeP<sub>2</sub>S<sub>12</sub>) among all different types of SSEs. Although significant progress has been achieved for the development of high ionic conductive SSEs, the fabrication of thin film SSEs at the nanoscale is also important for thin film batteries, 3D micro-batteries and interface engineering of electrode materials. In the past few years,

various thin films SSEs, such as  $\text{Li}_3\text{PO}_4$ ,  $\text{LiTaO}_3$ ,  $\text{LiNbO}_3$ ,  $\text{LiSiO}_4$ ,  $\text{Li}_7\text{La}_3\text{Zr}_2\text{O}_{12}$ , and  $\text{LiPON}$ , have been fabricated by ALD.<sup>201,304–309</sup> However, the ionic conductivities of the developed ALD SSEs are around  $10^{-8}$ – $10^{-9}$   $\text{S cm}^{-1}$ , which cannot be directly used as SSEs for SSBs. Moreover, these ALD SSEs are generally amorphous and the high-temperature post-annealing can cause shrinkage of the films, resulting in island-like structures. A recent achievement from Dasgupta's group reported an amorphous lithium borate-carbonate (LBCO) film which can be prepared by ALD, yielding the highest Li-ion conductivity ( $2.2 \times 10^{-6}$   $\text{S cm}^{-1}$  at room temperature) among all previously reported ALD-prepared Li-ion conductive compounds.<sup>310</sup> Although it is difficult for the ALD LBCO films to be directly used as SSEs for SSBs, they are still promising as an interface modification between SSEs and cathode/anode electrodes.

One of the most inhibiting factors of ASSLBs is the side reaction between anode/cathode and the SSE. Surface modification of the interface with ALD/MLD techniques has been demonstrated as a promising strategy that can alleviate specific problems associated with parasitic side reactions. On the anode side, the direct use of Li metal in the ASSLBs has problems associated with poor contact, uncontrollable side reactions and the formation of Li dendrites. Hu *et al.*<sup>311</sup> coated ALD- $\text{Al}_2\text{O}_3$  on a garnet electrolyte ( $\text{Li}_7\text{La}_{2.75}\text{Ca}_{0.25}\text{Zr}_{1.75}\text{Nb}_{0.25}\text{O}_{12}$ , LLCZN) to increase the interfacial contact and reduce the interfacial impedance from  $1710 \Omega \text{ cm}^{-2}$  to  $1 \Omega \text{ cm}^{-2}$  (Fig. 14(a)). The intimate

contact is derived from the high binding energy of Li with lithiated  $\text{Al}_2\text{O}_3$ . In addition, the ultrathin lithiated  $\text{Al}_2\text{O}_3$  can provide conductive  $\text{Li}^+$  ion pathways and prevent the garnet decomposition. Sun *et al.* compared the ALD- $\text{Al}_2\text{O}_3$  coating process on the Li metal anode and the NASICON-type LAMP [ $\text{Li}_{1.3}\text{Al}_{0.3}\text{Ti}_{1.7}(\text{PO}_4)_3$ ].<sup>312</sup> These results showed that the ALD coating on the electrolyte enables a much more stable Li/LAMP interface. Both Li penetration and Ti reduction are prevented by the dense ALD- $\text{Al}_2\text{O}_3$  coating (Fig. 14(b)). Apart from improving the interfacial stability of Li/oxide-based SSEs by coating ALD- $\text{Al}_2\text{O}_3$ , MLD-prepared inorganic–organic coating (alucone) has been developed as well to alleviate the interface problem between Li metal and  $\text{Li}_{10}\text{SnP}_2\text{S}_{12}$  sulfide-based SSEs<sup>313</sup> (Fig. 14(c)). An alucone interlayer, as an artificial SEI, significantly suppresses the side reactions by blocking electron transfer. Very recently, Dasgupta *et al.* used a suite of *operando* microscopy and spectroscopy techniques to study the impact of the ALD- $\text{Al}_2\text{O}_3$  on the electro-chemo-mechanical degradation of  $\text{Li}_{10}\text{GeP}_2\text{S}_{12}$  (LGPS) sulfide electrolytes (Fig. 14(d)). This ALD- $\text{Al}_2\text{O}_3$  interlayer was confirmed to delay degradation of the Li/LGPS interface by modifying the interphase chemistry and morphology.<sup>314</sup>

On the cathode side, the interfacial problem mainly exists between oxide cathode materials and sulfide-based SSEs. Due to the different affinities of  $\text{Li}^+$  ions towards oxides and sulfides, the space charge effect is one of the main obstacles that renders poor cycling stability. Moreover, the variable-valence-state

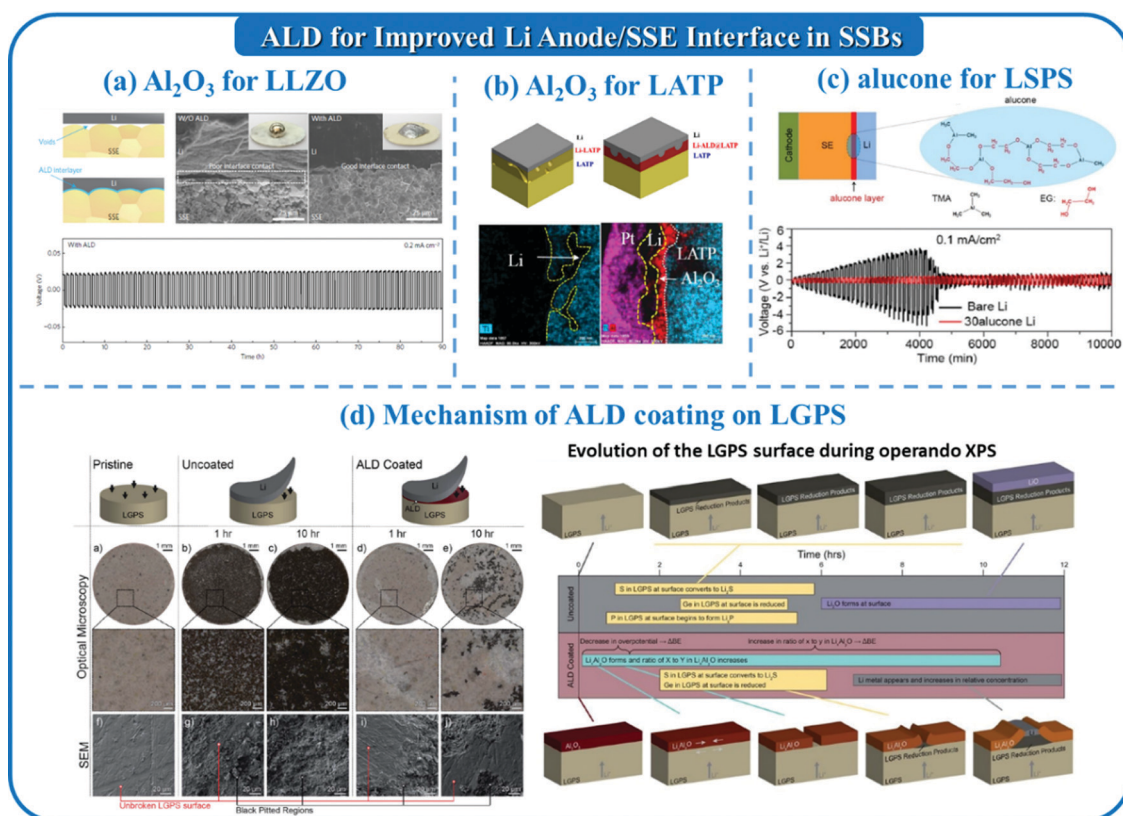


Fig. 14 ALD for improved anode interface in SSBs: (a) ALD  $\text{Al}_2\text{O}_3$  for LLZO and Li metal; (b) ALD  $\text{Al}_2\text{O}_3$  for LAMP and Li metal; (c) MLD alucone for LSPS and Li metal; (d) using *operando* microscopy and XPS to study the impact of the ALD- $\text{Al}_2\text{O}_3$  on the electro-chemo-mechanical degradation of LGPS.

transition metal elements in the cathode materials are reactive with sulfide electrolytes. It is recognized that the development of Li-ion conductive and chemically/electrochemically inactive cathode coating materials is essential. Lee's group demonstrated that ALD- $\text{Al}_2\text{O}_3$  layers coated on  $\text{LiCoO}_2$  (LCO) cathode materials can effectively prolong the cycle life of the ASSLBs.<sup>315</sup> High-resolution TEM and EELS aided in observing that the ALD- $\text{Al}_2\text{O}_3$  layer can reduce the thickness of the formed interface. The interdiffusion of elements from LCO cathode materials and  $\text{Li}_{3.15}\text{Ge}_{0.15}\text{P}_{0.85}\text{S}_4$  SSEs is also inhibited, as shown in Fig. 15(a). Sun *et al.* further demonstrated ALD processes for amorphous and Li-ion conductive  $\text{LiNbO}_x$  (LNO),  $\text{LiPO}_x$  (LPO), and  $\text{LiZrO}_x$  (LZO) coating layers on LCO and NMC cathode materials.<sup>316–318</sup> *In situ* XANES results imply that the LNO shell can suppress the interfacial reactions between LCO and  $\text{Li}_{10}\text{GeP}_2\text{S}_{12}$  during the charging and discharging processes (Fig. 15(b)), and a similar functionality was also verified for the LPO-coated and LZO-coated cathode materials. It should be noted that ALD processes (*i.e.* sub-cycles and deposition temperatures) can be easily tuned

to fabricate conformal cathode coating layers with different ionic conductivities, which is demonstrated in the LZO coating by Zhao *et al.* (Fig. 15(c)). In addition to the binary and ternary coating materials, the amorphous ALD-LBCO (including Li, B, C, and O elements) layer was verified to work well in a thin film battery, which shows a very promising ionic conductivity of  $2.2 \times 10^{-6} \text{ S cm}^{-1}$  at  $25^\circ\text{C}$  (Fig. 15(d)).<sup>310</sup> Therefore, ALD-LBCO is anticipated to be an ideal protection layer when applied to cathode materials for ASSLBs. In addition to the ionic conductivity of the interfacial layer, the electronic conductivity is also an important factor that can determine the battery performance. Recently, Deng *et al.* employed MLD to prepare poly(3,4-ethylenedioxythiophene) (PEDOT) as a semiconducting additive for cathode composites in the sulfide-based solid-state batteries<sup>319</sup> (Fig. 15(e)). The MLD-PEDOT modification not only significantly suppresses the side reactions but also realizes effective electron transfer at the cathode/SSE/carbon three-phase interface.

SSBs are promising energy storage systems and the future target for the battery community. However, the development of

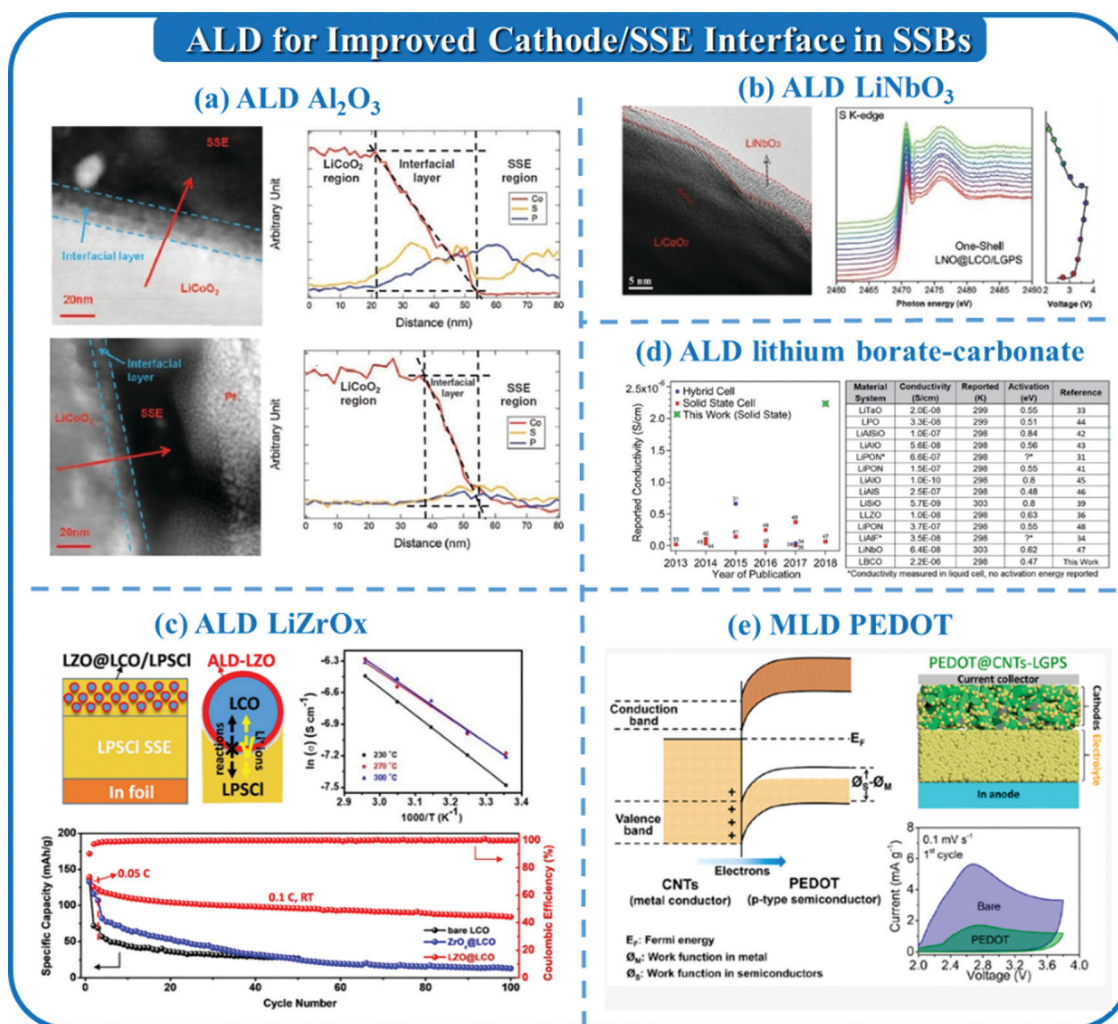


Fig. 15 (a) ALD  $\text{Al}_2\text{O}_3$  for  $\text{LiCoO}_2$  and SSEs; (b) ALD  $\text{LiNbO}_3$  for  $\text{LiCoO}_2$  and SSEs; (c) tuning the ionic conductive LZO coating via controlling the ALD process; (d) ALD deposited lithium borate-carbonate as SSEs; (e) MLD PEDOT coatings for additives in cathode composite to tune the electronic conductivity of the interface.

SSEs and interfacial issues are the major hurdles that need to be overcome for practical applications. Meanwhile, the application of ALD and MLD for SSBs is still in the early stage. To play a more important role, new ALD and MLD films with high ionic conductivity, electronic conductivity, and wide electrochemical windows need to be developed.

**2.1.2.4 ALD/MLD for Li metal anodes.** The practical energy density of present LIBs ( $\sim 240 \text{ W h kg}^{-1}$ ) has nearly approached its physicochemical energy density limit with only a 7–8% increase per year.<sup>320</sup> With a super high capacity ( $3860 \text{ mA h g}^{-1}$ ) and the lowest electrochemical potential ( $-3.04 \text{ V}$  vs. the standard hydrogen electrode), Li metal is strongly regarded as the most promising candidate for next-generation Li metal batteries (LMBs) beyond traditional LIBs. To date, some fundamental issues including poor safety and cycling stability still hinder the practical applications of the Li metal anode. Firstly, the formation of dendrites during electrochemical plating/stripping can penetrate the separator, triggering the failure of the battery due to internal short circuits. The risk of thermal runaway and cell combustion arising from shorting will significantly increase. Secondly, the formation of unstable SEI components due to uncontrolled side reactions between Li metal and liquid electrolyte leads to poor coulombic efficiency. In addition, the large volume fluctuation of Li during electrochemical cycling owing to its hostless nature further causes the formation of “dead” Li deposits and further aggravates parasitic side reactions.<sup>35</sup> The stability of the SEI is the most important factor that needs to be addressed in order to prevent further side reactions between Li and electrolyte. Nevertheless, naturally-formed SEI is heterogeneous with respect to composition, ionic conductivity, and mechanical properties, leading to fracture upon electrochemical cycling and continuous side reactions between Li and the electrolyte.<sup>321,322</sup> Therefore, an interphase design is critical to improving the stability of the SEI and is considered to be an effective approach to enhance the performance of Li metal anodes. The functions of the artificial SEI are summarized as: (1) a strong physical barrier against dendrite propagation; (2) preventing the side reactions between Li metal and the electrolyte; (3) regulating the  $\text{Li}^+$  flux on the surface of Li metal and uniformizing the Li nucleation and deposition.<sup>323</sup> There have been many studies reporting the construction of surface coatings on Li as a protective film, including metal oxides,<sup>324,325</sup> solid-state electrolytes,<sup>326,327</sup> and polymers.<sup>328,329</sup> These *ex situ* strategies can be realized by various coating techniques, such as chemical vapor deposition,<sup>330</sup> wet chemical methods,<sup>331</sup> and physical vapor deposition.<sup>332</sup> Among all of the coating methods, ALD is believed to be very promising due to its conformal coverage and accurate control over thickness in the nanoscale regime.<sup>19</sup> Ultra-thin protective films with homogeneous composition can be deposited on Li metal, and all the features achieved by ALD can be beneficial towards meeting the requirement of an ideal SEI. As an analogue technique to ALD, MLD is employed for the deposition of polymeric films rather than inorganic materials by ALD. As previously mentioned, MLD provides several unique advantages such as tunable

electrochemical properties and improved mechanical performance while maintaining the advantages of ALD.<sup>333</sup>

The investigation of ALD metal oxides for Li metal protection was reported by Noked's group for the first time.<sup>325</sup> In their work, a  $\sim 14 \text{ nm}$  thick ALD  $\text{Al}_2\text{O}_3$  layer was coated on Li by plasma-enhanced ALD (PEALD) with trimethylaluminum (TMA) and  $\text{O}_2$  plasma. When tested in Li–S batteries, the ALD-protected anodes showed improved capacity retention compared to bare Li for up to 100 cycles (Fig. 16(a)). Moreover, this  $\text{Al}_2\text{O}_3$  layer can effectively prevent the corrosion of the Li surface when exposed to the atmosphere, sulfur, and electrolyte. Following this work, there have been other studies on the protective effects of ALD  $\text{Al}_2\text{O}_3$  for Li. Dasgupta's group used TMA and  $\text{H}_2\text{O}$  as precursors to deposit an optimized  $\sim 2 \text{ nm}$  ultrathin  $\text{Al}_2\text{O}_3$  layer and investigated the plating/stripping of symmetric Li–Li cells.<sup>334</sup> They observed a greatly improved lifetime enabled by the coating layer and a smooth Li surface after 1000 electrochemical cycles. This work demonstrated that Li can transport through  $\text{Al}_2\text{O}_3$  during the Li plating process, which was confirmed from XPS results that indicated that Al still remained on the surface after Li plating. Based on their first work, Noked's group further studied the protective effects of ALD coating on Li against organic electrolyte quantitatively using mass spectrometry and *in situ* AFM.<sup>335</sup> They confirmed that both electrochemical degradation and solvent corrosion can be efficiently suppressed by ALD  $\text{Al}_2\text{O}_3$ . Moreover, Elam's group investigated the growth mechanism of ALD  $\text{Al}_2\text{O}_3$  deposition on Li by *in situ* quartz crystal microbalance and found enhanced wettability of the Li surface towards electrolytes.<sup>336</sup> Promisingly, the cycling life of ALD protected Li was four times longer than bare Li when the volume of electrolyte was only  $5 \mu\text{L}$ . Furthermore, Cui's group applied ALD  $\text{Al}_2\text{O}_3$  on a 3D hollow carbon host, which can guide Li deposition inside the hollow carbon spheres and prevent direct electrolyte contact, resulting in a high coulombic efficiency of 99% over 500 cycles.<sup>337</sup> Other than  $\text{Al}_2\text{O}_3$ , Cho's group recently reported a  $\text{ZrO}_2$  encapsulation layer on Li metal by plasma-thermal activated ALD for the first time, as shown in Fig. 16(b).<sup>338</sup> This conformal and ionically conductive  $\text{ZrO}_2$  layer with high- $k$  dielectric properties can suppress side reactions and stabilize Li metal. The protected Li also exhibited good heat tolerance up to  $170\text{--}180 \text{ }^\circ\text{C}$  due to the high thermal resistance of  $\text{ZrO}_2$ .

The development of lithium-containing compounds *via* ALD is also considered as a promising strategy to stabilize the Li metal anode. Elam's group developed an ultrathin and ionically conducting ALD  $\text{Li}_x\text{Al}_y\text{S}$  coating to stabilize the SEI and decrease the interfacial resistance.<sup>339</sup> In this ALD process, a newly developed coating of  $\text{Al}_2\text{S}_3$  by tris(dimethylamido) aluminum(III) and  $\text{H}_2\text{S}$  is combined with a reported process for  $\text{Li}_2\text{S}$  by combining lithium *tert*-butoxide ( $\text{LiO}^t\text{Bu}$ ) and  $\text{H}_2\text{S}$  subcycles. The electrochemically deposited Li with  $\text{Li}_x\text{Al}_y\text{S}$  coating was found to maintain a smooth surface, and the cycle life of Li–Cu cells was doubled compared to the bare Li. A new ALD process enabling the deposition of LiF (Fig. 16(c)) directly on Li was also developed recently by Elam's group.<sup>340</sup> In the synthesis of ALD LiF,  $\text{LiO}^t\text{Bu}$  and HF/pyridine solution were

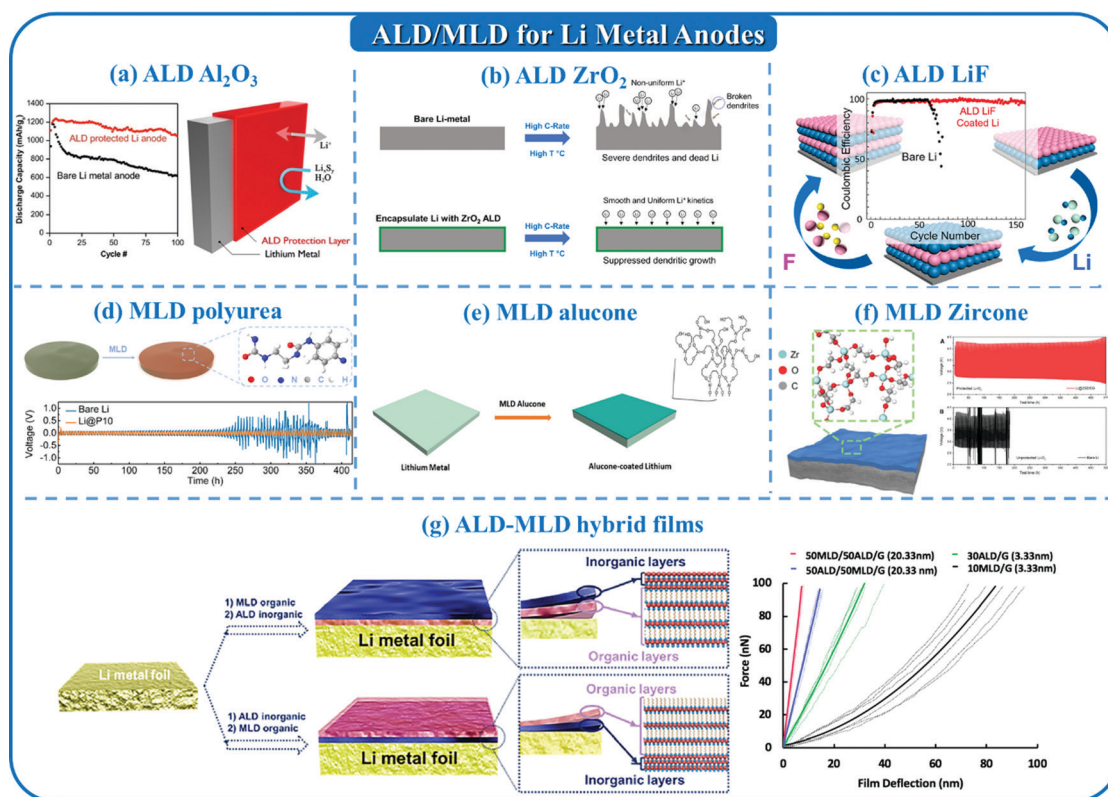


Fig. 16 ALD/MLD for Li metal anodes: (a) ALD  $\text{Al}_2\text{O}_3$ ; (b) ALD  $\text{ZrO}_2$ ; (c) ALD LiF; (d) MLD organic polyurea; (e) MLD hybrid inorganic–organic alucone; (f) MLD hybrid inorganic–organic zirconium; (g) ALD-MLD dual protective layer.

used as precursors for deposition at  $150\text{ }^\circ\text{C}$ , which is below the melting point of Li. A high shear modulus of 58 GPa was detected by nanoindentation measurements, which is higher than that required to prevent the growth of Li dendrites. Owing to the high dielectric value and great stability of LiF, the protected Li showed a stable coulombic efficiency of  $\sim 99.5\%$  for 170 cycles. Furthermore, Cui's group demonstrated selective ALD LiF deposited on the defect sites of h-BN films.<sup>341</sup> The LiF was primarily deposited on the defects of h-BN, thereby saturating the h-BN crystallites. As a result, the protected electrodes exhibit excellent cycling stability with more than 300 cycles at relatively high coulombic efficiency in an additive-free carbonate electrolyte.

To date, polymeric films have been reported as effective coating materials for Li metal with some interesting and unique mechanical properties. The fabrication of various MLD nanoscale coatings on Li has been reported by Elam's group and Sun's group. Different from ALD coatings, MLD coatings have good flexibility, lower density, and high softness, which can lead to improved electrochemical performance when using artificial SEI. A type of pure polymeric coating of 'polyurea' was reported to stabilize the SEI by our group for the first time, as shown in Fig. 16(d).<sup>342</sup> Abundant polar groups in this polymer can redistribute the Li-ion flux and lead to a uniform Li plating/stripping process. Both XPS and TOF-SIMS results confirmed that nitrogen remained on the surface after electrochemical cycling, suggesting that the protective film is mechanically

robust upon electrochemical cycling. As a result, a three-fold increase in cycle life was achieved in symmetric cells at a current of  $3\text{ mA cm}^{-2}$  and higher capacity retention was obtained in Li-LFP batteries for 200 cycles. A hybrid inorganic–organic MLD coating, alucone, has been reported by both Sun's group and Elam's group for use as a protective layer for Li metal anodes (Fig. 16(e)).<sup>343,344</sup> With a composition consisting of  $(-\text{Al}-\text{O}-\text{CH}_2-\text{CH}_2-\text{O}-)_n$  repeating units, alucone is synthesized by the sequential reactions of TMA and ethylene glycol (EG). Our results showed that alucone-protected Li had superior electrochemical performance compared to that of ALD  $\text{Al}_2\text{O}_3$  coatings.<sup>343</sup> The reason for the improved performance was revealed by RBS measurements on both electrochemically cycled  $\text{Al}_2\text{O}_3$  and alucone coated Li. The results demonstrated that the alucone coating was more effective than  $\text{Al}_2\text{O}_3$  in preventing film fracture under the large volume change during Li plating/stripping. Elam's group also found a similar conclusion that alucone coating can stabilize Li against dendrite growth and minimize side reactions.<sup>344</sup> Their results showed that the protected Li can yield longer cycle life and 39.5% higher capacity after 140 cycles in Li-S batteries with a high mass loading of  $\sim 5\text{ mg cm}^{-2}$ . Sun *et al.* recently reported the fabrication of MLD zirconium as a protective layer on Li metal at  $130\text{ }^\circ\text{C}$  using zirconium *tert*-butoxide and ethylene glycol as precursors, as shown in Fig. 16(f).<sup>345</sup> *In situ* synchrotron X-ray absorption spectroscopy was used to study the lithiation process of the zirconium thin films. Promisingly, the zirconium-coated Li showed a 10-fold increase in

cycle life in Li–O<sub>2</sub> batteries compared to those with unprotected Li due to its excellent air stability.

The electrical and mechanical properties of MLD thin films are different compared with their ALD counterparts. When used as protective coatings on Li, dense ALD films are expected to block the electron transport and reduce unwanted side reactions, whereas porous MLD films are expected to better accommodate the volume changes during plating/stripping because of their improved flexibility. Recently reported by Sun *et al.*, a dual protective layer for Li metal anodes was fabricated by combining ALD and MLD, leading to significantly enhanced electrochemical performances.<sup>346</sup> Inspired by natural SEI formation, this dual protective layer consisted of organic alucone as the outer layer and inorganic Al<sub>2</sub>O<sub>3</sub> as the inner layer. The concept and design of the ALD/MLD recipe are shown in Fig. 16(g). The mechanical properties of the protective layer were investigated by atomic force microscopy (AFM). The results showed both high strength and local flexibility, which are beneficial for suppressing crack formation upon electrochemical cycling. Results from SEM demonstrated that dendrite growth and dead Li formation can be effectively suppressed by the introduction of a dual-layer. Moreover, surface and interface analysis by both TOF-SIMS and RBS indicated an excellent robust feature of the protective layer. This work demonstrates the precise control over coating thickness and composition enabled by ALD and MLD techniques, which is difficult to achieve by other methods.

In this section, we have summarized the application of ALD/MLD coatings to address the challenges of Li metal anodes. The reasons for their enhanced electrochemical performances are mainly: (1) the electronically insulating properties of the coatings can induce Li deposition underneath the films. (2) The protective layers can serve as a physical barrier to suppress dendrite growth and/or accommodate volume change. (3) Side reactions between electrolyte and Li can be suppressed by coating. Ionic conductivity plays a crucial role in SEI as the Li-ion transport through the interphase considerably affects the electrochemical performances.<sup>347</sup> However, there are still very few reports on the fabrication of ALD/MLD coatings with high ionic conductivity directly on lithium. We strongly believe the development of new ALD/MLD processes for ionically conductive coatings on Li is of great importance to realize stable Li metal anodes for next-generation LMBs.

### 2.1.3 ALD/MLD for Na batteries and beyond

**2.1.3.1 ALD/MLD for Na ion batteries.** With the continuous consumption of resources due to the large demand for Li-ion batteries, the availability of Li sources has been dramatically reduced. Thus, it is necessary to develop a new energy storage system to replace Li-based batteries.<sup>348,349</sup> Na batteries, including Na-ion batteries (NIBs) and room temperature Na metal batteries, are recognized as promising alternatives to Li batteries due to the lower price and natural abundance of sodium, and similar intercalation chemistry to lithium.<sup>350–352</sup> The electrodes, including both the cathode and anode, are still the key components for high-performance Na batteries. ALD/MLD can be used for the fabrication of electrodes and engineering of the

electrode/electrolyte interfaces. Sun *et al.* were the first to demonstrate an ALD-fabricated sodium titanate as an anode for NIBs.<sup>353</sup> As shown in Fig. 17(a), the NaO<sup>t</sup>Bu, titanium(IV) isopropoxide (TTIP), and H<sub>2</sub>O were used as precursors at a deposition temperature of 200–275 °C. One ALD supercycle consists of two ALD sub-cycles, which include NaO<sup>t</sup>Bu–H<sub>2</sub>O and TTIP–H<sub>2</sub>O. The as-deposited sodium titanate was amorphous, and crystalline Na<sub>0.23</sub>TiO<sub>2</sub> was obtained after a post-annealing treatment. Carbon nanotubes (CNTs) were used as the substrate for electrode fabrication. The sodium titanates on CNTs delivered excellent electrochemical properties as anodes for NIBs with high energy density, exceptional rate performances and long lifespans. As shown in Fig. 17(a), the as-deposited amorphous sodium titanates demonstrated better electrochemical performances with high capacity compared to the crystalline Na<sub>0.23</sub>TiO<sub>2</sub>. Another work reported nitrogen-doped TiO<sub>2</sub> on CNTs (N-TiO<sub>2</sub>/CNTs) fabricated by plasma-enhanced ALD using N<sub>2</sub> plasma.<sup>354</sup> Furthermore, Rao *et al.* have grown ultrathin crystalline epitaxial thin films of MoS<sub>2</sub> on c-sapphire by ALD.<sup>355</sup> The MoS<sub>2</sub> films showed a high density of nanowalls and exhibited a high surface to volume ratio. The cell with the ALD-grown MoS<sub>2</sub> nanowall network presented remarkable electrochemical performances in both LIBs and NIBs, delivering a specific capacity of 667 mA h g<sup>-1</sup> and 1710 mA h g<sup>-1</sup> for LIBs and NIBs, respectively.

Similar to their application in LIBs, ALD/MLD techniques are also used to modify the SEI layer for anode materials in NIBs. Hu's group designed a novel hybrid nanostructure (Fig. 17(b)), consisting of Sn nanoparticles (SnNPs) attached to carbon nanofibers (CNFs) with another thin layer of ALD Al<sub>2</sub>O<sub>3</sub> for use as an anode in NIBs.<sup>356</sup> As shown in Fig. 17(b), without the ALD coating, the SnNPs detach and fall off from the underlying CNF substrate after sodiation/desodiation cycles. In contrast, the ALD Al<sub>2</sub>O<sub>3</sub> coating could conduct sodium ions after forming the Na–Al–O layer, allowing for the uniform sodiation of the SnNP core. The volume change of SnNP during cycling was accompanied by a conformal swelling and shrinking of the Na–Al–O layer. It was verified by *in situ* TEM that the ALD Al<sub>2</sub>O<sub>3</sub> coating was robust and deformed coherently with the SnNPs during the sodiation/desodiation process, effectively limiting the volume changes during cycling. As a result, the electrochemical stability was improved with the ALD Al<sub>2</sub>O<sub>3</sub> coating. Liu *et al.* further demonstrate the concept using a composite anode of SnO<sub>2</sub> nanoparticles on carbon cloth (CC) with the surface coating layer of ALD Al<sub>2</sub>O<sub>3</sub>.<sup>357</sup> Moreover, the ALD metal oxides of Al<sub>2</sub>O<sub>3</sub> and TiO<sub>2</sub> have also been deposited as a protective layer for conversion-type anodes such as CuO and NiCo<sub>2</sub>O<sub>4</sub>.<sup>358,359</sup> For example, Li's group demonstrated CuO nanowire electrode arrays grown on 3D Cu foams with ALD TiO<sub>2</sub> as protective coatings (as shown in Fig. 17(c)).<sup>359</sup> The CuO nanowire arrays delivered a high specific capacity of 592 mA h g<sup>-1</sup> and remarkable cycling performances with a high capacity retention of 82% over 1000 cycles.

On the cathode side, ALD Al<sub>2</sub>O<sub>3</sub> was also used to engineer the interface for different cathode materials, such as Na<sub>2/3</sub>(Mn<sub>0.54</sub>Ni<sub>0.13</sub>Co<sub>0.13</sub>)O<sub>2</sub>, P2-Na<sub>2/3</sub>Ni<sub>1/3</sub>Mn<sub>2/3</sub>O<sub>2</sub> and Na<sub>3</sub>V<sub>2</sub>(PO<sub>4</sub>)<sub>3</sub>.<sup>360–366</sup> For example, our group reported an ALD Al<sub>2</sub>O<sub>3</sub> coating for P2-type

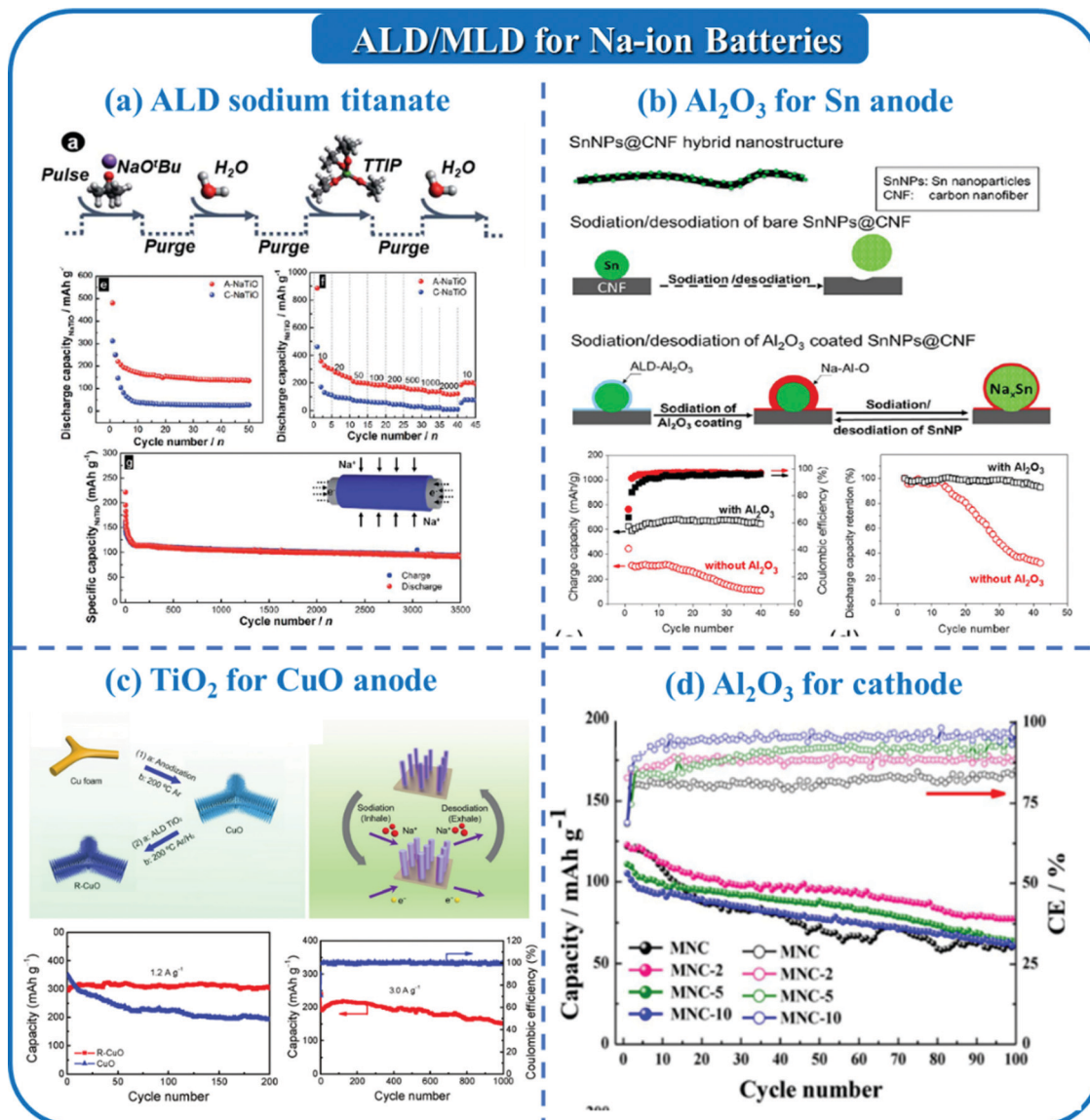


Fig. 17 ALD/MLD for Na-ion batteries: (a) ALD fabricated sodium titanate; (b) ALD  $\text{Al}_2\text{O}_3$  for Sn anode; (c) ALD  $\text{TiO}_2$  for CuO anode; (d) ALD  $\text{Al}_2\text{O}_3$  for  $\text{Na}_{2/3}(\text{Mn}_{0.54}\text{Ni}_{0.13}\text{Co}_{0.13})\text{O}_2$ .

$\text{Na}_{2/3}(\text{Mn}_{0.54}\text{Ni}_{0.13}\text{Co}_{0.13})\text{O}_2$  with an optimized thickness of 2  $\text{Al}_2\text{O}_3$  cycles, as shown in Fig. 17(d). Thick ALD  $\text{Al}_2\text{O}_3$  can reduce the utilization of active materials and increased the charge-transfer resistance upon cycling.<sup>360</sup> The role of ALD metal oxide coating in NIBs is similar to that of LIBs, which prevents the side reactions between the cathode and electrolyte, minimizes the transition metal dissolution, and provides structural stability against mechanical stresses which occur during the cycling process.

**2.1.3.2 ALD/MLD for Na metal batteries.** Room temperature Na metal batteries (NMBs), including Na-S, Na-Se, and Na- $\text{O}_2$  batteries, present higher energy densities compared to traditional LIBs and NIBs.<sup>367–370</sup> Sun's group demonstrated non-noble ALD  $\text{Co}_3\text{O}_4$  catalysts on CNTs as an air electrode for Na-air batteries.<sup>371</sup> As shown in Fig. 18(a), a conformal layer of

$\text{Co}_3\text{O}_4$  was formed on the CNT substrates by an ALD technique. In contrast, mechanically mixed CNT/ $\text{Co}_3\text{O}_4$  nanocomposites were prepared for comparison. The ALD deposited  $\text{Co}_3\text{O}_4$ -CNTs air electrodes can effectively improve the utilization of the catalytic centres and orientate the growth of the discharge products, resulting in an increased capacity and extended lifespan. Furthermore, we designed another 3D structured air electrode for Na- $\text{O}_2$  batteries,<sup>372</sup> in which graphene foam was used as the substrate and mesoporous  $\text{Mn}_3\text{O}_4$  with ALD Pd deposition was decorated on the graphene foam. In this 3D air electrode, the mesoporous  $\text{Mn}_3\text{O}_4$  and Pd nanoclusters acted as ORR and OER catalysts, respectively, resulting in a stable electrochemical performance for over 100 cycles in Na- $\text{O}_2$  batteries.

ALD has also been extended to Na-S and Na-Se battery applications. As shown in Fig. 18(b), we designed a novel

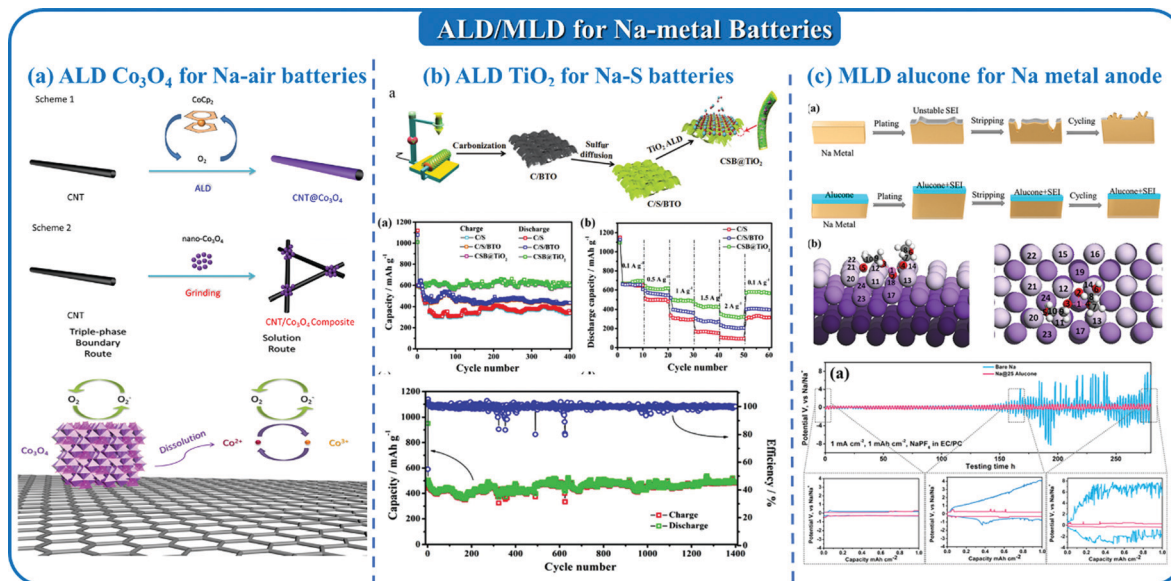


Fig. 18 ALD/MLD for Na metal batteries: (a) ALD  $\text{Co}_3\text{O}_4$  as a catalyst for Na–air batteries; (b) ALD  $\text{TiO}_2$  for Na–S batteries; (c) MLD alucone for a Na metal anode.

structured cathode material for Na–S batteries.<sup>373</sup> The C/S/BaTiO<sub>3</sub> composites were firstly fabricated *via* electrospinning and a subsequent annealing process. Then, ALD  $\text{TiO}_2$  was deposited on the C/S/BaTiO<sub>3</sub> composites as the protective layer. With the ALD  $\text{TiO}_2$  coating, the electrode showed enhanced stability with a discharge capacity of 611 mA h g<sup>-1</sup> after 400 cycles. The ALD coating can effectively adsorb the polysulfides, suppress the volume changes, reduce the interfacial resistance, and facilitate charge transfer and ion transport, resulting in improved electrochemical performances. Moreover, the ALD  $\text{Al}_2\text{O}_3$ -coated (Se/porous N-doped carbon nanofibers)@Se composites were rationally designed and fabricated as free-standing cathodes for Na–Se batteries. The ALD coated composite electrode with high Se loading (67%) delivered the high specific capacity of 503 mA h g<sup>-1</sup> after 1000 cycles with almost 100% capacity retention at the current density of 0.5 A g<sup>-1</sup>. The major function of the ALD  $\text{Al}_2\text{O}_3$  is to serve as an artificial barrier to limit the dissolution of sodium polyselenides and mitigate the shuttle effects in the electrolyte.

For room temperature Na metal batteries, the Na metal anode is another serious challenge that needs to be overcome. As an alkali metal, the issues of a Na metal anode can be summarized as (1) Na dendrite growth; (2) unstable SEI and dead Na layer formation; and (3) infinite volume change.<sup>374,375</sup> For the individual subcategories of Na metal batteries, there are other problems specific to the full cell system. For example, the O<sub>2</sub> diffusion to the anode is also a critical issue in Na–O<sub>2</sub> batteries.<sup>376</sup> Our previous review has summarized the recent development of Na metal anodes in detail.<sup>377</sup> ALD/MLD can play an important role in addressing the interfacial issues. Hu's group and our group reported ALD  $\text{Al}_2\text{O}_3$  as a protective layer for the Na metal anode.<sup>378,379</sup> The ultrathin  $\text{Al}_2\text{O}_3$  coating serves as a stable artificial SEI for Na metal, resulting in both carbonate-based and ether-based symmetric cells with enhanced electrochemical performances. Furthermore, our

group firstly demonstrated MLD alucone coatings for Na metal.<sup>380</sup> As shown in Fig. 18(c), the MLD alucone presented strong surface bonding on the surface of Na metal. Fig. 18(c) also shows the electrochemical performances of the symmetrical cells for both Na@25alucone and the pristine Na foil at 1 mA cm<sup>-2</sup>/1 mA h cm<sup>-2</sup> in the NaPF<sub>6</sub>-carbonate electrolyte. From the results, the Na@25alucone presented more stable plating/stripping performances with reduced dendrite growth and double the lifetime.

ALD was also used to fabricate SSEs for Na-based SSBs. Nuwayhid *et al.* firstly demonstrated a thermal ALD process for sodium phosphorus oxynitride (NaPON), thin-film SSEs.<sup>381</sup> In the ALD process, sodium *tert*-butoxide (NaOtBu) and DEPA were used as precursors with the deposition temperature at 250–400 °C. The ALD process produced a conformal film with a stoichiometry of Na<sub>4</sub>PO<sub>3</sub>N, corresponding to a sodium polyphosphazene structure. The ionic conductivity of the NaPON film was as high as 1.0 × 10<sup>-7</sup> S cm<sup>-1</sup> at 25 °C and up to 2.5 × 10<sup>-6</sup> S cm<sup>-1</sup> at 80 °C with an activation energy of 0.53 eV. Their promising result makes NaPON a viable SSE or passivation layer for Na-based SSBs.

**2.1.3.3 ALD/MLD for other batteries.** The application of ALD/MLD has also been extended to other battery systems, such as Al-ion, K-ion, and Zn-ion batteries.<sup>382–385</sup> For example, Huang's group demonstrated uniformly coated ALD amorphous V<sub>2</sub>O<sub>5</sub> on CNTs as a cathode for K-ion batteries.<sup>385</sup> The V<sub>2</sub>O<sub>5</sub>@CNT sponge cathode deposited by ALD exhibits a reversible capacity of 206 mA h g<sup>-1</sup> and stable cycling performances in the carbonate-based electrolyte. Liu *et al.* utilized ALD  $\text{Al}_2\text{O}_3$  coating to modify the solid electrolyte interphase (SEI) on a biomass carbon anode in K-ion batteries and improve the average CE from 99.0% to 99.6%.<sup>386</sup> ALD protection coatings were also proposed to be effective for Zn metal anodes, where ALD  $\text{TiO}_2$  and  $\text{Al}_2\text{O}_3$  was used as a demonstration.<sup>387</sup> The ALD layer can prevent gas generation on the Zn metal anode and maintain effective contact

between the Zn and electrolyte, resulting in enhanced coulombic efficiency. The protected Zn metal anode can be cycled in the Zn–MnO<sub>2</sub> batteries over 1000 cycles with a capacity retention of 85%. Furthermore, ALD was used to deposit nanoscale ZnO on the current collector as a binder-free cathode for rechargeable Al-ion batteries.<sup>383</sup> The electrochemical results showed that the binder-free ALD grown ZnO cathode manifested a high initial discharge capacity of 2563 mA h g<sup>-1</sup>, which was significantly higher than that of the cells fabricated with the ZnO powder as the cathode. However, the capacity decay is serious with only 245 mA h g<sup>-1</sup> at a current rate of 400 mA g<sup>-1</sup> after 50 cycles. Further efforts are needed to stabilize the cycling stability of this cathode material for Al-ion batteries.

In this section, the applications of ALD/MLD for Na batteries and beyond (including Na-ion batteries, Na-metal batteries, Al-ion batteries, Zn-ion batteries) have been discussed in detail. The studies on this topic are not as prominent compared to Li metal batteries, but promising progress has been reported. Firstly, several types of electrode materials were fabricated by ALD with controllable structure and thickness. Secondly, the ALD coating was deposited as a coating for both anode and cathode electrolytes in different battery systems. On the cathode side, the ALD layers were used to prevent side reactions and transition metal dissolution during cycling. On the anode side, the ALD coating served as a buffer layer to relieve the volume change and stabilize the SEI layer. In particular, the ALD/MLD coatings were effective for metal anodes, such as Na metal and Zn metal anodes. Thirdly, ALD was shown to be capable of fabricating catalysts for the air electrode in Na–O<sub>2</sub> batteries.

## 2.2 ALD/MLD for supercapacitors

**2.2.1 ALD for electrode fabrication.** Supercapacitors are another important electrochemical energy storage system with higher power density compared to batteries.<sup>388</sup> However, the energy density of supercapacitors is not as high as traditional LIBs. This makes supercapacitors suitable for applications that require short power bursts but not necessarily high energy density.<sup>389,390</sup> Another great advantage of supercapacitors is the extremely long lifetime due to the charge storage mechanism, which is based on splitting charge at the surface of the electrodes in an electric double layer without chemical reactions.<sup>391–393</sup> Moreover, supercapacitors are generally safer than batteries for high power-rating charging and discharging.<sup>394,395</sup>

The performance of supercapacitors is highly dependent on the surface/near-surface reactions on the electrodes, which is one of the most significant factors for determining the performance of the supercapacitor. ALD/MLD has been used to deposit active materials on different substrates to fabricate composite electrodes for supercapacitors.<sup>230,400,401</sup> For example, Yushin's group fabricated VO<sub>2</sub>/multi-walled carbon nanotube (MWCNT) composite electrodes by ALD with controlled thickness and porosity, greatly improving the electrical conductivity and cycling stability (Fig. 19(a)).<sup>396</sup> The results show that the thin VO<sub>2</sub> films on the MWCNTs present higher capacitance, in which the 10 nm thick VO<sub>2</sub> exhibited the highest capacitance of 1550 F g<sup>-1</sup> at a current density of 1 A g<sup>-1</sup>. Moreover, the charge–discharge

tests show stable performance with high capacitance retention over 5000 cycles. TiO<sub>2</sub> is also a promising candidate with impressive capacitance behaviour. However, the low ion diffusion coefficient and high electrical resistance limit its further application.<sup>402,403</sup> To address these issues, Sun *et al.* deposit TiO<sub>2</sub> on graphene to prepare TiO<sub>2</sub>–G composites for supercapacitors.<sup>397</sup> As shown in Fig. 19(b), the surface of the wrinkled graphene is uniformly covered by TiO<sub>2</sub> nanoparticles, in which the particle size is 10 nm after 100 ALD cycles. The 50 cycles–TiO<sub>2</sub>–G and 100 cycles–TiO<sub>2</sub>–G composites deliver the capacity of 75 F g<sup>-1</sup> and 84 F g<sup>-1</sup> at a scan rate of 10 mV, respectively. The composite electrode shows good cycling performance up to 1000 cycles at 2 A g<sup>-1</sup>, as shown in Fig. 19(b). The composite electrode deposited by ALD possesses excellent conductivity for charge transfer and open structures for ion diffusion. Furthermore, their group demonstrated that ALD TiO<sub>2</sub> coated on CNTs could lead to a higher capacitance of 135 F g<sup>-1</sup> at 1 A g<sup>-1</sup> with excellent stability over >1000 cycles.<sup>404</sup> Other transition metal oxides, such as NiO, Co<sub>3</sub>O<sub>4</sub>, Mn<sub>3</sub>O<sub>4</sub>, Fe<sub>2</sub>O<sub>3</sub>, WO<sub>3</sub>, *etc.*, were deposited by ALD on different conductive substrates to fabricate electrodes for supercapacitors.<sup>405–410</sup> For example, NiO is one of the most popular electrode materials due to the high theoretical specific capacitance of 2573 F g<sup>-1</sup>, environmental friendliness and low cost. Qin's group applied the ALD technique to deposit NiO nanoparticles of various sizes on nanoporous graphene (NG) as the electrode for a supercapacitor.<sup>405</sup> The NiO/NG composite with 500 ALD cycles presented the best performance with a high specific capacitance of up to 1005.8 F g<sup>-1</sup> at current densities of 1 A g<sup>-1</sup>. The ALD deposited metal oxides with controlled size and uniform coverage provide short ion diffusion pathways and the conductive substrate can significantly enhance the conductivity of the metal oxides. Moreover, noble metal oxides, such as RuO<sub>2</sub>, are considered as one of the highest performing pseudocapacitive material candidates.<sup>411</sup> Realized by ALD, a very small amount of RuO<sub>2</sub> (~9.3 wt% Ru) leads to a 40% increase in capacitance for the graphene electrodes,<sup>398</sup> as shown in Fig. 19(c). Moreover, the strong chemical bonding between RuO<sub>2</sub> and graphene results in excellent cycling stability with over 92% capacitance retention over 4000 cycles.

Additionally, metal sulfides and metal nitrides have also been used as electrode materials for supercapacitors.<sup>412</sup> This was exemplified by Wang's group, in which a Co<sub>9</sub>S<sub>8</sub> film was deposited on a Ni foam electrode.<sup>399</sup> The deposition process used bis(*N,N*-diisopropylacetamidinato)cobalt(II) and H<sub>2</sub>S as the precursors for the ALD Co<sub>9</sub>S<sub>8</sub> process, as shown in Fig. 19(d). With 2000 ALD cycles, 54 nm Co<sub>9</sub>S<sub>8</sub> was coated on the Ni foam to form the Co<sub>9</sub>S<sub>8</sub>/NF electrode. In the 2 M KOH aqueous electrolyte, the excellent specific capacitances of 1645, 1616, 1544, 1493, 1378, and 1309 F g<sup>-1</sup> can be obtained for the Co<sub>9</sub>S<sub>8</sub>/NF electrode at the current densities of 3, 6, 12, 15, 30, and 45 A g<sup>-1</sup>, respectively. Furthermore, the prepared electrode exhibited stable long-term cycling performance with 94% retention at a current density of 45 A g<sup>-1</sup> up to 2000 cycles. Other metal sulfides, such as MoS<sub>2</sub> and SnS<sub>2</sub>, were also developed by ALD as electrodes for supercapacitors.<sup>413,414</sup> For example, molybdenum hexacarbonyl [Mo(CO)<sub>6</sub>] and H<sub>2</sub>S were used as

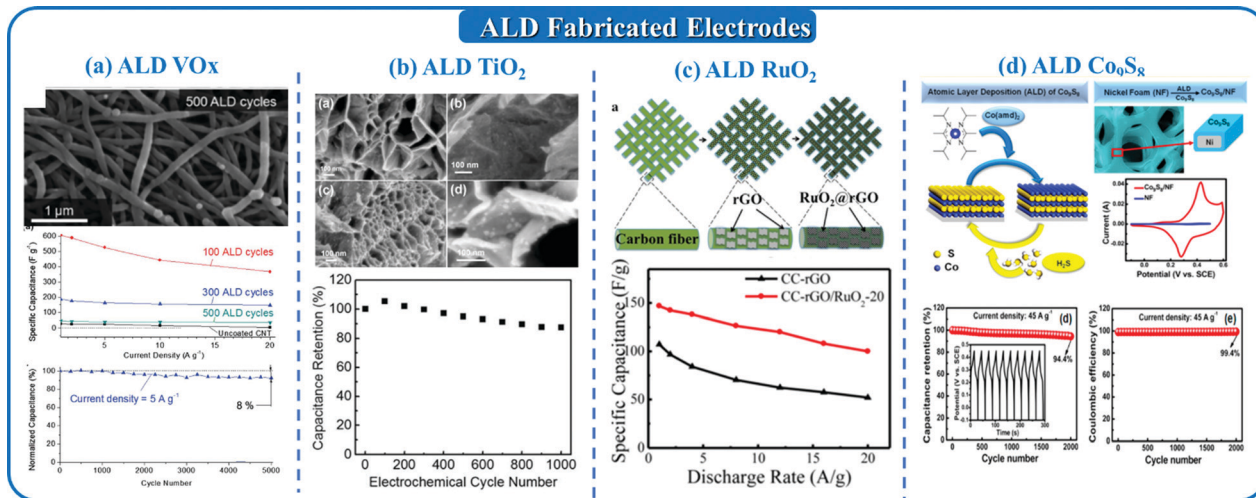


Fig. 19 ALD fabricated electrodes for supercapacitors: (a) ALD  $\text{VO}_x$ ,<sup>396</sup> (b) ALD  $\text{TiO}_2$ ,<sup>397</sup> (c) ALD  $\text{RuO}_2$ ,<sup>398</sup> (d) ALD  $\text{Co}_9\text{S}_8$ .<sup>399</sup>

precursors to deposit  $\text{MoS}_2$  on Ni foam substrates.<sup>413</sup> A high areal capacitance of  $3400 \text{ mF cm}^{-2}$  was obtained for the  $\text{MoS}_2/\text{NF}$  electrode with an optimized  $\text{MoS}_2$  thickness of 400 ALD cycles at a current density of  $3 \text{ mA cm}^{-2}$ . A high cycling stability ( $>80\%$  specific capacitance retention) was achieved for over 4500 cycles.

**2.2.2 ALD for the design of nanostructures.** To further improve the performance of supercapacitor electrodes, nanostructured materials need to be rationally designed in order to enhance the surface area and porosity. ALD/MLD techniques are promising techniques that can be used to design various nanostructures by using sacrificial templates. Lei's group designed well-defined Pt nanotube arrays and Pt/ $\text{MnO}_2$  core-shell nanotubes by ALD in anodic alumina templates and used them as current collectors.<sup>415</sup> In this process, the Pt NT array was first grown on the pre-patterned alumina template by ALD. Unlike the conventional ALD process for Pt deposition, an innovative ALD process for Pt was developed with a low  $\text{N}_2$  filling step used after pulsing. In their ALD Pt deposition process, the nucleation delay phenomenon largely decreased, and half of the Pt precursor was saved to obtain a similar Pt film deposited by the conventional ALD process. After the Pt deposition, mixed polydimethylsiloxane (PDMS) solution was used on the surface of the template followed by dissolving the backside alumina template. Then, a thin  $\text{MnO}_2$  layer was deposited on the Pt nanotubes by electrodeposition. The diameter and length of the Pt nanotubes are 180 nm and 2  $\mu\text{m}$ , respectively. The  $\text{MnO}_2$  shells were electrodeposited on Pt cores and controlled by the deposition times, as shown in Fig. 20(a). When the  $\text{MnO}_2$  deposition time was 30 s, the tube diameter and the shell thickness was about 240 and 30 nm, while the diameter and thickness reach up to about 340 and 80 nm respectively for 90 s deposition time (Fig. 20(a)). The Pt/ $\text{MnO}_2$ -30 s delivered a higher capacity of  $793 \text{ F g}^{-1}$  at a current density of  $2 \text{ A g}^{-1}$  compared to the  $530 \text{ F g}^{-1}$  of Pt/ $\text{MnO}_2$ -90 s. Moreover, the Pt/ $\text{MnO}_2$  presents good rate capability at different current densities, as shown in Fig. 20(a), which was attributed to the superior surface area of the Pt nanotube that could enable fast and reversible faradaic

reactions along with short ion diffusion paths. Another nanostructured TiC hollow sphere array was fabricated on a conductive substrate by the ALD-assisted template synthesis strategy,<sup>416</sup> as shown in Fig. 20(b). In a typical process, close-packed PS spheres were used as a template on the graphite substrate. ALD  $\text{TiO}_2$  was deposited on the template and the PS spheres were dissolved by toluene. Finally, the monolayer of TiC hollow nanosphere arrays was successfully formed after a high-temperature carbothermal reaction. The designed electrode delivered excellent electrochemical performances with high capacitance, ultra-long lifespan over 75 000 cycles with a high capacity retention of 98% and promising rate capability. Another interesting structure of  $\text{TiO}_2/\text{MnO}_2\text{-C}$  core/shell arrays were designed and fabricated using a combination of ALD and electrodeposition methods,<sup>417</sup> as shown in Fig. 20(c). A high specific capacitance of  $880 \text{ F g}^{-1}$  at  $2.5 \text{ A g}^{-1}$ , exceptional rate performances of  $735 \text{ F g}^{-1}$  at  $30 \text{ A g}^{-1}$  and excellent cycling stability of 94.3% capacitance retention after 20 000 cycles were obtained for the  $\text{TiO}_2/\text{MnO}_2\text{-C}$  electrodes. Some other nanostructures were further developed using ALD-assisted methods.<sup>238,417–423</sup> In a typical process, different types of templates are used to deposit ALD films. Afterwards, the templates are removed or transferred to create nanostructures by post-treatment processes. Then, the 3D nanostructures with high surface area and short ion diffusion paths are achieved with significantly improved electrochemical performances.

**2.2.3 MLD for electrode design.** MLD has also been reported as a fabrication method for electrode materials in supercapacitors. Because MLD films generally consist of pure polymers or organic-inorganic hybrid films, they are used to design porous metal oxides and carbon-containing composites with post-treatment methods. Qin's group was the first to demonstrate the use of MLD to design electrodes for supercapacitors, in which aromatic polyimide (PI) films were deposited on the surfaces of graphene and then carbonized to produce a nitrogen-doped carbon layer on graphene.<sup>424</sup> The as-prepared N-doped carbon layer-coated graphene electrodes exhibited a high capacitance of  $290.2 \text{ F g}^{-1}$  at  $1 \text{ A g}^{-1}$  with excellent rate properties

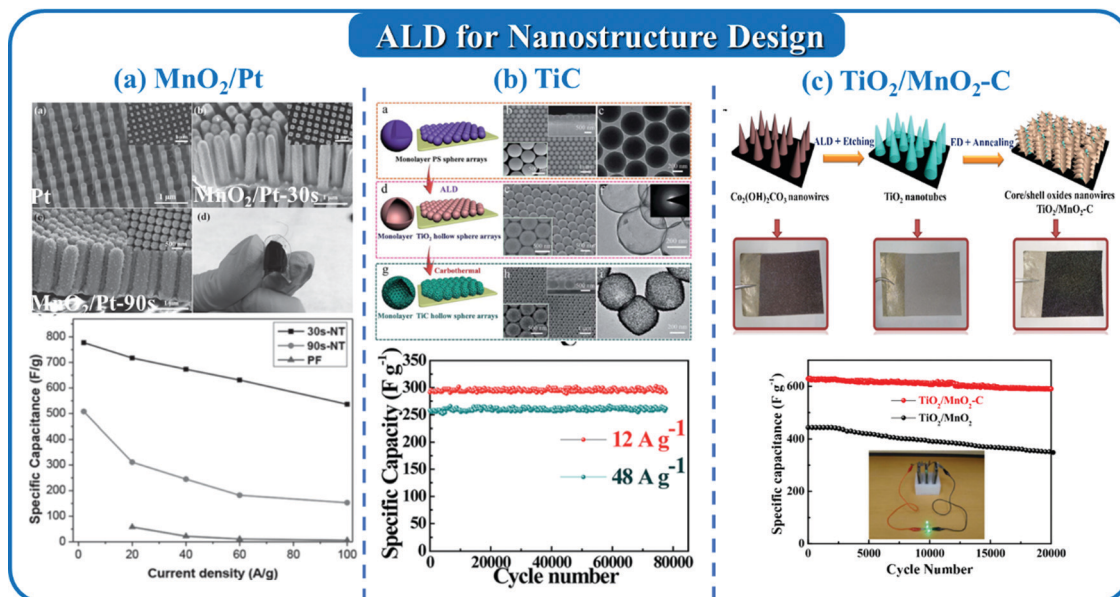


Fig. 20 ALD-designed nanostructured electrodes for supercapacitors: (a)  $\text{MnO}_2/\text{Pt}$ ;<sup>415</sup> (b)  $\text{TiC}$ ;<sup>416</sup> (c)  $\text{TiO}_2/\text{MnO}_2\text{-C}$ .<sup>417</sup>

and stability. In another example, a gap shell structure with an ultrathin and conformal porous carbon coating was successfully constructed through ALD and MLD processes followed by annealing and etching.<sup>425</sup> The as-obtained composite electrode exhibited a high capacitance of  $1034.6 \text{ F g}^{-1}$  at a current density of  $1 \text{ A g}^{-1}$  with superior rate capability. The gap-porous carbon derived by ALD/MLD can not only maintain the electrochemical reactivity of nickel sulfide but also provide a protective layer with a buffer area for volume change.

In this section, we summarized the development of ALD/MLD techniques for supercapacitor applications. Firstly, different materials, including metal oxides, metal sulfides and metal nitrides, were deposited by ALD on various conductive substrates to fabricate composite electrodes for supercapacitors. The conductive substrates, such as graphene, carbon nanotubes and Ni foam, provide improved electronic conductivity for the ALD-deposited materials. The nanoscale materials deposited by ALD can provide uniform coverage and short ion diffusion pathways, resulting in enhanced electrochemical performances. Secondly, by combining with other methods or using templates, ALD was used to design and fabricate nanostructured materials with high surface areas. Thirdly, MLD was used to create porous metal oxides and carbon-containing composites by post-treatment methods. However, the study of MLD films for supercapacitor applications is still in a state of infancy. This application of MLD is expected to be explored further in the future.

### 3. ALD/MLD for energy conversion

#### 3.1 ALD/MLD for electrocatalytic reactions

##### 3.1.1 ALD/MLD for proton-exchange membrane fuel cells

3.1.1.1 ALD of Pt on different substrates for improving ORR activity. Proton-exchange membrane fuel cells (PEMFCs) are

promising alternative power sources for transportation and portable applications due to their high efficiency in converting the chemical energy from hydrogen into electrical energy, near room temperature operation, and zero emissions.<sup>426</sup> During the operation of PEMFCs, the oxygen reduction reaction (ORR) is the rate-limiting reaction due to its inherently sluggish kinetics. Therefore, in order to achieve widespread commercial implementation of PEMFCs, developing a promising catalyst for enhanced oxygen reduction reaction (ORR) kinetics is of great significance. Platinum is reported as the most effective catalyst used for the ORR in PEMFC.<sup>427,428</sup> However, Pt is still facing a great challenge for commercial applications in PEMFCs due to its gradually increasing price and low abundance in the earth. ALD is a promising technique to solve the problems associated with reducing cost. ALD can not only precisely control the particle sizes ranging from single atom, sub-nanometer clusters, or nanoparticles in high-aspect-ratio and porous materials, but can also be used to design novel structures through surface engineering of the substrate to improve the activity of Pt catalysts.<sup>429</sup>

Aaltonen *et al.* made great progress in ALD synthesis by deposition of Ru metal from  $\text{RuCp}_2$  and  $\text{O}_2$ , and the process has been extended to other metals such as Pt, Rh, and Ir.<sup>430,431</sup> The intrinsic roughness of the surface induced by noble metal ALD processes can effectively increase the surface area of the catalyst, leading to a more efficient device.<sup>19,432</sup> Due to the self-limiting characteristic of the ALD process, the precursor should be volatile and thermally stable. In addition, precursors must chemisorb on the surface or react rapidly with the substrates and react aggressively with each other.<sup>433</sup> Until now, Pt precursors such as  $\text{MeCpPtMe}_3$ ,  $\text{Pt}(\text{acac})_2$  (acac = acetylacetonato) and platinum(II) hexafluoroacetylacetonate [ $\text{Pt}(\text{hfac})_2$ ] have been investigated for the deposition of Pt. However,  $\text{Pt}(\text{acac})_2$  has lower thermal stability, which makes it an unsuitable precursor for thermal ALD.<sup>434,435</sup> When using

Pt(hfac)<sub>2</sub> as the precursor, the formalin should be used as the reactants and the ALD process was found to be only effective at relatively high temperatures (200 °C).<sup>436</sup> Therefore, MeCpPtMe<sub>3</sub> is the most widely used Pt precursor in ALD for the preparation of Pt NPs used in the ORR. During the ALD Pt process, the island growth of Pt NPs occurs instead of thin film formation. In a whole Pt ALD cycle, the Pt precursors firstly bond with the functional groups on the surface of the substrates. Then the chemical ligands are removed by the introduction of O<sub>2</sub> or O<sub>3</sub>. The formed Pt atoms might aggregate to small clusters due to the limited number of functional groups on the substrate surface, which leads to the formation of Pt NPs instead of a thin film on the substrates. Hence, the selection of the substrate is of great importance for ALD Pt NPs, and it can significantly determine the ORR activity of the catalysts. Pt nanoparticles (NPs) are deposited on substrates such as oxides, carbon materials and other metals.

Carbon nanotubes (CNTs) are one of the most widely used carbon substrates for the deposition of Pt. Chen and co-workers prepared three carbon nanotube-supported Pt nanoparticles (Pt/CNT) with different sizes by tuning the number of ALD cycles (Fig. 21(a)).<sup>437</sup> In addition, they compared the ALD-prepared catalysts with those obtained by impregnation methods. During the ORR test, the ALD-Pt/CNT catalysts showed much higher activity and selectivity than those of the impregnation-Pt/CNT catalysts. It was found that the well-controlled Pt particle size and distribution, desirable Pt<sup>0</sup> 4f binding energy, and the Cl-free Pt surfaces of the ALD-Pt/CNT catalysts contributed to the outstanding ORR performance. Besides carbon-based supports, Yang and co-workers fabricated fibrous membranes of niobium-doped titania-supported platinum catalysts (Pt@Nb-TiO<sub>2</sub>) by a two-step approach (Fig. 21(b)).<sup>438</sup> Firstly, they synthesized Nb-TiO<sub>2</sub> fibrous membranes by electrospinning. Then the Pt NPs were deposited on Nb-TiO<sub>2</sub> by ALD. The as-prepared catalysts were further post-treated at 200 °C in 5% H<sub>2</sub> to improve the conductivity of Nb-TiO<sub>2</sub> fibres and obtain Pt NPs with better crystallinity. After the post-treatment, the ORR activity could reach as high as 0.28 mA cm<sup>-2</sup> at 0.9 V (vs. RHE) and it had very good stability with only a ~10% loss in ORR activity after 30k cycles. When Pt is deposited on TiSi<sub>2</sub> nanonets, Pt nanoparticles were observed to only grow on the (020) planes and the NPs exhibited 5-fold twinned structures with planes exposed, as shown in Fig. 21(c).<sup>439</sup> The interaction between Pt and the TiSi<sub>2</sub> nanonet *b* planes was the key to the formation of twinned Pt nanoparticles. At 0.9 V vs. RHE, the current density of the Pt/TiSi<sub>2</sub> catalysts was 0.16 mA cm<sup>-2</sup>, which is considerably higher than that of Pt/C (0.1 mA cm<sup>-2</sup>). The availability of non-carbon electrode constructions, such as the Pt@Nb-TiO<sub>2</sub> and Pt/TiSi<sub>2</sub>, permits fundamental studies to discern the role of the carbon support in existing devices.

To improve the mass activity of Pt catalysts and thereby reduce the cost of the catalyst, one of the most direct routes is to increase their atom utilization efficiency (AUE) by reducing the particle size to clusters or even single atoms.<sup>440</sup> However, the single atom Pt catalysts exhibit a 2 electron process instead of a 4 electron process during the ORR.<sup>441</sup> DFT results indicate that the breaking of the O-O bond can readily occur on Pt

nanoparticles. Meanwhile, for single atoms, the O<sub>2</sub> molecule is end-on adsorbed on isolated Pt atoms (which avoids O-O cleavage), resulting in the selective production of H<sub>2</sub>O<sub>2</sub>.<sup>442,443</sup> It has been reported that Pt single atoms can not only be deposited on carbon-based supports,<sup>444,445</sup> but also on a metal surface, forming the single atom alloys (SAAs). Sun *et al.* successfully deposited Pt single atoms on octahedral Pd NPs due to the similar lattice constants between Pd and Pt. To obtain Pt single atoms, we only conducted one cycle of ALD by using MeCpPtMe<sub>3</sub> and O<sub>2</sub> as precursors.<sup>446</sup> The atomic-resolution STEM image (Fig. 21(d)) clearly illustrates the presence of Pt-isolated atoms on the Pd(111) surfaces. With the formation of the SAA structure, the Pt atoms on Pd exhibited more metallic state compared to that on NCNTs. The coordination number of Pt-Pd is fitted to be 0.8 in the EXAFS spectra, which further provides direct evidence of the presence of isolated Pt atoms on octahedral Pd particles. In the ORR, the octahedral Pt/Pd SAA catalysts exhibited a mass activity of 1.09 A mg<sup>-1</sup> normalized by the Pt mass at 0.9 V vs. RHE, which is 8.3 times greater than that of the Pt/C catalyst (0.13 A mg<sup>-1</sup>).

**3.1.1.2 Improvement of the ORR durability by area selective ALD and MLD.** In addition to the activity, durability is another important parameter for evaluating Pt catalysts. The harsh conditions (strong acid environment, high oxygen concentration, high humidity and *etc.*) at the cathode might gradually deactivate Pt catalysts, resulting in the loss of Pt performance due to Pt NP migration and agglomeration. Thus, there is a significant need for the development of highly active and durable Pt catalysts that can withstand harsh conditions for long-term testing. It has been reported that the creation of the porous layer of inorganic oxide is an effective route for the stabilization of supported metal NPs. The surrounding oxide layer, which has weaker bonding to metal NPs, can provide an additional energy barrier to restrict the diffusion and migration of the metal NPs across the biphasic support surface. However, for many methods, precise control over the thickness of the porous overlayers is difficult to achieve and results in a decrease in ORR activity from mass transfer resistance. By using ALD, the thickness of the stabilizer can be precisely controlled. McNeary *et al.* stabilized carbon black-based Pt catalysts with ALD-deposited TiO<sub>2</sub>.<sup>447</sup> They found that ten cycles of TiO<sub>2</sub> ALD on the functionalized substrate yielded well dispersed, locally homogeneous TiO<sub>2</sub> structures that could surround the small Pt nanoparticles. The catalysts with the addition of TiO<sub>2</sub> ALD nanostructures maintained around 70% mass activity after the accelerated durability testing (ADT).

By manipulating the surface functional groups of Pt catalysts, area selective ALD can be achieved, which means that the location of deposited materials is precisely controlled, avoiding the coverage of Pt active sites.<sup>336,448,449</sup> One of the most successful designs for highly stable catalysts is Pt catalysts encapsulated in zirconia nanocages by area-selective ALD.<sup>450</sup> The synthetic strategy is depicted in Fig. 22(a). The ALD Pt NPs were firstly deposited on nitrogen-doped carbon nanotubes (NCNTs). Then oleylamine was attached to the Pt NP surface

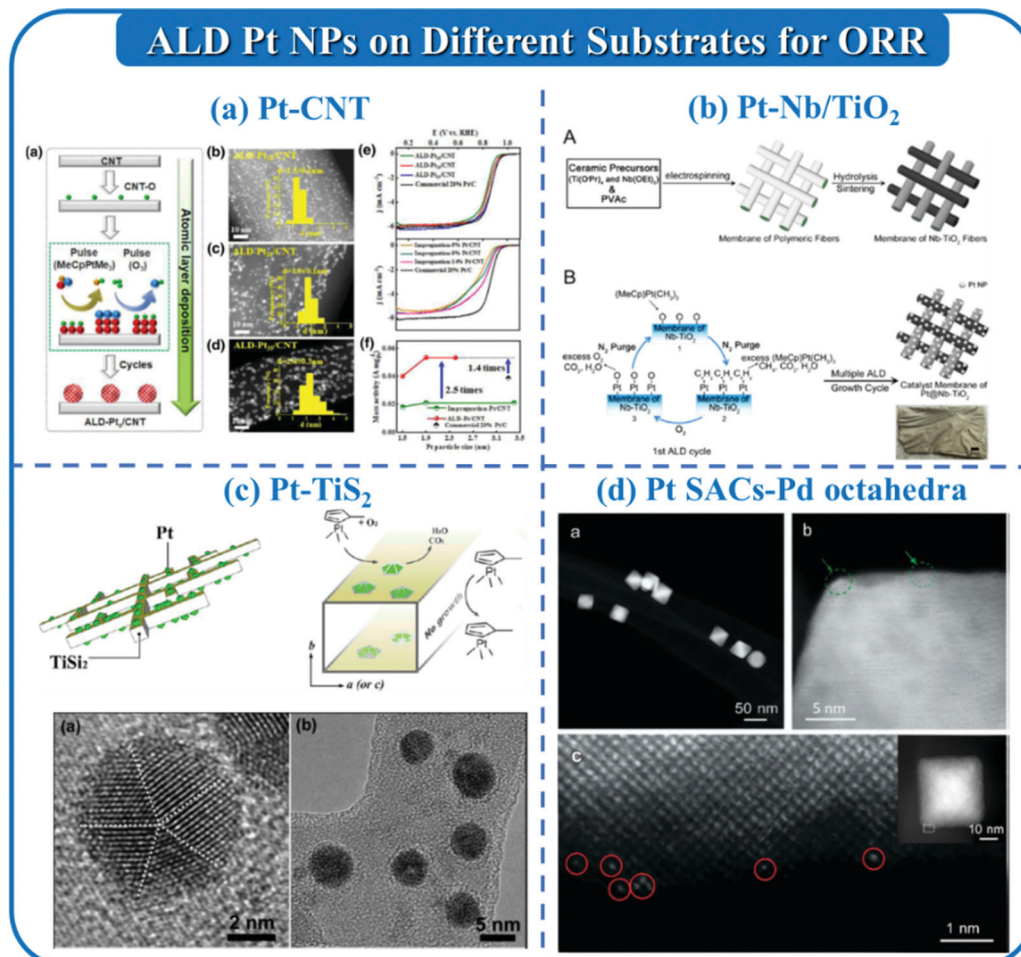


Fig. 21 ALD of Pt NPs on different substrates by using MeCpPtMe<sub>3</sub> for ORR: (a) Pt NPs on CNTs; (b) Pt NPs on Nb–TiO<sub>2</sub>; (c) Pt NPs on TiS<sub>2</sub>; (d) Pt single atoms on octahedral Pd NPs.

as a blocking agent, which results in the selective deposition of zirconia around the Pt NPs, instead of on the Pt surface due to the blocking agent. The Pt catalyst encapsulated in zirconium nanocages showed very high activity and stability towards the ORR in acid media. The novel catalyst exhibited 9 times higher stability than ALD-Pt on NCNTs without the zirconia nanocage and 10 times higher stability compared to the state-of-the-art commercial Pt/C catalyst. Pt NPs encapsulated in a zirconia nanocage also showed six times greater ORR activity than a Pt/C catalyst. The remarkably stable performance with this novel catalyst is attributed to the presence of the zirconia nanocages, which prevent Pt NPs from migrating and agglomerating on the support. In addition, the higher surface area of small Pt NPs and the synergistic effects between Pt and ZrO<sub>2</sub> resulted in the enhanced activity of Pt/ZrO<sub>2</sub> catalysts. Besides ZrO<sub>2</sub>, TaO<sub>x</sub> has also been reported as an alloying additive that can enhance the activity and durability of various catalysts. Our group deposited TaO<sub>x</sub> NPs on a commercial Pt/C catalyst by area-selective ALD.<sup>451</sup> Due to the blocking agent, TaO<sub>x</sub> particles are selectively nucleated and grown around Pt NPs. With the formation of the triple-junction structure at the interface, the sample with 35 ALD cycles of TaO<sub>x</sub> on the Pt/C surface exhibited superior

stability compared with Pt/C. After 120 h ADT, the activity in a membrane electrode assembly (MEA) remained 88%. These examples show that it is critical to design novel Pt encapsulation catalysts with open or holey nanocage architectures by precisely controlling ALD metal oxide layers. The open or holey nanocage architectures are essential for achieving good performance because they allow reactants, such as oxygen and protons, to reach the Pt surface.

Molecular layer deposition (MLD), as an analogue of ALD, has been employed to produce inorganic–organic hybrid thin films with many advantages. Alucone is considered as a promising material as the interlayer to improve the stability of catalysts. However, the poor conductivity of MLD coatings greatly hinders their application in electrochemical systems. Recently, Sun *et al.* prepared a porous structure by annealing the alucone MLD layer. With the deposition of Pt NPs on the porous structure, the Pt catalysts were anchored on the surface and exhibited good performance.<sup>452</sup> As shown in Fig. 22(b), 30 cycles of MLD alucone (TMA–GLY) thin film were firstly deposited on the NCNTs using sequential exposures of TMA and glycerol at 150 °C. After annealing the NCNT-MLD material at 400 °C for 3 h, Pt NPs are selectively deposited on the porous

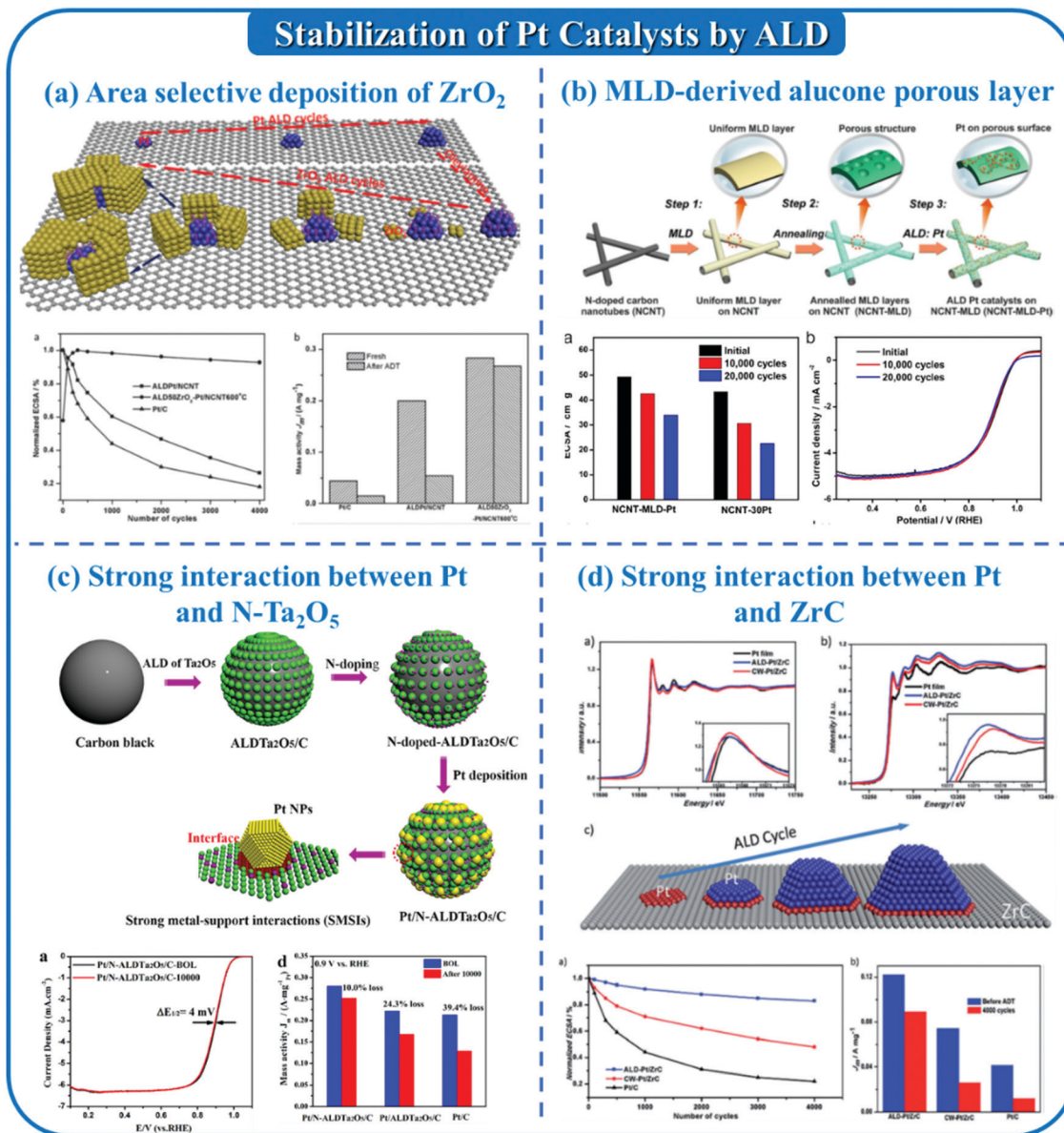


Fig. 22 ALD/MLD for Pt catalyst stabilization: (a) area-selective ALD of  $ZrO_2$ ; (b) MLD alucone-derived porous carbon layer; (c) ALD of Pt on N-Ta<sub>2</sub>O<sub>5</sub>; (d) ALD of Pt on ZrC substrates.

structure by an ALD method. The Pt catalysts show significantly enhanced ORR activity and durability compared to that without the MLD interlayer.

**3.1.1.3 Improvement of ORR durability by enhancing the interactions between Pt single atoms and supports.** Carbon-based substrates have many advantages, such as large surface area, high electrical conductivity and well-developed pore structure, and thus have been widely applied as the support material in electrochemistry. However, the weak interactions between the carbon support and metal particles lead to Pt NP migration and agglomeration, and eventually a rapid degradation of electrocatalyst performance. To solve these issues, enhancing the interaction between Pt NPs and carbon supports by ALD

oxide has been proposed. The strong metal-support interactions (SMSIs) can improve the activity and durability of the Pt catalysts by tuning the electronic structure and hindering metal particle migration. In addition, the preparation of metal oxide-decorated carbon composites for the deposition of Pt NPs can maintain the good electroconductivity of the substrates. By introducing metal oxide NPs to the position between the Pt catalyst and carbon support, a stable and strong interface between the Pt and metal oxide can be achieved, which plays a significant role in preventing the rapid degradation of the catalytic activity.

For example, Sun *et al.* synthesized extremely stable Pt NPs immobilized on a carbon support *via* a bridge layer of nitrogen-doped tantalum oxide (N-Ta<sub>2</sub>O<sub>5</sub>).<sup>331</sup> Firstly, the Ta<sub>2</sub>O<sub>5</sub> NPs were developed by ALD to decorate the carbon black surface. Then,

NH<sub>3</sub> treatment of the ALDTa<sub>2</sub>O<sub>5</sub>/C support was conducted to dope N species, leading to the formation of N-doped-Ta<sub>2</sub>O<sub>5</sub>/C with enhanced conductivity. Finally, a microwave-assisted ethylene glycol (EG) reduction method was used to deposit Pt NPs on different supports. X-ray absorption spectroscopy indicated that the total unoccupied density of states of Pt in the Pt/N-ALDTa<sub>2</sub>O<sub>5</sub>/C is higher than that of 0.826 for Pt/ALDTa<sub>2</sub>O<sub>5</sub>/C and 0.795 for Pt/C. This result provides the most direct evidence for the electronic effects and SMSIs formed between the Pt NPs and N-Ta<sub>2</sub>O<sub>5</sub>/C support. The as-prepared Pt/N-ALDTa<sub>2</sub>O<sub>5</sub>/C catalyst showed around two times higher mass activity compared to Pt/C after 10 000 cycles of ADT (Fig. 22(c)). Another metal oxide used for increasing the interaction between Pt and the support is ZrO<sub>2</sub>. Cheng and co-workers synthesized ALD-ZrO<sub>2</sub>/nitrogen-doped graphene nanosheets (ZrO<sub>2</sub>/NGNs) as the support for Pt NPs.<sup>453</sup> The unique triple-interface of ZrO<sub>2</sub>-Pt-NGN induced strong interaction between the Pt NPs and supports. As a result, the Pt-ZrO<sub>2</sub>/NGN catalyst exhibited 2.2 times higher durability than that of Pt/NGNs in ORR testing. These attempts provide more strategies for the preparation of well-dispersed, nanoscale metal compounds for carbon surface modification towards achieving controllable and well-defined metal-support interfaces.

In addition to the introduction of metal oxides between the carbon support and Pt NPs, the substitution of the carbon-based support with other materials is another promising strategy for improving the durability of Pt catalysts. Among various supports, ZrC has many advantages, such as high conductivity, strong electrochemical corrosion resistance, high stability, and good thermal conductivity, which makes it as a good substitute for Vulcan XC-72 (carbon black) support. Based on this, Sun *et al.* used a ZrC support as a substitute for a carbon-based support for the ALD of Pt NPs.<sup>454</sup> As shown in Fig. 22(d), we synthesized a robust Pt-on-ZrC nanocomposite catalyst with strong metal-support interactions by ALD. The quantitative XANES results showed that the interactions between Pt and the ZrC support by ALD are much higher than that prepared from the conventional chemical reduction method. Due to the strong interaction between Pt and ZrC, the exhibited ORR activity was 9 times greater than Pt/C after the extended durability test.

**3.1.1.4 ALD for MEA systems.** On the anode side, the fast hydrogen oxidation reaction (HOR) is driven by a small amount of Pt/C catalyst. However, when the Pt loading is lower than 0.025 mg cm<sup>-2</sup>, the HOR performance would obviously decrease due to the very thin layer thickness. Therefore, the Pt loading at the anode needs to be further decreased for fuel cell automotive applications. Hsieh *et al.* directly deposited Pt NPs by ALD on a gas diffusion electrode consisting of CNT and GO. The MEA was fabricated using an ALD-Pt electrode as the anode to study the performance of a single cell, which offered improved catalytic activity.<sup>455,456</sup> Recently, Shu *et al.* deposited Pt NPs on a gas diffusion layer by the ALD method.<sup>457,458</sup> The formed catalyst layer exhibited around 2.5 times higher mass activity than that of the MEA with the anode prepared using the commercial catalyst. Perng and co-workers grew Pt NPs on

nitric acid-treated CNTs with ALD for catalysis in PEMFCs.<sup>459</sup> The Pt loading amount of the anode and cathode (0.019 and 0.044 mg cm<sup>-2</sup>, respectively) in the MEA is significantly reduced. In addition, the PEMFC test indicated that the specific power density of ALD-prepared MEA is 11 times higher than that made from commercial catalysts. This result revealed that ALD can significantly decrease the Pt loading of the electrodes in PEMFCs. To achieve extremely low Pt loading while maintaining high PEMFC performance and durability, Sun *et al.* prepared a series of membrane electrode assemblies (MEAs) with low Pt loading in the anode layer through the use of ALD.<sup>460</sup> The best ALDPt-MEA with an ultralow anode Pt loading of 0.01 mg cm<sup>-2</sup> displays a high surface area of 155 m<sup>2</sup> g<sub>Pt</sub><sup>-1</sup>. During the PEMFC test, the ALDPt-MEA exhibited a power density of 0.78 W cm<sup>-2</sup>, and maintained around 90% after ADT (Fig. 23(a)). The above studies demonstrated that the application of ALD for Pt deposition directly on the carbon layer of the electrodes can effectively reduce the Pt loading while enhancing the Pt dispersion, utilization, and durability, thus enhancing their performance on MEA anodes.

In addition to the fabrication of active Pt catalysts, ALD has also been applied for the improvement of membrane properties. Moghaddam and Shannon prepared a silicon-based inorganic-organic membrane as a substitute for Nafion-based PEMFCs (Fig. 23(b)).<sup>461</sup> Silicon-based inorganic-organic membranes have a number of advantages over Nafion, including higher proton conductivity, a lack of volume change, and membrane electrode assembly capabilities. A silicon membrane with pore diameters of ~5–7 nm was firstly fabricated, followed by the addition of a self-assembled molecular monolayer on the pore surface. Plasma-directed atomic layer deposition (PD-ALD) was employed to create a 2 nm thick hydrophilic silica aperture at the mouth of the pores. With the formation of the silica layer, the diameter of the pores is reduced, and the proton conductivity value is significantly increased, which is two to three orders of magnitude higher than that of Nafion at low humidity. The MEA with this membrane exhibited much higher power density than previously achieved with a dry hydrogen feed and an air-breathing cathode. Inside the membrane, the catalysts are expected to catalyze water production. The introduction of metal oxide nanoparticles that have hygroscopic properties, such as TiO<sub>2</sub>, can absorb the water produced in the cathode reaction. Uhm and Lee coated an ultrathin layer of hydrophilic TiO<sub>2</sub> on a hydrophobic microporous gas diffusion layer (GDL) at the cathode by ALD to maintain the power performance of PEFC cathodes operating under extremely low humidity.<sup>462</sup> They found that the TiO<sub>2</sub>-coated GDL resulted in higher performance than the as-received GDL at low humidity operation.

### 3.1.2 ALD for electrocatalytic small organic molecule oxidation

**3.1.2.1 ALD for electrocatalytic methanol oxidation.** The direct methanol fuel cell (DMFC) has received more and more attention due to its high efficiency, high power density and short start-up transient-response time. Despite considerable advances in these points, the widespread application of DMFCs has been hindered by several technical and economic barriers. The low

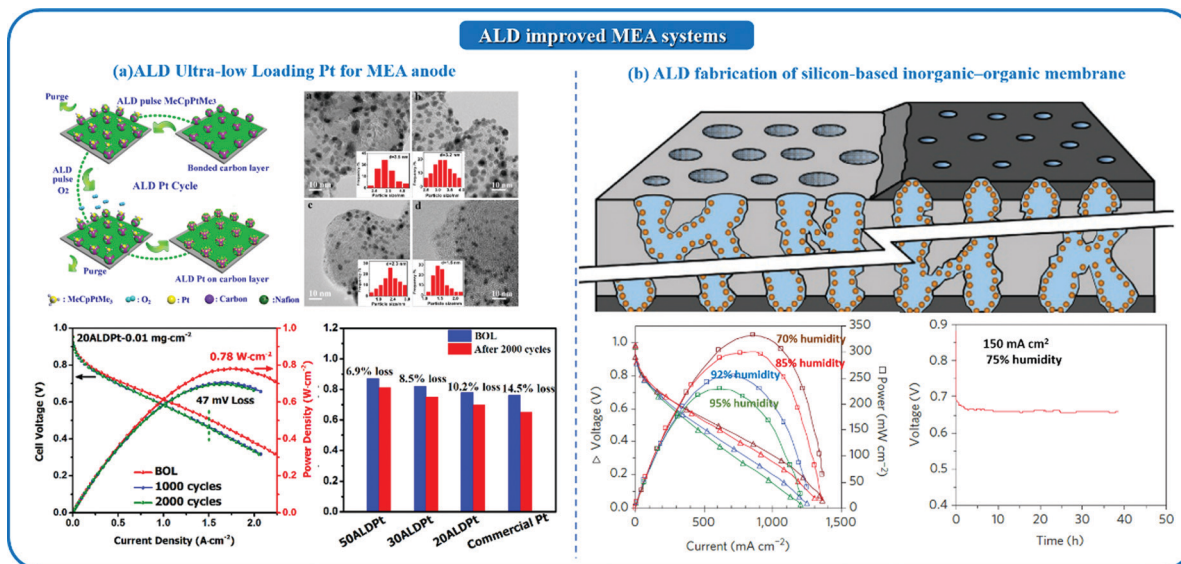


Fig. 23 The application of ALD towards the fabrication of MEA systems: (a) ALD fabrication of ultra-low Pt loading anode; (b) ALD-modified silicon-based inorganic-organic membrane.

electrocatalytic activity of commercial Pt/C catalysts toward the MOR and serious CO poisoning are the most severe challenges. By using ALD, Hsieh *et al.* fabricated Pt NPs on carbon powders, offering superior catalytic activity toward MOR. They found that the ALD-Pt catalyst offers not only an improved catalytic activity toward methanol oxidation but also superior CO tolerance, as compared to commercial Pt/C. The substrates for Pt loading can also significantly affect the MOR activity.<sup>463</sup> Qin and co-workers prepared a Pt/CNT catalyst coated with N-doped carbon (NC-Pt/CNTs) by ALD (Fig. 24(a)).<sup>464</sup> Firstly, Pt NPs and polyimide (PI) are sequentially deposited on CNTs by ALD. Subsequently, the catalysts were annealed at 600 °C in a H<sub>2</sub> atmosphere, and the PI was carbonized to produce porous N-doped carbon. It was observed that the current density of NC-Pt/CNTs was 0.76 A mg<sub>Pt</sub><sup>-1</sup>, which is 2.7 times higher than that of commercial Pt/C and 1.7 times higher than that of Pt/CNTs. The interactions between Pt and the N-doped carbon can weaken the Pt-CO bond, resulting in enhanced catalytic activity and durability for the MOR.

In addition to carbon substrates, metal oxide substrates have proven to be effective in minimizing the effect of CO poisoning. Peng and co-workers prepared a Pt@ZnO catalyst on carbon cloth *via* ALD.<sup>465</sup> Firstly, they deposited a ZnO seed layer on carbon cloth, followed by hydrothermal growth of high-density vertical aligned ZnO nanorods (NRs). To increase the surface hydrophilicity of the ZnO NR arrays, UV light irradiation was used prior to the deposition of Pt NPs on ZnO by ALD. XPS results indicated that Zn(OH)<sub>2</sub> species were formed on the ZnO NR arrays, which may enhance CO tolerance *via* a bifunctional mechanism. The negative binding energy shift of the Pt 4f peak and the positive shift of the Zn 2p peak suggest that charge transfer occurs between the ZnO support and the Pt NPs. The electronic modification of surface Pt atoms *via* ligand effects could lower the adsorption energy of CO and improve the electrocatalytic activity on MOR. Thanks to the

ZnO substrates, the catalysts exhibited 90% higher methanol oxidation activity than commercial Pt/C with the same Pt loading. Sun and co-workers deposited a 1.5 nm SnO<sub>2</sub> interfacial layer to anchor Pt NPs on CNTs by using SnCl<sub>4</sub> and H<sub>2</sub>O as precursors (Fig. 24(b)).<sup>466</sup> In the electrochemical testing, the ECSA of Pt-SnO<sub>2</sub>/CNTs is 1.36 times higher than that of Pt/CNTs. In addition, the Pt-SnO<sub>2</sub>/CNTs also shows higher activity towards the MOR than Pt/CNTs, as indicated by a 52 mV more negative onset potential, along with larger specific and mass activities. Recently, Mo<sub>2</sub>C has also been used as an anode material for the direct oxidation of hydrocarbons in fuel cells. Chen and co-workers demonstrated a highly active and stable Pt nanoparticle/Mo<sub>2</sub>C nanotube catalyst for methanol electro-oxidation.<sup>467</sup> The peak current density of Pt NPs/Mo<sub>2</sub>C for the MOR is 1.5 times higher than that of the commercial Pt/C catalysts.

A convenient way to modify the strong CO intermediate bonding interactions with the Pt catalyst is to make alloys or bi-metallic surfaces. To obtain bimetallic catalysts, the two metal precursors should have similar properties, as the ALD process is carried out using one precursor cycle followed by another precursor cycle. For example, Sairanen *et al.* prepared Pt-Co bimetallic catalysts by using Pt(acac)<sub>2</sub> and Co(acac)<sub>3</sub> as precursors.<sup>434</sup> When compared with ALD mono-metallic Pt, the onset potential decreased by 50 mV and the current intensities of the Pt-Co catalysts were 1.5 times higher, which might be attributed to the electronic effect of Co on Pt. Other widely used catalysts for MOR are Pt-Ru bimetallic catalysts. It has been reported that the removal of CO is much faster on a Pt-Ru surface than on pure Pt.<sup>468,469</sup> For instance, Johansson and co-workers prepared highly dispersed Ru-decorated Pt nanoparticles using MeCpPtMe<sub>3</sub>, Ru(EtCp)<sub>2</sub> and O<sub>2</sub> as the precursors.<sup>470</sup> The Pt nanoparticles decorated with 5 ALD Ru cycles exhibited much better catalytic activity towards the MOR

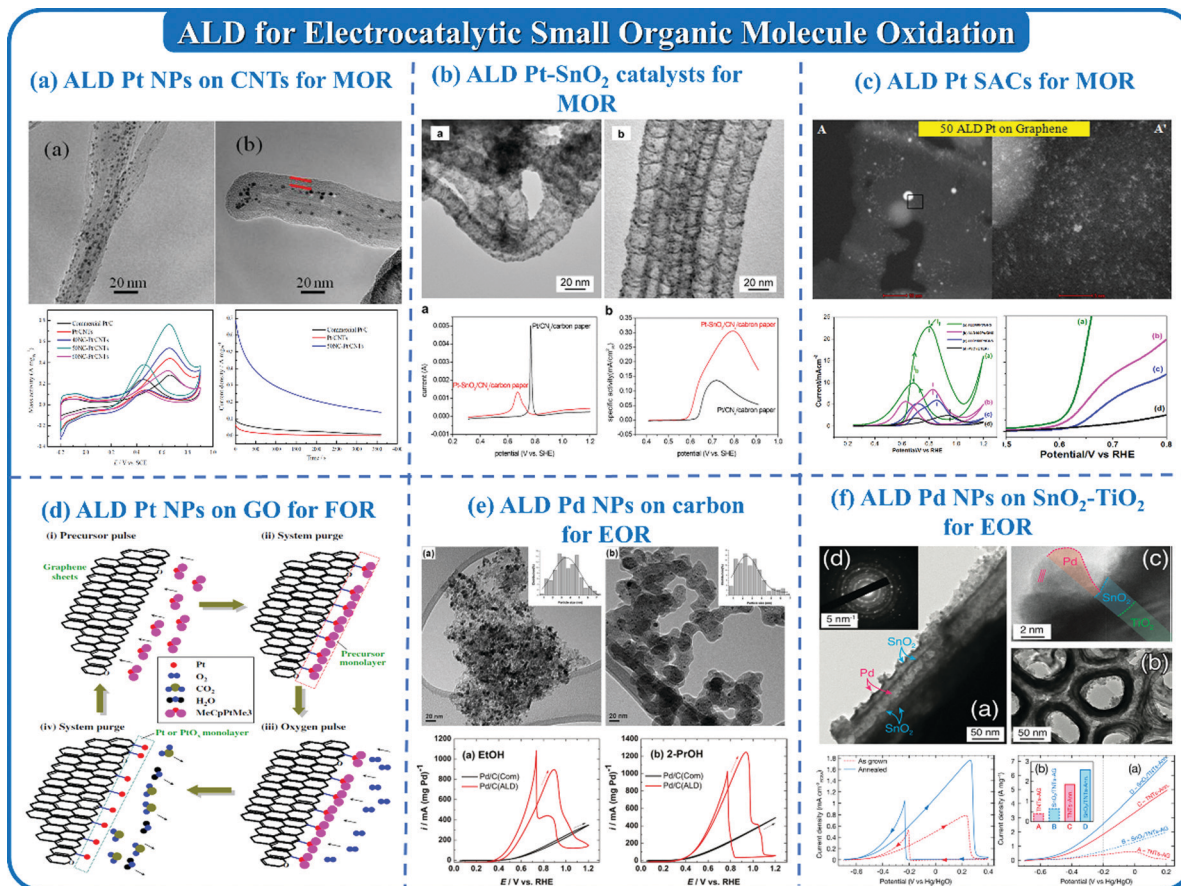


Fig. 24 ALD Pt and Pd NPs for electrocatalytic small organic molecule oxidation: (a) Pt–CNTs for MOR; (b) Pt–SnO<sub>2</sub> for MOR; (c) Pt SACs on graphene for MOR; (d) Pt NPs–GO for FOR; (e) Pt NPs on porous carbon for FOR; (f) Pd NPs on SnO<sub>2</sub>–TiO<sub>2</sub> for EOR.

compared with the undecorated Pt catalyst. Shim and co-workers synthesized Ru onto a porous Pt mesh by ALD and applied the heterogeneous Pt–Ru catalysts directly as the anode in direct methanol solid oxide fuel cells (DMSOFCs).<sup>471</sup> The obtained Pt/Ru catalyst after 100 ALD cycles outperformed pure Pt by more than 1 order of magnitude in terms of power output. The authors also deposited Ru by ALD on a porous Ni mesh to substitute Pt catalysts. The maximum power density of the Ni/ALD Ru sample was found to be comparable to that of the Pt/ALD Ru sample, despite the dramatic reduction (<10%) in precious metal catalyst loading.<sup>472</sup> The good performance of the Ni/ALD Ru sample is due to the stabilizing effect of the Ni surface after ALD deposition of Ru and the prevention of carbon formation.

Decreasing the size of Pt nanoparticles is an effective route to increasing the surface area of Pt catalysts. In addition, the formation of clusters and single atoms can improve atom utilization to a new level. In 2013, Sun *et al.* reported a practical synthesis for single Pt atoms anchored to graphene nanosheets using the ALD technique.<sup>473</sup> In this study, the Pt catalysts from single atoms, subnanometer clusters to nanoparticles were precisely controlled by the ALD method. Among the three types of Pt catalysts, the single atom catalysts exhibited the best activity (Fig. 24(c)). XAFS analysis revealed that the superior performance of single atoms was contributed

by the low-coordination environment and partially unoccupied 5d states.

**3.1.2.2 ALD for electrocatalytic formic acid oxidation.** The fuel cells based on formic acid are particularly well-suited for applications related to room-temperature power generation and portable electronics. The performance of a direct formic acid fuel cell (DFAFC) is largely determined by the catalyst deposited on the anode for formic acid oxidation (FAO). Pt is an effective catalyst for FAO. Hsieh and co-workers fabricated Pt nanocatalysts supported on graphene oxide (GO) sheets by ALD and investigated their electrocatalytic performance in FAO.<sup>474,475</sup> The ALD-Pt atoms were decorated on the edges of the GO sheets with the presence of dangling bonds and oxygen functionalities (Fig. 24(d)), which resulted in unique FAO catalytic activity. During the FAO process on Pt, the ratio of the current density of the first anodic peak ( $J_{1st}$ ) to the second anodic peak ( $J_{2nd}$ ) clearly provides a clue regarding the reaction pathway (direct or indirect oxidation). They found that the ratio of  $J_{1st}/J_{2nd}$  for the Pt–GO catalyst is approximately 99.8%, and a high ratio of 93.7% can be reached after 100 CV cycles, indicating that the ALD-Pt catalyst displays the capability to regenerate the CO-adsorbed surface after cycling. The presence of Pt–O species can increase the anti-poisoning ability during

FAO in addition to improvement of the catalytic activity. The Pt–O species can induce abundant Pt–O<sub>ads</sub> and Pt–(OH)<sub>ads</sub> to strip the CO-adsorbed sites (according to this reaction step: Pt–(CO)<sub>ads</sub> + Pt–O<sub>ads</sub> → 2Pt + CO<sub>2</sub>), thus resulting in a high CO tolerance.

Pd can substitute Pt for electrochemical FAO due to its good stability and high-power densities. In addition, the reaction pathway of formic acid is on Pd a direct dehydrogenation process without the formation of CO species. Santinacci *et al.* prepared three-dimensionally (3D) nanoarchitected Pd–Ni bimetallic catalysts by ALD on high-aspect-ratio nanoporous alumina templates.<sup>476</sup> The deposition of NiO is carried out with the use of nickelocene and O<sub>3</sub> precursors and the formed NiO film is reduced to metallic Ni by a reductive annealing process under a H<sub>2</sub> atmosphere. The growth of Pd clusters uses palladium hexafluoroacetylacetonate (Pd(hfac)<sub>2</sub>) and formaldehyde, which is commonly used for Pd ALD. The electron microscopy images show a homogeneous deposition of granularly-structured Pd onto the Ni substrate. The deposited Pt NPs preferred the growth along the [220] direction on the amorphous NiO film. The oxidized Ni is a more suitable substrate for obtaining three-dimensional growth of Pd islands, which are ideal for electrocatalytic applications. The FAO on the Pd/Ni nanocatalysts proceeds through a direct dehydrogenation mechanism according to the cyclic voltammetry curves. The as-prepared Pd/Ni bimetallic system Pd (40 ALD cycles)/Ni (1000 ALD cycles) demonstrates a high activity of 0.83 A mg<sup>-1</sup> toward the FAO, with a Pd loading amount of 0.06 ng cm<sup>-2</sup>. The strong interaction between Pd and Ni, the electronic effects between the alloyed Pd/Ni metals and the mass transport effect in 3D nanostructures might be the reason for the enhanced electrochemical properties. Besides the deposition of Pd on the substrates, ALD was also used to deposit a SiO<sub>2</sub> layer for stabilizing Pd-based catalysts for FAO. Zahmakiran *et al.* prepared trimetallic PdCoNi NPs supported on TiO<sub>2</sub> nanopowders (PdCoNi/TiO<sub>2</sub>) by a wet-impregnation method. After the preparation, ALD was utilized to improve the catalytic durability of PdCoNi/TiO<sub>2</sub> by growing SiO<sub>2</sub> layers among the PdCoNi alloy NPs by using 3-aminopropyltriethoxysilane and oleylamine as the Si source and surface protection groups, respectively.<sup>477</sup> Due to the existence of free –NH<sub>2</sub> functionalities, the resulting PdCoNi/TiO<sub>2</sub>-ALD-SiO<sub>2</sub> nanocatalyst displays almost two times higher activity than PdCoNi/TiO<sub>2</sub> in FAO. The –NH<sub>2</sub> functionalities grafted onto the support might affect the formic acid adsorption/storage process. The O–H bond cleavage in formic acid is facilitated by the –NH<sub>2</sub> functionalities leading to the formation of metal-bound formate species which accelerate the dehydrogenation process and produce H<sub>2</sub> and CO<sub>2</sub>. Moreover, the SiO<sub>2</sub> layer-protected PdCoNi alloy NPs showed unprecedented catalytic stability against sintering and leaching throughout the reusability experiments.

**3.1.2.3 ALD for electrocatalytic ethanol oxidation.** Ethanol has also been applied in the fuel cells, due to their low cost, easy storage, low toxicity and pollutant emission, and high energy density. In addition, ethanol can be easily produced in large

quantities by the fermentation of biomass from agriculture. However, the C–C bond is difficult to break at low temperature during the ethanol oxidation process. Hence, the development of highly active electrocatalysts is critical to achieving the commercialization of direct ethanol fuel cells (DEFCs). Hsieh *et al.* investigated the ethanol oxidation reaction (EOR) activity of ALD Pt NPs with different sizes and found that the ALD-Pt catalysts with smaller size exhibited relatively high catalytic activity, CO tolerance, and stability.<sup>478</sup>

However, the ethanol oxidation kinetics on Pt-based catalysts in acidic media is slow, incomplete, and mostly leads to the production of acetic acid and acetaldehyde. Pd is considered to be a promising alternative to Pt for the EOR in an alkaline medium due to it being relatively more abundant and having higher tolerance towards carbonaceous species from ethanol oxidation. Rikkinen and co-workers demonstrated that Pd nanoparticle catalysts on a porous carbon support can be prepared with ALD.<sup>479</sup> Due to the narrow size and good dispersion on the carbon support (Fig. 24(e)), the ALD-Pd/C exhibited better mass activity compared with the commercial material. Chen and Wang used chemical vapor-deposited three-dimensional graphite-coated nickel foam as the substrate for the deposition of Pd NPs.<sup>480</sup> Benefitting from the advantages of ALD, the Pd loading can be reduced to as low as 50 μg cm<sup>-2</sup>. The peaking current density of ALD-Pd/GNF with 450 cycles was about 2.64 times (39.97 mA cm<sup>-2</sup>) higher than that of commercial Pd/C (15.17 mA cm<sup>-2</sup>). Nevertheless, carbon-based materials are not stable and corrode under these reaction conditions. TiO<sub>2</sub> is well-known for its high stability and its strong metal-support interaction with Pt group metals. Baranova and Santinacci grew Pd NPs with precisely controlled sizes on TiO<sub>2</sub> nanotubes (TNTs) by ALD.<sup>481</sup> They found that the EOR activity of Pd NPs can be enhanced by annealing the TiO<sub>2</sub> nanotubes, since anatase is more conductive than the amorphous TiO<sub>2</sub>. The 500 ALD cycle Pd/TNTs system showed the best catalytic activity and satisfactory stability in alkaline media. The peak current for ethanol oxidation can reach approximately 2.25 A mg<sup>-1</sup>. In addition to TNTs, they also investigated the EOR activity of Pd NPs on SnO<sub>2</sub>-coated TNTs (Fig. 24(f)). The XPS results indicated that the top surface of the SnO<sub>2</sub> layer is reduced to metallic Sn during the deposition of the Pd particles, which facilitated the ALD process of Pd.<sup>482</sup> The activity of Pd NPs for the EOR was further enhanced on SnO<sub>2</sub> compared with that on TiO<sub>2</sub> surfaces. The positive impact of the addition of Sn species on a Pd catalyst can be attributed to the preferred deposition of Pd on metallic Sn, facilitation of OH adsorption on the SnO<sub>2</sub> layer, and the strong metal-support interaction between Pd and SnO<sub>2</sub>. These studies indicated that the use of ALD to grow metallic nanoparticles onto three-dimensional nanostructured substrates appears to be a very promising approach for the preparation of well-defined catalysts for ethanol and other alcohol electrooxidation.

**3.1.3 ALD for electrocatalytic oxygen evolution reactions.** The electrochemical oxygen evolution reaction (OER) is the core reaction process in water splitting for renewable energy conversion devices. However, due to the slow reaction kinetics of

the OER, the energy conversion efficiency is limited to a certain extent. At present, the commercial electrocatalysts for the OER are RuO<sub>2</sub> catalysts. Unfortunately, high cost and poor durability have hindered their further development and applications. Therefore, it is of great importance to developing effective OER catalysts by various methods. Finke and Hoffmann reported that ALD fabricated TiO<sub>2</sub> coatings on IrO<sub>2</sub>, RuO<sub>2</sub> and F-doped SnO<sub>2</sub> can tune the surface charge density, and consequently tune the catalytic activity of the electrocatalyst.<sup>483</sup> For example, the TiO<sub>2</sub>/IrO<sub>2</sub> catalyst exhibited a current density of 0.9 mA cm<sup>-2</sup> at 350 mV overpotential, which is a 9-fold increase compared with that of IrO<sub>2</sub>. With the different ALD cycles of TiO<sub>2</sub>, the oxidation state of Ti and the potential of zero charge can be adjusted, resulting in the tuned activity of the electrocatalysts.

To substitute the noble metals, many researchers have developed highly catalytic and low-cost transition metal compounds. Nowadays, cobalt and cobalt oxides have been extensively applied in electrocatalysis, especially for the OER, because of their

high catalytic activity and good stability. By using ALD, the as-prepared Co-based catalysts can be uniformly deposited onto the substrates and the thickness can be accurately controlled. Yilmaz and Uyar reported ALD of highly monodisperse Co<sub>3</sub>O<sub>4</sub> nanocrystals of different sizes on N-doped electrospun carbon nanofibers (Co@nCNFs) for the OER.<sup>484</sup> The obtained Co@nCNFs with an average Co<sub>3</sub>O<sub>4</sub> particle size of 3 nm exhibited the turnover frequency (TOF) value of 0.14 s<sup>-1</sup> at an overpotential of 550 mV, which is *ca.* 3 and *ca.* 15-fold higher than those of bulk Co and the standard state-of-the-art IrO<sub>x</sub> catalyst, respectively. Li and co-workers synthesized a homogeneous N-doped cobalt oxide thin film on high-surface-area CNTs (N-CoO<sub>x</sub>/CNTs) by plasma-enhanced ALD at 200 °C.<sup>485</sup> The overpotential of the OER for the N-CoO<sub>x</sub>/CNTs electrocatalyst was only 420 mV at 10 mA cm<sup>-2</sup> (Fig. 25(a)). They found that the intrinsic crystal structure and chemical composition of cobalt oxides were tailored after N-doping and the resulting NCoO<sub>x</sub>/CNTs electrocatalyst displays remarkable electrocatalytic activity and stability

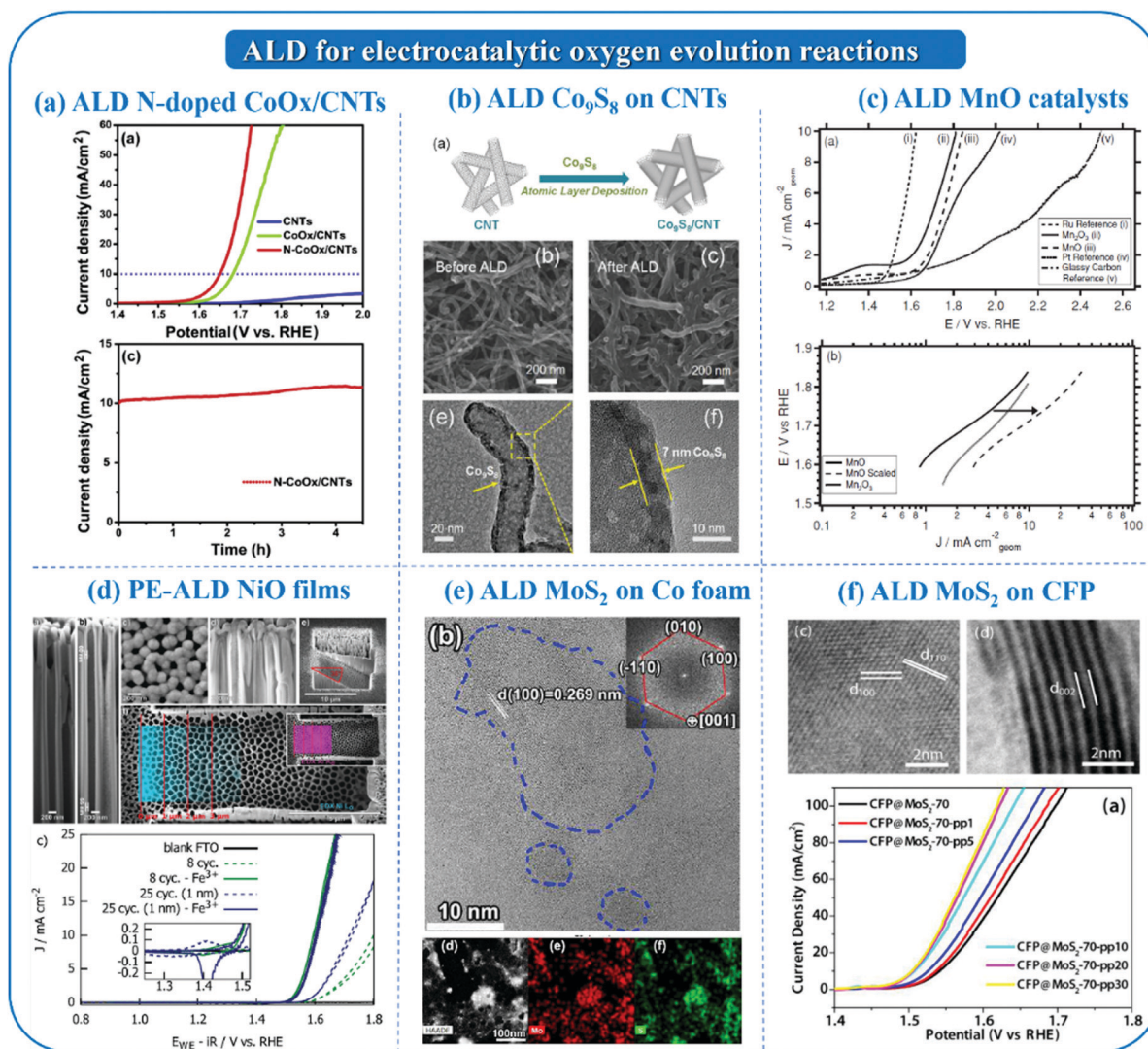


Fig. 25 ALD fabrication of OER catalysts: (a) N-doped CoO<sub>x</sub>/carbon nanotubes; (b) Co<sub>9</sub>S<sub>8</sub> on CNTs; (c) MnO catalysts; (d) NiO film; (e) MoS<sub>2</sub> on Co foam; (f) MoS<sub>2</sub> nanoflakes on CFP.

towards the OER. In addition to oxides, a uniform thin layer of  $\text{Co}_9\text{S}_8$  was synthesized on CNTs by using bis(*N,N'*-diisopropylacetamidinato)cobalt(II) and  $\text{H}_2\text{S}$  precursors.<sup>486</sup> With the deposition of 200 ALD cycles, a 7 nm  $\text{Co}_9\text{S}_8$  thin layer on the CNTs can be obtained as shown in Fig. 25(b). The ALD-synthesized  $\text{Co}_9\text{S}_8/\text{CNT}$  catalyst exhibited an overpotential of 369 mV with a current density of  $10 \text{ mA cm}^{-2}$ , which is much smaller than that of  $\text{RuO}_2$  (409 mV), and  $\text{CoO}_x/\text{CNT}$  (431 mV). The Tafel slope of an ALD-synthesized  $\text{Co}_9\text{S}_8/\text{CNT}$  electrocatalyst was  $58 \text{ mV dec}^{-1}$ , indicating that the Tafel kinetics of the  $\text{Co}_9\text{S}_8/\text{CNT}$  electrocatalyst was favored during the OER process. In addition, the LSV curves were maintained well after the 2000 cycles scan, which indicated the good stability of the ALD-prepared  $\text{Co}_9\text{S}_8$  electrocatalyst. Cobalt phosphate (CoPi)-based electrocatalysts have also exhibited good performance towards the OER. Palma *et al.* deposited CoPi films by using bis(cyclopentadienyl)cobalt(II) ( $\text{CoCp}_2$ ), trimethyl phosphate and  $\text{O}_2$  as precursors.<sup>487</sup> The Co-to-P atomic ratio can be controlled by tuning the ALD process and is found to significantly affect the activity of the prepared electrocatalyst. The current density increased from  $1.77 \text{ mA cm}^{-2}$  to  $2.89 \text{ mA cm}^{-2}$  at 1.8 V vs. RHE, concurrently with a Co-to-P ratio increase from 1.6 to 1.9. The results highlight the role of stoichiometric composition of Co in CoPi on its activity. Rongé *et al.* developed a plasma-enhanced process to obtain CoPi films without the need for a phosphidation step. The as-prepared CoPi films exhibited an overpotential of 509 mV with a current density of  $10 \text{ mA cm}^{-2}$ , which is much smaller than that of  $\text{Co}_3\text{O}_4$ .<sup>488</sup> In addition, this catalyst can enable hydrogen evolution after either a thermal or electrochemical reduction step.

Besides Co-based transition metals, Mn- and Ni-based metal oxides were also prepared by ALD for the OER. For example, Bent *et al.* prepared MnO catalysts on glassy carbon electrodes through the use of a  $\text{Mn}(\text{EtCp})_2$  precursor.<sup>489</sup> The as-deposited films of MnO can be converted to  $\text{Mn}_2\text{O}_3$  via annealing. In OER testing, the  $\text{Mn}_2\text{O}_3$  catalyst could reach a current density of  $10 \text{ mA cm}^{-2}$  at 1.81 V, while the MnO catalyst required 1.84 V, as shown in Fig. 25(c). The small differences in the OER are attributable to differences in surface area. Following this study, the authors prepared NiO thin films using Nickelocene and  $\text{O}_3$  at 275 °C.<sup>490</sup> The ALD-grown NiO thin films were studied as an OER electrocatalyst with the incorporation of Fe from the electrolyte. They characterized the activity of NiO towards the OER in both trace Fe and Fe-saturated 0.1 M KOH electrolytes and found that the Fe-saturated electrolyte significantly increases the OER activity of the NiO films. Bein further confirmed that when a 1 nm layer of the PE-ALD NiO catalyst is deposited on a porous transparent conductive oxide (TCO) substrate, their OER activity can be further improved (Fig. 25(d)).<sup>491</sup>

Mo-S sites along the edges of  $\text{MoS}_2$  are very active for the OER owing to the excellent chemisorption of the oxygen-containing intermediates. Liu and co-workers reported ALD of ultrafine  $\text{MoS}_2$  nanocrystals over a porous Co foam by using  $\text{Mo}(\text{CO})_6$  and  $\text{H}_2\text{S}$  as precursors (Fig. 25(e)).<sup>492</sup> The ALD-derived  $\text{Co}@/\text{MoS}_2$  only requires an overpotential of 270 mV to reach a current density of  $10 \text{ mA cm}^{-2}$ . Furthermore, the  $\text{Co}@/\text{MoS}_2$  electrode exhibited excellent stability, showing no noticeable

degradation after operating at  $20 \text{ mA cm}^{-2}$  for 50 hours and  $100 \text{ mA cm}^{-2}$  for an additional 50 hours. In order to further improve the activity, plasma treatment was proved as an effective route to generate vacancies and structural disorder on the surface of  $\text{MoS}_2$ , which can further increase the exposure of the active site. Liu *et al.* fabricated  $\text{MoS}_2$  nanoflakes that were obtained by ALD using  $\text{MoCl}_5$  and  $\text{H}_2\text{S}$  on a carbon fibre paper (CFP) surface (Fig. 25(f)).<sup>493</sup> When the  $\text{CFP}@/\text{MoS}_2$  was treated by plasma for 20 s, the current density increased to  $80.42 \text{ mA cm}^{-2}$  at 1.6 V vs. RHE, which is two times higher than that of  $\text{CFP}@/\text{MoS}_2$  ( $43.89 \text{ mA cm}^{-2}$ ). In addition, the Tafel slope decreased from 65.8 to 61.2  $\text{mV dec}^{-1}$  when the plasma treatment time increases from 0 to 20 s, which further indicates that the plasma treatment can improve the activity of  $\text{MoS}_2$  nanoflakes.

### 3.1.4 ALD for electrocatalytic hydrogen evolution reactions

**3.1.4.1 ALD of Pt-based catalysts.** Hydrogen is a clean fuel and can be applied as the energy source in PEMFCs. Water electrolysis is considered a promising green route for the production of hydrogen. The hydrogen evolution reaction (HER) is one half-reaction during water electrolysis, and Pt-based catalysts have exhibited good activity during the hydrogen evolution process. The HER process on Pt particles contains two half-reactions, which are the Volmer reaction and the desorption reaction (Heyrovsky reaction or Tafel reaction). Many previous studies indicated that the Tafel mechanism usually occurs on Pt NPs due to the high H coverage on Pt surfaces. By using the ALD method, Pt-based catalysts have been synthesized to decrease the Pt content, thus reducing the cost. Alshareef and co-workers reported the fabrication of monolithic, self-standing, 3D graphitic carbon scaffolds with conformally deposited Pt by ALD (Fig. 26(a)).<sup>494</sup> The as-prepared Pt on a 3D network of laser-scribed graphene (Pt/LSG) electrode exhibited comparable activity with the benchmark Pt/C electrode. It should be noted that the mass loading ( $0.04 \text{ mg cm}^{-2}$ ) of Pt/LSG was much smaller than that of a commercial Pt/C catalyst ( $0.5 \text{ mg cm}^{-2}$ ). The synergistic effect between the ALD Pt and the 3D network of the laser scribed graphene provides an avenue for maximized utilization of Pt loading and enhanced HER activity. Another reported strategy to lower Pt loadings by ALD is to use tungsten monocarbide (WC) as the support.<sup>495</sup> Chen *et al.* deposited Pt onto WC powders using ALD to obtain a Pt-WC core-shell catalyst for the HER. The Pt-WC core-shell exhibited equivalent HER activities compared to bulk Pt catalysts, while the Pt loading amount is reduced 10 times.

Downsizing noble metal nanocatalysts to clusters or even single atoms is an effective strategy to significantly increase their catalytic activity and efficiency. In 2013, Sun *et al.* firstly reported isolated single Pt atoms anchored to graphene nanosheets by an ALD method for the MOR. Subsequently, we synthesized Pt single atoms on N-doped graphene nanosheets (NGNs) through the ALD method (Fig. 26(b)).<sup>496</sup> The HER activity and reaction mechanism on Pt single atoms were carefully investigated. At an overpotential of 0.05 V, the mass activity of the ALD50Pt/NGNs catalyst reached  $10.1 \text{ A mg}^{-1}$ , which was much greater than the ALD100Pt/NGN catalyst and Pt/C catalyst. Synchrotron characterization and DFT analysis

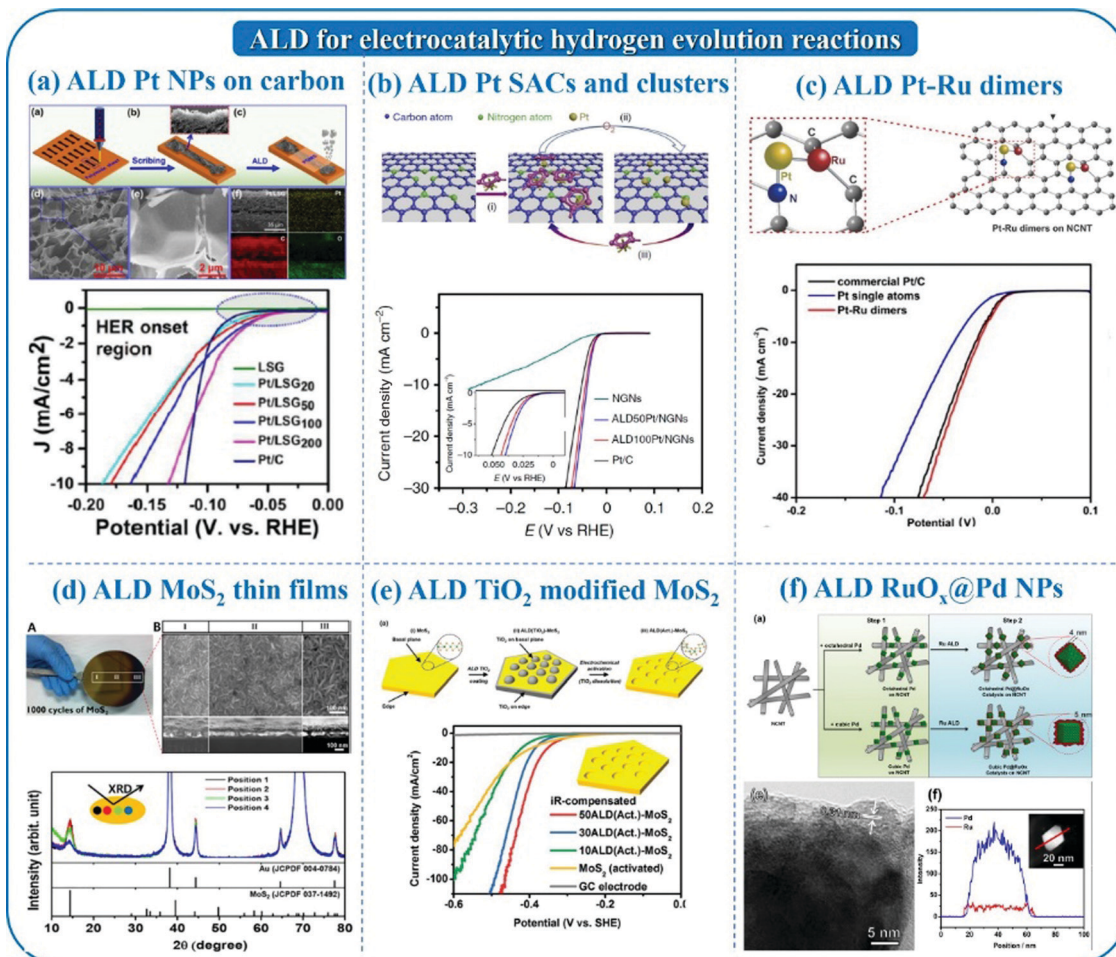


Fig. 26 ALD fabrication of HER catalysts: (a) Pt NPs on 3D graphitic carbon; (b) Pt single atoms and clusters; (c) Pt–Ru dimer catalysts; (d) MoS<sub>2</sub> thin films; (e) TiO<sub>2</sub> modified MoS<sub>2</sub> nanoflakes; (f) RuO<sub>x</sub>@Pd NPs.

revealed that the Pt single atoms are strongly anchored on the substrates due to the SMSIs. In addition, according to the DFT results, the interaction between single Pt atoms and N-dopants is much larger than that of Pt atoms/C-substrates, indicating that Pt atoms are bonded to N-sites. Due to the unique electronic structure of Pt single atom catalysts, several H could adsorb on one Pt atom, followed by the formation of H<sub>2</sub> on the isolated Pt atom. According to the DFT calculations results, during the HER process, four H atoms can be adsorbed on Pt single atoms, and the interaction between the Pt and H atoms reduced the repulsion between the H atoms. The desorption process is similar to the Tafel reaction (H<sub>ads</sub> + H<sub>ads</sub> → H<sub>2</sub>), and leads to a Tafel slope that is similar to the Volmer–Tafel mechanism (29 mV dec<sup>-1</sup>).<sup>497</sup>

Recently, dual-metal catalysts were found to greatly enhance catalytic performance due to the synergistic effects. The method by pyrolyzing two metal precursors simultaneously has been reported as a successful route for the preparation of dual-metal catalysts. However, the detailed location of each metal site can hardly be controlled. The ALD technique provides the possibility to achieve atomically precise metal clusters, even bimetallic catalysts. Through careful control of

the ALD deposition conditions, the second metal can be selectively deposited on the initial metal deposition sites, enabling the formation of bimetallic dimer structures. Very recently, Sun *et al.* successfully prepare high-quality one-to-one A–B bimetallic dimer structures (Pt–Ru dimers) by ALD. As shown in Fig. 26(c),<sup>498</sup> the atomic resolution HAADF-STEM images illustrate that a dimer-like structure was successfully prepared by a two-step ALD process. The different contrast of the two atoms reflects that the dimer is composed of Pt and Ru. The EXAFS R space curve fitting results based on the Ru K-edge and Pt L<sub>3</sub>-edge indicated that the coordination number of Pt–Ru is close to 1, confirming the formation of Pt–Ru dimer structures. Benefiting from the unique bimetallic dimer sites, the Pt–Ru dimers exhibited 50 times higher HER activity compared to commercial Pt/C catalysts and the dimer structure was maintained after the long-term durability test. The Pt–Ru dimer HER mechanism and reaction route were systematically explained by first-principles calculations. We found that when three hydrogen atoms connect with the Pt atom (3H–Pt), and three bonds with the Ru atom (3H–Ru), a hydrogen atom can be released from the Ru atom. The Pt–Ru dimer generates a synergistic effect by modulating the electronic structure which

evolves from metallic to semiconducting during the hydrogen adsorption, resulting in an increase in the unoccupied orbitals and a decrease of the bonding between the Ru and H, thus playing a vital role in the high HER activity. These findings demonstrate that the remarkable performance of the single Pt atoms and Pt–X dimer can be mainly attributed to their unique electronic structure. In addition, these ALD approaches for SACs provide a promising approach for the rational design of highly active and stable bimetallic dimers, which have great potential for application in various catalytic reactions.

**3.1.4.2 ALD of MoS<sub>2</sub> catalysts.** Recently, molybdenum disulfide (MoS<sub>2</sub>) has attracted attention due to its biomimetic hydrogen evolving activity. It should be noted that MoS<sub>2</sub> has poor activity for the HER in its bulk form, which is due to the small amount of HER active sites at the basal planes. The HER activity of MoS<sub>2</sub> can be improved by tuning the exposed surface of the crystalline MoS<sub>2</sub> to increase the number of active edge sites. Min and co-workers prepared an amorphous MoS<sub>2</sub> catalyst on Au by the ALD method. During the ALD process, the molybdenum hexacarbonyl (Mo(CO)<sub>6</sub>) and dimethyldisulfide (CH<sub>3</sub>S<sub>2</sub>CH<sub>3</sub>) are employed as Mo and S precursors, respectively.<sup>499</sup> The required overpotential for a designated current density of 100 μA cm<sup>-2</sup> on the MoS<sub>2</sub> film is 165 mV. The turnover frequency on each active site of the amorphous MoS<sub>2</sub> film is calculated to be 3 H<sub>2</sub> per s at 0.215 V. The Tafel slope is 47 mV dec<sup>-1</sup> indicating that the HER process follows the Volmer–Heyrovsky mechanism on the amorphous MoS<sub>2</sub> surface. However, the weak adhesion of MoS<sub>2</sub> on Au caused the unstable activity of the ALD-MoS<sub>2</sub>/Au catalysts. The authors tried to use carbon fibre papers (CFPs) as the alternative to replace the Au substrate, as CFPs can provide a large surface area and strengthen the adhesion of the ALD MoS<sub>2</sub>.<sup>500</sup> Different from the amorphous MoS<sub>2</sub> on a Au surface, the ALD-MoS<sub>x</sub> on CFP exhibited a mixture of amorphous and nano-crystalline phases. Because of the formation of nano-crystalline MoS<sub>2</sub>, the turnover frequency of the MoS<sub>x</sub>/CFP is smaller than that of the amorphous ALD-MoS<sub>2</sub>/Au. However, the MoS<sub>x</sub>/CFP catalyst exhibits very good stability with no obvious change in the polarization curves after 1000 CV cycles, due to the strong interaction between MoS<sub>x</sub> and CFP. To achieve the direct growth of nanocrystalline MoS<sub>2</sub> by ALD, Bae and Shin demonstrated that the nonideal growth mode operates when MoS<sub>2</sub> is deposited by ALD on planar surfaces using MoCl<sub>5</sub> and H<sub>2</sub>S as the precursors (Fig. 26(d)).<sup>501</sup> This nonideal mode of growth shows that the growth thickness does not linearly increase with the number of cycles. Interestingly, the relative ratios of the edge sites and basal planes of MoS<sub>2</sub> can be controlled by tuning the ALD conditions. At low growth temperatures, the MoS<sub>2</sub> with mixed 2H and 1T phases can be deposited due to the incorporation of chlorine impurities. They found that the as-prepared planar MoS<sub>2</sub> films exhibited good HER performance, with a current density of 20 mA cm<sup>-2</sup> at -0.3 V and a Tafel slope of 50–60 mV dec<sup>-1</sup>.

To make the MoS<sub>2</sub> more active, many studies focused on synthesizing MoS<sub>2</sub> catalysts with more edge sites or to further improve the active edge sites by modification. Kim and Kuech

attempted to make use of basal plane sites which account for the majority of the MoS<sub>2</sub> materials in bulk form.<sup>502</sup> They firstly ALD deposited TiO<sub>2</sub> on the bulk MoS<sub>2</sub> particles. A thin layer of TiO<sub>2</sub> is formed on the edge sites of the MoS<sub>2</sub> and TiO<sub>2</sub> islands are formed on the basal planes. Then they dissolved the TiO<sub>2</sub> layers by an *in situ* electrochemical activation method. After this process, the localized surface distortions are created on the MoS<sub>2</sub> basal planes. The TiO<sub>2</sub> coatings on the basal planes and edge sites completely disappeared on the surface of MoS<sub>2</sub> catalysts after the electrochemical activation process, as shown in Fig. 26(e). In addition, the degree of surface distortion on the MoS<sub>2</sub> basal planes can be tuned by controlling the ALD TiO<sub>2</sub> coating cycles from 10 to 50. With the increase of the surface distortions on the MoS<sub>2</sub> basal plane, the HER catalytic activity was increased. The as-prepared MoS<sub>2</sub> catalysts exhibited a much smaller Tafel slope (80–90 mV dec<sup>-1</sup>) compared with that of pristine MoS<sub>2</sub> (180 mV dec<sup>-1</sup>). According to the DFT calculations, the hydrogen-binding energy is reduced on the local flexure of MoS<sub>2</sub> layers, which results in the improved HER kinetics. This result suggests that the ALD technique can be used for the decoration of the catalysts by induced physical changes including defects, defect-mediated strain, and flexure of surface layers.

**3.1.4.3 ALD of other catalysts.** Transition metal sulfides have high stability and conductivity, which allows them to be applied from catalysis to photovoltaics. Among them, nickel sulfide exhibited good activity for the HER. Farha and Hupp constructed nickel sulfide (NiS<sub>x</sub>) layers by using bis(*N,N'*-di-*tert*-butylacetamidinato)nickel(II) (Ni(amd)<sub>2</sub>) vapor and hydrogen sulfide gas as the precursors.<sup>503</sup> *In situ* quartz crystal microbalance (QCM) studies revealed a linear GPC of 9.3 ng cm<sup>-2</sup> per cycle growth behavior for NiS<sub>x</sub> films. The ALD NiS<sub>x</sub> catalysts exhibited the overpotential of 440 and 576 mV at a current density of 10 mA cm<sup>-2</sup> in acidic and pH 7 phosphate buffer aqueous reaction media, respectively. In addition to two binary sulfides, ternary sulfides can also be achieved by the ALD method. For example, Fe<sub>x</sub>Co<sub>1-x</sub>S<sub>y</sub> films were grown by ALD at 120 °C from the precursors, including bis(*N,N'*-diisopropylacetamidinato)-cobalt(II), bis(*N,N'*-diisopropylacetamidinato)-iron(II), and H<sub>2</sub>S.<sup>504</sup> The ternary Fe<sub>x</sub>Co<sub>1-x</sub>S<sub>y</sub> was achieved by repeatedly growing one or multiple cycles of FeS<sub>y</sub> followed by one or multiple cycles of CoS<sub>y</sub>. In addition, the elemental composition of the ternary sulfide Fe<sub>x</sub>Co<sub>1-x</sub>S<sub>y</sub> can be tuned by controlling the cycle ratio of FeS<sub>y</sub> and CoS<sub>y</sub>. The as-prepared Fe<sub>0.54</sub>Co<sub>0.46</sub>S<sub>0.92</sub>/CNTs/CC electrode achieved -10 mA cm<sup>-2</sup> at an overpotential of -70 mV in alkaline solution, which indicates the effectiveness of the ALD method. Transition-metal carbides (TMCs) have also attracted a lot of attention due to their peculiar electronic structures and their broad applications in electrocatalysis. Wang and co-workers synthesized smooth, pure, crystalline nickel carbide (Ni<sub>3</sub>C) films on CNTs by using bis(1,4-di-*tert*-butyl-1,3-diazabutadienyl)nickel(II) and H<sub>2</sub> plasma with an ideal self-limiting ALD growth fashion.<sup>505</sup> The as-prepared ALD Ni<sub>3</sub>C/CNT catalyst showed an onset overpotential of -77 mV (at -0.1 mA cm<sup>-2</sup>), and an

overpotential of  $-132$  mV to reach  $-10$  mA cm $^{-2}$  in 1 M KOH aqueous solution.

Recently, several studies reported that rationally designed Ru-based catalysts exhibited good HER performance. For example, the anomalous crystalline structure of Ru on g-C $_3$ N $_4$  was prepared by Qiao *et al.* and it exhibited comparable HER activity with Pt in alkaline solutions.<sup>506</sup> By using ALD, Sun *et al.* fabricated Pd@RuO $_x$  core-shell catalysts by using octahedral and cubic Pd NPs with two typical surface atom arrangements as the substrates (Fig. 26(f)).<sup>507</sup> Due to the similar lattice constants of Pd and Ru, Ru atoms were selectively deposited on Pd particles instead of N-doped CNT substrates by using bis(ethylcyclopentadienyl)ruthenium(II) and O $_2$  as precursors. The ALD cycles can easily tune the thickness of the RuO $_x$  shell. The as-prepared octahedral Pd@RuO $_x$ /NCNT exhibited better activity and stability for the HER in acid solution compared with the cubic one. According to the XAS and XPS results, the Ru shell consists of metallic Ru and Ru(IV). DFT calculation results indicated that the H\* can be easily detached on the octahedral Pd@RuO $_x$ , and resulted in a better HER activity.

## 3.2 ALD/MLD for photoelectrocatalysis

### 3.2.1 ALD/MLD for photovoltaics

**3.2.1.1 ALD/MLD for dye-sensitized cells (DSSCs).** Renewable solar energy is regarded as the most promising alternative clean energy source for fossil fuels. To realize cost-effective and performance-competitive solar cells, dye-sensitized solar cells (DSSCs) have been extensively explored since 1991 and garnered increasing research attention over the past few decades.<sup>508,509</sup> The advantages of DSSCs are their low cost, simple manufacturing process, lightweight, flexibility, low toxicity, *etc.* A typical DSSC consists of several parts, including the photoanode on a conductive substrate, sensitizer, electrolyte and counter electrode.<sup>510,511</sup> The excited electrons are generated from the photoanode under the visible light irradiation when the photoanode experiences photo-excitation of the absorbed dye molecules. The electrons are then injected into the conduction band of a semiconductor and further to produce the electric current with an external circuit. The dye is then restored to the original state by electron donation from the redox electrolyte. Moreover, the charge is returned from the external to the cycling circuit on the counter electrode in the cell.<sup>512</sup> The performances of the DSSCs are determined by each component in the cell. For example, the function of the photoanode in DSSCs is to support the sensitizer loading and transport the photo-excited electrons from the sensitizer to the external circuit. In this case, both high surface area and fast charge transportation are the keys to achieving high-efficiency photoanodes for DSSCs.

ALD and MLD techniques have been used to design and fabricate photoanode materials for DSSCs.<sup>513,514</sup> To minimize the time scale for transferring the injected electrons to the conducting oxide, a thin semiconductor oxide is required on the conductive substrate. ALD is an ideal technique to fabricate core-shell-structured photoanodes. TiO $_2$  is one of the most widely used semiconductor photoanode materials and can also be easily deposited by ALD technique.<sup>515-523</sup> As shown in Fig. 27(a), a thin TiO $_2$  shell was deposited by ALD onto high

surface area ITO and ZrO $_2$  core nanoparticles.<sup>524</sup> The ALD TiO $_2$  was deposited at 120 °C with a GPC of 0.6 Å using TiCl $_4$  and H $_2$ O as precursors. With an N719 dye, the results indicate that with the increase of the thickness of the TiO $_2$  shell (to 1.8–2.4 nm), the short-circuit current densities, open-circuit voltages, and back electron transfer lifetimes all increased. When further increasing the thickness of TiO $_2$  (> 3 nm), electron trapping in the TiO $_2$  shell occurs, increasing back electron transfer (BET) and decreasing device efficiencies. In addition, ALD-designed core-shell photoelectrodes can provide a practical alternative for maximizing solar cell efficiencies by enhancing electron transport through mesoporous films. Another candidate metal oxide for photoanode applications is ZnO, which is also a routine material deposited by ALD.<sup>525,526</sup> Grätzel's group fabricated a ZnO nanoshell by ALD on a 2.5 μm thick Al $_2$ O $_3$  mesoporous scaffold and used it as a photoanode for DSSCs, as shown in Fig. 27(b).<sup>527</sup> With a ZnO nanoshell of 3–6 nm, a maximum power conversion efficiency of 4% was achieved with the standard organic sensitizer and Co $^{2+}$ /Co $^{3+}$  redox mediator. A high-power conversion efficiency (PCE) of 7% was achieved with a similar ZnO nanostructure in the CH $_3$ NH $_3$ PbI $_3$  based solid-state solar cells. The comparison of the photovoltaic performance and the electron transfer dynamics between different metal oxide photoanodes is also interesting. However, the morphological differences between the different metal oxides hamper the fair comparison. ALD techniques can circumvent this issue by depositing these oxides on an insulating mesoporous template and using them directly as photoanodes. Grätzel's group deposited different thicknesses of ZnO and TiO $_2$  on mesoporous alumina for photoanode applications in DSSCs.<sup>528</sup> The results showed that the best performance was achieved with 5 nm ZnO or TiO $_2$  overlayer films yielding a high-power conversion efficiency of 4.4%. Moreover, the transport rate of electrons through ZnO is faster compared to the TiO $_2$ .

In addition, other types of core-shell structures were developed by ALD as a photoanode for DSSCs.<sup>529-542</sup> In 2006, Yang's group demonstrated the core-shell structures of Al $_2$ O $_3$  or TiO $_2$  shells on ZnO nanowires by ALD,<sup>543</sup> as shown in Fig. 27(c). The results showed that the ALD Al $_2$ O $_3$  could act as an insulating barrier regardless of thickness and that the cell  $V_{oc}$  could be improved at the expense of a larger decrease in  $J_{sc}$ . However, when the TiO $_2$  shell thickness was 10–25 nm, it caused an obvious increase in  $V_{oc}$ , resulting in an improvement in conversion efficiency up to 2.25%. Another similar TiO $_2$ -ZnO core-shell structure was demonstrated with a TiO $_2$  shell on ZnO nanocrystallites.<sup>544</sup> The ultrathin layer of ALD-TiO $_2$  can effectively enhance the power conversion efficiency from 5.2% to 6.3%. The ALD-TiO $_2$  layer increases the open-circuit voltage and suppressed surface charge recombination without impairing the photocurrent density. Hupp *et al.* designed a doubly coaxial photoanode architecture based on templated SiO $_2$  aerogels.<sup>545</sup> As shown in Fig. 27(d), the first layer of ZnO was deposited on the template by ALD to create the electronically interconnected, low density, and high-surface-area semiconductor framework. Then, another layer of thin conformal oxide of alumina, zirconia, or titania was further deposited *via* ALD to suppress the

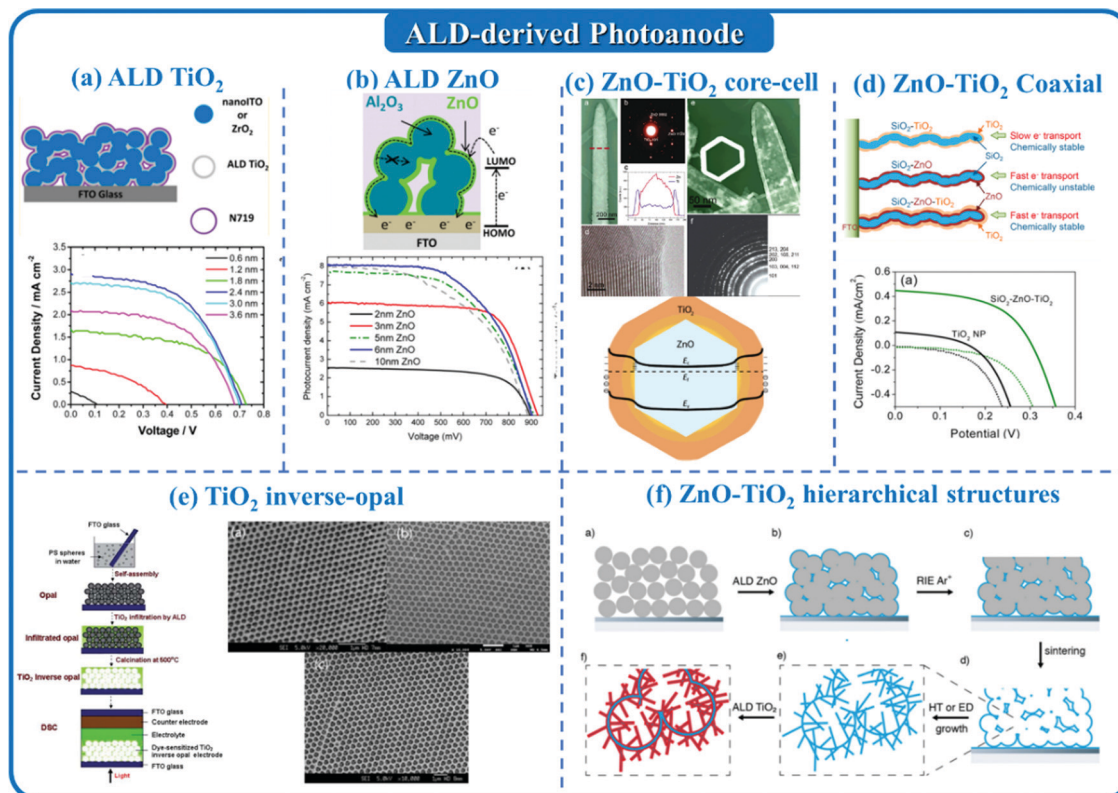


Fig. 27 ALD-derived photoanodes for DSSCs: (a) ALD  $\text{TiO}_2$ ; (b) ALD  $\text{ZnO}$ ; (c)  $\text{ZnO-TiO}_2$  core-shell; (d)  $\text{ZnO-TiO}_2$  coaxial; (e)  $\text{TiO}_2$  inverse-opal; (f)  $\text{ZnO-TiO}_2$  hierarchical structure.

dissolution of  $\text{ZnO}$ . The doubly coaxial structure of the  $\text{SiO}_2\text{-ZnO-TiO}_2$  photoanode showed 2 orders of magnitude faster electron transport compared to the  $\text{SiO}_2\text{-TiO}_2$  structure. The fast electron transport by the coaxial core-shell-shell structure enables good charge-collection efficiencies even with redox shuttles capable of rapidly intercepting injected electrons.

Surface area is an important parameter that affects the sensitizer loading and cell efficiency. The design of a hierarchical nanostructure is an effective approach to increasing the effective surface area. ALD has been used to fabricate hierarchical nanostructures using a sacrificial template or through the combination of other approaches. For example, 3D colloidal silica was used as a sacrificial template on a conductive substrate.<sup>546</sup> After the deposition of ALD  $\text{TiO}_2$ , the silica spheres were etched using a 2% HF solution to form the  $\text{TiO}_2$  inverse opal photoanode. The Ta-doped  $\text{TiO}_2$  films were deposited by repeated super-cycles of two groups of sub-cycles dedicated for  $\text{Ta}_2\text{O}_5$  and  $\text{TiO}_2$ , respectively. The content of Ta in the  $\text{TiO}_2$  films affects the cell performances. The photoconversion efficiency was effectively increased by Ta doping, which increased the electron concentration. However, excessive Ta doping decreased the  $J_{\text{sc}}$  and photoconversion efficiency. The 3.4 atom%-doped  $\text{TiO}_2$  inverse opal electrode presented a high photoconversion efficiency of 1.56%, which was 23% higher than that of pure  $\text{TiO}_2$ .<sup>546</sup> In another study, different sizes of polystyrene spheres were used as a template and then ALD was applied to deposit  $\text{TiO}_2$  thin layers (Fig. 27(e)).<sup>547</sup> The results showed that the  $\text{TiO}_2$

inverse opal with a size of 288 nm demonstrated a high power conversion efficiency of 2.22%. The smaller size of the  $\text{TiO}_2$  inverse opal with higher surface areas led to higher efficiency. More complex nanostructures were further designed for a novel self-assembled 3D  $\text{ZnO}$  nanostructure.<sup>548</sup> As shown in Fig. 27(f), a poly(methylmethacrylate) (PMMA) micro-template was used to fabricate a  $\text{ZnO}$  3D host backbone by ALD. Afterwards,  $\text{ZnO}$  nanowires were grown on the 3D host backbone *via* a hydrothermal method. Finally, another 10 nm dense  $\text{TiO}_2$  overlayer was deposited throughout the 3D  $\text{ZnO}$  host by ALD. With an increased surface area attributed to the  $\text{ZnO}$  nanowires, the photocurrents increased to  $4 \text{ mA cm}^{-2}$ . The ALD  $\text{TiO}_2$  overlayer can effectively reduce dark currents, recombine the photo-generated electrons from the conduction band of the semiconductor to the electrolyte and increase the transport rate.

Beyond the design core-shell structure photoanodes, ALD has been more widely used to modify the interfaces in DSSCs, including passivation, barrier, and blocking layers. Different metal oxides have been demonstrated to engineer the interfaces in DSSCs. For example, ALD  $\text{Al}_2\text{O}_3$  is one of the most popular and routine materials used for this purpose.<sup>549-554</sup> As shown in Fig. 28(a), ALD  $\text{Al}_2\text{O}_3$  was deposited on cadmium sulfide (CdS) quantum dot-sensitized solar cells as a barrier layer.<sup>555</sup> It was found that the ALD  $\text{Al}_2\text{O}_3$  layer can suppress the dark current and increase electron lifetimes with increasing  $\text{Al}_2\text{O}_3$  thickness. The thickness of the ALD barrier layer affected the performance of the cell, in which a thin layer leads to an increase in open-circuit

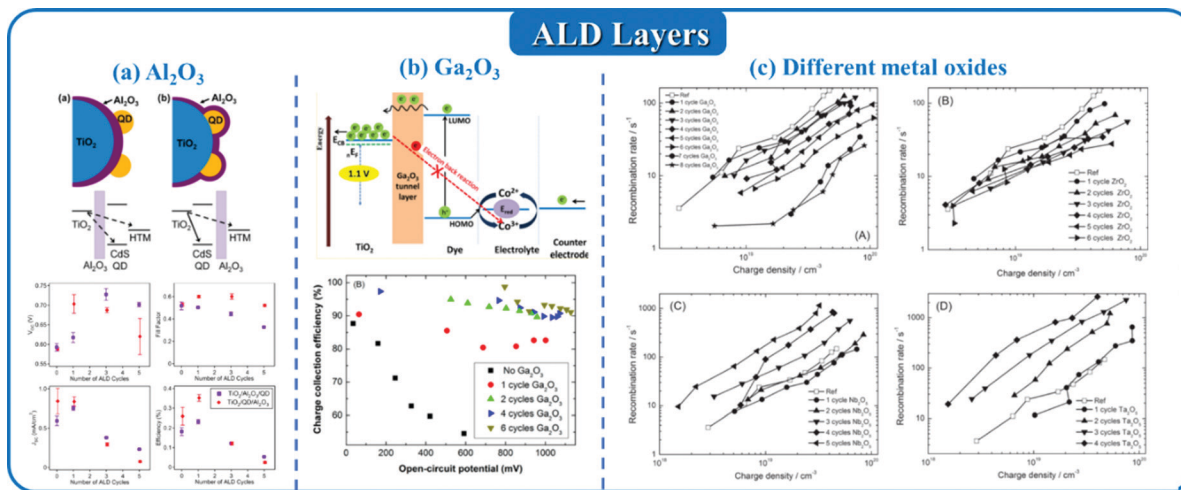


Fig. 28 ALD layer modification for the interface in DSSCs: (a)  $\text{Al}_2\text{O}_3$ ; (b)  $\text{Ga}_2\text{O}_3$ ; (c) different metal oxides.

voltage and efficiency, however, a thicker layer resulted in a loss of photocurrent and decreased efficiency. Other metal oxides, such as  $\text{Ga}_2\text{O}_3$ ,  $\text{TiO}_2$ ,  $\text{In}_2\text{O}_3$ , *etc.*, were also developed to modify the interface of the photoanodes.<sup>556–558</sup> As shown in Fig. 28(b), the surface of the porous substrate was passivated using a sub-nanometer-thick  $\text{Ga}_2\text{O}_3$  tunnelling overlayer by ALD.<sup>557</sup> The ALD  $\text{Ga}_2\text{O}_3$  leads to a high open-circuit potential of 1.1 V with an organic D- $\pi$ -A sensitizer and a cobalt redox mediator. Moreover, the electron back reaction is effectively reduced with the  $\text{Ga}_2\text{O}_3$  overlayer, which leads to improved charge collection efficiency and fill factor up to 30% and 15%, respectively. To understand the influence of tunnelling layers on blocking the interfacial charge carrier recombination reaction (Fig. 28(c)), the recombination characteristics, electronic properties on the surface, transport rate, and injection dynamics were investigated for different metal oxides of  $\text{Ga}_2\text{O}_3$ ,  $\text{ZrO}_2$ ,  $\text{Nb}_2\text{O}_5$ , and  $\text{Ta}_2\text{O}_5$ .<sup>559</sup> The results showed that both  $\text{Ga}_2\text{O}_3$  and  $\text{ZrO}_2$  are good candidates as tunnelling layers to limit the interfacial recombination of photogenerated carriers. Moreover, pentavalent oxides such as  $\text{Nb}_2\text{O}_5$  and  $\text{Ta}_2\text{O}_5$  introduce shallow donor levels below the conduction band of titanium dioxide.<sup>559</sup>

One of the issues of DSSCs is the charge loss which occurs at the interface between the conductive substrate and electrolyte. To suppress the substrate/electrolyte recombination, a thin oxide blocking layer is usually used on the surface of the conductive substrate. Different metal oxides, such as  $\text{Al}_2\text{O}_3$ ,  $\text{HfO}_2$ ,  $\text{TiO}_2$ , *etc.*, have been deposited by ALD and used as blocking layers.<sup>560–567</sup> For example, Parsons's group demonstrated an ALD  $\text{TiO}_2$  layer as a blocking layer for DSSCs with significantly impeded charge recombination in functional DSSCs, leading to improved photocurrents, open-circuit photovoltages, and fill factors.<sup>560</sup> Compared to the blocking layer fabricated by other methods (hydrolysis and spin casting), with the thinner ALD films, a better performance was achieved, which is attributed to the lower pinhole density.

Besides the photoanode, the counter electrode is another important component of DSSCs. The electrons were transferred

by the counter electrode from the external circuit back to the redox electrolyte, further catalyzing the reduction of the redox couple. Different conductive materials, such as Pt, Ru, metal sulfides, and metal nitrides, *etc.* have been studied as counter electrodes for DSSCs.<sup>510,512,514</sup> ALD was also applied to fabricate the counter electrode, including Pt, Ru, conductive polymers and  $\text{MoS}_2$ , *etc.*<sup>568–573</sup> For example, Pt nanoparticles were deposited by ALD on indium tin oxide/polyethylene naphthalate substrates.<sup>568</sup> The ALD deposited Pt showed better performance compared to the electrodeposited and sputtered Pt counter electrodes with relative improvements in the efficiency of 19% and 29%, respectively. In addition, ALD was shown to be practical for fabricating a large area counter electrode with an efficiency of 3.1%.

**3.2.1.2 ALD/MLD for perovskite solar cells (PSCs).** The metal halide perovskite solar cells (PSCs) utilize novel thin-film photovoltaic technology and have attracted increasing attention over the past decade due to their remarkable PCE of over 25%.<sup>574,575</sup> Generally, the PSCs have a sandwich-type structure including a conductive substrate, perovskite layer, and charge transport layer (electron transport layer and hole transport layer).<sup>576–578</sup> The cell performance and stability are determined by several factors, such as perovskite/contact interfaces, internal and external degradation, *etc.*<sup>579–581</sup> The ALD fabrication method is regarded as a promising tool to address the challenges in PSCs.

ALD is ideal for the fabrication of perovskite thin films due to its advantages which include controllable thickness and uniformity. For ALD-derived perovskite, another advantage is the improved adhesion with a wide range of substrates. However, the direct growth of halide compounds by ALD is challenging. In 2015, Sargent's group demonstrated an ALD-assisted process to synthesize perovskite  $\text{CH}_3\text{NH}_3\text{PbI}_3$  thin films.<sup>582</sup> As shown in Fig. 29(a), the ALD PbS was first deposited as a seed layer on the glass substrate, in which  $\text{H}_2\text{S}$  and  $\text{Pb}(\text{tmhd})_2$  were used as precursors. The GPC of PbS was  $\sim 1.3$  Å. Afterwards, the PbS film

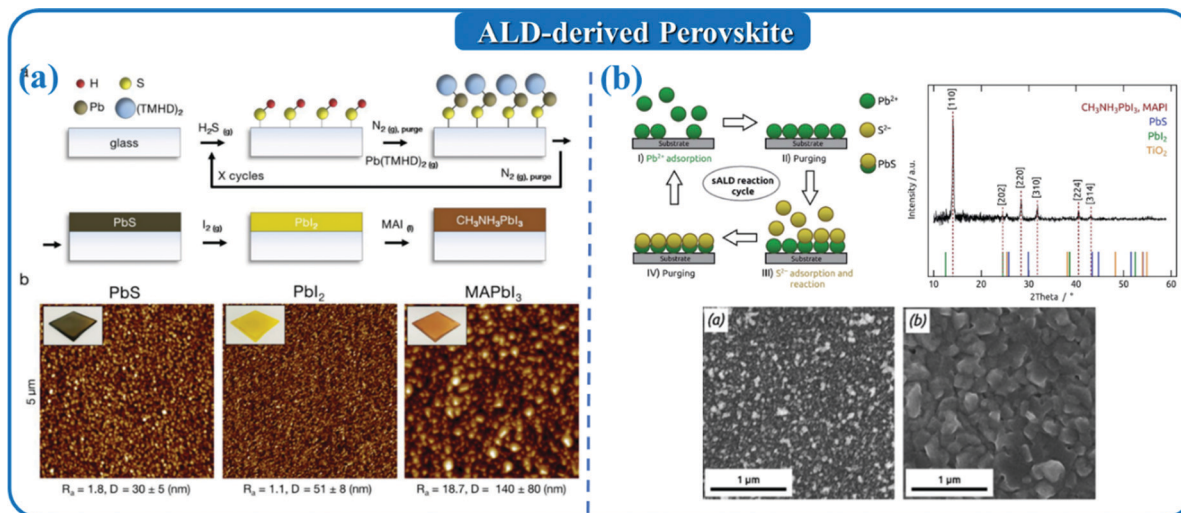


Fig. 29 ALD-derived perovskite thin films of  $\text{CH}_3\text{NH}_3\text{PbI}_3$ .

was converted to  $\text{PbI}_2$  through exposure to iodine gas. The  $\text{PbI}_2$  was subsequently converted to  $\text{CH}_3\text{NH}_3\text{PbI}_3$  through a 60 s dip in methylammonium iodide in IPA. The surface roughness and morphology are shown in the AFM images in Fig. 29(a). The morphology of the final  $\text{CH}_3\text{NH}_3\text{PbI}_3$  perovskite film is primarily determined by the methylammonium iodide treatment, and the thickness of the  $\text{CH}_3\text{NH}_3\text{PbI}_3$  perovskite film is thicker than the initial ALD  $\text{PbS}$  film. Another similar process was reported by Julien *et al.*,<sup>583</sup> as shown in Fig. 29(b). The  $\text{PbS}$  thin films were firstly deposited on planar and porous substrates by ALD, in which the polycrystalline p-type  $\text{PbS}$  films are found to be stoichiometric and pure. The  $\text{CH}_3\text{NH}_3\text{PbI}_3$  perovskite film was obtained by annealing the ALD  $\text{PbS}$  film at  $150^\circ\text{C}$  in the presence of vapors from methylammonium iodide. As seen in the XRD results, the perovskite  $\text{CH}_3\text{NH}_3\text{PbI}_3$  was successfully synthesized by this multistep approach. The SEM images indicate that the grain size of the ALD  $\text{PbS}$  is approximately 40–70 nm and the converted perovskite film has a more densely packed layer with large grain sizes. The direct synthesis of perovskite  $\text{CH}_3\text{NH}_3\text{PbI}_3$  has yet to be successful. However, Popov *et al.* have moved forward to fabricate metal iodides by ALD,<sup>584</sup> which are closer to the ALD perovskite  $\text{CH}_3\text{NH}_3\text{PbI}_3$ . In their process, lead silylamide ( $\text{Pb}(\text{btsa})_2$ ) and  $\text{SnI}_4$  were used as precursors and the deposition temperature was below  $90^\circ\text{C}$ . The roughness of the substrate surface significantly affected the crystalline texture and morphology of the  $\text{PbI}_2$  films, in which the films are dense on smooth substrates and porous on rough substrates. This ALD  $\text{PbI}_2$  film presents high film quality, uniformity, and scalability.

Charge transport layers are essential for the performance and efficiency of PSCs.<sup>585,586</sup> The charge transport layer is used to selectively extract photo-generated charges from the perovskite layer and transport the electrons/holes to the electrodes.<sup>587,588</sup> The charge transport layers are generally divided into electron transport layers, which transport photo-excited electrons, and hole transport layers, which transport holes. The main characteristics required of an ideal charge

transport layer include charge selectivity, high conductivity, chemical stability, transparency, and pinhole-free dense morphology.<sup>57,8</sup> Meanwhile, the thickness of the charge transport layers is required to be thin in order to reduce the charge transfer resistance of the photogenerated charges. With this in mind, ALD is an ideal approach to deposit a charge transport layer with conformal and dense film growth. Among the different materials,  $\text{TiO}_2$  has been extensively studied as a charge transport layer in PSCs. In the early studies, the ALD  $\text{TiO}_2$  layers were deposited as a hole blocking layer in PSCs.<sup>589,590</sup> For example, Grätzel's group demonstrated the sub-nanometer ALD  $\text{TiO}_2$  overlayer for high efficiency solid-state mesoscopic solar cells using a perovskite absorber, which effectively blocked the parasitic back reactions.<sup>589</sup> Subsequently, ALD- $\text{TiO}_2$  was further studied as an electron transport layer for PSCs.<sup>507,591–604</sup> Jung's group reported flexible perovskite solar cells with a high power conversion efficiency of 12.2%. As shown in Fig. 30(a), the amorphous and compact  $\text{TiO}_2$  was deposited by ALD with a thickness of 20 nm. The fast electron transport leads to the excellent performance of the PSCs, which was proven by the time-resolved photoluminescence and impedance studies. Additionally, the flexibility of the device is remarkable, in which it can maintain 95% of the initial PCE after 1000 bending cycles with a bending radius of 10 mm. Afterward, Li's group further investigated the effect of  $\text{TiO}_2$  thickness on the performance and clarified the mechanism behind the improved performance.<sup>605</sup> Different thicknesses of the  $\text{TiO}_2$  film, ranging from 5–20 nm, were optimized, in which a high efficiency of 13.6% was achieved with the 10 nm thick  $\text{TiO}_2$  layer. The optimized electron transport layer provided by ALD- $\text{TiO}_2$  delivered several advantages including high transmittance, low leakage current, and low charge transfer resistance and recombination rate.<sup>605</sup> The post-treatment process of the ALD- $\text{TiO}_2$  electron transport layer also influences cell performance. Martinson *et al.* explored two strategies which include annealing at  $500^\circ\text{C}$  and UV- $\text{O}_3$  treatments for the ALD- $\text{TiO}_2$  electron transport layer.<sup>339</sup> The results showed that the

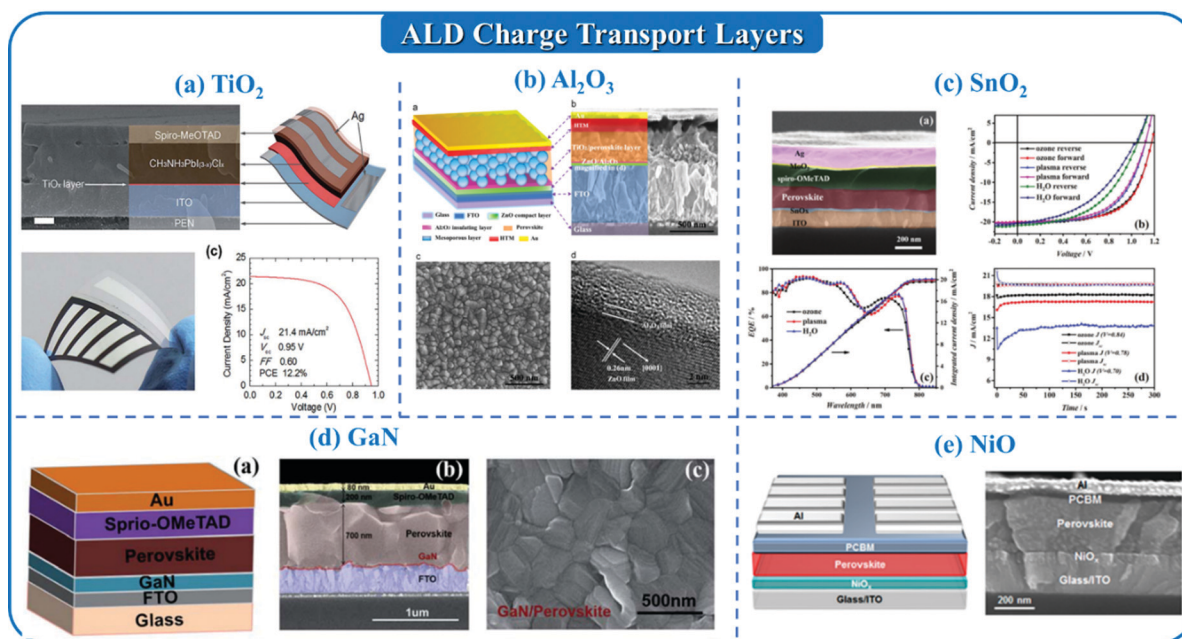


Fig. 30 ALD deposited charge transport layers for PSCs: (a)  $\text{TiO}_2$ ; (b)  $\text{Al}_2\text{O}_3$ ; (c)  $\text{SnO}_2$ ; (d) GaN; (e) NiO.

room-temperature UV- $\text{O}_3$  treatment for ALD- $\text{TiO}_2$  is considered as a more effective way to improve the efficiency comparable to crystalline  $\text{TiO}_2$  thin films synthesized by higher temperature methods. To show the advantages of ALD- $\text{TiO}_2$ , other methods were also investigated for the fabrication of  $\text{TiO}_2$  electron transport layers. Tian's group demonstrated a comparison between ALD and spin-coating methods for the synthesis of  $\text{TiO}_2$  electron transport layers.<sup>606</sup> Compared to the spin-coating, the ALD  $\text{TiO}_2$  electron transport layer is more uniform, and presented reduced interfacial charge accumulation, and accelerated electron transport. In another study, the ALD approach was proven to be superior to the spray pyrolysis and sol-gel methods.<sup>565</sup> The results showed that high-temperature sintering is not mandatory to achieve high-performance PSCs and that low-temperature fabrication of a compact layer by ALD can provide high efficiency on flexible substrates.

$\text{SnO}_2$  is another promising electron transport layer candidate for PSCs due to its deep conduction band, high electron bulk mobility, wide optical bandgap, and excellent chemical stability.<sup>575,607–611</sup> Hagfeldt's group firstly demonstrated the use of ALD  $\text{SnO}_2$  instead of  $\text{TiO}_2$  as an electron transport layer with an almost hysteresis-free efficiency of 18% and a high voltage up to 1.19 V.<sup>612</sup> Compared to  $\text{TiO}_2$ , the PSCs with  $\text{SnO}_2$  as an electron transport layer delivered better performances with high voltages and remarkably good stability over time. A barrier-free charge transport across the  $\text{SnO}_2$ /perovskite interface was achieved, resulting in highly stable current densities. Moreover, the ALD deposition parameters have obvious influences on the properties of the deposited materials. As shown in Fig. 30(c), Hu *et al.* studied different oxidant precursors, including  $\text{H}_2\text{O}$ ,  $\text{O}_3$ , and  $\text{O}_2$  plasma, for use in the deposition of ALD  $\text{SnO}_2$  and their effects on the PSCs.<sup>613</sup> The results

showed that the ALD  $\text{SnO}_2$  electron transport layer deposited using  $\text{O}_3$  has the best performance with a stable PCE of 15.3% and a remarkably high  $V_{\text{oc}}$  of 1.17 V. During the ALD process, an interfacial layer of  $\text{PbI}_2$  was formed between the  $\text{SnO}_2$  and perovskite. Different oxidant precursors resulted in different extraction barriers at the interfaces, in which the barriers were the largest for  $\text{H}_2\text{O}$ -deposited  $\text{SnO}_2$  and the smallest one is  $\text{O}_3$ -deposited  $\text{SnO}_2$ . The smaller barrier led to superior electron extraction. Another important parameter for the ALD process is the deposition temperature. Kuang *et al.* studied the ALD  $\text{SnO}_2$  electron transport layer deposited at different temperatures in the range of 50–200 °C.<sup>614</sup> The ALD- $\text{SnO}_2$  deposited at 200 °C contributed to cell stability; however, the efficiency decreased by approximately 50% for the counterpart device using the 50 °C  $\text{SnO}_2$ . The post-treatment of the ALD layers also has an influence on the cell performance. Jeong *et al.* demonstrated ALD- $\text{SnO}_2$  exposed to different post-annealing temperatures of 180 °C and 300 °C and used them as electron transport layers.<sup>615</sup> As a result, the PSCs with the ALD  $\text{SnO}_2$ -180 °C layer showed the highest power conversion efficiency of 18.3% and better reproducibility. The higher power conversion efficiency of ALD  $\text{SnO}_2$ -180 °C based PCSs compared to the as-deposited  $\text{SnO}_2$  was attributed to the enhanced electron-transport properties, thus improving the electrical conductivity. However, although the conductivity of the ALD  $\text{SnO}_2$ -300 °C was highest, the poor hole blocking ability of ALD  $\text{SnO}_2$ -300 °C led to a lower power conversion efficiency. Another similar study was demonstrated by Wang *et al.*,<sup>616</sup> in which the PSCs with a lower temperature (100 °C) post-treatment under air resulted in a higher power conversion efficiency of 20.3% than that of the PSCs with the as-deposited  $\text{SnO}_2$  and  $\text{SnO}_2$  annealed at higher temperatures of 200 and 300 °C.

Some other materials, such as GaN, and  $\text{Nb}_2\text{O}_5$ , *etc.* have also been demonstrated as electron transport layers for PSCs.<sup>617–619</sup> For example, as shown in Fig. 30(d), Wei *et al.* deposited a compact and amorphous n-type GaN layer by plasma-enhanced ALD at 280 °C to be used as an electron transport layer for PSCs.<sup>618</sup> The GaN-based PSCs exhibited higher efficiency of 15.18% with less hysteresis than the GaN-free device (10.38% efficiency). The improved performance with the GaN layer can be attributed to the improved electron extraction and reduced recombination at the FTO/perovskite interface. In addition, the bilayer structure was further designed as an electron transport layer for PSCs.<sup>620</sup> As shown in Fig. 30(b), an ultra-thin  $\text{Al}_2\text{O}_3$  insulating layer was deposited between the electron transport layer of ZnO and perovskite for PSCs.<sup>621</sup> This insulating layer with an electron transport layer can suppress the carrier's recombination process and improve the conversion efficiency of PSCs. The designed interface with ZnO/ $\text{Al}_2\text{O}_3$  resulted in PSCs with high efficiency of 15.55%, in which the thickness of the  $\text{Al}_2\text{O}_3$  insulating layer is only 4 Å. Another bilayer structure of  $\text{TiO}_2/\text{WO}_3$  was designed and fabricated by a combination of ALD and spin-coating processes on a conductive substrate to prevent the contact between the fluorine-doped tin oxide (FTO) and perovskite.<sup>602</sup> The PSCs with the  $\text{TiO}_2/\text{WO}_3$  electron transport bilayer exhibited an enhanced power conversion efficiency of up to 20.14%, which was much better than the single  $\text{WO}_3$  or  $\text{TiO}_2$  electron transport layer-based devices.

For the hole transport layers, NiO has proven to be one of the most popular materials due to its good optical transparency, high chemical stability, and ability to align the band edges of the perovskite layers.<sup>575,578</sup> The advantages of NiO as a hole transport layer can be summarized as: (1) suitable work function and large bandgap; (2) efficient hole extraction and low electrode polarization restricted to the interface of NiO; (3) high transparency in the visible spectral range.<sup>586</sup> ALD holds obvious advantages in the fabrication of NiO hole transport layers compared to other methods, such as sol-gel processes.<sup>622–624</sup> Seo *et al.* first demonstrated ultra-thin NiO by ALD as a hole transport layer for PSCs.<sup>625</sup> The results showed that the work function and hole concentration of the thin NiO hole transport

layers increased due to the overlap of the Debye length, resulting in an enhanced photovoltaic activity. A post-annealing process of the NiO layer can reduce the hydroxylated NiOOH on the surface, leading to higher electrical conductivity and better interfacial properties. The inverted planar PSCs with ALD NiO hole extraction layers exhibited a high efficiency of up to 16.40% with negligible hysteresis. Similarly, another work also demonstrated the influence of the post-treatment of ALD NiO on the PSC performances.<sup>626</sup> The PSCs with post-annealed ALD NiO layers delivered a higher efficiency of 17.07% when compared to the pristine NiO-based device, which had an efficiency of 13.98%. To improve the device reliability for large-scale fabrication, an atmospheric pressure spatial ALD process was developed to deposit NiO hole extraction layers, as shown in Fig. 30(e).<sup>627</sup> The PSCs with NiO hole extraction layers exhibited a high-power conversion efficiency of 17.1%. The NiO obtained by spatial ALD has improved uniformity with an average roughness of <0.6 nm. Importantly, the simply prepared and high-quality ALD NiO films are compatible with the large-throughput fabrication of perovskite optoelectronics.

The passivation layers at the perovskite absorber and contact layer interfaces in PSCs are generally used to reduce the concentration of surface defects that induce undesirable carrier recombination. ALD  $\text{Al}_2\text{O}_3$  is one of the most commonly used passivation layer materials for PSCs.<sup>628–636</sup> For example, as shown in Fig. 31(a), a thin layer of ALD  $\text{Al}_2\text{O}_3$  was deposited on  $\text{CH}_3\text{NH}_3\text{PbI}_{3-x}\text{Cl}_x$  for PSCs to reduce the hysteresis loss and stabilize the devices against humid conditions.<sup>637</sup> As a result, the PSCs with the ALD  $\text{Al}_2\text{O}_3$  layer exhibited a high efficiency of 18.8% with a significantly reduced hysteresis. Furthermore, the  $\text{Al}_2\text{O}_3$  passivation layer can significantly improve the PSC's stability against ambient humidity while retaining 60–70% of the initial efficiency after 70 days. However, the pristine cell without the  $\text{Al}_2\text{O}_3$  layer suffered from a drastic fall to 12% of its initial PCE during the study period. In another study, two ALD layers were deposited for the PSCs; one being a ZnO passivation layer and the other one being the  $\text{Al}_2\text{O}_3$  encapsulation layer, as shown in Fig. 31(b).<sup>638</sup> The fabricated PSC device showed a remarkable efficiency of 16.5% with high reproducibility. The  $\text{Al}_2\text{O}_3$  encapsulation layer can effectively enhance the ambient

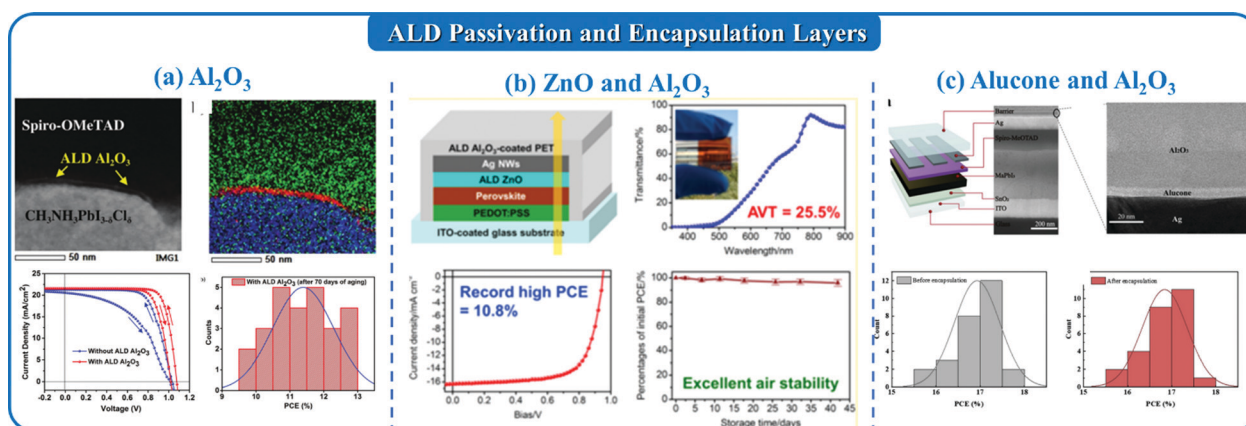


Fig. 31 ALD deposited passivation and encapsulation layers: (a)  $\text{Al}_2\text{O}_3$ ; (b) ZnO and  $\text{Al}_2\text{O}_3$ ; (c) alucone and  $\text{Al}_2\text{O}_3$ .

stability of the PSCs due to its ability to act as an effective gas diffusion barrier. To further improve the operational stability of PSCs in a humid environment, an alternating organic-inorganic encapsulation structure was deposited by ALD/MLD and found to exhibit an excellent water vapor transmittance rate, as shown in Fig. 31(c).<sup>639</sup> The PSCs with the Al<sub>2</sub>O<sub>3</sub>/alucone hybrid encapsulation layer survived at 80% relative humidity and 30 °C for over 2000 h while preserving 96% of its initial performance.

### 3.2.2 ALD/MLD for photoelectrochemical water splitting.

Another important energy conversion device is the photoelectrochemical (PEC) water splitting cell, which splits water into H<sub>2</sub> and O<sub>2</sub> through the use of sunlight.<sup>640–642</sup> It is a renewable approach to convert solar energy into storable fuels. In a PEC water-splitting cell, the photoelectrodes mainly consist of H<sub>2</sub>-evolving p and O<sub>2</sub>-evolving photoelectrodes. For the O<sub>2</sub>-evolving photoanode, n-type semiconductor materials are used to drive the holes to the interface between the semiconductor and electrolyte.<sup>643–645</sup> Electron-hole pairs are generated when the energy of the light is greater than the bandgap on the photoanode. The holes, where the water oxidation occurs, move to the surface. The protons are reduced to form molecular hydrogen and the electrons are collected at the metal cathode.<sup>642,646</sup> On the H<sub>2</sub>-evolving photocathode, the p-type semiconductor facilitates electron transfer to the electrolyte interface for the reduction reaction. The proton is reduced by acquiring the electrons to evolve hydrogen gas at the photocathode surface, and the holes move back to the counter electrode, where water oxidation takes place.<sup>642,646</sup> Therefore, the choice of semiconductor material is the key to achieving high-performance PEC water splitting devices.<sup>647–650</sup> The semiconductor generally requires a suitable bandgap, high conductivity, excellent stability and low cost, and should be environmentally friendly.

Fe<sub>2</sub>O<sub>3</sub> possesses a suitable bandgap and low-cost, which makes it a desirable candidate as a photoelectrode for PEC

water splitting devices.<sup>651–655</sup> Wang's group demonstrated ALD Fe<sub>2</sub>O<sub>3</sub> on a TiSi<sub>2</sub> nanonet as a photoelectrode,<sup>656</sup> as shown in Fig. 32(a). The TiSi<sub>2</sub> nanonet was used as a charge transport layer to improve the charge collection. The photocurrents of 1.6 and 2.7 mA cm<sup>-2</sup> were achieved at 1.23 and 1.53 V (*vs.* RHE) without any additional oxygen-evolving catalysts. Another p-LaFeO<sub>3</sub>/n-Fe<sub>2</sub>O<sub>3</sub> heterojunction structure was reported by Chen's group.<sup>657</sup> The La<sub>2</sub>O<sub>3</sub> layer was first deposited on the β-FeOOH nanorods by ALD, followed by the formation of the p-LaFeO<sub>3</sub>/n-Fe<sub>2</sub>O<sub>3</sub> heterojunction which was obtained by a post-annealing process. Because of the well-matched band levels of LaFeO<sub>3</sub> and α-Fe<sub>2</sub>O<sub>3</sub>, the photocurrent density was promoted from 0.37 to 0.58 mA cm<sup>-2</sup> at 1.23 V *versus* RHE. The significant improvement could be attributed to the accelerated charge separation within the space depletion layer induced by the built-in potential.<sup>657</sup>

TiO<sub>2</sub> was the first reported photoelectrode for water splitting; however, its solar-to-fuel conversion efficiency is the major limitation.<sup>658–663</sup> The main challenges for the TiO<sub>2</sub> photoelectrode are the carrier diffusion length, optical penetration depth, and inefficient electron collection. Peng *et al.* demonstrated an ALD TiO<sub>2</sub> layer on nano antimony-doped tin oxide (nanoATO) films as photoelectrodes for PEC water splitting, as shown in Fig. 32(b).<sup>664</sup> The nanoATO-ALD TiO<sub>2</sub> photoelectrode delivered a high photocurrent density of 0.58 mA cm<sup>-2</sup> under 1.5 G AM (~sunlight of 100 mW cm<sup>-2</sup>), which is 3 times higher than that of the planar TiO<sub>2</sub> electrodes on FTO glass. It was further reported that the thickness of the ALD TiO<sub>2</sub> layer and post-treatment process are also critical factors that affect the water splitting capabilities.<sup>665</sup> ALD TiO<sub>2</sub> was deposited on hematite nanorod arrays as photoelectrodes. In this study, different post-annealing temperatures of 400, 650 and 750 °C, were investigated. It was found that with an annealing temperature of 650 °C, significant photocurrent can be observed. Furthermore, the thickness of the ALD TiO<sub>2</sub> was

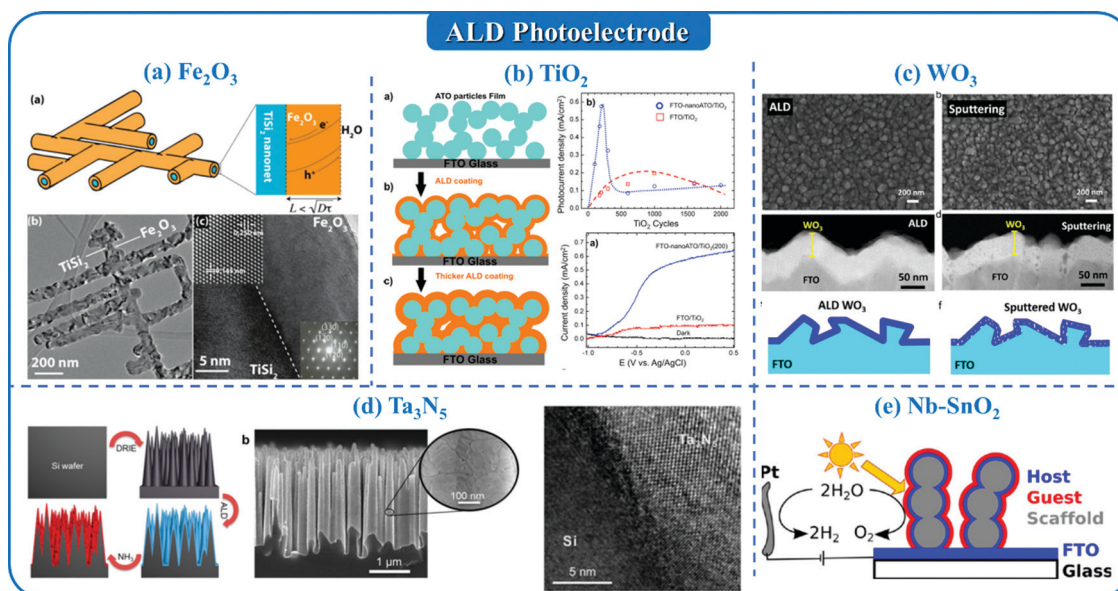


Fig. 32 ALD-fabricated photoelectrodes for PEC water splitting devices: (a) Fe<sub>2</sub>O<sub>3</sub>; (b) TiO<sub>2</sub>; (c) WO<sub>3</sub>; (d) Ta<sub>3</sub>N<sub>5</sub>; (e) SnO<sub>2</sub>.

optimized. Below a critical thickness, the PEC performance was steadily enhanced. If the thickness of the  $\text{TiO}_2$  layer was too thick, the hole transfer from hematite to liquid was blocked because of the formation of a substantive heterojunction. With the optimized annealing temperature and thickness for the ALD  $\text{TiO}_2$  layer, a high photocurrent of  $1.9 \text{ mA cm}^{-2}$  at  $1.23 \text{ V}$  (*vs.* RHE) under AM 1.5 simulated solar illumination was achieved.

In addition to  $\text{TiO}_2$ , other metal oxides, such as  $\text{Ga}_2\text{O}_3$ ,  $\text{SnO}_2$ ,  $\text{ZnO}$ ,  $\text{HfO}_2$ ,  $\text{WO}_3$ , *etc.*, have been deposited by ALD on different substrates and used as effective photoelectrodes for PEC water splitting devices.<sup>57,666–677</sup> For example, as shown in Fig. 32(c), Zhao *et al.* compared two different deposition techniques which included sputtering and ALD for the deposition of  $\text{WO}_3$  thin film photoelectrodes.<sup>678</sup> For the sputtered  $\text{WO}_3$ , the film possessed obvious nanosized holes throughout the surface. Meanwhile, for the ALD  $\text{WO}_3$  film, no obvious microholes or other physical defects were observed. The highest performance was achieved for  $\text{WO}_3$  films deposited by ALD after annealing in air, which led to the fewest physical defects and an appropriate amount of oxygen vacancies.<sup>678</sup> Another Nb-doped  $\text{SnO}_2$  was deposited by ALD and demonstrated by Grätzel's group (Fig. 32(e)).<sup>679</sup> The doped films were deposited using  $\text{SnO}_2$  and  $\text{Nb}_2\text{O}_5$  subcycles in which the content of Nb was controlled from 0–4%. The conductivity of the  $\text{SnO}_2$  was improved with Nb-doping, in which the conductivity reached a maximum with 2% Nb in  $\text{SnO}_2$ . With another layer of hematite, the architecture showed a significant photocurrent plateau of  $2.26 \text{ mA cm}^{-2}$  at  $1.4 \text{ V}$  *vs.* RHE.

Besides the metal oxide, metal nitrides such as tantalum nitride have received increasing attention due to their favourable bandgaps and band edge positions that straddle both the reduction and oxidation potentials of water.<sup>680,681</sup> Narkeviciute *et al.* fabricated core-shell  $\text{Ta}_3\text{N}_5$  on a Si substrate by ALD (Fig. 32(d)).<sup>680</sup> The  $\text{Ta}_3\text{N}_5$  was obtained by the nitridation of amorphous  $\text{Ta}_2\text{O}_5$  under  $\text{NH}_3$ . The thinner  $\text{Ta}_3\text{N}_5$  shells resulted in superior photocurrents and absorbed-photon-to-current efficiencies indicating minimal carrier diffusion lengths on the order of tens of nanometers.

Similar to other applications, ALD is also used to design different 3D-structured photoelectrodes for PEC water splitting devices aimed towards achieving high specific surface area, direct electron transport pathways, and excellent light-harvesting abilities.<sup>170,682–691</sup> In an early study, Cheng's group reported a 3D ordered urchin-like hollow  $\text{TiO}_2/\text{ZnO}$  nanorod structure on transparent FTO as a photoanode for photoelectrochemical hydrogen generation,<sup>692</sup> as shown in Fig. 33(a). In a typical process, a monolayer of PS microspheres was assembled onto the FTO substrate to act as a sacrificial template. Then, 20 nm of  $\text{TiO}_2$  and 10 nm of  $\text{ZnO}$  were deposited onto the PS spheres by ALD. Afterwards,  $\text{ZnO}$  nanorods were grown onto the surface of  $\text{TiO}_2/\text{ZnO}$  hollow spheres with a hydrothermal approach. With a CdS sensitizer, a photocurrent of  $3.6 \text{ mA cm}^{-2}$  (at 0 V *vs.* Ag/AgCl) was generated by the urchin-like  $\text{TiO}_2/\text{ZnO}$  photoanode, which is much higher than that of the 2D and 1D structure. The higher surface area provided by the nanostructured electrode for quantum dot loading contributed to the enhanced light scattering ability. Another interesting 3D-structured cactus-like  $\text{WO}_3@\text{ZnWO}_4@\text{ZnO}-\text{ZnO}$  was demonstrated by Zhang's group, fabricated by combining ALD with a hydrothermal process.<sup>693</sup> As shown in Fig. 33(b), the well-aligned  $\text{WO}_3$  nanosheet array was grown on FTO glass by the hydrothermal method. Subsequently, the amorphous  $\text{ZnO}$  layer was coated on the  $\text{WO}_3$  nanosheets by ALD and further annealed in air to form a  $\text{ZnWO}_4$  buffer layer. Finally, another set of  $\text{ZnO}$  nanosheets was grown on the surface by a secondary hydrothermal process. As a result, the fabricated 3D photoelectrode photocurrent density was 3.8 times higher ( $\sim 1.57 \text{ mA cm}^{-2}$ ) at  $1.23 \text{ V}$  *vs.* RHE than the pristine  $\text{WO}_3$  photoanode after long-term continuous illumination. Their group further developed another  $\text{ZnO}-\text{GaON}$  core-shell nanowire structure by PE-ALD,<sup>694</sup> as shown in Fig. 33(c). The  $\text{ZnO}$  nanowire was firstly grown on the FTO substrate *via* a hydrothermal method with an ALD  $\text{ZnO}$  seed layer. Afterwards, a  $\text{GaON}$  film was further deposited on the  $\text{ZnO}$  nanowire by a PE-ALD process. To grow the  $\text{GaON}$  film,  $\text{NH}_3$  and  $\text{O}_2$  gas were introduced simultaneously at a specific flow ratio in the plasma

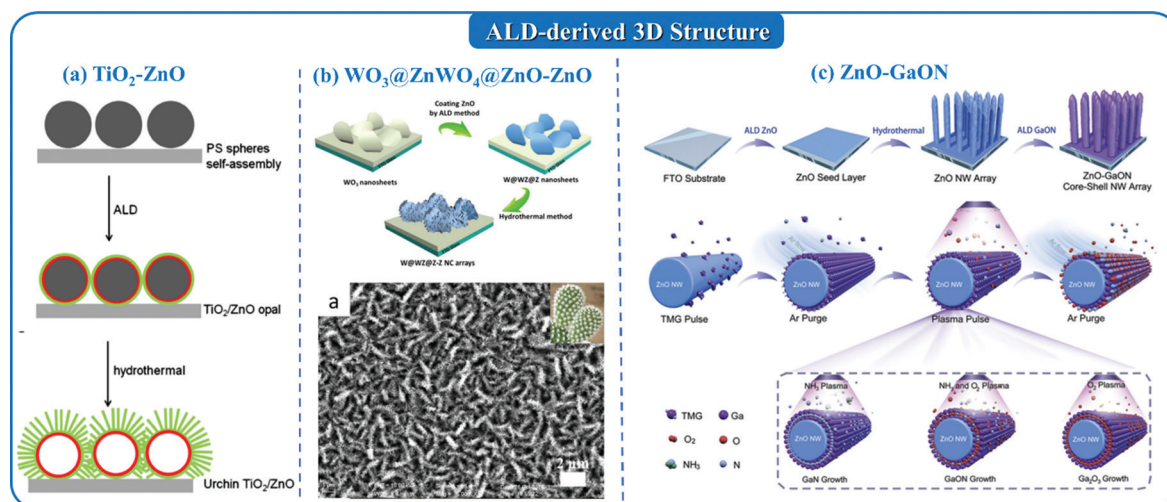


Fig. 33 ALD-derived 3D structured photoelectrodes for PEC water splitting devices: (a)  $\text{TiO}_2-\text{ZnO}$ ; (b)  $\text{WO}_3@\text{ZnWO}_4@\text{ZnO}-\text{ZnO}$ ; (c)  $\text{ZnO}-\text{GaON}$ .

pulse step. The unique structure of ZnO–GaON core–shell nanowires with optimized ALD GaON shell thickness exhibited a significant electric field enhancement and light trapping ability, which improved the photocurrent from  $\sim 0.24$  (pristine ZnO) to  $2.25 \text{ mA cm}^{-2}$  at  $1.23 \text{ V}$  versus RHE.

To improve the PEC device performance, numerous transition-metal/metal oxides, such as nickel (and NiO) and cobalt (and  $\text{Co}_3\text{O}_4$ ), have been used as catalysts for oxygen-evolution. ALD was also widely reported as a method to deposit transition-metal catalysts on photoelectrodes for PEC water splitting.<sup>609,695–700</sup> Yang *et al.* fabricated a conformal, biphasic  $\text{CoO}_x$  catalyst by PE-ALD and used it as a photoelectrode with high activity and compatibility.<sup>701</sup> A compact and continuous nanocrystalline  $\text{Co}_3\text{O}_4$  spinel was deposited by PE-ALD, which provides effective protection for the underlying substrate. Furthermore, disordered surface layers composing of  $\text{Co(OH)}_2$  were obtained at a reduced deposition temperature and significantly improved electrocatalytic activity. This  $\text{Co(OH)}_2$  layer promoted chemical and structural transformation, leading to a high concentration of catalytically active sites. As a result, the  $\text{Co}_3\text{O}_4/\text{Co(OH)}_2$  thin films exhibited high activity towards water splitting with enhanced durability.

Passivation layers are widely used to suppress the surface recombination that occurs on photoelectrodes for PEC water splitting devices. ALD is an ideal technique to deposit the passivation layer, which has also been introduced in the above sections for solar cells.  $\text{TiO}_2$  is one of the most popular materials as a passivation layer and has been deposited by ALD.<sup>591,702–710</sup> For example, Yang's group fabricated an epitaxial rutile  $\text{TiO}_2$  shell by ALD on  $\text{TiO}_2$  nanowires as the passivation layer.<sup>711</sup> When coated with a 150-ALD-cycle  $\text{TiO}_2$  shell, the photocatalytic activity of the  $1.8 \mu\text{m}$  long  $\text{TiO}_2$  nanowire was enhanced 1.5 times ( $1.5 \text{ V}$  vs. RHE) higher, reaching a current density of  $1.1 \text{ mA cm}^{-2}$ . This ALD  $\text{TiO}_2$  coating improved the charge collection efficiency due to the passivation of surface states and an increase in surface area. Moreover, Paracchino *et al.*, examined several factors that determine the performance and stability of  $\text{Cu}_2\text{O}$  photocathodes with ALD-deposited overlayers.<sup>712</sup> It was found that the ALD deposition temperature

is critical towards the device performance, and determines the energy level positions as well as crystallinity. With a more crystalline overlayer, 62% stability over 10 hours of testing was achieved for the  $\text{Cu}_2\text{O}$  photocathodes. Some other metal oxides deposited by ALD, such as  $\text{Al}_2\text{O}_3$ ,  $\text{SnO}_2$ ,  $\text{Ta}_2\text{O}_5$ , ZnO, *etc.*, were also reported as passivation layers for PEC water splitting devices.<sup>713–720</sup> For example, ALD  $\text{Al}_2\text{O}_3$  was deposited on  $\text{TiO}_2$  nanotubes as a passivation layer and was used as a photoanode for PEC water splitting.<sup>721</sup> The optimized ALD coating exhibited an enhanced photocurrent density by 0.8 times compared to the pristine  $\text{TiO}_2$  nanotubes. The improvement was mainly ascribed to the reduction of the electron–hole recombination and decreased surface defect density combined with the field-effect passivation induced by the ALD  $\text{Al}_2\text{O}_3$  shells. In another work, 2 nm of ALD-ZnO was fabricated on the spin-cast PC71BM thin-film n-type organic semiconductor photoanode as a passivation layer.<sup>722</sup> As a result, the passivated photoelectrode exhibited increased stability for 1000 s and a photocurrent of  $30 \mu\text{A cm}^{-2}$  at  $E = 1.23 \text{ V}$  versus RHE, which was nearly 300% and 600% of those in the un-passivated PC71BM, respectively. The results revealed that the ALD ZnO can tunnel the hole transfer through passivation layers and improve the adhesion to the organic semiconductor, thus lowering Ohmic resistance.

## 4. Large scale ALD/MLD

With significant efforts from the community, ALD and MLD techniques have been widely proven as effective and promising tools for energy storage and conversion applications, particularly for the fields of batteries and fuel cells. However, one of the major concerns is the practicality of large-scale deposition for industrial applications.<sup>723</sup> To address this concern, large-scale spatial ALD systems have been proposed and developed.<sup>724</sup> In a spatial ALD process, the precursors are pulsed simultaneously and continuously, but at a different physical location in the reactor.<sup>725–727</sup> Fig. 34(a) shows the concept of roll-to-roll ALD, which uses a typical spatial ALD process. In this roll-to-roll process, the reactor is divided into individual spaces, exposing

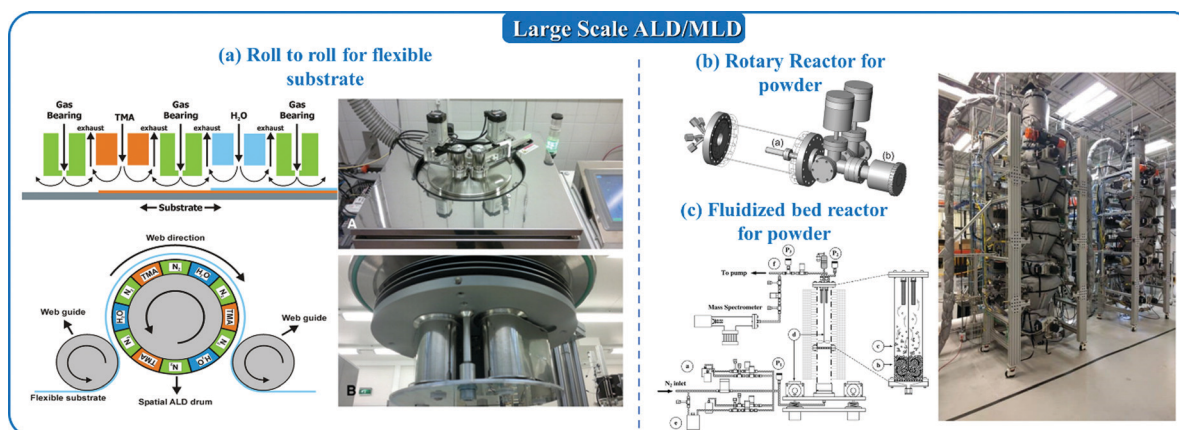


Fig. 34 Large scale ALD/MLD: (a) roll-to-roll techniques for flexible substrates; (b) rotary reactor for powder; (c) fluidized bed reactor for powder.

the precursors to the substrate in different regions and moving the substrates through the reactor.<sup>728–731</sup> This roll-to-roll ALD process allows very high deposition rates while maintaining the desired ALD properties such as film quality and conformality. Subsequently, another roll-to-roll reactor was designed, consisting of a central drum that contains one or more half-reaction zones for individual precursors, as illustrated in Fig. 34(a). This upgrade allows for the avoidance of the mechanical contact between the deposition side of the foil and the reactor and further minimizes the amount of moving parts.<sup>728</sup> These roll-to-roll ALD reactors are ideal for large scale flexible substrates requiring fast deposition rates.<sup>732</sup> For energy storage and conversion applications, they are promising to carry out roll-to-roll ALD coatings on electrodes at the industrial level.

Another reactor design is used for large-scale powder depositions. It is also very important and practical for energy storage and conversion applications, such as ALD/MLD coatings on cathode/anode powders for batteries, and catalysis deposition on carbon powders for fuel cells. One of the options for ALD/MLD deposition on powders is the rotary reactor, which is presented in Fig. 34(b). The rotary reactor allows for static reactant exposures that can utilize the ALD precursors more efficiently.<sup>733–735</sup> Another possibility is the fluidized bed reactor, which has been studied intensively for different ALD/MLD processes.<sup>736–749</sup> For example, Fig. 34(c) shows a typical fluidized bed reactor for ALD deposition on powder. This reactor allows for the optimization of the process variables at any scale. Combined with *in situ* mass spectrometry, the precursors can be fully utilized to maximize precursor utilization and surface saturation. Some ALD companies have already commercialized the fluidized bed reactor with the capabilities of process material at the ton level, as shown in Fig. 34.<sup>750</sup> Moreover, many types of films can be deposited in these reactors on virtually any particle substrate using this gas-phase reaction process.<sup>738</sup>

## 5. Conclusions

In this comprehensive review, we summarize the development and understanding of ALD/MLD techniques for energy storage and conversion applications, focusing on batteries, supercapacitors, fuel cells, solar cells and photoelectrochemical water splitting. In general, ALD/MLD are very promising techniques that can address the challenges for energy storage and conversion due to their unique properties such as precise thickness control, excellent uniformity and conformity, and tunable composition. The main content of this review is as follows:

(1) ALD/MLD techniques are used to fabricate electrode materials for LIBs and NIBs. Various types of metal oxides ( $\text{SnO}_2$ ,  $\text{ZnO}$ , and  $\text{TiO}_2$ , *etc.*) have been deposited on different substrates (such as graphene, carbon nanotubes, and stainless steel) as anode materials. Several Li/Na-containing compounds ( $\text{LiCoO}_2$ ,  $\text{LiFePO}_4$ , and  $\text{NaTiO}_x$ ) have been developed as cathodes for LIBs and NIBs. Meanwhile, MLD is proposed to synthesize organic electrodes for batteries. Benefitting from the advantages

of ALD/MLD, the morphologies, structures, compositions, and particle sizes are precisely controlled by adjusting the ALD/MLD parameters, resulting in excellent electrochemical performances. However, as we discussed above, the drawbacks of ALD/MLD for electrode fabrication are also obvious. The major concern is the low GPC of ALD/MLD films, which is in the range of Å per cycle for most of the procedures. To reach a high enough loading of the active materials, hundreds or even thousands of ALD cycles are required to obtain a thick electrode. This time-consuming process has less commercial viability for standard battery technologies, particularly when compared with composite/powder-based electrodes. Nevertheless, it still needs to be pointed out that ALD/MLD is still promising for the design and fabrication of thin film batteries or micro-batteries with thin electrodes.

(2) Rather than electrode fabrication, ALD/MLD is more promising for the engineering of the interface between the electrode and electrolytes in LIBs and NIBs, especially on the cathode side. ALD  $\text{Al}_2\text{O}_3$  is the most popular coating layer used to modify the surface of cathode materials. The electrochemical performances of  $\text{Al}_2\text{O}_3$ -coated cathode materials are significantly improved with only a few cycles of ALD. The protection mechanism of ALD  $\text{Al}_2\text{O}_3$  has been intensively studied by different approaches, such as *in operando* XRD, *in operando* XANES, and STEM-EELS. The most widely recognized explanation is that the thin ALD  $\text{Al}_2\text{O}_3$  can prevent the electrolyte decomposition, HF corrosion, and transition metal dissolution. Some other metal oxides have been further investigated as a coating for cathode materials, in which ALD  $\text{Al}_2\text{O}_3$  still performs the best among them. However, the metal oxides are generally non-ionic conductive, which will limit the Li-ion transport across the interface. In this case, Li-ion conductive solid-state electrolytes have been developed to replace the metal oxide coatings for cathode materials. The solid-state electrolyte coating enables fast Li transport and achieves even better electrochemical performances compared to their respective metal oxides. Beyond surface coating, ALD films are used to tailor the structures of the cathodes with further post-treatments, such as doping the lattice and modifying the grain boundary.

(3) On the anode interface of LIBs and NIBs, the ALD/MLD coatings serve two purposes. On one hand, the ALD/MLD layers are deposited as an artificial SEI to prevent the side reactions between the anode materials and liquid electrolytes. On the other hand, the ALD/MLD surface coating can relieve the volume change of the anode materials during lithiation/delithiation. Generally, when depositing coating layers for anodes, MLD presents more promising properties and better electrochemical performances compared to ALD due to the enhanced flexibility for volume change accommodation. Beyond the conventional anode materials, Li metal and Na metal are excellent candidates for next-generation Li metal batteries and Na metal batteries, respectively. The application of ALD/MLD has also been extended to artificial SEI fabrication for Li and Na metal anodes. Similar to regular anodes, the MLD layers deliver better performances than that of ALD coatings for alkali metal anodes. Additionally, the organic–inorganic hybrid coatings have been proven to be ideal layers with excellent

electrochemical, chemical and mechanical properties. Moreover, the ALD/MLD techniques have been applied to address the interfacial issues for SSBs, in which ALD/MLD layers are used to prevent the side reaction between the electrodes and SSEs.

(4) ALD/MLD has also been used to deposit catalysts with controllable particle sizes for metal–air batteries and fuel cells. For metal–air batteries, precisely controlled catalysis is the key to tune the discharge product composition and morphologies. Moreover, selective ALD deposition can be applied to stabilize the catalysts. For electrocatalytic applications, ALD has been shown to be an ideal technique to deposit catalysts with controllable particle sizes in high-aspect-ratio and porous materials. It can be further used to design novel structures and modify the surface of the substrate to stabilize the catalysts. Moreover, ALD can be used to precisely deposit single atoms and even dimer catalysts on the different substrates, which improves the activity to a new level.

(5) ALD/MLD has been used to develop nanostructure materials for different applications, such as batteries, supercapacitors, solar cells and photoelectrochemical water splitting. Generally, different types of templates are used to deposit ALD films. Afterwards, the templates are removed or transferred to create hollow nanostructures by post-treatment processes. Finally, the 3D nanostructures with high surface area and short ion diffusion paths are achieved with significantly improved performances for different energy-related devices.

(6) For photovoltaics of DSSCs, perovskite and photoelectrochemical water splitting, ALD/MLD is used to deposit the core–shell structure of the photoelectrode with minimized electron transfer routes to the conductive substrate. Moreover, ALD has been more widely used to modify the interfaces in DSSCs, including passivation, barrier, and blocking layers, with significantly improved performances.

(7) The potential of large scale ALD/MLD for energy applications has been further discussed. On one hand, roll-to-roll ALD/MLD has been widely developed for flexible substrates and is suitable for battery electrodes, fuel cell membranes and solar cell substrates. On the other hand, the rotary and fluidized bed reactors are designed for the mass production of powder samples, which is ideal for cathode/anode material manufacturing.

## 6. Perspective

Significant progress in the fields of ALD/MLD for energy applications has been reported over the past decade and ALD/MLD techniques are gradually becoming recognized by the energy storage and conversion communities as powerful and effective tools. However, challenges still remain and need to be addressed, at the same time, enormous potential is expected to be exploited. We list the detailed potential directions and perspectives below.

(1) Extension of other ALD chemistries for energy applications. Currently, the most popular materials deposited by ALD for energy applications are various metal oxides and noble metals. In the ALD community, other types of materials, such as nitrides,

sulfides, and fluorides, have been successfully synthesized by ALD (or PEALD). These materials have unique properties compared to metal oxides and are expected to be applied in energy applications. For example, metal nitrides generally show higher electronic conductivity and chemical stability compared to metal oxides, and can be used as a substrate for fuel cell catalysis or as coatings for cathode/anode materials for batteries. Furthermore, metal fluorides have been predicted to have the widest electrochemical stability windows, especially at high potential. These materials would be ideal coatings for cathode materials in batteries. With this in mind, more opportunities and possibilities should arise for ALD/MLD chemistry in energy applications.

(2) Development and application of new MLD chemistry. The developed MLD chemistries are plentiful and attractive, however, their application in energy is still in an early stage. Firstly, the organic electrodes fabricated by MLD for Li and Na storage are interesting with various electrochemical active sites. Secondly, the fabrication of Li-ion and Na ion conductive MLD films is also challenging, putting forward the requirement for new MLD chemistries. Meanwhile, for fuel cell applications, highly conductive and catalytically active MLD thin films are expected to be explored as catalysts in fuel cells. Furthermore, the post-treatment of MLD films can be used to design and synthesize porous and carbon-containing films.

(3) Investigation of the properties of ALD/MLD films. Although numerous materials have been synthesized by ALD/MLD techniques, their properties have not been fully studied, such as chemical stability, electrochemical stability, and mechanical stability. These properties are always predicted from simulations or inferred from the same bulk materials. However, the properties of ALD/MLD films at the nanoscale or atomic scale are relatively different compared to the bulk materials. In this case, the understanding and characterization of ALD/MLD films at the nanoscale are critical for the community.

(4) Tuning of the mechanical properties of ALD/MLD films. Recent studies reveal that the mechanical properties also affect the electrochemical performances of the electrode, particularly the materials with large volume change. However, there are few examples of research focusing on the mechanical properties of the ALD/MLD films. Thus, it is also important to connect the mechanical properties of the coating layer to the electrochemical performances of the batteries.

(5) Rationally designing films by ALD/MLD. Various individual ALD/MLD films have been studied for energy applications. However, individual films cannot meet all the requirements for different applications. The combination of different ALD/MLD films for hybrid coating designs is required to meet the demands of specific applications.

(6) Mechanistic insight behind the electrochemical performance. It has been widely proven that ALD/MLD is effective in improving the performances of various systems. However, the functionality and mechanisms of ALD/MLD layers are still unclear. Thus, advanced characterization methods, especially *in situ* techniques, are the key for providing a deep understanding and will provide guidance towards future ALD/MLD material design.

(7) Currently, there is a need to demonstrate the practical applications of ALD/MLD technologies in energy storage and conversion for large-scale production. In particular, it is urgent to realize the mass production of ALD coatings on powder materials, such as cathode materials for batteries.

## Author contributions

X. Sun and J. Lu supervised the overall work; Y. Zhao, L. Zhang, J. Liu, K. Amine, J. Lu, and X. Sun designed the content of the review; J. Liu and Y. Zhao organized the introduction; L. Zhang wrote the electrocatalytic reactions for fuel cell application section; K. Adair wrote the Li-S batteries application section and edited the manuscript; Y. Sun wrote the Li-metal anode application section; F. Zhao wrote the solid-state Li battery application section; T. Wu and B. Xuan focused on the Li-O<sub>2</sub> battery applications; Y. Zhao organized and wrote all the other parts of Li-ion batteries, Na batteries and beyond, supercapacitors, and photoelectrocatalysis applications; all authors read and commented on the manuscript.

## Conflicts of interest

There are no conflicts to declare.

## Acknowledgements

X. Sun would like to acknowledge the funding support by the Natural Science and Engineering Research Council of Canada (NSERC), the Canada Research Chair Program (CRC), the Canada Foundation for Innovation (CFI), Ontario Research Fund (ORF), Mitacs and the University of Western Ontario (UWO). Y. Zhao would like to acknowledge the Mitacs Elevate Postdoctoral Fellowship. J. Liu is grateful for funding support from NSERC, CFI, BC Knowledge Development Fund (BCKDF), and the University of British Columbia (UBC). The work at Argonne National Laboratory was supported by the U.S. Department of Energy (DOE), Office of Energy Efficiency and Renewable Energy, Vehicle Technologies Office. Argonne National Laboratory is operated for DOE Office of Science by UChicago Argonne, LLC, under contract number DE-AC02-06CH11357.

## References

- D. Larcher and J. M. Tarascon, *Nat. Chem.*, 2015, **7**, 19–29.
- A. Manthiram, X. Yu and S. Wang, *Nat. Rev. Mater.*, 2017, **2**, 16103.
- Y. Li and J. Lu, *ACS Energy Lett.*, 2017, **2**, 1370–1377.
- T. Famprikis, P. Canepa, J. A. Dawson, M. S. Islam and C. Masquelier, *Nat. Mater.*, 2019, **18**, 1278–1291.
- Y. Liu, Y. Zhu and Y. Cui, *Nat. Energy*, 2019, **4**, 540–550.
- Y. Yuan, K. Amine, J. Lu and R. Shahbazian-Yassar, *Nat. Commun.*, 2017, **8**, 15806.
- Y.-J. Wang, B. Fang, D. Zhang, A. Li, D. P. Wilkinson, A. Ignaszak, L. Zhang and J. Zhang, *Electrochem. Energy Rev.*, 2018, **1**, 1–34.
- L. Xu, S. Tang, Y. Cheng, K. Wang, J. Liang, C. Liu, Y.-C. Cao, F. Wei and L. Mai, *Joule*, 2018, **2**, 1991–2015.
- S. Kalluri, M. Yoon, M. Jo, H. K. Liu, S. X. Dou, J. Cho and Z. Guo, *Adv. Mater.*, 2017, **29**, 1605807.
- J. Kim, H. Lee, H. Cha, M. Yoon, M. Park and J. Cho, *Adv. Energy Mater.*, 2018, **8**, 1702028.
- X. Li and X. Sun, *Adv. Funct. Mater.*, 2018, **28**, 1801323.
- J. Song, B. Xiao, Y. Lin, K. Xu and X. Li, *Adv. Energy Mater.*, 2018, **8**, 1703082.
- Z. P. Cano, D. Banham, S. Ye, A. Hintennach, J. Lu, M. Fowler and Z. Chen, *Nat. Energy*, 2018, **3**, 279–289.
- N. Tian, B.-A. Lu, X.-D. Yang, R. Huang, Y.-X. Jiang, Z.-Y. Zhou and S.-G. Sun, *Electrochem. Energy Rev.*, 2018, **1**, 54–83.
- M. Leskela and M. Ritala, *Thin Solid Films*, 2002, **409**, 138–146.
- M. Leskela and M. Ritala, *Angew. Chem.*, 2003, **42**, 5548–5554.
- M. Knez, K. Nielsch and L. Niinistö, *Adv. Mater.*, 2007, **19**, 3425–3438.
- S. M. George, *Chem. Rev.*, 2010, **110**, 111–131.
- R. W. Johnson, A. Hultqvist and S. F. Bent, *Mater. Today*, 2014, **17**, 236–246.
- M. Liu, X. Li, S. K. Karuturi, A. I. Tok and H. J. Fan, *Nanoscale*, 2012, **4**, 1522–1528.
- C. Marichy, M. Bechelany and N. Pinna, *Adv. Mater.*, 2012, **24**, 1017–1032.
- M. Noked, C. Liu, J. Hu, K. Gregorczyk, G. W. Rubloff and S. B. Lee, *Acc. Chem. Res.*, 2016, **49**, 2336–2346.
- M. Mäntymäki, M. Ritala and M. Leskelä, *Coatings*, 2018, **8**, 277.
- V. P. Prasad, N. Bahlawane, F. Mattelaer, G. Rampelberg, C. Detavernier, L. Fang, Y. Jiang, K. Martens, I. P. Parkin and I. Papakonstantinou, *Mater. Today Chem.*, 2019, **12**, 396–423.
- X. Meng, X. Q. Yang and X. Sun, *Adv. Mater.*, 2012, **24**, 3589–3615.
- K. X. Wang, X. H. Li and J. S. Chen, *Adv. Mater.*, 2015, **27**, 527–545.
- X. Wang and G. Yushin, *Energy Environ. Sci.*, 2015, **8**, 1889–1904.
- B. Ahmed, C. Xia and H. N. Alshareef, *Nano Today*, 2016, **11**, 250–271.
- C. Guan and J. Wang, *Adv. Sci.*, 2016, **3**, 1500405.
- L. Ma, R. B. Nuwayhid, T. Wu, Y. Lei, K. Amine and J. Lu, *Adv. Mater. Interfaces*, 2016, **3**, 1600564.
- W. Lu, L. Liang, X. Sun, X. Sun, C. Wu, L. Hou, J. Sun and C. Yuan, *Nanomaterials*, 2017, **7**, 325.
- X. Meng, *J. Mater. Chem. A*, 2017, **5**, 10127–10149.
- B. Yan, X. Li, Z. Bai, X. Song, D. Xiong, M. Zhao, D. Li and S. Lu, *J. Power Sources*, 2017, **338**, 34–48.
- Y. Zhao and X. Sun, *ACS Energy Lett.*, 2018, **3**, 899–914.
- Y. Zhao, K. Zheng and X. Sun, *Joule*, 2018, **2**, 2583–2604.
- H. C. M. Knoops, M. E. Donders, M. C. M. van de Sanden, P. H. L. Notten and W. M. M. Kessels, *J. Vac. Sci. Technol., A*, 2012, **30**, 010801.

- 37 X. Meng, *Energy Storage Mater.*, 2020, **30**, 296–328.
- 38 O. Nilsen, V. Miiikkulainen, K. B. Gandrud, E. Østreng, A. Ruud and H. Fjellvåg, *Phys. Status Solidi A*, 2014, **211**, 357–367.
- 39 K. Share, A. Westover, M. Li and C. L. Pint, *Chem. Eng. Sci.*, 2016, **154**, 3–19.
- 40 Q. Sun, K. C. Lau, D. Geng and X. Meng, *Batteries Supercaps*, 2018, **1**, 41–68.
- 41 O. Tiurin and Y. Ein-Eli, *Adv. Mater. Interfaces*, 2019, **6**, 1901455.
- 42 F. Yu, L. Du, G. Zhang, F. Su, W. Wang and S. Sun, *Adv. Funct. Mater.*, 2019, **30**, 1906890.
- 43 J. Zhang, G. Zhang, Z. Chen, H. Dai, Q. Hu, S. Liao and S. Sun, *Energy Storage Mater.*, 2020, **26**, 513–533.
- 44 Z. Zhao, Y. Kong, Z. Zhang, G. Huang and Y. Mei, *J. Mater. Res.*, 2019, **35**, 701–719.
- 45 X. Li, X. Meng, J. Liu, D. Geng, Y. Zhang, M. N. Banis, Y. Li, J. Yang, R. Li, X. Sun, M. Cai and M. W. Verbrugge, *Adv. Funct. Mater.*, 2012, **22**, 1647–1654.
- 46 V. Aravindan, K. B. Jinesh, R. R. Prabhakar, V. S. Kale and S. Madhavi, *Nano Energy*, 2013, **2**, 720–725.
- 47 M. Xie, X. Sun, S. M. George, C. Zhou, J. Lian and Y. Zhou, *ACS Appl. Mater. Interfaces*, 2015, **7**, 27735–27742.
- 48 B. Ahmed, D. H. Anjum, Y. Gogotsi and H. N. Alshareef, *Nano Energy*, 2017, **34**, 249–256.
- 49 D. V. Nazarov, M. Y. Maximov, P. A. Novikov, A. A. Popovich, A. O. Silin, V. M. Smirnov, N. P. Bobrysheva, O. M. Osmolovskaya, M. G. Osmolovsky and A. M. Rumyantsev, *J. Vac. Sci. Technol., A*, 2017, **35**, 01B137.
- 50 M. Y. Maximov, P. A. Novikov, D. V. Nazarov, A. M. Rumyantsev, A. O. Silin, Y. Zhang and A. A. Popovich, *J. Electron. Mater.*, 2017, **46**, 6571–6577.
- 51 X. Meng, M. N. Banis, D. Geng, X. Li, Y. Zhang, R. Li, H. Abou-Rachid and X. Sun, *Appl. Surf. Sci.*, 2013, **266**, 132–140.
- 52 X. Meng, D. Geng, J. Liu, R. Li and X. Sun, *Nanotechnology*, 2011, **22**, 165602.
- 53 C. Ban, M. Xie, X. Sun, J. J. Travis, G. Wang, H. Sun, A. C. Dillon, J. Lian and S. M. George, *Nanotechnology*, 2013, **24**, 424002.
- 54 M.-L. Lee, C.-Y. Su, Y.-H. Lin, S.-C. Liao, J.-M. Chen, T.-P. Perng, J.-W. Yeh and H. C. Shih, *J. Power Sources*, 2013, **244**, 410–416.
- 55 M. Xie, X. Sun, C. Zhou, A. S. Cavanagh, H. Sun, T. Hu, G. Wang, J. Lian and S. M. George, *J. Electrochem. Soc.*, 2015, **162**, A974–A981.
- 56 H. Wang, G. Jia, Y. Guo, Y. Zhang, H. Geng, J. Xu, W. Mai, Q. Yan and H. J. Fan, *Adv. Mater. Interfaces*, 2016, **3**, 1600375.
- 57 J. Liu, P. Zhou, T. Han, J. Huang, J. Liu, J. Li and P. V. Braun, *Mater. Lett.*, 2018, **219**, 12–15.
- 58 S. K. Panda and H. Shin, *Mater. Res. Innovations*, 2015, **19**, S5-694.
- 59 M. Li, X. Li, W. Li, X. Meng, Y. Yu and X. Sun, *Electrochem. Commun.*, 2015, **57**, 43–47.
- 60 K. J. Hong and S. O. Kim, *Energy Storage Mater.*, 2016, **2**, 27–34.
- 61 S. Lu, H. Wang, J. Zhou, X. Wu and W. Qin, *Nanoscale*, 2017, **9**, 1184–1192.
- 62 X. Sun, C. Zhou, M. Xie, H. Sun, T. Hu, F. Lu, S. M. Scott, S. M. George and J. Lian, *J. Mater. Chem. A*, 2014, **2**, 7319–7326.
- 63 M. Yu, A. Wang, Y. Wang, C. Li and G. Shi, *Nanoscale*, 2014, **6**, 11419–11424.
- 64 X. Sun, C. Zhou, M. Xie, T. Hu, H. Sun, G. Xin, G. Wang, S. M. George and J. Lian, *Chem. Commun.*, 2014, **50**, 10703–10706.
- 65 Keith E. Gregorczyk, A. C. Kozen, X. Chen, M. A. Schroede, M. Noked, A. Cao, L. Hu and G. W. Rubloff, *ACS Nano*, 2015, **9**, 464–473.
- 66 S. Fleischmann, M. Zeiger, A. Quade, A. Kruth and V. Presser, *ACS Appl. Mater. Interfaces*, 2018, **10**, 18675–18684.
- 67 D. K. Nandi, U. K. Sen, D. Choudhury, S. Mitra and S. K. Sarkar, *Electrochim. Acta*, 2014, **146**, 706–713.
- 68 D. K. Nandi, U. K. Sen, D. Choudhury, S. Mitra and S. K. Sarkar, *ACS Appl. Mater. Interfaces*, 2014, **6**, 6606–6615.
- 69 D. K. Nandi, U. K. Sen, S. Sinha, A. Dhara, S. Mitra and S. K. Sarkar, *Phys. Chem. Chem. Phys.*, 2015, **17**, 17445–17453.
- 70 D. K. Nandi, U. K. Sen, A. Dhara, S. Mitra and S. K. Sarkar, *RSC Adv.*, 2016, **6**, 38024–38032.
- 71 T. Dobbelaere, F. Mattelaer, P. M. Vereecken and C. Detavernier, *J. Vac. Sci. Technol., A*, 2017, **35**, 041513.
- 72 X. Meng, Y. Cao, J. A. Libera and J. W. Elam, *Chem. Mater.*, 2017, **29**, 9043–9052.
- 73 X. Meng, K. He, D. Su, X. Zhang, C. Sun, Y. Ren, H.-H. Wang, W. Weng, L. Trahey, C. P. Canlas and J. W. Elam, *Adv. Funct. Mater.*, 2014, **24**, 5435–5442.
- 74 M. Chen, X. Liu, M. Qi, J. Xiang, J. Yin, Q. Chen and X. Xia, *Mater. Technol.*, 2017, **32**, 888–892.
- 75 Y. Liang, Z. Tao and J. Chen, *Adv. Energy Mater.*, 2012, **2**, 742–769.
- 76 Y. Liang, Y. Jing, S. Gheyhani, K. Y. Lee, P. Liu, A. Facchetti and Y. Yao, *Nat. Mater.*, 2017, **16**, 841–848.
- 77 Y. Liang and Y. Yao, *Joule*, 2018, **2**, 1690–1706.
- 78 Y. Lu, Q. Zhang, L. Li, Z. Niu and J. Chen, *Chem*, 2018, **4**, 2786–2813.
- 79 M. Nisula and M. Karppinen, *Nano Lett.*, 2016, **16**, 1276–1281.
- 80 M. Nisula and M. Karppinen, *J. Mater. Chem. A*, 2018, **6**, 7027–7033.
- 81 Y. Fang, X.-Y. Yu and X. W. Lou, *Matter*, 2019, **1**, 90–114.
- 82 W. T. Jing, Y. Zhang, Y. Gu, Y. F. Zhu, C. C. Yang and Q. Jiang, *Matter*, 2019, **1**, 720–733.
- 83 Y. Zhao, X. Li, B. Yan, D. Xiong, D. Li, S. Lawes and X. Sun, *Adv. Energy Mater.*, 2016, **6**, 1502175.
- 84 Y. Lu, L. Yu and X. W. Lou, *Chem*, 2018, **4**, 972–996.
- 85 C. G. Carvajal, S. Rout, R. Mundle and A. K. Pradhan, *Langmuir*, 2017, **33**, 11–18.
- 86 X. Wang, L. Fan, D. Gong, J. Zhu, Q. Zhang and B. Lu, *Adv. Funct. Mater.*, 2016, **26**, 1104–1111.
- 87 J. H. Jeun, K. Y. Park, D. H. Kim, W. S. Kim, H. C. Kim, B. S. Lee, H. Kim, W. R. Yu, K. Kang and S. H. Hong, *Nanoscale*, 2013, **5**, 8480–8483.

- 88 J. Luo, X. Xia, Y. Luo, C. Guan, J. Liu, X. Qi, C. F. Ng, T. Yu, H. Zhang and H. J. Fan, *Adv. Energy Mater.*, 2013, **3**, 737–743.
- 89 X. Xia, Z. Zeng, X. Li, Y. Zhang, J. Tu, N. C. Fan, H. Zhang and H. J. Fan, *Nanoscale*, 2013, **5**, 6040–6047.
- 90 C. Zhu, X. Xia, J. Liu, Z. Fan, D. Chao, H. Zhang and H. J. Fan, *Nano Energy*, 2014, **4**, 105–112.
- 91 M. Kim, J. Lee, S. Lee, S. Seo, C. Bae and H. Shin, *ChemSusChem*, 2015, **8**, 2363–2371.
- 92 H. Zhang, W. Ren and C. Cheng, *Nanotechnology*, 2015, **26**, 274002.
- 93 J.-H. Jean, H. Kwak, W.-S. Kim, H.-C. Kim, K.-Y. Park, H. Kim, H.-S. Yang, W.-R. Yu, K. Kang and S.-H. Hong, *J. Solid State Electrochem.*, 2017, **21**, 2365–2371.
- 94 B. Yan, X. Li, Z. Bai, Y. Zhao, L. Dong, X. Song, D. Li, C. Langford and X. Sun, *Nano Energy*, 2016, **24**, 32–44.
- 95 E. Østreg, K. B. Gandrud, Y. Hu, O. Nilsen and H. Fjellvåg, *J. Mater. Chem. A*, 2014, **2**, 15044–15051.
- 96 H. Jung, K. Gerasopoulos, A. A. Talin and R. Ghodssi, *J. Power Sources*, 2017, **340**, 89–97.
- 97 F. Mattelaer, K. Geryl, G. Rampelberg, J. Dendooven and C. Detavernier, *ACS Appl. Mater. Interfaces*, 2017, **9**, 13121–13131.
- 98 S. Fleischmann, D. Leistenschneider, V. Lemkova, B. Krüner, M. Zeiger, L. Borchardt and V. Presser, *Chem. Mater.*, 2017, **29**, 8653–8662.
- 99 X. Chen, E. Pomerantseva, P. Banerjee, K. Gregorczyk, R. Ghodssi and G. Rubloff, *Chem. Mater.*, 2012, **24**, 1255–1261.
- 100 X. Chen, E. Pomerantseva, K. Gregorczyk, R. Ghodssi and G. Rubloff, *RSC Adv.*, 2013, **3**, 4294.
- 101 F. Mattelaer, K. Geryl, G. Rampelberg, T. Dobbelaere, J. Dendooven and C. Detavernier, *RSC Adv.*, 2016, **6**, 114658.
- 102 M. E. Donders, W. M. Arnoldbik, H. C. M. Knoop, W. M. M. Kessels and P. H. L. Notten, *J. Electrochem. Soc.*, 2013, **160**, A3066–A3071.
- 103 V. Miikkulainen, A. Ruud, E. Østreg, O. Nilsen, M. Laitinen, T. Sajavaara and H. Fjellvåg, *J. Phys. Chem. C*, 2013, **118**, 1258–1268.
- 104 F. Mattelaer, P. M. Vereecken, J. Dendooven and C. Detavernier, *Chem. Mater.*, 2015, **27**, 3628–3635.
- 105 M. J. Young, H.-D. Schnabel, A. M. Holder, S. M. George and C. B. Musgrave, *Adv. Funct. Mater.*, 2016, **26**, 7895–7907.
- 106 H.-E. Nieminen, V. Miikkulainen, D. Settapani, L. Simonelli, P. Hönicke, C. Zech, Y. Kayser, B. Beckhoff, A.-P. Honkanen, M. J. Heikkilä, K. Mizohata, K. Meinander, O. M. E. Ylivaara, S. Huotari and M. Ritala, *J. Phys. Chem. C*, 2019, **123**, 15802–15814.
- 107 J. Wang and X. Sun, *Energy Environ. Sci.*, 2012, **5**, 5163–5185.
- 108 J. Wang and X. Sun, *Energy Environ. Sci.*, 2015, **8**, 1110–1138.
- 109 Y. Liu, J. Liu, J. Wang, M. N. Banis, B. Xiao, A. Lushington, W. Xiao, R. Li, T. K. Sham, G. Liang and X. Sun, *Nat. Commun.*, 2018, **9**, 929.
- 110 K. B. Gandrud, A. Pettersen, O. Nilsen and H. Fjellvåg, *J. Mater. Chem. A*, 2013, **1**, 9054–9059.
- 111 J. Liu, B. Xiao, M. N. Banis, R. Li, T.-K. Sham and X. Sun, *Electrochim. Acta*, 2015, **162**, 275–281.
- 112 J. Liu, B. Wang, Q. Sun, R. Li, T.-K. Sham and X. Sun, *Adv. Mater. Interfaces*, 2016, **3**, 1600468.
- 113 T. Dobbelaere, F. Mattelaer, J. Dendooven, P. Vereecken and C. Detavernier, *Chem. Mater.*, 2016, **28**, 3435–3445.
- 114 T. Dobbelaere, F. Mattelaer, A. K. Roy, P. Vereecken and C. Detavernier, *J. Mater. Chem. A*, 2017, **5**, 330–338.
- 115 J. W. Choi and D. Aurbach, *Nat. Rev. Mater.*, 2016, **1**, 16013.
- 116 L. Wang, B. Chen, J. Ma, G. Cui and L. Chen, *Chem. Soc. Rev.*, 2018, **47**, 6505–6602.
- 117 B. Xiao and X. Sun, *Adv. Energy Mater.*, 2018, **8**, 1802057.
- 118 C. Zhan, T. Wu, J. Lu and K. Amine, *Energy Environ. Sci.*, 2018, **11**, 243–257.
- 119 Y. Ding, Z. P. Cano, A. Yu, J. Lu and Z. Chen, *Electrochem. Energy Rev.*, 2019, **2**, 1–28.
- 120 I. Takahashi, H. Kiuchi, A. Ohma, T. Fukunaga and E. Matsubara, *J. Phys. Chem. C*, 2020, **124**, 9243–9248.
- 121 T. Li, X.-Z. Yuan, L. Zhang, D. Song, K. Shi and C. Bock, *Electrochem. Energy Rev.*, 2020, **3**, 43–80.
- 122 J. Liu and X. Sun, *Nanotechnology*, 2015, **26**, 024001.
- 123 X. Meng, *Nanotechnology*, 2015, **26**, 020501.
- 124 Y. S. Jung, A. S. Cavanagh, A. C. Dillon, M. D. Groner, S. M. George and S.-H. Lee, *J. Electrochem. Soc.*, 2010, **157**, A75.
- 125 L. Chen, R. E. Warburton, K.-S. Chen, J. A. Libera, C. Johnson, Z. Yang, M. C. Hersam, J. P. Greeley and J. W. Elam, *Chem*, 2018, **4**, 2418–2435.
- 126 J.-T. Lee, F.-M. Wang, C.-S. Cheng, C.-C. Li and C.-H. Lin, *Electrochim. Acta*, 2010, **55**, 4002–4006.
- 127 D. Guan, J. A. Jeevarajan and Y. Wang, *Nanoscale*, 2011, **3**, 1465–1469.
- 128 L. A. Riley, S. Van Atta, A. S. Cavanagh, Y. Yan, S. M. George, P. Liu, A. C. Dillon and S.-H. Lee, *J. Power Sources*, 2011, **196**, 3317–3324.
- 129 I. D. Scott, Y. S. Jung, A. S. Cavanagh, Y. Yan, A. C. Dillon, S. M. George and S. H. Lee, *Nano Lett.*, 2011, **11**, 414–418.
- 130 Y. Seok Jung, A. S. Cavanagh, Y. Yan, S. M. George and A. Manthiram, *J. Electrochem. Soc.*, 2011, **158**, A1298.
- 131 H.-M. Cheng, F.-M. Wang, J. P. Chu, R. Santhanam, J. Rick and S.-C. Lo, *J. Phys. Chem. C*, 2012, **116**, 7629–7637.
- 132 D. Guan and Y. Wang, *Ionics*, 2012, **19**, 1–8.
- 133 D. Liu, Y. Liu, S. L. Candelaria, G. Cao, J. Liu and Y.-H. Jeong, *J. Vac. Sci. Technol., A*, 2012, **30**, 01A123.
- 134 M. Bettge, Y. Li, B. Sankaran, N. D. Rago, T. Spila, R. T. Haasch, I. Petrov and D. P. Abraham, *J. Power Sources*, 2013, **233**, 346–357.
- 135 M. Choi, G. Ham, B.-S. Jin, S.-M. Lee, Y. M. Lee, G. Wang and H.-S. Kim, *J. Alloys Compd.*, 2014, **608**, 110–117.
- 136 X. Fang, M. Ge, J. Rong, Y. Che, N. Aroonyadet, X. Wang, Y. Liu, A. Zhang and C. Zhou, *Energy Technol.*, 2014, **2**, 159–165.

- 137 J. W. Kim, J. J. Travis, E. Hu, K.-W. Nam, S. C. Kim, C. S. Kang, J.-H. Woo, X.-Q. Yang, S. M. George, K. H. Oh, S.-J. Cho and S.-H. Lee, *J. Power Sources*, 2014, **254**, 190–197.
- 138 X. Dai, A. Zhou, J. Xu, B. Yang, L. Wang and J. Li, *J. Power Sources*, 2015, **298**, 114–122.
- 139 C. A. Kim, H. J. Choi, J. H. Lee, S. Y. Yoo, J. W. Kim, J. H. Shim and B. Kang, *Electrochim. Acta*, 2015, **184**, 134–142.
- 140 J. W. Kim, D. H. Kim, D. Y. Oh, H. Lee, J. H. Kim, J. H. Lee and Y. S. Jung, *J. Power Sources*, 2015, **274**, 1254–1262.
- 141 Y. Su, S. Cui, Z. Zhuo, W. Yang, X. Wang and F. Pan, *ACS Appl. Mater. Interfaces*, 2015, **7**, 25105–25112.
- 142 Y. Shi, M. Zhang, D. Qian and Y. S. Meng, *Electrochim. Acta*, 2016, **203**, 154–161.
- 143 G. H. Waller, P. D. Brooke, B. H. Rainwater, S. Y. Lai, R. Hu, Y. Ding, F. M. Alamgir, K. H. Sandhage and M. L. Liu, *J. Power Sources*, 2016, **306**, 162–170.
- 144 M. Xie, T. Hu, L. Yang and Y. Zhou, *RSC Adv.*, 2016, **6**, 63250–63255.
- 145 D. H. K. Jackson and T. F. Kuech, *J. Power Sources*, 2017, **365**, 61–67.
- 146 N. Dannehl, S. O. Steinmuller, D. V. Szabo, M. Pein, F. Sigel, L. Esmezjan, U. Hasenkox, B. Schwarz, S. Indris and H. Ehrenberg, *ACS Appl. Mater. Interfaces*, 2018, **10**, 43131–43143.
- 147 S. Neudeck, A. Mazilkin, C. Reitz, P. Hartmann, J. Janek and T. Brezesinski, *Sci. Rep.*, 2019, **9**, 5328.
- 148 H. V. Ramasamy, S. Sinha, J. Park, M. Gong, V. Aravindan, J. Heo and Y.-S. Lee, *J. Electrochem. Sci. Technol.*, 2019, **10**, 196–205.
- 149 H. Yu, Y. Gao and X. Liang, *J. Electrochem. Soc.*, 2019, **166**, A2021–A2027.
- 150 W. Zhu, X. Huang, T. Liu, Z. Xie, Y. Wang, K. Tian, L. Bu, H. Wang, L. Gao and J. Zhao, *Coatings*, 2019, **9**, 92.
- 151 J. Song, X. Han, K. J. Gaskell, K. Xu, S. B. Lee and L. Hu, *J. Nanopart. Res.*, 2014, **16**, 2745.
- 152 S. Fang, D. Jackson, M. L. Dreibelbis, T. F. Kuech and R. J. Hamers, *J. Power Sources*, 2018, **373**, 184–192.
- 153 T. Teranishi, Y. Yoshikawa, M. Yoneda, A. Kishimoto, J. Halpin, S. O'Brien, M. Modreanu and I. M. Povey, *ACS Appl. Energy Mater.*, 2018, **1**, 3277–3282.
- 154 J. R. Croy, D. C. O'Hanlon, S. Sharifi-Asl, M. Murphy, A. Mane, C.-W. Lee, S. E. Trask, R. Shahbazian-Yassar and M. Balasubramanian, *Chem. Mater.*, 2019, **31**, 3891–3899.
- 155 B. Huang, R. Wang, Y. Gong, B. He and H. Wang, *Front. Chem.*, 2019, **7**, 107.
- 156 K. Leung, Y. Qi, K. R. Zavadil, Y. S. Jung, A. C. Dillon, A. S. Cavanagh, S. H. Lee and S. M. George, *J. Am. Chem. Soc.*, 2011, **133**, 14741–14754.
- 157 A. M. Wise, C. Ban, J. N. Weker, S. Misra, A. S. Cavanagh, Z. Wu, Z. Li, M. S. Whittingham, K. Xu, S. M. George and M. F. Toney, *Chem. Mater.*, 2015, **27**, 6146–6154.
- 158 P. Yan, J. Zheng, X. Zhang, R. Xu, K. Amine, J. Xiao, J.-G. Zhang and C.-M. Wang, *Chem. Mater.*, 2016, **28**, 857–863.
- 159 D. S. Hall, R. Gauthier, A. Eldesoky, V. S. Murray and J. R. Dahn, *ACS Appl. Mater. Interfaces*, 2019, **11**, 14095–14100.
- 160 J. Zhao, G. Qu, J. C. Flake and Y. Wang, *Chem. Commun.*, 2012, **48**, 8108–8110.
- 161 J. Zhao and Y. Wang, *J. Phys. Chem. C*, 2012, **116**, 11867–11876.
- 162 X. Zhang, I. Belharouak, L. Li, Y. Lei, J. W. Elam, A. Nie, X. Chen, R. S. Yassar and R. L. Axelbaum, *Adv. Energy Mater.*, 2013, **3**, 1299–1307.
- 163 J. Zhao and Y. Wang, *Nano Energy*, 2013, **2**, 882–889.
- 164 J.-Z. Kong, C. Ren, G.-A. Tai, X. Zhang, A.-D. Li, D. Wu, H. Li and F. Zhou, *J. Power Sources*, 2014, **266**, 433–439.
- 165 H. M. Cho, M. V. Chen, A. C. MacRae and Y. S. Meng, *ACS Appl. Mater. Interfaces*, 2015, **7**, 16231–16239.
- 166 J.-Z. Kong, S.-S. Wang, G.-A. Tai, L. Zhu, L.-G. Wang, H.-F. Zhai, D. Wu, A.-D. Li and H. Li, *J. Alloys Compd.*, 2016, **657**, 593–600.
- 167 M. R. Laskar, D. H. Jackson, Y. Guan, S. Xu, S. Fang, M. Dreibelbis, M. K. Mahanthappa, D. Morgan, R. J. Hamers and T. F. Kuech, *ACS Appl. Mater. Interfaces*, 2016, **8**, 10572–10580.
- 168 D. Mohanty, K. Dahlberg, D. M. King, L. A. David, A. S. Sefat, D. L. Wood, C. Daniel, S. Dhar, V. Mahajan, M. Lee and F. Albano, *Sci. Rep.*, 2016, **6**, 26532.
- 169 R. L. Patel, J. Park and X. Liang, *RSC Adv.*, 2016, **6**, 98768–98776.
- 170 C. Qin, J. Cao, J. Chen, G. Dai, T. Wu, Y. Chen, Y. Tang, A. Li and Y. Chen, *Dalton Trans.*, 2016, **45**, 9669–9675.
- 171 K. Sharma, D. Routkevitch, N. Varaksa and S. M. George, *J. Vac. Sci. Technol., A*, 2016, **34**, 01A146.
- 172 M. Xie, X. Sun, H. Sun, T. Porcelli, S. M. George, Y. Zhou and J. Lian, *J. Mater. Chem. A*, 2016, **4**, 537–544.
- 173 J.-Z. Kong, H.-F. Zhai, X. Qian, M. Wang, Q.-Z. Wang, A.-D. Li, H. Li and F. Zhou, *J. Alloys Compd.*, 2017, **694**, 848–856.
- 174 M. R. Laskar, D. H. Jackson, S. Xu, R. J. Hamers, D. Morgan and T. F. Kuech, *ACS Appl. Mater. Interfaces*, 2017, **9**, 11231–11239.
- 175 F. Mattelaer, P. M. Vereecken, J. Dendooven and C. Detavernier, *Adv. Mater. Interfaces*, 2017, **4**, 1601237.
- 176 S. Sarkar, R. L. Patel, X. Liang and J. Park, *ACS Appl. Mater. Interfaces*, 2017, **9**, 30599–30607.
- 177 Y. Gao, R. L. Patel, K. Y. Shen, X. Wang, R. L. Axelbaum and X. Liang, *ACS Omega*, 2018, **3**, 906–916.
- 178 C.-C. Wang, J.-W. Lin, Y.-H. Yu, K.-H. Lai, K.-F. Chiu and C.-C. Kei, *ACS Sustainable Chem. Eng.*, 2018, **6**, 16941–16950.
- 179 C. Zhang, J. Su, T. Wang, K. Yuan, C. Chen, S. Liu, T. Huang, J. Wu, H. Lu and A. Yu, *ACS Sustainable Chem. Eng.*, 2018, **6**, 7890–7901.
- 180 J. Ahn, E. K. Jang, S. Yoon, S.-J. Lee, S.-J. Sung, D.-H. Kim and K. Y. Cho, *Appl. Surf. Sci.*, 2019, **484**, 701–709.
- 181 H. Gao, J. Cai, G.-L. Xu, L. Li, Y. Ren, X. Meng, K. Amine and Z. Chen, *Chem. Mater.*, 2019, **31**, 2723–2730.
- 182 Y. Gao, Z. Shang, X. He, T. White, J. Park and X. Liang, *Electrochim. Acta*, 2019, **318**, 513–524.
- 183 J. Zhao and Y. Wang, *J. Solid State Electrochem.*, 2012, **17**, 1049–1058.
- 184 X. Li, J. Liu, X. Meng, Y. Tang, M. N. Banis, J. Yang, Y. Hu, R. Li, M. Cai and X. Sun, *J. Power Sources*, 2014, **247**, 57–69.

- 185 B. Xiao, J. Liu, Q. Sun, B. Wang, M. N. Banis, D. Zhao, Z. Wang, R. Li, X. Cui, T. K. Sham and X. Sun, *Adv. Sci.*, 2015, **2**, 1500022.
- 186 S. Deng, B. Xiao, B. Wang, X. Li, K. Kaliyappan, Y. Zhao, A. Lushington, R. Li, T.-K. Sham, H. Wang and X. Sun, *Nano Energy*, 2017, **38**, 19–27.
- 187 B. Xiao, B. Wang, J. Liu, K. Kaliyappan, Q. Sun, Y. Liu, G. Dadheech, M. P. Balogh, L. Yang, T.-K. Sham, R. Li, M. Cai and X. Sun, *Nano Energy*, 2017, **34**, 120–130.
- 188 X. Li, J. Liu, M. N. Banis, A. Lushington, R. Li, M. Cai and X. Sun, *Energy Environ. Sci.*, 2014, **7**, 768–778.
- 189 O. Srur-Lavi, V. Miikkulainen, B. Markovsky, J. Grinblat, M. Talianker, Y. Fleger, G. Cohen-Taguri, A. Mor, Y. Tal-Yosef and D. Aurbach, *J. Electrochem. Soc.*, 2017, **164**, A3266–A3275.
- 190 J. Xie, J. Zhao, Y. Liu, H. Wang, C. Liu, T. Wu, P.-C. Hsu, D. Lin, Y. Jin and Y. Cui, *Nano Res.*, 2017, **10**, 3754–3764.
- 191 J. S. Park, X. Meng, J. W. Elam, S. Hao, C. Wolverton, C. Kim and J. Cabana, *Chem. Mater.*, 2014, **26**, 3128–3134.
- 192 W. D. Richards, L. J. Miara, Y. Wang, J. C. Kim and G. Ceder, *Chem. Mater.*, 2015, **28**, 266–273.
- 193 Y. Zhu, X. He and Y. Mo, *ACS Appl. Mater. Interfaces*, 2015, **7**, 23685–23693.
- 194 A. Kraysberg, H. Drezner, M. Auinat, A. Shapira, N. Solomatin, P. Axmann, M. Wohlfahrt-Mehrens and Y. Ein-Eli, *ChemNanoMat*, 2015, **1**, 577–585.
- 195 J. S. Park, A. U. Mane, J. W. Elam and J. R. Croy, *Chem. Mater.*, 2015, **27**, 1917–1920.
- 196 D. H. K. Jackson, M. R. Laskar, S. Fang, S. Xu, R. G. Ellis, X. Li, M. Dreibelbis, S. E. Babcock, M. K. Mahanthappa, D. Morgan, R. J. Hamers and T. F. Kuech, *J. Vac. Sci. Technol., A*, 2016, **34**, 031503.
- 197 J. S. Park, A. U. Mane, J. W. Elam and J. R. Croy, *ACS Omega*, 2017, **2**, 3724–3729.
- 198 Y. Zhou, Y. Lee, H. Sun, J. M. Wallas, S. M. George and M. Xie, *ACS Appl. Mater. Interfaces*, 2017, **9**, 9614–9619.
- 199 A. Shapira, O. Tiurin, N. Solomatin, M. Auinat, A. Meitav and Y. Ein-Eli, *ACS Appl. Energy Mater.*, 2018, **1**, 6809–6823.
- 200 J. Xie, A. D. Sendek, E. D. Cubuk, X. Zhang, Z. Lu, Y. Gong, T. Wu, F. Shi, W. Liu, E. J. Reed and Y. Cui, *ACS Nano*, 2017, **11**, 7019–7027.
- 201 E. Kazyak, K.-H. Chen, K. N. Wood, A. L. Davis, T. Thompson, A. R. Bielinski, A. J. Sanchez, X. Wang, C. Wang, J. Sakamoto and N. P. Dasgupta, *Chem. Mater.*, 2017, **29**, 3785–3792.
- 202 B. Xiao, H. Liu, J. Liu, Q. Sun, B. Wang, K. Kaliyappan, Y. Zhao, M. N. Banis, Y. Liu, R. Li, T. K. Sham, G. A. Botton, M. Cai and X. Sun, *Adv. Mater.*, 2017, **29**, 1703764.
- 203 H.-H. Ryu, K.-J. Park, C. S. Yoon and Y.-K. Sun, *Chem. Mater.*, 2018, **30**, 1155–1163.
- 204 P. Yan, J. Zheng, J. Liu, B. Wang, X. Cheng, Y. Zhang, X. Sun, C. Wang and J.-G. Zhang, *Nat. Energy*, 2018, **3**, 600–605.
- 205 X. Cheng, J. Zheng, J. Lu, Y. Li, P. Yan and Y. Zhang, *Nano Energy*, 2019, **62**, 30–37.
- 206 J.-Z. Kong, Y. Chen, Y.-Q. Cao, Q.-Z. Wang, A.-D. Li, H. Li and F. Zhou, *J. Alloys Compd.*, 2019, **799**, 89–98.
- 207 M. Amirmaleki, C. Cao, B. Wang, Y. Zhao, T. Cui, J. Tam, X. Sun, Y. Sun and T. Filleter, *Nanoscale*, 2019, **11**, 18730–18738.
- 208 Y. S. Jung, A. S. Cavanagh, L. A. Riley, S. H. Kang, A. C. Dillon, M. D. Groner, S. M. George and S. H. Lee, *Adv. Mater.*, 2010, **22**, 2172–2176.
- 209 Y. S. Jung, P. Lu, A. S. Cavanagh, C. Ban, G.-H. Kim, S.-H. Lee, S. M. George, S. J. Harris and A. C. Dillon, *Adv. Energy Mater.*, 2013, **3**, 213–219.
- 210 I. Lahiri, S.-M. Oh, J. Y. Hwang, C. Kang, M. Choi, H. Jeon, R. Banerjee, Y.-K. Sun and W. Choi, *J. Mater. Chem.*, 2011, **21**, 13621.
- 211 A. J. Loebl, C. J. Oldham, C. K. Devine, B. Gong, S. E. Atanasov, G. N. Parsons and P. S. Fedkiw, *J. Electrochem. Soc.*, 2013, **160**, A1971–A1978.
- 212 H.-Y. Wang and F.-M. Wang, *J. Power Sources*, 2013, **233**, 1–5.
- 213 Y. Zhao, Y. Huang, Q. Wang, K. Wang, M. Zong, L. Wang, W. Zhang and X. Sun, *RSC Adv.*, 2013, **3**, 14480.
- 214 Y. Zhao, Y. Huang, X. Sun, H. Huang, K. Wang, M. Zong and Q. Wang, *Electrochim. Acta*, 2014, **120**, 128–132.
- 215 Y. Zhao, Z. Song, X. Li, Q. Sun, N. Cheng, S. Lawes and X. Sun, *Energy Storage Mater.*, 2016, **2**, 35–62.
- 216 Y. Zhao, X. Li, B. Yan, D. Li, S. Lawes and X. Sun, *J. Power Sources*, 2015, **274**, 869–884.
- 217 D. Wang, J. Yang, J. Liu, X. Li, R. Li, M. Cai, T.-K. Sham and X. Sun, *J. Mater. Chem. A*, 2014, **2**, 2306.
- 218 N. Yesibolati, M. Shahid, W. Chen, M. N. Hedhili, M. C. Reuter, F. M. Ross and H. N. Alshareef, *Small*, 2014, **10**, 2849–2858.
- 219 D. Guan and C. Yuan, *J. Electrochem. Energy Convers. Storage*, 2016, **13**, 021004.
- 220 M. Mao, F. Yan, C. Cui, J. Ma, M. Zhang, T. Wang and C. Wang, *Nano Lett.*, 2017, **17**, 3830–3836.
- 221 B. Joshi, E. Samuel, M.-W. Kim, S. Park, M. T. Swihart, W. Y. Yoon and S. S. Yoon, *Chem. Eng. J.*, 2018, **338**, 72–81.
- 222 H. Zhang, Z. Chen, R. Hu, J. Liu, J. Cui, W. Zhou and C. Yang, *J. Mater. Chem. A*, 2018, **6**, 4374–4385.
- 223 C. Guan, X. Wang, Q. Zhang, Z. Fan, H. Zhang and H. J. Fan, *Nano Lett.*, 2014, **14**, 4852–4858.
- 224 M. Q. Snyder, S. A. Trebukhova, B. Ravdel, M. C. Wheeler, J. DiCarlo, C. P. Tripp and W. J. DeSisto, *J. Power Sources*, 2007, **165**, 379–385.
- 225 J.-H. Lee, M.-H. Hon, Y.-W. Chung and I.-C. Leu, *Appl. Phys. A: Mater. Sci. Process.*, 2010, **102**, 545–550.
- 226 J. Liu, X. Li, M. Cai, R. Li and X. Sun, *Electrochim. Acta*, 2013, **93**, 195–201.
- 227 T. Hu, M. Xie, J. Zhong, H.-T. Sun, X. Sun, S. Scott, S. M. George, C.-S. Liu and J. Lian, *Carbon*, 2014, **76**, 141–147.
- 228 A. L. Lipson, K. Puntambekar, D. J. Comstock, X. Meng, M. L. Geier, J. W. Elam and M. C. Hersam, *Chem. Mater.*, 2014, **26**, 935–940.
- 229 B. Ahmed, M. Shahid, D. H. Nagaraju, D. H. Anjum, M. N. Hedhili and H. N. Alshareef, *ACS Appl. Mater. Interfaces*, 2015, **7**, 13154–13163.

- 230 C. Guan, Y. Wang, M. Zacharias, J. Wang and H. J. Fan, *Nanotechnology*, 2015, **26**, 014001.
- 231 M. H. Jung, *J. Colloid Interface Sci.*, 2017, **505**, 631–641.
- 232 W. Shi, H. Zhao and B. Lu, *Nanotechnology*, 2017, **28**, 165403.
- 233 X. Cheng, Y. Li, L. Sang, J. Ma, H. Shi, X. Liu, J. Lu and Y. Zhang, *Electrochim. Acta*, 2018, **269**, 241–249.
- 234 W. U. Rehman, Y. Xu, X. Du, X. Sun, I. Ullah, Y. Zhang, Y. Jin, B. Zhang and X. Li, *Appl. Surf. Sci.*, 2018, **445**, 359–367.
- 235 S. Xie, D. Cao, Y. She, H. Wang, J. W. Shi, M. K. H. Leung and C. Niu, *Chem. Commun.*, 2018, **54**, 7782–7785.
- 236 J. K. Yoon, S. Nam, H. C. Shim, K. Park, T. Yoon, H. S. Park and S. Hyun, *Materials*, 2018, **11**, 803.
- 237 Y. Jin, H. Yu, Y. Gao, X. He, T. A. White and X. Liang, *J. Power Sources*, 2019, **436**, 226859.
- 238 Y. Li, T. Liang, R. Wang, B. He, Y. Gong and H. Wang, *ACS Appl. Mater. Interfaces*, 2019, **11**, 19115–19122.
- 239 K. Feng, M. Li, W. Liu, A. G. Kashkooli, X. Xiao, M. Cai and Z. Chen, *Small*, 2018, **14**, 1702737.
- 240 Y. Gao, R. Yi, Y. C. Li, J. Song, S. Chen, Q. Huang, T. E. Mallouk and D. Wang, *J. Am. Chem. Soc.*, 2017, **139**, 17359–17367.
- 241 Y. Li, K. Yan, H.-W. Lee, Z. Lu, N. Liu and Y. Cui, *Nat. Energy*, 2016, **1**, 15029.
- 242 J. Lu, Z. Chen, F. Pan, Y. Cui and K. Amine, *Electrochem. Energy Rev.*, 2018, **1**, 35–53.
- 243 H. Wu and Y. Cui, *Nano Today*, 2012, **7**, 414–429.
- 244 F. Dou, L. Shi, G. Chen and D. Zhang, *Electrochem. Energy Rev.*, 2019, **2**, 149–198.
- 245 Y. He, X. Yu, Y. Wang, H. Li and X. Huang, *Adv. Mater.*, 2011, **23**, 4938–4941.
- 246 C. R. Becker, S. M. Prokes and C. T. Love, *ACS Appl. Mater. Interfaces*, 2016, **8**, 530–537.
- 247 S.-Y. Kim and Y. Qi, *J. Electrochem. Soc.*, 2014, **161**, F3137–F3143.
- 248 S. Hy, Y. H. Chen, H. M. Cheng, C. J. Pan, J. H. Cheng, J. Rick and B. J. Hwang, *ACS Appl. Mater. Interfaces*, 2015, **7**, 13801–13807.
- 249 A. Kohandehghan, P. Kalisvaart, K. Cui, M. Kupsta, E. Memarzadeh and D. Mitlin, *J. Mater. Chem. A*, 2013, **1**, 12850.
- 250 J. Li, X. Xiao, Y.-T. Cheng and M. W. Verbrugge, *J. Phys. Chem. Lett.*, 2013, **4**, 3387–3391.
- 251 E. Memarzadeh Lotfabad, P. Kalisvaart, K. Cui, A. Kohandehghan, M. Kupsta, B. Olsen and D. Mitlin, *Phys. Chem. Chem. Phys.*, 2013, **15**, 13646–13657.
- 252 Y. Li, Y. Sun, G. Xu, Y. Lu, S. Zhang, L. Xue, J. S. Jur and X. Zhang, *J. Mater. Chem. A*, 2014, **2**, 11417–11425.
- 253 B. Zhu, N. Liu, M. McDowell, Y. Jin, Y. Cui and J. Zhu, *Nano Energy*, 2015, **13**, 620–625.
- 254 Y. Bai, D. Yan, C. Yu, L. Cao, C. Wang, J. Zhang, H. Zhu, Y.-S. Hu, S. Dai, J. Lu and W. Zhang, *J. Power Sources*, 2016, **308**, 75–82.
- 255 E. M. Lotfabad, P. Kalisvaart, A. Kohandehghan, K. Cui, M. Kupsta, B. Farbod and D. Mitlin, *J. Mater. Chem. A*, 2014, **2**, 2504–2516.
- 256 S. B. Son, Y. Wang, J. Xu, X. Li, M. Groner, A. Stokes, Y. Yang, Y. T. Cheng and C. Ban, *ACS Appl. Mater. Interfaces*, 2017, **9**, 40143–40150.
- 257 D. M. Piper, J. J. Travis, M. Young, S. B. Son, S. C. Kim, K. H. Oh, S. M. George, C. Ban and S. H. Lee, *Adv. Mater.*, 2014, **26**, 1596–1601.
- 258 Y. He, D. M. Piper, M. Gu, J. J. Travis, S. M. George, S.-H. Lee, A. Genc, L. Pullan, J. Liu, S. X. Mao, J.-G. Zhang, C. Ban and C. Wang, *ACS Nano*, 2014, **8**, 11816–11823.
- 259 L. Luo, H. Yang, P. Yan, J. J. Travis, Y. Lee, N. Liu, D. M. Piper, S. Zhang, C. Ban, S.-H. Lee, P. Zhao, S. M. George, J.-G. Zhang, Y. Cui and C.-M. Wang, *ACS Nano*, 2015, **9**, 5559–5566.
- 260 Y. Ma, J. M. Martinez de la Hoz, I. Angarita, J. M. Berrio-Sanchez, L. Benitez, J. M. Seminario, S. B. Son, S. H. Lee, S. M. George, C. Ban and P. B. Balbuena, *ACS Appl. Mater. Interfaces*, 2015, **7**, 11948–11955.
- 261 D. Molina Piper, Y. Lee, S.-B. Son, T. Evans, F. Lin, D. Nordlund, X. Xiao, S. M. George, S.-H. Lee and C. Ban, *Nano Energy*, 2016, **22**, 202–210.
- 262 J. M. Wallas, B. C. Welch, Y. Wang, J. Liu, S. E. Hafner, R. Qiao, T. Yoon, Y.-T. Cheng, S. M. George and C. Ban, *ACS Appl. Energy Mater.*, 2019, **2**, 4135–4143.
- 263 J. Liu, H. Zhu and M. H. A. Shiraz, *Front. Energy Res.*, 2018, **6**, 10.
- 264 D. M. Stewart, A. J. Pearse, N. S. Kim, E. J. Fuller, A. A. Talin, K. Gregorczyk, S. B. Lee and G. W. Rubloff, *Chem. Mater.*, 2018, **30**, 2526–2534.
- 265 M. Létiche, E. Eustache, J. Freixas, A. Demortière, V. De Andrade, L. Morgenroth, P. Tilmant, F. Vaurette, D. Troadec, P. Roussel, T. Brousse and C. Lethien, *Adv. Energy Mater.*, 2017, **7**, 1601402.
- 266 A. Pearse, T. Schmitt, E. Sahadeo, D. M. Stewart, A. Kozen, K. Gerasopoulos, A. A. Talin, S. B. Lee, G. W. Rubloff and K. E. Gregorczyk, *ACS Nano*, 2018, **12**, 4286–4294.
- 267 J. Lu, Y. J. Lee, X. Luo, K. C. Lau, M. Asadi, H. H. Wang, S. Brombosz, J. Wen, D. Zhai, Z. Chen, D. J. Miller, Y. S. Jeong, J. B. Park, Z. Z. Fang, B. Kumar, A. Salehi-Khojin, Y. K. Sun, L. A. Curtiss and K. Amine, *Nature*, 2016, **529**, 377–382.
- 268 J. Lu, L. Li, J. B. Park, Y. K. Sun, F. Wu and K. Amine, *Chem. Rev.*, 2014, **114**, 5611–5640.
- 269 J. Wang, Y. Li and X. Sun, *Nano Energy*, 2013, **2**, 443–467.
- 270 A. C. Luntz, V. Viswanathan, J. Voss, J. B. Varley, J. K. Nørskov, R. Scheffler and A. Speidel, *J. Phys. Chem. Lett.*, 2013, **4**, 3494–3499.
- 271 J. B. Varley, V. Viswanathan, J. K. Nørskov and A. C. Luntz, *Energy Environ. Sci.*, 2014, **7**, 720–727.
- 272 B. D. McCloskey, A. Speidel, R. Scheffler, D. C. Miller, V. Viswanathan, J. S. Hummelshoj, J. K. Nørskov and A. C. Luntz, *J. Phys. Chem. Lett.*, 2012, **3**, 997–1001.
- 273 J. Lu, Y. Lei, K. C. Lau, X. Luo, P. Du, J. Wen, R. S. Assary, U. Das, D. J. Miller, J. W. Elam, H. M. Albishri, D. A. El-Hady, Y. K. Sun, L. A. Curtiss and K. Amine, *Nat. Commun.*, 2013, **4**, 2383.
- 274 Y. Lei, J. Lu, X. Luo, T. Wu, P. Du, X. Zhang, Y. Ren, J. Wen, D. J. Miller, J. T. Miller, Y. K. Sun, J. W. Elam and K. Amine, *Nano Lett.*, 2013, **13**, 4182–4189.

- 275 X. Luo, M. Piernawieja-Hermida, J. Lu, T. Wu, J. Wen, Y. Ren, D. Miller, Z. Zak Fang, Y. Lei and K. Amine, *Nanotechnology*, 2015, **26**, 164003.
- 276 J. Yang, D. Ma, Y. Li, P. Zhang, H. Mi, L. Deng, L. Sun and X. Ren, *J. Power Sources*, 2017, **360**, 215–220.
- 277 J. Yang, H. Mi, S. Luo, Y. Li, P. Zhang, L. Deng, L. Sun and X. Ren, *J. Power Sources*, 2017, **368**, 88–96.
- 278 Y. Bae, D.-H. Ko, S. Lee, H.-D. Lim, Y.-J. Kim, H.-S. Shim, H. Park, Y. Ko, S. K. Park, H. J. Kwon, H. Kim, H.-T. Kim, Y.-S. Min, D. Im and K. Kang, *Adv. Energy Mater.*, 2018, **8**, 1702661.
- 279 C. Gong, L. Zhao, S. Li, H. Wang, Y. Gong, R. Wang and B. He, *Electrochim. Acta*, 2018, **281**, 338–347.
- 280 J.-W. Jung, D.-W. Choi, C. K. Lee, K. R. Yoon, S. Yu, J. Y. Cheong, C. Kim, S.-H. Cho, J.-S. Park, Y. J. Park and I.-D. Kim, *Nano Energy*, 2018, **46**, 193–202.
- 281 Z. Zhang, K. Tan, Y. Gong, H. Wang, R. Wang, L. Zhao and B. He, *J. Power Sources*, 2019, **437**, 226908.
- 282 J. Lu, L. Cheng, K. C. Lau, E. Tyo, X. Luo, J. Wen, D. Miller, R. S. Assary, H. H. Wang, P. Redfern, H. Wu, J. B. Park, Y. K. Sun, S. Vajda, K. Amine and L. A. Curtiss, *Nat. Commun.*, 2014, **5**, 4895.
- 283 Y. Lei, F. Mehmood, S. Lee, J. Greeley, B. Lee, S. Seifert, R. E. Winans, J. W. Elam, R. J. Meyer, P. C. Redfern, D. Teschner, R. Schlögl, M. J. Pellin, L. A. Curtiss and S. Vajda, *Science*, 2010, **328**, 224.
- 284 G. Kwon, G. A. Ferguson, C. J. Heard, E. C. Tyo, C. Yin, J. DeBartolo, S. N. Seifert, R. E. Winans, J. Kropf, J. Greeley, R. L. Johnston, L. A. Curtiss, M. J. Pellin and S. Vajda, *ACS Nano*, 2013, **7**, 5808–5817.
- 285 S. Lee, L. M. Molina, M. J. Lopez, J. A. Alonso, B. Hammer, B. Lee, S. Seifert, R. E. Winans, J. W. Elam, M. J. Pellin and S. Vajda, *Angew. Chem.*, 2009, **48**, 1467–1471.
- 286 S. Vajda, M. J. Pellin, J. P. Greeley, C. L. Marshall, L. A. Curtiss, G. A. Ballentine, J. W. Elam, S. Catillon-Mucherie, P. C. Redfern, F. Mehmood and P. Zapol, *Nat. Mater.*, 2009, **8**, 213–216.
- 287 H.-S. Shin, G. W. Seo, K. Kwon, K.-N. Jung, S. I. Lee, E. Choi, H. Kim, J.-H. Hwang and J.-W. Lee, *APL Mater.*, 2018, **6**, 047702.
- 288 J. Xie, X. Yao, I. P. Madden, D. E. Jiang, L. Y. Chou, C. K. Tsung and D. Wang, *J. Am. Chem. Soc.*, 2014, **136**, 8903–8906.
- 289 C. Zhao, C. Yu, M. N. Banis, Q. Sun, M. Zhang, X. Li, Y. Liu, Y. Zhao, H. Huang, S. Li, X. Han, B. Xiao, Z. Song, R. Li, J. Qiu and X. Sun, *Nano Energy*, 2017, **34**, 399–407.
- 290 H. Kim, J. T. Lee, D.-C. Lee, A. Magasinski, W.-I. Cho and G. Yushin, *Adv. Energy Mater.*, 2013, **3**, 1308–1315.
- 291 X. Li, A. Lushington, J. Liu, R. Li and X. Sun, *Chem. Commun.*, 2014, **50**, 9757–9760.
- 292 M. Yu, W. Yuan, C. Li, J.-D. Hong and G. Shi, *J. Mater. Chem. A*, 2014, **2**, 7360.
- 293 M. Yu, A. Wang, F. Tian, H. Song, Y. Wang, C. Li, J. D. Hong and G. Shi, *Nanoscale*, 2015, **7**, 5292–5298.
- 294 X. Li, A. Lushington, Q. Sun, W. Xiao, J. Liu, B. Wang, Y. Ye, K. Nie, Y. Hu, Q. Xiao, R. Li, J. Guo, T. K. Sham and X. Sun, *Nano Lett.*, 2016, **16**, 3545–3549.
- 295 R. Carter, L. Oakes, N. Muralidharan, A. P. Cohn, A. Douglas and C. L. Pint, *ACS Appl. Mater. Interfaces*, 2017, **9**, 7185–7192.
- 296 Y. Chen, S. Lu, J. Zhou, X. Wu, W. Qin, O. Ogoke and G. Wu, *J. Mater. Chem. A*, 2017, **5**, 102–112.
- 297 X. Meng, Y. Liu, Y. Cao, Y. Ren, W. Lu and J. W. Elam, *Adv. Mater. Interfaces*, 2017, **4**, 1700096.
- 298 X. Han, Y. Xu, X. Chen, Y.-C. Chen, N. Weadock, J. Wan, H. Zhu, Y. Liu, H. Li, G. Rubloff, C. Wang and L. Hu, *Nano Energy*, 2013, **2**, 1197–1206.
- 299 X. Li, M. Banis, A. Lushington, X. Yang, Q. Sun, Y. Zhao, C. Liu, Q. Li, B. Wang, W. Xiao, C. Wang, M. Li, J. Liang, R. Li, Y. Hu, L. Goncharova, H. Zhang, T. K. Sham and X. Sun, *Nat. Commun.*, 2018, **9**, 4509.
- 300 Z. Gao, H. Sun, L. Fu, F. Ye, Y. Zhang, W. Luo and Y. Huang, *Adv. Mater.*, 2018, **30**, e1705702.
- 301 F. Zheng, M. Kotobuki, S. Song, M. O. Lai and L. Lu, *J. Power Sources*, 2018, **389**, 198–213.
- 302 J. Liang, X. Li, Y. Zhao, L. V. Goncharova, W. Li, K. R. Adair, M. N. Banis, Y. Hu, T. K. Sham, H. Huang, L. Zhang, S. Zhao, S. Lu, R. Li and X. Sun, *Adv. Energy Mater.*, 2019, **9**, 1902125.
- 303 A. Miura, N. C. Rosero-Navarro, A. Sakuda, K. Tadanaga, N. H. H. Phuc, A. Matsuda, N. Machida, A. Hayashi and M. Tatsumisago, *Nat. Rev. Chem.*, 2019, **3**, 189–198.
- 304 J. Liu, M. N. Banis, X. Li, A. Lushington, M. Cai, R. Li, T.-K. Sham and X. Sun, *J. Phys. Chem. C*, 2013, **117**, 20260–20267.
- 305 B. Wang, J. Liu, Q. Sun, R. Li, T. K. Sham and X. Sun, *Nanotechnology*, 2014, **25**, 504007.
- 306 A. C. Kozen, A. J. Pearse, C.-F. Lin, M. Noked and G. W. Rubloff, *Chem. Mater.*, 2015, **27**, 5324–5331.
- 307 M. Nisula, Y. Shindo, H. Koga and M. Karppinen, *Chem. Mater.*, 2015, **27**, 6987–6993.
- 308 B. Wang, J. Liu, M. Norouzi Banis, Q. Sun, Y. Zhao, R. Li, T. K. Sham and X. Sun, *ACS Appl. Mater. Interfaces*, 2017, **9**, 31786–31793.
- 309 B. Wang, Y. Zhao, M. N. Banis, Q. Sun, K. R. Adair, R. Li, T. K. Sham and X. Sun, *ACS Appl. Mater. Interfaces*, 2018, **10**, 1654–1661.
- 310 E. Kazyak, K.-H. Chen, A. L. Davis, S. Yu, A. J. Sanchez, J. Lasso, A. R. Bielinski, T. Thompson, J. Sakamoto, D. J. Siegel and N. P. Dasgupta, *J. Mater. Chem. A*, 2018, **6**, 19425–19437.
- 311 X. Han, Y. Gong, K. K. Fu, X. He, G. T. Hitz, J. Dai, A. Pearse, B. Liu, H. Wang, G. Rubloff, Y. Mo, V. Thangadurai, E. D. Wachsman and L. Hu, *Nat. Mater.*, 2017, **16**, 572–579.
- 312 Y. Liu, Q. Sun, Y. Zhao, B. Wang, P. Kaghazchi, K. R. Adair, R. Li, C. Zhang, J. Liu, L. Y. Kuo, Y. Hu, T. K. Sham, L. Zhang, R. Yang, S. Lu, X. Song and X. Sun, *ACS Appl. Mater. Interfaces*, 2018, **10**, 31240–31248.
- 313 C. Wang, Y. Zhao, Q. Sun, X. Li, Y. Liu, J. Liang, X. Li, X. Lin, R. Li, K. R. Adair, L. Zhang, R. Yang, S. Lu and X. Sun, *Nano Energy*, 2018, **53**, 168–174.
- 314 A. L. Davis, R. Garcia-Mendez, K. N. Wood, E. Kazyak, K.-H. Chen, G. Teeter, J. Sakamoto and N. P. Dasgupta, *J. Mater. Chem. A*, 2020, **8**, 6291–6302.

- 315 J. H. Woo, J. E. Trevey, A. S. Cavanagh, Y. S. Choi, S. C. Kim, S. M. George, K. H. Oh and S.-H. Lee, *J. Electrochem. Soc.*, 2012, **159**, A1120–A1124.
- 316 C. Wang, X. Li, Y. Zhao, M. N. Banis, J. Liang, X. Li, Y. Sun, K. R. Adair, Q. Sun, Y. Liu, F. Zhao, S. Deng, X. Lin, R. Li, Y. Hu, T. K. Sham, H. Huang, L. Zhang, R. Yang, S. Lu and X. Sun, *Small Methods*, 2019, **3**, 1900261.
- 317 X. Li, Z. Ren, M. Norouzi Banis, S. Deng, Y. Zhao, Q. Sun, C. Wang, X. Yang, W. Li, J. Liang, X. Li, Y. Sun, K. Adair, R. Li, Y. Hu, T.-K. Sham, H. Huang, L. Zhang, S. Lu, J. Luo and X. Sun, *ACS Energy Lett.*, 2019, **4**, 2480–2488.
- 318 S. Deng, X. Li, Z. Ren, W. Li, J. Luo, J. Liang, J. Liang, M. N. Banis, M. Li, Y. Zhao, X. Li, C. Wang, Y. Sun, Q. Sun, R. Li, Y. Hu, H. Huang, L. Zhang, S. Lu, J. Luo and X. Sun, *Energy Storage Mater.*, 2020, **27**, 117–123.
- 319 S. Deng, Y. Sun, X. Li, Z. Ren, J. Liang, K. Doyle-Davis, J. Liang, W. Li, M. Norouzi Banis, Q. Sun, R. Li, Y. Hu, H. Huang, L. Zhang, S. Lu, J. Luo and X. Sun, *ACS Energy Lett.*, 2020, **5**, 1243–1251.
- 320 X.-B. Cheng, R. Zhang, C.-Z. Zhao and Q. Zhang, *Chem. Rev.*, 2017, **117**, 10403–10473.
- 321 C. Fang, X. Wang and Y. S. Meng, *Trends Chem.*, 2019, **1**, 152–158.
- 322 S. Shi, P. Lu, Z. Liu, Y. Qi, L. G. Hector, H. Li and S. J. Harris, *J. Am. Chem. Soc.*, 2012, **134**, 15476–15487.
- 323 D. Lin, Y. Liu and Y. Cui, *Nat. Nanotechnol.*, 2017, **12**, 194–206.
- 324 L. Wang, L. Zhang, Q. Wang, W. Li, B. Wu, W. Jia, Y. Wang, J. Li and H. Li, *Energy Storage Mater.*, 2018, **10**, 16–23.
- 325 A. C. Kozen, C.-F. Lin, A. J. Pearse, M. A. Schroeder, X. Han, L. Hu, S.-B. Lee, G. W. Rubloff and M. Noked, *ACS Nano*, 2015, **9**, 5884–5892.
- 326 W. Wang, X. Yue, J. Meng, J. Wang, X. Wang, H. Chen, D. Shi, J. Fu, Y. Zhou, J. Chen and Z. Fu, *Energy Storage Mater.*, 2019, **18**, 414–422.
- 327 N.-W. Li, Y.-X. Yin, C.-P. Yang and Y.-G. Guo, *Adv. Mater.*, 2016, **28**, 1853–1858.
- 328 N.-W. Li, Y. Shi, Y.-X. Yin, X.-X. Zeng, J.-Y. Li, C.-J. Li, L.-J. Wan, R. Wen and Y.-G. Guo, *Angew. Chem., Int. Ed.*, 2018, **57**, 1505–1509.
- 329 J. Luo, C.-C. Fang and N.-L. Wu, *Adv. Energy Mater.*, 2018, **8**, 1701482.
- 330 D. Lin, Y. Liu, W. Chen, G. Zhou, K. Liu, B. Dunn and Y. Cui, *Nano Lett.*, 2017, **17**, 3731–3737.
- 331 Z. Song, M. N. Banis, L. Zhang, B. Wang, L. Yang, D. Banham, Y. Zhao, J. Liang, M. Zheng, R. Li, S. Ye and X. Sun, *Nano Energy*, 2018, **53**, 716–725.
- 332 L. Wang, Q. Wang, W. Jia, S. Chen, P. Gao and J. Li, *J. Power Sources*, 2017, **342**, 175–182.
- 333 X. Meng, *J. Mater. Chem. A*, 2017, **5**, 18326–18378.
- 334 E. Kazayak, K. N. Wood and N. P. Dasgupta, *Chem. Mater.*, 2015, **27**, 6457–6462.
- 335 C.-F. Lin, A. C. Kozen, M. Noked, C. Liu and G. W. Rubloff, *Adv. Mater. Interfaces*, 2016, **3**, 1600426.
- 336 X. Liu, Q. Zhu, Y. Lang, K. Cao, S. Chu, B. Shan and R. Chen, *Angew. Chem., Int. Ed.*, 2017, **56**, 1648–1652.
- 337 J. Xie, J. Wang, H. R. Lee, K. Yan, Y. Li, F. Shi, W. Huang, A. Pei, G. Chen, R. Subbaraman, J. Christensen and Y. Cui, *Sci. Adv.*, 2018, **4**, 5168.
- 338 P. K. Alaboina, S. Rodrigues, M. Rottmayer and S.-J. Cho, *ACS Appl. Mater. Interfaces*, 2018, **10**, 32801–32808.
- 339 I. S. Kim, R. T. Haasch, D. H. Cao, O. K. Farha, J. T. Hupp, M. G. Kanatzidis and A. B. Martinson, *ACS Appl. Mater. Interfaces*, 2016, **8**, 24310–24314.
- 340 L. Chen, K.-S. Chen, X. Chen, G. Ramirez, Z. Huang, N. R. Geise, H.-G. Steinrück, B. L. Fisher, R. Shahbazian-Yassar, M. F. Toney, M. C. Hersam and J. W. Elam, *ACS Appl. Mater. Interfaces*, 2018, **10**, 26972–26981.
- 341 J. Xie, L. Liao, Y. Gong, Y. Li, F. Shi, A. Pei, J. Sun, R. Zhang, B. Kong, R. Subbaraman, J. Christensen and Y. Cui, *Sci. Adv.*, 2017, **3**, 3170.
- 342 Y. Sun, Y. Zhao, J. Wang, J. Liang, C. Wang, Q. Sun, X. Lin, K. R. Adair, J. Luo, D. Wang, R. Li, M. Cai, T.-K. Sham and X. Sun, *Adv. Mater.*, 2019, **31**, 1806541.
- 343 Y. Zhao, L. V. Goncharova, Q. Sun, X. Li, A. Lushington, B. Wang, R. Li, F. Dai, M. Cai and X. Sun, *Small Methods*, 2018, **2**, 1700417.
- 344 L. Chen, Z. Huang, R. Shahbazian-Yassar, J. A. Libera, K. C. Klavetter, K. R. Zavadil and J. W. Elam, *ACS Appl. Mater. Interfaces*, 2018, **10**, 7043–7051.
- 345 K. R. Adair, C. Zhao, M. N. Banis, Y. Zhao, R. Li, M. Cai and X. Sun, *Angew. Chem., Int. Ed.*, 2019, **58**, 15797–15802.
- 346 Y. Zhao, M. Amirmaleki, Q. Sun, C. Zhao, A. Codireni, L. V. Goncharova, C. Wang, K. Adair, X. Li, X. Yang, F. Zhao, R. Li, T. Filleter, M. Cai and X. Sun, *Matter*, 2019, **1**, 1215–1231.
- 347 X.-B. Cheng, R. Zhang, C.-Z. Zhao, F. Wei, J.-G. Zhang and Q. Zhang, *Adv. Sci.*, 2016, **3**, 1500213.
- 348 Y. Liang, W. H. Lai, Z. Miao and S. L. Chou, *Small*, 2018, **14**, 1702514.
- 349 M. Á. Muñoz-Márquez, D. Saurel, J. L. Gómez-Cámer, M. Casas-Cabanas, E. Castillo-Martínez and T. Rojo, *Adv. Energy Mater.*, 2017, **7**, 1700463.
- 350 W. Luo, F. Shen, C. Bommier, H. Zhu, X. Ji and L. Hu, *Acc. Chem. Res.*, 2016, **49**, 231–240.
- 351 B. Xiao, T. Rojo and X. Li, *ChemSusChem*, 2019, **12**, 133–144.
- 352 B. Xiao, F. A. Soto, M. Gu, K. S. Han, J. Song, H. Wang, M. H. Engelhard, V. Murugesan, K. T. Mueller, D. Reed, V. L. Sprenkle, P. B. Balbuena and X. Li, *Adv. Energy Mater.*, 2018, **8**, 1801441.
- 353 J. Liu, M. N. Banis, B. Xiao, Q. Sun, A. Lushington, R. Li, J. Guo, T.-K. Sham and X. Sun, *J. Mater. Chem. A*, 2015, **3**, 24281–24288.
- 354 J. Lin, D. Ma, Y. Li, P. Zhang, H. Mi, L. Deng, L. Sun and X. Ren, *Dalton Trans.*, 2017, **46**, 13101–13107.
- 355 M. B. Sreedhara, S. Gope, B. Vishal, R. Datta, A. J. Bhattacharyya and C. N. R. Rao, *J. Mater. Chem. A*, 2018, **6**, 2302–2310.
- 356 X. Han, Y. Liu, Z. Jia, Y. C. Chen, J. Wan, N. Weadock, K. J. Gaskell, T. Li and L. Hu, *Nano Lett.*, 2014, **14**, 139–147.
- 357 Y. Liu, X. Fang, M. Ge, J. Rong, C. Shen, A. Zhang, H. A. Enaya and C. Zhou, *Nano Energy*, 2015, **16**, 399–407.

- 358 H. Kou, X. Li, H. Shan, L. Fan, B. Yan and D. Li, *J. Mater. Chem. A*, 2017, **5**, 17881–17888.
- 359 J. Ni, Y. Jiang, F. Wu, J. Maier, Y. Yu and L. Li, *Adv. Funct. Mater.*, 2018, **28**, 1707179.
- 360 K. Kaliyappan, J. Liu, A. Lushington, R. Li and X. Sun, *ChemSusChem*, 2015, **8**, 2537–2543.
- 361 J. Alvarado, C. Ma, S. Wang, K. Nguyen, M. Kodur and Y. S. Meng, *ACS Appl. Mater. Interfaces*, 2017, **9**, 26518–26530.
- 362 L. Dong, L. RuiXian, J. Feng, C. Long, G. Wang, H. Kou, M. Zhao, L. Dong, X. Li and D. Li, *Mater. Lett.*, 2017, **205**, 75–78.
- 363 K. Kaliyappan, J. Liu, B. Xiao, A. Lushington, R. Li, T.-K. Sham and X. Sun, *Adv. Funct. Mater.*, 2017, **27**, 1701870.
- 364 C. Luo, A. Langrock, X. Fan, Y. Liang and C. Wang, *J. Mater. Chem. A*, 2017, **5**, 18214–18220.
- 365 Y. Xu, M. Zhou, C. Zhang, C. Wang, L. Liang, Y. Fang, M. Wu, L. Cheng and Y. Lei, *Nano Energy*, 2017, **38**, 304–312.
- 366 S. Chu, X. Jia, J. Wang, K. Liao, W. Zhou, Y. Wang and Z. Shao, *Composites, Part B*, 2019, **173**, 106913.
- 367 H. Yadegari, Q. Sun and X. Sun, *Adv. Mater.*, 2016, **28**, 7065–7093.
- 368 Q. Sun, X. Lin, H. Yadegari, W. Xiao, Y. Zhao, K. R. Adair, R. Li and X. Sun, *J. Mater. Chem. A*, 2018, **6**, 1473–1484.
- 369 H. Yadegari and X. Sun, *Acc. Chem. Res.*, 2018, **51**, 1532–1540.
- 370 X. Lin, F. Sun, Q. Sun, S. Wang, J. Luo, C. Zhao, X. Yang, Y. Zhao, C. Wang, R. Li and X. Sun, *Chem. Mater.*, 2019, **31**, 9024–9031.
- 371 Q. Sun, J. Liu, X. Li, B. Wang, H. Yadegari, A. Lushington, M. N. Banis, Y. Zhao, W. Xiao, N. Chen, J. Wang, T.-K. Sham and X. Sun, *Adv. Funct. Mater.*, 2017, **27**, 1606662.
- 372 H. Yadegari, M. Norouzi Banis, A. Lushington, Q. Sun, R. Li, T.-K. Sham and X. Sun, *Energy Environ. Sci.*, 2017, **10**, 286–295.
- 373 D. Ma, Y. Li, J. Yang, H. Mi, S. Luo, L. Deng, C. Yan, M. Rauf, P. Zhang, X. Sun, X. Ren, J. Li and H. Zhang, *Adv. Funct. Mater.*, 2018, **28**, 1705537.
- 374 Y. Zhao, X. Yang, L. Y. Kuo, P. Kaghazchi, Q. Sun, J. Liang, B. Wang, A. Lushington, R. Li, H. Zhang and X. Sun, *Small*, 2018, **14**, e1703717.
- 375 Y. Zhao, J. Liang, Q. Sun, L. V. Goncharova, J. Wang, C. Wang, K. R. Adair, X. Li, F. Zhao, Y. Sun, R. Li and X. Sun, *J. Mater. Chem. A*, 2019, **7**, 4119–4125.
- 376 X. Lin, Q. Sun, H. Yadegari, X. Yang, Y. Zhao, C. Wang, J. Liang, A. Koo, R. Li and X. Sun, *Adv. Funct. Mater.*, 2018, **28**, 1801904.
- 377 Y. Zhao, K. R. Adair and X. Sun, *Energy Environ. Sci.*, 2018, **11**, 2673–2695.
- 378 W. Luo, C.-F. Lin, O. Zhao, M. Noked, Y. Zhang, G. W. Rubloff and L. Hu, *Adv. Energy Mater.*, 2017, **7**, 1601526.
- 379 Y. Zhao, L. V. Goncharova, A. Lushington, Q. Sun, H. Yadegari, B. Wang, W. Xiao, R. Li and X. Sun, *Adv. Mater.*, 2017, **29**, 1606663.
- 380 Y. Zhao, L. V. Goncharova, Q. Zhang, P. Kaghazchi, Q. Sun, A. Lushington, B. Wang, R. Li and X. Sun, *Nano Lett.*, 2017, **17**, 5653–5659.
- 381 R. B. Nuwayhid, A. Jarry, G. W. Rubloff and K. E. Gregorczyk, *ACS Appl. Mater. Interfaces*, 2020, **12**, 21641–21650.
- 382 N. D. Schuppert, S. Mukherjee, A. M. Bates, E.-J. Son, M. J. Choi and S. Park, *J. Power Sources*, 2016, **316**, 160–169.
- 383 D. Pal, A. Mathur, A. Singh, S. Pakhira, R. Singh and S. Chattopadhyay, *ChemistrySelect*, 2018, **3**, 12512–12523.
- 384 K. Zhao, C. Wang, Y. Yu, M. Yan, Q. Wei, P. He, Y. Dong, Z. Zhang, X. Wang and L. Mai, *Adv. Mater. Interfaces*, 2018, **5**, 1800848.
- 385 F. Ye, D. Lu, X. Gui, T. Wang, X. Zhuang, W. Luo and Y. Huang, *J. Materiomics*, 2019, **5**, 344–349.
- 386 L. Tao, L. Liu, R. Chang, H. He, P. Zhao and J. Liu, *J. Power Sources*, 2020, **463**, 228172.
- 387 H. He, H. Tong, X. Song, X. Song and J. Liu, *J. Mater. Chem. A*, 2020, **8**, 7836–7846.
- 388 C. Zhong, Y. Deng, W. Hu, J. Qiao, L. Zhang and J. Zhang, *Chem. Soc. Rev.*, 2015, **44**, 7484–7539.
- 389 A. González, E. Goikolea, J. A. Barrena and R. Mysyk, *Renewable Sustainable Energy Rev.*, 2016, **58**, 1189–1206.
- 390 M. F. El-Kady, Y. Shao and R. B. Kaner, *Nat. Rev. Mater.*, 2016, **1**, 16033.
- 391 G. Wang, L. Zhang and J. Zhang, *Chem. Soc. Rev.*, 2012, **41**, 797–828.
- 392 Y. Shao, M. F. El-Kady, L. J. Wang, Q. Zhang, Y. Li, H. Wang, M. F. Mousavi and R. B. Kaner, *Chem. Soc. Rev.*, 2015, **44**, 3639–3665.
- 393 H. Liu, X. Liu, S. Wang, H.-K. Liu and L. Li, *Energy Storage Mater.*, 2020, **28**, 122–145.
- 394 Y. Li, X. Han, T. Yi, Y. He and X. Li, *J. Energy Chem.*, 2019, **31**, 54–78.
- 395 D. Chen, K. Jiang, T. Huang and G. Shen, *Adv. Mater.*, 2020, **32**, e1901806.
- 396 S. Boukhalfa, K. Evanoff and G. Yushin, *Energy Environ. Sci.*, 2012, **5**, 6872.
- 397 X. Sun, M. Xie, G. Wang, H. Sun, A. S. Cavanagh, J. J. Travis, S. M. George and J. Lian, *J. Electrochem. Soc.*, 2012, **159**, A364–A369.
- 398 F. Yang, L. Zhang, A. Zuzuarregui, K. Gregorczyk, L. Li, M. Beltran, C. Tollan, J. Brede, C. Rogero, A. Chuvilin and M. Knez, *ACS Appl. Mater. Interfaces*, 2015, **7**, 20513–20519.
- 399 H. Li, Y. Gao, Y. Shao, Y. Su and X. Wang, *Nano Lett.*, 2015, **15**, 6689–6695.
- 400 K. Hong, M. Cho and S. O. Kim, *ACS Appl. Mater. Interfaces*, 2015, **7**, 1899–1906.
- 401 L. Iglesias, V. Vega, J. García, B. Hernando and V. C. M. Prida, *Front. Phys.*, 2015, **3**, 12.
- 402 P. Avasthi, A. Kumar and V. Balakrishnan, *ACS Appl. Nano Mater.*, 2019, **2**, 1484–1495.
- 403 F. Naeem, S. Naeem, Y. Zhao, D. Wang, J. Zhang, Y. Mei and G. Huang, *Nanoscale Res. Lett.*, 2019, **14**, 92.
- 404 X. Sun, M. Xie, J. J. Travis, G. Wang, H. Sun, J. Lian and S. M. George, *J. Phys. Chem. C*, 2013, **117**, 22497–22508.
- 405 C. Chen, C. Chen, P. Huang, F. Duan, S. Zhao, P. Li, J. Fan, W. Song and Y. Qin, *Nanotechnology*, 2014, **25**, 504001.
- 406 C. Guan, X. Qian, X. Wang, Y. Cao, Q. Zhang, A. Li and J. Wang, *Nanotechnology*, 2015, **26**, 094001.

- 407 R. M. Silva, G. Clavel, Y. Fan, P. Amsalem, N. Koch, R. F. Silva and N. Pinna, *Adv. Mater. Interfaces*, 2016, **3**, 1600313.
- 408 L. Yu, G. Wang, G. Wan, G. Wang, S. Lin, X. Li, K. Wang, Z. Bai and Y. Xiang, *Dalton Trans.*, 2016, **45**, 13779–13786.
- 409 Z. Hai, M. Karbalaee Akbari, Z. Wei, C. Xue, H. Xu, J. Hu and S. Zhuiykov, *Electrochim. Acta*, 2017, **246**, 625–633.
- 410 M. Li and H. He, *Vacuum*, 2017, **143**, 371–379.
- 411 R. Warren, F. Sammoura, F. Tounsi, M. Sanghadasa and L. Lin, *J. Mater. Chem. A*, 2015, **3**, 15568–15575.
- 412 E. Kao, C. Yang, R. Warren, A. Kozinda and L. Lin, *Sens. Actuators, A*, 2016, **240**, 160–166.
- 413 D. K. Nandi, S. Sahoo, S. Sinha, S. Yeo, H. Kim, R. N. Bulakhe, J. Heo, J. J. Shim and S. H. Kim, *ACS Appl. Mater. Interfaces*, 2017, **9**, 40252–40264.
- 414 M. Z. Ansari, N. Parveen, D. K. Nandi, R. Ramesh, S. A. Ansari, T. Cheon and S. H. Kim, *Sci. Rep.*, 2019, **9**, 10225.
- 415 L. Wen, Y. Mi, C. Wang, Y. Fang, F. Grote, H. Zhao, M. Zhou and Y. Lei, *Small*, 2014, **10**, 3162–3168.
- 416 Y. Zhong, X. Xia, J. Zhan, Y. Wang, X. Wang and J. Tu, *J. Mater. Chem. A*, 2016, **4**, 18717–18722.
- 417 Q. Xiong, C. Zheng, H. Chi, J. Zhang and Z. Ji, *Nanotechnology*, 2017, **28**, 055405.
- 418 Y.-Q. Cao, X. Qian, W. Zhang, S.-S. Wang, M. Li, D. Wu and A.-D. Li, *J. Electrochem. Soc.*, 2017, **164**, A3493–A3498.
- 419 L. Yu, G. Wan, Y. Qin and G. Wang, *Electrochim. Acta*, 2018, **268**, 283–294.
- 420 X. Zang, C. Shen, E. Kao, R. Warren, R. Zhang, K. S. Teh, J. Zhong, M. Wei, B. Li, Y. Chu, M. Sanghadasa, A. Schwartzberg and L. Lin, *Adv. Mater.*, 2018, **30**, 1704754.
- 421 L. Yu, G. Wan, X. Peng, Z. Dou, X. Li, K. Wang, S. Lin and G. Wang, *RSC Adv.*, 2016, **6**, 14199–14204.
- 422 S. A. Sherrill, J. Duay, Z. Gui, P. Banerjee, G. W. Rubloff and S. B. Lee, *Phys. Chem. Chem. Phys.*, 2011, **13**, 15221–15226.
- 423 R. Wang, C. Xia, N. Wei and H. N. Alshareef, *Electrochim. Acta*, 2016, **196**, 611–621.
- 424 Y. Chen, Z. Gao, B. Zhang, S. Zhao and Y. Qin, *J. Power Sources*, 2016, **315**, 254–260.
- 425 J.-B. Fang, C. Liu, Y.-Q. Cao and A.-D. Li, *J. Mater. Res.*, 2019, **35**, 738–746.
- 426 B. C. Steele and A. Heinzl, *Nature*, 2001, **414**, 345–352.
- 427 L. Wei, Z. Y. Zhou, S. P. Chen, C. D. Xu, D. Su, M. E. Schuster and S. G. Sun, *Chem. Commun.*, 2013, **49**, 11152–11154.
- 428 L. Zhang, K. Doyle-Davis and X. Sun, *Energy Environ. Sci.*, 2019, **12**, 492–517.
- 429 N. Cheng, Y. Shao, J. Liu and X. Sun, *Nano Energy*, 2016, **29**, 220–242.
- 430 T. Aaltonen, A. Rahtu, M. Ritala and M. Leskelä, *Electrochem. Solid-State Lett.*, 2003, **6**, C130.
- 431 T. Aaltonen, M. Ritala, T. Sajavaara, J. Keinonen and M. Leskelä, *Chem. Mater.*, 2003, **15**, 1924–1928.
- 432 S. D. Elliott, *Langmuir*, 2010, **26**, 9179–9182.
- 433 N. E. Richey, C. de Paula and S. F. Bent, *J. Chem. Phys.*, 2020, **152**, 040902.
- 434 E. Sairanen, M. C. Figueiredo, R. Karinen, A. Santasalo-Aarnio, H. Jiang, J. Sainio, T. Kallio and J. Lehtonen, *Appl. Catal., B*, 2014, **148–149**, 11–21.
- 435 M. Utriainen, M. Kröger-Laukkanen, L.-S. Johansson and L. Niinistö, *Appl. Surf. Sci.*, 2000, **157**, 151–158.
- 436 V. R. Anderson, N. Leick, J. W. Clancey, K. E. Hurst, K. M. Jones, A. C. Dillon and S. M. George, *J. Phys. Chem. C*, 2014, **118**, 8960–8970.
- 437 J. Gan, J. Zhang, B. Zhang, W. Chen, D. Niu, Y. Qin, X. Duan and X. Zhou, *J. Energy Chem.*, 2020, **45**, 59–66.
- 438 Q. Du, J. Wu and H. Yang, *ACS Catal.*, 2013, **4**, 144–151.
- 439 J. Xie, X. Yang, B. Han, Y. Shao-Horn and D. Wang, *ACS Nano*, 2013, **7**, 6337–6345.
- 440 L. Zhang, L. T. Røling, X. Wang, M. Vara, M. Chi, J. Liu, S. I. Choi, J. Park, J. A. Herron, Z. Xie, M. Mavrikakis and Y. Xia, *Science*, 2015, **349**, 412–416.
- 441 C. H. Choi, M. Kim, H. C. Kwon, S. J. Cho, S. Yun, H. T. Kim, K. J. Mayrhofer, H. Kim and M. Choi, *Nat. Commun.*, 2016, **7**, 10922.
- 442 R. Shen, W. Chen, Q. Peng, S. Lu, L. Zheng, X. Cao, Y. Wang, W. Zhu, J. Zhang, Z. Zhuang, C. Chen, D. Wang and Y. Li, *Chem*, 2019, **5**, 2099–2110.
- 443 S. Siahrostami, A. Verdager-Casadevall, M. Karamad, D. Deiana, P. Malacrida, B. Wickman, M. Escudero-Escribano, E. A. Paoli, R. Frydendal, T. W. Hansen, I. Chorkendorff, I. E. Stephens and J. Rossmeisl, *Nat. Mater.*, 2013, **12**, 1137–1143.
- 444 Y. Chen, S. Ji, Y. Wang, J. Dong, W. Chen, Z. Li, R. Shen, L. Zheng, Z. Zhuang, D. Wang and Y. Li, *Angew. Chem., Int. Ed.*, 2017, **56**, 6937–6941.
- 445 Y. Qu, Z. Li, W. Chen, Y. Lin, T. Yuan, Z. Yang, C. Zhao, J. Wang, C. Zhao, X. Wang, F. Zhou, Z. Zhuang, Y. Wu and Y. Li, *Nat. Catal.*, 2018, **1**, 781–786.
- 446 L. Zhang, H. Liu, S. Liu, M. Norouzi Banis, Z. Song, J. Li, L. Yang, M. Markiewicz, Y. Zhao, R. Li, M. Zheng, S. Ye, Z.-J. Zhao, G. A. Botton and X. Sun, *ACS Catal.*, 2019, **9**, 9350–9358.
- 447 W. W. McNeary, A. E. Linico, C. Ngo, S. van Rooij, S. Haussener, M. E. Maguire, S. Pylypenko and A. W. Weimer, *J. Appl. Electrochem.*, 2018, **48**, 973–984.
- 448 J. Cai, J. Zhang, K. Cao, M. Gong, Y. Lang, X. Liu, S. Chu, B. Shan and R. Chen, *ACS Appl. Nano Mater.*, 2018, **1**, 522–530.
- 449 Y. Wen, J. Cai, J. Zhang, J. Yang, L. Shi, K. Cao, R. Chen and B. Shan, *Chem. Mater.*, 2018, **31**, 101–111.
- 450 N. Cheng, M. N. Banis, J. Liu, A. Riese, X. Li, R. Li, S. Ye, S. Knights and X. Sun, *Adv. Mater.*, 2015, **27**, 277–281.
- 451 Z. Song, B. Wang, N. Cheng, L. Yang, D. Banham, R. Li, S. Ye and X. Sun, *J. Mater. Chem. A*, 2017, **5**, 9760–9767.
- 452 L. Zhang, Y. Zhao, M. N. Banis, K. Adair, Z. Song, L. Yang, M. Markiewicz, J. Li, S. Wang, R. Li, S. Ye and X. Sun, *Nano Energy*, 2019, **60**, 111–118.
- 453 N. Cheng, J. Liu, M. N. Banis, D. Geng, R. Li, S. Ye, S. Knights and X. Sun, *Int. J. Hydrogen Energy*, 2014, **39**, 15967–15974.
- 454 N. Cheng, M. Norouzi Banis, J. Liu, A. Riese, S. Mu, R. Li, T.-K. Sham and X. Sun, *Energy Environ. Sci.*, 2015, **8**, 1450–1455.
- 455 C.-T. Hsieh, Y.-Y. Liu, D.-Y. Tzou and W.-Y. Chen, *J. Phys. Chem. C*, 2012, **116**, 26735–26743.

- 456 Y.-C. Hsueh, C.-C. Wang, C.-C. Kei, Y.-H. Lin, C. Liu and T.-P. Perng, *J. Catal.*, 2012, **294**, 63–68.
- 457 T. Shu, D. Dang, D.-W. Xu, R. Chen, S.-J. Liao, C.-T. Hsieh, A. Su, H.-Y. Song and L. Du, *Electrochim. Acta*, 2015, **177**, 168–173.
- 458 T. Shu, S.-J. Liao, C.-T. Hsieh, A. K. Roy, Y.-Y. Liu, D.-Y. Tzou and W.-Y. Chen, *Electrochim. Acta*, 2012, **75**, 101–107.
- 459 C. Liu, C. C. Wang, C. C. Kei, Y. C. Hsueh and T. P. Perng, *Small*, 2009, **5**, 1535–1538.
- 460 Z. Song, M. Norouzi Banis, H. Liu, L. Zhang, Y. Zhao, J. Li, K. Doyle-Davis, R. Li, S. Knights, S. Ye, G. A. Botton, P. He and X. Sun, *ACS Catal.*, 2019, **9**, 5365–5374.
- 461 S. Moghaddam, E. Pengwang, Y. B. Jiang, A. R. Garcia, D. J. Burnett, C. J. Brinker, R. I. Masel and M. A. Shannon, *Nat. Nanotechnol.*, 2010, **5**, 230–236.
- 462 M. Choun, S. Chung, H. Jeon, S. Uhm and J. Lee, *Electrochem. Commun.*, 2012, **24**, 108–111.
- 463 C.-T. Hsieh, D.-Y. Tzou and M.-T. Jiang, *J. Electroanal. Chem.*, 2017, **794**, 139–147.
- 464 H. Yang, B. Zhang, B. Zhang, Z. Gao and Y. Qin, *Chin. J. Catal.*, 2018, **39**, 1038–1043.
- 465 C.-Y. Su, Y.-C. Hsueh, C.-C. Kei, C.-T. Lin and T.-P. Perng, *J. Phys. Chem. C*, 2013, **117**, 11610–11618.
- 466 Y. Chen, J. Wang, X. Meng, Y. Zhong, R. Li, X. Sun, S. Ye and S. Knights, *Int. J. Hydrogen Energy*, 2011, **36**, 11085–11092.
- 467 K. Zhang, W. Yang, C. Ma, Y. Wang, C. Sun, Y. Chen, P. Duchesne, J. Zhou, J. Wang, Y. Hu, M. N. Banis, P. Zhang, F. Li, J. Li and L. Chen, *NPG Asia Mater.*, 2015, **7**, e153.
- 468 X. Jiang, T. M. Gür, F. B. Prinz and S. F. Bent, *Chem. Mater.*, 2010, **22**, 3024–3032.
- 469 A.-C. Johansson, J. V. Larsen, M. A. Verheijen, K. B. Haugshøj, H. F. Clausen, W. M. M. Kessels, L. H. Christensen and E. V. Thomsen, *J. Catal.*, 2014, **311**, 481–486.
- 470 A. C. Johansson, R. B. Yang, K. B. Haugshøj, J. V. Larsen, L. H. Christensen and E. V. Thomsen, *Int. J. Hydrogen Energy*, 2013, **38**, 11406–11414.
- 471 H. J. Jeong, J. W. Kim, K. Bae, H. Jung and J. H. Shim, *ACS Catal.*, 2015, **5**, 1914–1921.
- 472 H. Jeong, J. W. Kim, J. Park, J. An, T. Lee, F. B. Prinz and J. H. Shim, *ACS Appl. Mater. Interfaces*, 2016, **8**, 30090–30098.
- 473 S. Sun, G. Zhang, N. Gauquelin, N. Chen, J. Zhou, S. Yang, W. Chen, X. Meng, D. Geng, M. N. Banis, R. Li, S. Ye, S. Knights, G. A. Botton, T.-K. Sham and X. Sun, *Sci. Rep.*, 2013, **3**, 1775.
- 474 C.-T. Hsieh, W.-Y. Chen, D.-Y. Tzou, A. K. Roy and H.-T. Hsiao, *Int. J. Hydrogen Energy*, 2012, **37**, 17837–17843.
- 475 C.-T. Hsieh, H.-T. Hsiao, D.-Y. Tzou, P.-Y. Yu, P.-Y. Chen and B.-S. Jang, *Mater. Chem. Phys.*, 2015, **149–150**, 359–367.
- 476 L. Assaud, E. Monyoncho, K. Pitzschel, A. Allagui, M. Petit, M. Hanbucken, E. A. Baranova and L. Santinacci, *Beilstein J. Nanotechnol.*, 2014, **5**, 162–172.
- 477 N. Caner, A. Bulut, M. Yurderi, I. E. Ertas, H. Kivrak, M. Kaya and M. Zahmakiran, *Appl. Catal., B*, 2017, **210**, 470–483.
- 478 R.-S. Juang, C.-T. Hsieh, J.-Q. Hsiao, H.-T. Hsiao, D.-Y. Tzou and M. M. Huq, *J. Power Sources*, 2015, **275**, 845–851.
- 479 E. Rikkinen, A. Santasalo-Aarnio, S. Airaksinen, M. Borghei, V. Viitanen, J. Sainio, E. I. Kauppinen, T. Kallio and A. O. I. Krause, *J. Phys. Chem. C*, 2011, **115**, 23067–23073.
- 480 Y. Jiang, J. Chen, J. Zhang, A. Li, Y. Zeng, F. Zhou, G. Wang and R. Wang, *RSC Adv.*, 2016, **6**, 13207–13216.
- 481 L. Assaud, N. Brazeau, M. K. Barr, M. Hanbucken, S. Ntais, E. A. Baranova and L. Santinacci, *ACS Appl. Mater. Interfaces*, 2015, **7**, 24533–24542.
- 482 M. K. S. Barr, L. Assaud, N. Brazeau, M. Hanbücken, S. Ntais, L. Santinacci and E. A. Baranova, *J. Phys. Chem. C*, 2017, **121**, 17727–17736.
- 483 C. E. Finke, S. T. Omelchenko, J. T. Jasper, M. F. Lichterman, C. G. Read, N. S. Lewis and M. R. Hoffmann, *Energy Environ. Sci.*, 2019, **12**, 358–365.
- 484 M. A. Khalily, B. Patil, E. Yilmaz and T. Uyar, *Nanoscale Adv.*, 2019, **1**, 1224–1231.
- 485 X. Sun, X. Yang, H. Xiang, H. Mi, P. Zhang, X. Ren, Y. Li and X. Li, *Electrochim. Acta*, 2019, **296**, 964–971.
- 486 H. Li, Z. Guo and X. Wang, *J. Mater. Chem. A*, 2017, **5**, 21353–21361.
- 487 V. Di Palma, G. Zafeiropoulos, T. Goldsweert, W. M. M. Kessels, M. C. M. van de Sanden, M. Creatore and M. N. Tsampas, *Electrochem. Commun.*, 2019, **98**, 73–77.
- 488 J. Rongé, T. Dobbelaere, L. Henderick, M. M. Minjauw, S. P. Sree, J. Dendooven, J. A. Martens and C. Detavernier, *Nanoscale Adv.*, 2019, **1**, 4166–4172.
- 489 K. L. Pickrahn, S. W. Park, Y. Gorlin, H.-B.-R. Lee, T. F. Jaramillo and S. F. Bent, *Adv. Energy Mater.*, 2012, **2**, 1269–1277.
- 490 K. L. Nardi, N. Yang, C. F. Dickens, A. L. Strickler and S. F. Bent, *Adv. Energy Mater.*, 2015, **5**, 1500412.
- 491 A. G. Hufnagel, A.-K. Henß, R. Hoffmann, O. E. O. Zeman, S. Häringer, D. Fattakhova-Rohlfing and T. Bein, *Adv. Mater. Interfaces*, 2018, **5**, 1701531.
- 492 D. Xiong, Q. Zhang, W. Li, J. Li, X. Fu, M. F. Cerqueira, P. Alpuim and L. Liu, *Nanoscale*, 2017, **9**, 2711–2717.
- 493 Y. Huang, L. Liu and X. Liu, *Nanotechnology*, 2019, **30**, 095402.
- 494 P. Nayak, Q. Jiang, N. Kurra, X. Wang, U. Buttner and H. N. Alshareef, *J. Mater. Chem. A*, 2017, **5**, 20422–20427.
- 495 I. J. Hsu, Y. C. Kimmel, X. Jiang, B. G. Willis and J. G. Chen, *Chem. Commun.*, 2012, **48**, 1063–1065.
- 496 N. Cheng, S. Stambula, D. Wang, M. N. Banis, J. Liu, A. Riese, B. Xiao, R. Li, T. K. Sham, L. M. Liu, G. A. Botton and X. Sun, *Nat. Commun.*, 2016, **7**, 13638.
- 497 Y. Lei, Y. Wang, Y. Liu, C. Song, Q. Li, D. Wang and Y. Li, *Angew. Chem., Int. Ed.*, 2020, **59**, 20794–20812.
- 498 L. Zhang, R. Si, H. Liu, N. Chen, Q. Wang, K. Adair, Z. Wang, J. Chen, Z. Song, J. Li, M. N. Banis, R. Li, T. K. Sham, M. Gu, L. M. Liu, G. A. Botton and X. Sun, *Nat. Commun.*, 2019, **10**, 4936.
- 499 S. Shin, Z. Jin, D. H. Kwon, R. Bose and Y. S. Min, *Langmuir*, 2015, **31**, 1196–1202.

- 500 D. H. Kwon, Z. Jin, S. Shin, W. S. Lee and Y. S. Min, *Nanoscale*, 2016, **8**, 7180–7188.
- 501 T. A. Ho, C. Bae, S. Lee, M. Kim, J. M. Montero-Moreno, J. H. Park and H. Shin, *Chem. Mater.*, 2017, **29**, 7604–7614.
- 502 Y. Kim, D. H. K. Jackson, D. Lee, M. Choi, T.-W. Kim, S.-Y. Jeong, H.-J. Chae, H. W. Kim, N. Park, H. Chang, T. F. Kuech and H. J. Kim, *Adv. Funct. Mater.*, 2017, **27**, 1701825.
- 503 Y. Cimen, A. W. Peters, J. R. Avila, W. L. Hoffeditz, S. Goswami, O. K. Farha and J. T. Hupp, *Langmuir*, 2016, **32**, 12005–12012.
- 504 W. Xiong, Z. Guo, H. Li, R. Zhao and X. Wang, *ACS Energy Lett.*, 2017, **2**, 2778–2785.
- 505 W. Xiong, Q. Guo, Z. Guo, H. Li, R. Zhao, Q. Chen, Z. Liu and X. Wang, *J. Mater. Chem. A*, 2018, **6**, 4297–4304.
- 506 Y. Zheng, Y. Jiao, Y. Zhu, L. H. Li, Y. Han, Y. Chen, M. Jaroniec and S.-Z. Qiao, *J. Am. Chem. Soc.*, 2016, **138**, 16174–16181.
- 507 L. Zhang, Z.-J. Zhao, M. Norouzi Banis, L. Li, Y. Zhao, Z. Song, Z. Wang, T.-K. Sham, R. Li, M. Zheng, J. Gong and X. Sun, *J. Mater. Chem. A*, 2018, **6**, 24397–24406.
- 508 T. W. Hamann, R. A. Jensen, A. B. F. Martinson, H. Van Ryswyk and J. T. Hupp, *Energy Environ. Sci.*, 2008, **1**, 66.
- 509 N. Tétreault and M. Grätzel, *Energy Environ. Sci.*, 2012, **5**, 8506.
- 510 K. Fan, J. Yu and W. Ho, *Mater. Horiz.*, 2017, **4**, 319–344.
- 511 J. M. Cole, G. Pepe, O. K. Al Bahri and C. B. Cooper, *Chem. Rev.*, 2019, **119**, 7279–7327.
- 512 M. Ye, X. Wen, M. Wang, J. Iocozzia, N. Zhang, C. Lin and Z. Lin, *Mater. Today*, 2015, **18**, 155–162.
- 513 A. F. Palmstrom, P. K. Santra and S. F. Bent, *Nanoscale*, 2015, **7**, 12266–12283.
- 514 D. H. Kim, M. D. Losego, Q. Peng and G. N. Parsons, *Adv. Mater. Interfaces*, 2016, **3**, 1600354.
- 515 A. K. Chandiran, P. Comte, R. Humphry-Baker, F. Kessler, C. Yi, M. K. Nazeeruddin and M. Grätzel, *Adv. Funct. Mater.*, 2013, **23**, 2775–2781.
- 516 I. Dirnstorfer, H. Mähne, T. Mikolajick, M. Knaut, M. Albert and K. Dubnack, *J. Vac. Sci. Technol., A*, 2013, **31**, 01A116.
- 517 X. Gao, J. Chen and C. Yuan, *J. Power Sources*, 2013, **240**, 503–509.
- 518 J. Y. Kim, K. H. Lee, J. Shin, S. H. Park, J. S. Kang, K. S. Han, M. M. Sung, N. Pinna and Y. E. Sung, *Nanotechnology*, 2014, **25**, 504003.
- 519 A. F. Palmstrom, G. E. Eperon, T. Leijtens, R. Prasanna, S. N. Habisreutinger, W. Nemeth, E. A. Gaulding, S. P. Dunfield, M. Reese, S. Nanayakkara, T. Moot, J. Werner, J. Liu, B. To, S. T. Christensen, M. D. McGehee, M. F. A. M. van Hest, J. M. Luther, J. J. Berry and D. T. Moore, *Joule*, 2019, **3**, 2193–2204.
- 520 D. H. Kim, H. J. Koo, J. S. Jur, M. Woodroof, B. Kalanyan, K. Lee, C. K. Devine and G. N. Parsons, *Nanoscale*, 2012, **4**, 4731–4738.
- 521 J. W. Lee, J. Lee, C. Kim, C. Y. Cho and J. H. Moon, *Sci. Rep.*, 2014, **4**, 6804.
- 522 W. Song, H. Wang, G. Liu, M. Peng and D. Zou, *Nano Energy*, 2016, **19**, 1–7.
- 523 J. Y. Kim, J. S. Kang, J. Shin, J. Kim, S. J. Han, J. Park, Y. S. Min, M. J. Ko and Y. E. Sung, *Nanoscale*, 2015, **7**, 8368–8377.
- 524 L. Alibabaei, B. H. Farnum, B. Kalanyan, M. K. Brennaman, M. D. Losego, G. N. Parsons and T. J. Meyer, *Nano Lett.*, 2014, **14**, 3255–3261.
- 525 A. B. F. Martinson, J. W. Elam, J. T. Hupp and M. J. Pellin, *Nano Lett.*, 2007, **8**, 2183–2187.
- 526 T. W. Hamann, A. B. F. Martinson, J. W. Elam, M. J. Pellin and J. T. Hupp, *Adv. Mater.*, 2008, **20**, 1560–1564.
- 527 A. K. Chandiran, M. Abdi-Jalebi, A. Yella, M. I. Dar, C. Yi, S. A. Shivashankar, M. K. Nazeeruddin and M. Grätzel, *Nano Lett.*, 2014, **14**, 1190–1195.
- 528 A. K. Chandiran, M. Abdi-Jalebi, M. K. Nazeeruddin and M. G. Tzel, *ACS Nano*, 2014, **8**, 2261–2268.
- 529 J.-S. Jeong, B.-H. Choe, J.-H. Lee, J.-J. Lee and W.-Y. Choi, *J. Electron. Mater.*, 2013, **43**, 375–380.
- 530 A. R. Pascoe, L. Bourgeois, N. W. Duffy, W. Xiang and Y.-B. Cheng, *J. Phys. Chem. C*, 2013, **117**, 25118–25126.
- 531 T. R. Garvey, B. H. Farnum and R. Lopez, *Nanoscale*, 2015, **7**, 2400–2408.
- 532 R. R. Knauf, B. Kalanyan, G. N. Parsons and J. L. Dempsey, *J. Phys. Chem. C*, 2015, **119**, 28353–28360.
- 533 H. Lu, W. Tian, J. Guo and L. Li, *Sci. Rep.*, 2015, **5**, 12765.
- 534 C. Wang, Z. Yu, C. Bu, P. Liu, S. Bai, C. Liu, K. K. Kondamareddy, W. Sun, K. Zhan, K. Zhang, S. Guo and X. Zhao, *J. Power Sources*, 2015, **282**, 596–601.
- 535 N. S. McCool, J. R. Swierk, C. T. Nemes, C. A. Schmuttenmaer and T. E. Mallouk, *J. Phys. Chem. Lett.*, 2016, **7**, 2930–2934.
- 536 L. Alibabaei, R. J. Dillon, C. E. Reilly, M. K. Brennaman, K. R. Wee, S. L. Marquard, J. M. Papanikolas and T. J. Meyer, *ACS Appl. Mater. Interfaces*, 2017, **9**, 39018–39026.
- 537 C. Karam, C. Guerra-Nuñez, R. Habchi, Z. Herro, N. Abboud, A. Khoury, S. Tingry, P. Miele, I. Utke and M. Bechelany, *Mater. Des.*, 2017, **126**, 314–321.
- 538 J. Maçaira, L. Andrade and A. Mendes, *Sol. Energy*, 2017, **158**, 905–916.
- 539 D. Wang, B. D. Sherman, B. H. Farnum, M. V. Sheridan, S. L. Marquard, M. S. Eberhart, C. J. Dares and T. J. Meyer, *Proc. Natl. Acad. Sci. U. S. A.*, 2017, **114**, 9809–9813.
- 540 C. Karam, R. Habchi, S. Tingry, P. Miele and M. Bechelany, *ACS Appl. Nano Mater.*, 2018, **1**, 3705–3714.
- 541 L. Tian, J. Fohlinger, Z. Zhang, P. B. Pati, J. Lin, T. Kubart, Y. Hua, J. Sun, L. Kloos, G. Boschloo, L. Hammarstrom and H. Tian, *Chem. Commun.*, 2018, **54**, 3739–3742.
- 542 J.-Y. Kim, K.-Y. Shin, M. H. Raza, N. Pinna and Y.-E. Sung, *Korean J. Chem. Eng.*, 2019, **36**, 1157–1163.
- 543 M. Law, L. E. Greene, A. Radenovic, T. Kuykendall, J. Liphardt and P. Yang, *J. Phys. Chem. B*, 2006, **110**, 22652–22663.
- 544 K. Park, Q. Zhang, B. B. Garcia, X. Zhou, Y. H. Jeong and G. Cao, *Adv. Mater.*, 2010, **22**, 2329–2332.
- 545 V. O. Williams, N. C. Jeong, C. Prasittichai, O. K. Farha, M. J. Pellin and J. T. Hupp, *ACS Nano*, 2012, **6**, 6185–6196.

- 546 J.-H. Choi, S.-H. Kwon, Y.-K. Jeong, I. Kim and K.-H. Kim, *J. Electrochem. Soc.*, 2011, **158**, B749–B753.
- 547 L. Liu, S. K. Karuturi, L. T. Su and A. I. Y. Tok, *Energy Environ. Sci.*, 2011, **4**, 209–215.
- 548 P. Labouchere, A. K. Chandiran, T. Moehl, H. Harms, S. Chavhan, R. Tena-Zaera, M. K. Nazeeruddin, M. Gratzel and N. Tetreault, *Adv. Energy Mater.*, 2014, **4**, 1400217.
- 549 C. Lin, F.-Y. Tsai, M.-H. Lee, C.-H. Lee, T.-C. Tien, L.-P. Wang and S.-Y. Tsai, *J. Mater. Chem.*, 2009, **19**, 2999.
- 550 T. P. Brennan, J. R. Bakke, I. K. Ding, B. E. Hardin, W. H. Nguyen, R. Mondal, C. D. Bailie, G. Y. Margulis, E. T. Hoke, A. Sellinger, M. D. McGehee and S. F. Bent, *Phys. Chem. Chem. Phys.*, 2012, **14**, 12130–12140.
- 551 T. P. Brennan, O. Trejo, K. E. Roelofs, J. Xu, F. B. Prinz and S. F. Bent, *J. Mater. Chem. A*, 2013, **1**, 7566.
- 552 X. Gao, D. Guan, J. Huo, J. Chen and C. Yuan, *Nanoscale*, 2013, **5**, 10438–10446.
- 553 W. Dong, L. Yang, T. Meng and Q. Chen, *Surf. Coat. Technol.*, 2015, **276**, 116–120.
- 554 G. Natu, Z. Huang, Z. Ji and Y. Wu, *Langmuir*, 2012, **28**, 950–956.
- 555 K. E. Roelofs, T. P. Brennan, J. C. Dominguez, C. D. Bailie, G. Y. Margulis, E. T. Hoke, M. D. McGehee and S. F. Bent, *J. Phys. Chem. C*, 2013, **117**, 5584–5592.
- 556 V. Ganapathy, B. Karunakaran and S.-W. Rhee, *J. Power Sources*, 2010, **195**, 5138–5143.
- 557 A. K. Chandiran, N. Tetreault, R. Humphry-Baker, F. Kessler, E. Baranoff, C. Yi, M. K. Nazeeruddin and M. Gratzel, *Nano Lett.*, 2012, **12**, 3941–3947.
- 558 T. P. Brennan, J. T. Tanskanen, K. E. Roelofs, J. W. F. To, W. H. Nguyen, J. R. Bakke, I. K. Ding, B. E. Hardin, A. Sellinger, M. D. McGehee and S. F. Bent, *J. Phys. Chem. C*, 2013, **117**, 24138–24149.
- 559 A. K. Chandiran, M. K. Nazeeruddin and M. Grätzel, *Adv. Funct. Mater.*, 2014, **24**, 1615–1623.
- 560 D. H. Kim, M. Woodroof, K. Lee and G. N. Parsons, *ChemSusChem*, 2013, **6**, 1014–1020.
- 561 L. Kavan, N. Tetreault, T. Moehl and M. Grätzel, *J. Phys. Chem. C*, 2014, **118**, 16408–16418.
- 562 L. Li, S. Chen, C. Xu, Y. Zhao, N. G. Rudawski and K. J. Ziegler, *ACS Appl. Mater. Interfaces*, 2014, **6**, 20978–20984.
- 563 J.-H. Yum, T. Moehl, J. Yoon, A. K. Chandiran, F. Kessler, P. Gratia and M. Grätzel, *J. Phys. Chem. C*, 2014, **118**, 16799–16805.
- 564 L. Li, C. Xu, Y. Zhao, S. Chen and K. J. Ziegler, *ACS Appl. Mater. Interfaces*, 2015, **7**, 12824–12831.
- 565 F. Di Giacomo, V. Zardetto, G. Lucarelli, L. Cinà, A. Di Carlo, M. Creatore and T. M. Brown, *Nano Energy*, 2016, **30**, 460–469.
- 566 V. Manthina and A. G. Agrios, *Thin Solid Films*, 2016, **598**, 54–59.
- 567 J. Song, A. Ge, B. Piercy, M. D. Losego and T. Lian, *Chem. Phys.*, 2018, **512**, 68–74.
- 568 D. Garcia-Alonso, V. Zardetto, A. J. M. Mackus, F. De Rossi, M. A. Verheijen, T. M. Brown, W. M. M. Kessels and M. Creatore, *Adv. Energy Mater.*, 2014, **4**, 1300831.
- 569 W. L. Hoffeditz, M. J. Katz, P. Deria, A. B. Martinson, M. J. Pellin, O. K. Farha and J. T. Hupp, *ACS Appl. Mater. Interfaces*, 2014, **6**, 8646–8650.
- 570 Y. Noh and O. Song, *Electron. Mater. Lett.*, 2014, **10**, 263–266.
- 571 S. Abdelnasser, M. A. Sakr and M. Serry, *Microelectron. Eng.*, 2019, **216**, 111045.
- 572 T. Jeong, S.-Y. Ham, B. Koo, P. Lee, Y.-S. Min, J.-Y. Kim and M. J. Ko, *J. Ind. Eng. Chem.*, 2019, **80**, 106–111.
- 573 D.-J. Yun, H. Ra, J.-M. Kim, E. Oh, J. Lee, M.-H. Jeong, Y. J. Jeong, H. Yang and J. Jang, *Org. Electron.*, 2019, **65**, 349–356.
- 574 K. O. Brinkmann, T. Gahlmann and T. Riedl, *Sol. RRL*, 2019, **4**, 1900332.
- 575 J. A. Raiford, S. T. Oyakhire and S. Bent, *Energy Environ. Sci.*, 2020, **13**, 1997–2023.
- 576 K. Deng and L. Li, *Adv. Mater. Interfaces*, 2016, **3**, 1600505.
- 577 B. Macco, H. C. M. Knoop, M. A. Verheijen, W. Beyer, M. Creatore and W. M. M. Kessels, *Sol. Energy Mater. Sol. Cells*, 2017, **173**, 111–119.
- 578 S. Seo, S. Jeong, H. Park, H. Shin and N. G. Park, *Chem. Commun.*, 2019, **55**, 2403–2416.
- 579 V. Zardetto, B. L. Williams, A. Perrotta, F. Di Giacomo, M. A. Verheijen, R. Andriessen, W. M. M. Kessels and M. Creatore, *Sustainable Energy Fuels*, 2017, **1**, 30–55.
- 580 P. Rong, S. Ren and Q. Yu, *Crit. Rev. Anal. Chem.*, 2019, **49**, 336–349.
- 581 P. Schulz, D. Cahen and A. Kahn, *Chem. Rev.*, 2019, **119**, 3349–3417.
- 582 B. R. Sutherland, S. Hoogland, M. M. Adachi, P. Kanjanaboos, C. T. Wong, J. J. McDowell, J. Xu, O. Voznyy, Z. Ning, A. J. Houtepen and E. H. Sargent, *Adv. Mater.*, 2015, **27**, 53–58.
- 583 V. M. Koch, M. K. S. Barr, P. Büttner, I. Mínguez-Bacho, D. Döhler, B. Winzer, E. Reinhardt, D. Segets and J. Bachmann, *J. Mater. Chem. A*, 2019, **7**, 25112–25119.
- 584 G. Popov, M. Mattinen, T. Hatanpää, M. Vehkamäki, M. Kemell, K. Mizohata, J. Räisänen, M. Ritala and M. Leskelä, *Chem. Mater.*, 2019, **31**, 1101–1109.
- 585 N. G. Park, *Adv. Energy Mater.*, 2020, **10**, 1903106.
- 586 L. Xu, X. Chen, J. Jin, W. Liu, B. Dong, X. Bai, H. Song and P. Reiss, *Nano Energy*, 2019, **63**, 103860.
- 587 J. W. Lee and N. G. Park, *Adv. Energy Mater.*, 2019, **10**, 1903249.
- 588 R. Wang, M. Mujahid, Y. Duan, Z. K. Wang, J. Xue and Y. Yang, *Adv. Funct. Mater.*, 2019, **29**, 1808843.
- 589 A. K. Chandiran, A. Yella, M. T. Mayer, P. Gao, M. K. Nazeeruddin and M. Gratzel, *Adv. Mater.*, 2014, **26**, 4309–4312.
- 590 Y. Wu, X. Yang, H. Chen, K. Zhang, C. Qin, J. Liu, W. Peng, A. Islam, E. Bi, F. Ye, M. Yin, P. Zhang and L. Han, *Appl. Phys. Express*, 2014, **7**, 052301.
- 591 A. Mettenbörger, Y. Gönüllü, T. Fischer, T. Heisig, A. Sasinska, C. Maccato, G. Carraro, C. Sada, D. Barreca, L. Mayrhofer, M. Moseler, A. Held and S. Mathur, *Nano Energy*, 2016, **19**, 415–427.

- 592 K. E. Roelofs, V. L. Pool, D. A. Bobb-Semple, A. F. Palmstrom, P. K. Santra, D. G. Van Campen, M. F. Toney and S. F. Bent, *Adv. Mater. Interfaces*, 2016, **3**, 1600580.
- 593 A. E. Shalan, S. Narra, T. Oshikiri, K. Ueno, X. Shi, H.-P. Wu, M. M. Elshanawany, E. Wei-Guang Diao and H. Misawa, *Sustainable Energy Fuels*, 2017, **1**, 1533–1540.
- 594 V. Zardetto, F. Di Giacomo, G. Lucarelli, W. M. M. Kessels, T. M. Brown and M. Creatore, *Sol. Energy*, 2017, **150**, 447–453.
- 595 W. Tan, O. L. Hendricks, A. C. Meng, M. R. Braun, M. D. McGehee, C. E. D. Chidsey and P. C. McIntyre, *Adv. Mater. Interfaces*, 2018, **5**, 1800191.
- 596 V. Zardetto, F. di Giacomo, H. Lifka, M. A. Verheijen, C. H. L. Weijtens, L. E. Black, S. Veenstra, W. M. M. Kessels, R. Andriessen and M. Creatore, *Adv. Mater. Interfaces*, 2018, **5**, 1701456.
- 597 Y. Zhu, K. Deng, H. Sun, B. Gu, H. Lu, F. Cao, J. Xiong and L. Li, *Adv. Sci.*, 2018, **5**, 1700614.
- 598 D. Chen, A. Su, X. Li, S. Pang, W. Zhu, H. Xi, J. Chang, J. Zhang, C. Zhang and Y. Hao, *Sol. Energy*, 2019, **188**, 239–246.
- 599 T. W. Kim, S. Uchida, T. Kondo and H. Segawa, *Appl. Phys. Lett.*, 2019, **115**, 203902.
- 600 M. Kong, H. Hu, K. Qin, B. Dong, L. Wan and P. Guo, *Mater. Res. Express*, 2019, **6**, 095501.
- 601 S. Na, S. Lee, W.-G. Choi, C.-G. Park, S. O. Ryu and T. Moon, *J. Vac. Sci. Technol., A*, 2019, **37**, 010902.
- 602 Y. You, W. Tian, L. Min, F. Cao, K. Deng and L. Li, *Adv. Mater. Interfaces*, 2019, **7**, 1901406.
- 603 W. Zhu, W. Chai, Z. Zhang, D. Chen, J. Chang, S. Liu, J. Zhang, C. Zhang and Y. Hao, *Org. Electron.*, 2019, **74**, 103–109.
- 604 Y. Wang, D. Wang, H. Qu, J. Cheng, Y. Fang, C. Zhang and Q. Chen, *Thin Solid Films*, 2020, **696**, 137786.
- 605 H. Lu, Y. Ma, B. Gu, W. Tian and L. Li, *J. Mater. Chem. A*, 2015, **3**, 16445–16452.
- 606 L. Chen, J.-R. Wang, L.-Q. Xie, C. Zhan, Z. Qiu, J.-Z. Zhou, J.-W. Yan, B.-W. Mao and Z.-Q. Tian, *Electrochem. Commun.*, 2016, **68**, 40–44.
- 607 S. Albrecht, M. Saliba, J. P. Correa Baena, F. Lang, L. Kegelmann, M. Mews, L. Steier, A. Abate, J. Rappich, L. Korte, R. Schlattmann, M. K. Nazeeruddin, A. Hagfeldt, M. Grätzel and B. Rech, *Energy Environ. Sci.*, 2016, **9**, 81–88.
- 608 C. Wang, D. Zhao, C. R. Grice, W. Liao, Y. Yu, A. Cimaroli, N. Shrestha, P. J. Roland, J. Chen, Z. Yu, P. Liu, N. Cheng, R. J. Ellingson, X. Zhao and Y. Yan, *J. Mater. Chem. A*, 2016, **4**, 12080–12087.
- 609 J. Kim, T. Iivonen, J. Hämäläinen, M. Kemell, K. Meinander, K. Mizohata, L. Wang, J. Räisänen, R. Beranek, M. Leskelä and A. Devi, *Chem. Mater.*, 2017, **29**, 5796–5805.
- 610 L. Hoffmann, K. O. Brinkmann, J. Malerczyk, D. Rogalla, T. Becker, D. Theirich, I. Shutsko, P. Gorrn and T. Riedl, *ACS Appl. Mater. Interfaces*, 2018, **10**, 6006–6013.
- 611 Y. Lee, S. Lee, G. Seo, S. Paek, K. T. Cho, A. J. Huckaba, M. Calizzi, D. W. Choi, J. S. Park, D. Lee, H. J. Lee, A. M. Asiri and M. K. Nazeeruddin, *Adv. Sci.*, 2018, **5**, 1800130.
- 612 J. P. Correa Baena, L. Steier, W. Tress, M. Saliba, S. Neutzner, T. Matsui, F. Giordano, T. J. Jacobsson, A. R. Srimath Kandada, S. M. Zakeeruddin, A. Petrozza, A. Abate, M. K. Nazeeruddin, M. Grätzel and A. Hagfeldt, *Energy Environ. Sci.*, 2015, **8**, 2928–2934.
- 613 T. Hu, T. Becker, N. Pourdavoud, J. Zhao, K. O. Brinkmann, R. Heiderhoff, T. Gahlmann, Z. Huang, S. Olthof, K. Meerholz, D. Tobbens, B. Cheng, Y. Chen and T. Riedl, *Adv. Mater.*, 2017, **29**, 1606656.
- 614 Y. Kuang, V. Zardetto, R. van Gils, S. Karwal, D. Koushik, M. A. Verheijen, L. E. Black, C. Weijtens, S. Veenstra, R. Andriessen, W. M. M. Kessels and M. Creatore, *ACS Appl. Mater. Interfaces*, 2018, **10**, 30367–30378.
- 615 S. Jeong, S. Seo, H. Park and H. Shin, *Chem. Commun.*, 2019, **55**, 2433–2436.
- 616 C. Wang, C. Xiao, Y. Yu, D. Zhao, R. A. Awni, C. R. Grice, K. Ghimire, I. Constantinou, W. Liao, A. J. Cimaroli, P. Liu, J. Chen, N. J. Podraza, C.-S. Jiang, M. M. Al-Jassim, X. Zhao and Y. Yan, *Adv. Energy Mater.*, 2017, **7**, 1700414.
- 617 A. Guerrero, G. Garcia-Belmonte, I. Mora-Sero, J. Bisquert, Y. S. Kang, T. J. Jacobsson, J.-P. Correa-Baena and A. Hagfeldt, *J. Phys. Chem. C*, 2016, **120**, 8023–8032.
- 618 H. Wei, J. Wu, P. Qiu, S. Liu, Y. He, M. Peng, D. Li, Q. Meng, F. Zaera and X. Zheng, *J. Mater. Chem. A*, 2019, **7**, 25347–25354.
- 619 A. S. Subbiah, A. K. Dhara, N. Mahuli, S. Banerjee and S. K. Sarkar, *Energy Technol.*, 2020, **8**, 1900878.
- 620 R. D. Chavan, M. M. Tavakoli, D. Prochowicz, P. Yadav, S. S. Lote, S. P. Bhoite, A. Nimbalkar and C. K. Hong, *ACS Appl. Mater. Interfaces*, 2020, **12**, 8098–8106.
- 621 H. Si, Q. Liao, Z. Zhang, Y. Li, X. Yang, G. Zhang, Z. Kang and Y. Zhang, *Nano Energy*, 2016, **22**, 223–231.
- 622 J. Tang, D. Jiao, L. Zhang, X. Zhang, X. Xu, C. Yao, J. Wu and Z. Lan, *Sol. Energy*, 2018, **161**, 100–108.
- 623 M. Jošt, T. Bertram, D. Koushik, J. A. Marquez, M. A. Verheijen, M. D. Heinemann, E. Köhnen, A. Al-Ashouri, S. Braunger, F. Lang, B. Rech, T. Unold, M. Creatore, I. Lauermann, C. A. Kaufmann, R. Schlattmann and S. Albrecht, *ACS Energy Lett.*, 2019, **4**, 583–590.
- 624 J. Tirado, M. Vásquez-Montoya, C. Roldán-Carmona, M. Ralaiarisoa, N. Koch, M. K. Nazeeruddin and F. Jaramillo, *ACS Appl. Energy Mater.*, 2019, **2**, 4890–4899.
- 625 S. Seo, I. J. Park, M. Kim, S. Lee, C. Bae, H. S. Jung, N. G. Park, J. Y. Kim and H. Shin, *Nanoscale*, 2016, **8**, 11403–11412.
- 626 D. Koushik, M. Jošt, A. Dučinskas, C. Burgess, V. Zardetto, C. Weijtens, M. A. Verheijen, W. M. M. Kessels, S. Albrecht and M. Creatore, *J. Mater. Chem. C*, 2019, **7**, 12532–12543.
- 627 B. Zhao, L. C. Lee, L. Yang, A. J. Pearson, H. Lu, X. J. She, L. Cui, K. H. L. Zhang, R. L. Z. Hoye, A. Karani, P. Xu, A. Sadhanala, N. C. Greenham, R. H. Friend, J. L. MacManus-Driscoll and D. Di, *ACS Appl. Mater. Interfaces*, 2018, **10**, 41849–41854.
- 628 W. Li, J. Li, L. Wang, G. Niu, R. Gao and Y. Qiu, *J. Mater. Chem. A*, 2013, **1**, 11735.

- 629 J.-J. Shi, W. Dong, Y.-Z. Xu, C.-H. Li, S.-T. Lv, L.-F. Zhu, J. Dong, Y.-H. Luo, D.-M. Li, Q.-B. Meng and Q. Chen, *Chin. Phys. Lett.*, 2013, **30**, 128402.
- 630 X. Dong, X. Fang, M. Lv, B. Lin, S. Zhang, J. Ding and N. Yuan, *J. Mater. Chem. A*, 2015, **3**, 5360–5367.
- 631 H. Wei, J. Shi, X. Xu, J. Xiao, J. Luo, J. Dong, S. Lv, L. Zhu, H. Wu, D. Li, Y. Luo, Q. Meng and Q. Chen, *Phys. Chem. Chem. Phys.*, 2015, **17**, 4937–4944.
- 632 M. Kot, C. Das, Z. Wang, K. Henkel, Z. Rouissi, K. Wojciechowski, H. J. Snaith and D. Schmeisser, *ChemSusChem*, 2016, **9**, 3401–3406.
- 633 D. Koushik, W. J. H. Verhees, D. Zhang, Y. Kuang, S. Veenstra, M. Creatore and R. E. I. Schropp, *Adv. Mater. Interfaces*, 2017, **4**, 1700043.
- 634 Y. Lv, P. Xu, G. Ren, F. Chen, H. Nan, R. Liu, D. Wang, X. Tan, X. Liu, H. Zhang and Z. K. Chen, *ACS Appl. Mater. Interfaces*, 2018, **10**, 23928–23937.
- 635 D. Koushik, L. Hazendonk, V. Zardetto, V. Vandalon, M. A. Verheijen, W. M. M. Kessels and M. Creatore, *ACS Appl. Mater. Interfaces*, 2019, **11**, 5526–5535.
- 636 H.-S. Yun, K. Noh, J. Kim, S. H. Noh, G.-H. Kim, W. Lee, H. B. Na, T.-S. Yoon, J. Jang, Y. Kim and S.-Y. Cho, *Phys. Status Solidi RRL*, 2019, **14**, 1900573.
- 637 D. Koushik, W. J. H. Verhees, Y. Kuang, S. Veenstra, D. Zhang, M. A. Verheijen, M. Creatore and R. E. I. Schropp, *Energy Environ. Sci.*, 2017, **10**, 91–100.
- 638 C.-Y. Chang, K.-T. Lee, W.-K. Huang, H.-Y. Siao and Y.-C. Chang, *Chem. Mater.*, 2015, **27**, 5122–5130.
- 639 H. Wang, Y. Zhao, Z. Wang, Y. Liu, Z. Zhao, G. Xu, T.-H. Han, J.-W. Lee, C. Chen, D. Bao, Y. Huang, Y. Duan and Y. Yang, *Nano Energy*, 2020, **69**, 104375.
- 640 T. Wang, Z. Luo, C. Li and J. Gong, *Chem. Soc. Rev.*, 2014, **43**, 7469–7484.
- 641 Y. He, T. Hamann and D. Wang, *Chem. Soc. Rev.*, 2019, **48**, 2182–2215.
- 642 W. Yang, R. R. Prabhakar, J. Tan, S. D. Tilley and J. Moon, *Chem. Soc. Rev.*, 2019, **48**, 4979–5015.
- 643 D. Bae, B. Seger, P. C. Vesborg, O. Hansen and I. Chorkendorff, *Chem. Soc. Rev.*, 2017, **46**, 1933–1954.
- 644 D. Li, J. Shi and C. Li, *Small*, 2018, **14**, 1704179.
- 645 S. Shen, J. Chen, M. Wang, X. Sheng, X. Chen, X. Feng and S. S. Mao, *Prog. Mater. Sci.*, 2018, **98**, 299–385.
- 646 S. Wang, G. Liu and L. Wang, *Chem. Rev.*, 2019, **119**, 5192–5247.
- 647 T. Yao, X. An, H. Han, J. Q. Chen and C. Li, *Adv. Energy Mater.*, 2018, **8**, 1800210.
- 648 I. V. Bagal, N. R. Chodankar, M. A. Hassan, A. Waseem, M. A. Johar, D.-H. Kim and S.-W. Ryu, *Int. J. Hydrogen Energy*, 2019, **44**, 21351–21378.
- 649 S. Bellani, M. R. Antognazza and F. Bonaccorso, *Adv. Mater.*, 2019, **31**, e1801446.
- 650 S. Chandrasekaran, L. Yao, L. Deng, C. Bowen, Y. Zhang, S. Chen, Z. Lin, F. Peng and P. Zhang, *Chem. Soc. Rev.*, 2019, **48**, 4178–4280.
- 651 M. T. Mayer, C. Du and D. Wang, *J. Am. Chem. Soc.*, 2012, **134**, 12406–12409.
- 652 L. Liu, *Mater. Lett.*, 2015, **159**, 284–288.
- 653 Q. Liu, F. Cao, F. Wu, W. Tian and L. Li, *RSC Adv.*, 2015, **5**, 79440–79446.
- 654 L. Steier, J. Luo, M. Schreier, M. T. Mayer, T. Sajavaara and M. G. tzel, *ACS Nano*, 2015, **9**, 11775.
- 655 Gurudayal, R. A. John, P. P. Boix, C. Yi, C. Shi, M. C. Scott, S. A. Veldhuis, A. M. Minor, S. M. Zakeeruddin, L. H. Wong, M. Gratzel and N. Mathews, *ChemSusChem*, 2017, **10**, 2449–2456.
- 656 Y. Lin, S. Zhou, S. W. Sheehan and D. Wang, *J. Am. Chem. Soc.*, 2011, **133**, 2398–2401.
- 657 Q. Peng, J. Wang, Z. Feng, C. Du, Y. Wen, B. Shan and R. Chen, *J. Phys. Chem. C*, 2017, **121**, 12991–12998.
- 658 I. A. Cordova, Q. Peng, I. L. Ferrall, A. J. Rieth, P. G. Hoertz and J. T. Glass, *Nanoscale*, 2015, **7**, 8584–8592.
- 659 D. Wang, H. Chen, G. Chang, X. Lin, Y. Zhang, A. Aldabahi, C. Peng, J. Wang and C. Fan, *ACS Appl. Mater. Interfaces*, 2015, **7**, 14072–14078.
- 660 M. Pavlenko, K. Siuzdak, E. Coy, M. Jancelewicz, S. Jurga and I. Iatsunskyi, *Int. J. Hydrogen Energy*, 2017, **42**, 30076–30085.
- 661 A. N. El-Shazly, A. H. Hegazy, M. M. Rashad, M. F. El-Shahat and N. K. Allam, *J. Alloys Compd.*, 2018, **739**, 178–183.
- 662 E. Kao, H. S. Park, X. Zang and L. Lin, *Int. J. Photoenergy*, 2019, **2019**, 1–8.
- 663 Y. Gun, G. Y. Song, V. H. Quy, J. Heo, H. Lee, K. S. Ahn and S. H. Kang, *ACS Appl. Mater. Interfaces*, 2015, **7**, 20292–20303.
- 664 Q. Peng, B. Kalanyan, P. G. Hoertz, A. Miller, D. H. Kim, K. Hanson, L. Alibabaei, J. Liu, T. J. Meyer, G. N. Parsons and J. T. Glass, *Nano Lett.*, 2013, **13**, 1481–1488.
- 665 X. Li, P. S. Bassi, P. P. Boix, Y. Fang and L. H. Wong, *ACS Appl. Mater. Interfaces*, 2015, **7**, 16960–16966.
- 666 T. Hisatomi, J. Brillet, M. Cornuz, F. Le Formal, N. Tetreault, K. Sivula and M. Gratzel, *Faraday Discuss.*, 2012, **155**, 223–232.
- 667 J. Ji, W. Zhang, H. Zhang, Y. Qiu, Y. Wang, Y. Luo and L. Hu, *J. Mater. Sci.: Mater. Electron.*, 2013, **24**, 3474–3480.
- 668 M. Liu, C.-Y. Nam, C. T. Black, J. Kamcev and L. Zhang, *J. Phys. Chem. C*, 2013, **117**, 13396–13402.
- 669 C. Li, T. Hisatomi, O. Watanabe, M. Nakabayashi, N. Shibata, K. Domen and J.-J. Delaunay, *Energy Environ. Sci.*, 2015, **8**, 1493–1500.
- 670 M.-W. Kim, K. Kim, T. Y. Ohm, H. Yoon, B. Joshi, E. Samuel, M. T. Swihart, S. K. Choi, H. Park and S. S. Yoon, *Chem. Eng. J.*, 2018, **333**, 721–729.
- 671 M. Li, X. Tu, Y. Wang, Y. Su, J. Hu, B. Cai, J. Lu, Z. Yang and Y. Zhang, *Nano-Micro Lett.*, 2018, **10**, 45.
- 672 S. Haschke, Y. Zhuo, S. Schlicht, M. K. S. Barr, R. Kloth, M. E. Dufond, L. Santinacci and J. Bachmann, *Adv. Mater. Interfaces*, 2019, **6**, 1801432.
- 673 X. Huai, L. Girardi, R. Lu, S. Gao, Y. Zhao, Y. Ling, G. A. Rizzi, G. Granozzi and Z. Zhang, *Nano Energy*, 2019, **65**, 104020.
- 674 T.-G. Kim, B. Joshi, C.-W. Park, E. Samuel, M.-W. Kim, M. T. Swihart and S. S. Yoon, *J. Alloys Compd.*, 2019, **798**, 35–44.

- 675 C.-C. Wang, C.-Y. Chou, S.-R. Yi and H.-D. Chen, *Int. J. Hydrogen Energy*, 2019, **44**, 28685–28697.
- 676 B. Alfakes, C. Garlisi, J. Villegas, A. Al-Hagri, S. Tamalampudi, N. S. Rajput, J.-Y. Lu, E. Lewin, J. Sá, I. Almansouri, G. Palmisano and M. Chiesa, *Surf. Coat. Technol.*, 2020, **385**, 125352.
- 677 K.-I. Liu and T.-P. Perng, *ACS Appl. Energy Mater.*, 2020, **3**, 4238–4244.
- 678 Y. Zhao, S. Balasubramanyam, R. Sinha, R. Lavrijsen, M. A. Verheijen, A. A. Bol and A. Bieberle-Hütter, *ACS Appl. Energy Mater.*, 2018, **1**, 5887–5895.
- 679 M. Stefik, M. Cornuz, N. Mathews, T. Hisatomi, S. Mhaisalkar and M. Gratzel, *Nano Lett.*, 2012, **12**, 5431–5435.
- 680 I. Narkeviciute, P. Chakthranont, A. J. Mackus, C. Hahn, B. A. Pinaud, S. F. Bent and T. F. Jaramillo, *Nano Lett.*, 2016, **16**, 7565–7572.
- 681 H. Hajibabaei, D. J. Little, A. Pandey, D. Wang, Z. Mi and T. W. Hamann, *ACS Appl. Mater. Interfaces*, 2019, **11**, 15457–15466.
- 682 A. Kargar, K. Sun, Y. Jing, C. Choi, H. Jeong, G. Y. Jung, S. Jin and D. Wang, *ACS Nano*, 2013, **7**, 9407–9415.
- 683 Z. Li, C. Yao, F. Wang, Z. Cai and X. Wang, *Nanotechnology*, 2014, **25**, 504005.
- 684 W. Ren, H. Zhang, D. Kong, B. Liu, Y. Yang and C. Cheng, *Phys. Chem. Chem. Phys.*, 2014, **16**, 22953–22957.
- 685 Q. Nie, L. Yang, C. Cao, Y. Zeng, G. Wang, C. Wang and S. Lin, *Chem. Eng. J.*, 2017, **325**, 151–159.
- 686 Z. Wang, X. Li, H. Ling, C. K. Tan, L. P. Yeo, A. C. Grimsdale and A. I. Y. Tok, *Small*, 2018, **14**, e1800395.
- 687 X. Chai, H. Zhang, Q. Pan, J. Bian, Z. Chen and C. Cheng, *Appl. Surf. Sci.*, 2019, **470**, 668–676.
- 688 N. Nasori, T. Dai, X. Jia, A. Rubiyanto, D. Cao, S. Qu, Z. Wang, Z. Wang and Y. Lei, *J. Semicond.*, 2019, **40**, 052701.
- 689 Y. Fu, C.-L. Dong, W. Zhou, Y.-R. Lu, Y.-C. Huang, Y. Liu, P. Guo, L. Zhao, W.-C. Chou and S. Shen, *Appl. Catal., B*, 2020, **260**, 118206.
- 690 W. Hu, N. D. Quang, S. Majumder, E. Park, D. Kim, H.-S. Choi and H. S. Chang, *J. Alloys Compd.*, 2020, **819**, 153349.
- 691 K. R. Nandanapalli, D. Mudusu, J. S. Yu and S. Lee, *J. Colloid Interface Sci.*, 2020, **558**, 9–20.
- 692 C. Cheng, H. Zhang, W. Ren, W. Dong and Y. Sun, *Nano Energy*, 2013, **2**, 779–786.
- 693 K. Yuan, Q. Cao, X. Li, H.-Y. Chen, Y. Deng, Y.-Y. Wang, W. Luo, H.-L. Lu and D. W. Zhang, *Nano Energy*, 2017, **41**, 543–551.
- 694 H.-P. Ma, J.-H. Yang, J.-J. Tao, K.-P. Yuan, P.-H. Cheng, W. Huang, J.-C. Wang, Q.-X. Guo, H.-L. Lu and D. W. Zhang, *Nano Energy*, 2019, **66**, 104089.
- 695 X. Yang, C. Du, R. Liu, J. Xie and D. Wang, *J. Catal.*, 2013, **304**, 86–91.
- 696 K. M. Young and T. W. Hamann, *Chem. Commun.*, 2014, **50**, 8727–8730.
- 697 S. Oh, S. Jung, Y. H. Lee, J. T. Song, T. H. Kim, D. K. Nandi, S.-H. Kim and J. Oh, *ACS Catal.*, 2018, **8**, 9755–9764.
- 698 C.-C. Wang, P.-H. Chou, Y.-H. Yu and C.-C. Kei, *Electrochim. Acta*, 2018, **284**, 211–219.
- 699 J. Zhao, T. M. Gill and X. Zheng, *Nano Res.*, 2018, **11**, 3499–3508.
- 700 S. A. Lee, T. H. Lee, C. Kim, M.-J. Choi, H. Park, S. Choi, J. Lee, J. Oh, S. Y. Kim and H. W. Jang, *ACS Catal.*, 2019, **10**, 420–429.
- 701 J. Yang, J. K. Cooper, F. M. Toma, K. A. Walczak, M. Favaro, J. W. Beeman, L. H. Hess, C. Wang, C. Zhu, S. Gul, J. Yano, C. Kisielowski, A. Schwartzberg and I. D. Sharp, *Nat. Mater.*, 2017, **16**, 335–341.
- 702 J. Qiu, G. Zeng, P. Pavaskar, Z. Li and S. B. Cronin, *Phys. Chem. Chem. Phys.*, 2014, **16**, 3115–3121.
- 703 H. Wang, W. Zhu, B. Chong and K. Qin, *Int. J. Hydrogen Energy*, 2014, **39**, 90–99.
- 704 X. Yang, R. Liu, C. Du, P. Dai, Z. Zheng and D. Wang, *ACS Appl. Mater. Interfaces*, 2014, **6**, 12005–12011.
- 705 G. Yun, G. Y. Song, B.-E. Ahn, S.-K. Lee, J. Heo, K.-S. Ahn and S. H. Kang, *Appl. Surf. Sci.*, 2016, **366**, 561–566.
- 706 J. Yan, S. Wu, X. Zhai, X. Gao and X. Li, *J. Power Sources*, 2017, **342**, 460–466.
- 707 P. J. Reed, H. Mehrabi, Z. G. Schichtl and R. H. Coridan, *ACS Appl. Mater. Interfaces*, 2018, **10**, 43691–43698.
- 708 L. Meng, W. Tian, F. Wu, F. Cao and L. Li, *J. Mater. Sci. Technol.*, 2019, **35**, 1740–1746.
- 709 Z. Wang, X. Li, C. K. Tan, C. Qian, A. C. Grimsdale and A. I. Y. Tok, *Appl. Surf. Sci.*, 2019, **470**, 800–806.
- 710 S. Choi, J. Hwang, T. H. Lee, H.-H. Kim, S.-P. Hong, C. Kim, M.-J. Choi, H. K. Park, S. S. M. Bhat, J. M. Suh, J. Lee, K. S. Choi, S.-H. Hong, J. C. Shin and H. W. Jang, *Chem. Eng. J.*, 2020, **392**, 123688.
- 711 Y. J. Hwang, C. Hahn, B. Liu and P. Yang, *ACS Nano*, 2012, **6**, 5060–5069.
- 712 A. Paracchino, N. Mathews, T. Hisatomi, M. Stefik, S. D. Tilley and M. Grätzel, *Energy Environ. Sci.*, 2012, **5**, 8673.
- 713 L. Kavan, L. Steier and M. Grätzel, *J. Phys. Chem. C*, 2016, **121**, 342–350.
- 714 S. W. Shin, M. P. Suryawanshi, H. K. Hong, G. Yun, D. Lim, J. Heo, S. H. Kang and J. H. Kim, *Electrochim. Acta*, 2016, **219**, 470–481.
- 715 M. Zeng, X. Peng, J. Liao, G. Wang, Y. Li, J. Li, Y. Qin, J. Wilson, A. Song and S. Lin, *Phys. Chem. Chem. Phys.*, 2016, **18**, 17404–17413.
- 716 M. Forster, R. J. Potter, Y. Yang, Y. Li and A. J. Cowan, *ChemPhotoChem*, 2018, **2**, 183–189.
- 717 F. Haydous, W. Si, V. A. Guzenko, F. Waag, E. Pomjakushina, M. El Kazzi, L. Sévery, A. Wokaun, D. Pergolesi and T. Lippert, *J. Phys. Chem. C*, 2018, **123**, 1059–1068.
- 718 R. Wang, X. Li, L. Wang, X. Zhao, G. Yang, A. Li, C. Wu, Q. Shen, Y. Zhou and Z. Zou, *Nanoscale*, 2018, **10**, 19621–19627.
- 719 J. Gao, X. Sun, Y. Wang, Y. Li, X. Li, C. Chen and J. Ni, *Appl. Surf. Sci.*, 2020, **499**, 143971.
- 720 M.-W. Kim, B. Joshi, E. Samuel, H. Seok, A. Aldalbahi, M. Almoqli, M. T. Swihart and S. S. Yoon, *Appl. Catal., B*, 2020, **271**, 118928.

- 721 Q. Gui, Z. Xu, H. Zhang, C. Cheng, X. Zhu, M. Yin, Y. Song, L. Lu, X. Chen and D. Li, *ACS Appl. Mater. Interfaces*, 2014, **6**, 17053–17058.
- 722 L. Wang, D. Yan, D. W. Shaffer, X. Ye, B. H. Layne, J. J. Concepcion, M. Liu and C.-Y. Nam, *Chem. Mater.*, 2018, **30**, 324–335.
- 723 J. M. Jarmo Maula, *Chin. Opt. Lett.*, 2010, **8**, 53–58.
- 724 P. Poodt, D. C. Cameron, E. Dickey, S. M. George, V. Kuznetsov, G. N. Parsons, F. Roozeboom, G. Sundaram and A. Vermeer, *J. Vac. Sci. Technol., A*, 2012, **30**, 010802.
- 725 A. Goulas and J. R. van Ommen, *KONA Powder Part. J.*, 2014, **31**, 234–246.
- 726 D. Muñoz-Rojas, T. Maindron, A. Esteve, F. Pierrat, J. C. S. Kools and J. M. Decams, *Mater. Today Chem.*, 2019, **12**, 96–120.
- 727 D. Muñoz-Rojas and J. MacManus-Driscoll, *Mater. Horiz.*, 2014, **1**, 314–320.
- 728 P. Poodt, R. Knaapen, A. Illiberi, F. Roozeboom and A. van Asten, *J. Vac. Sci. Technol., A*, 2012, **30**, 01A142.
- 729 K. Ali, K.-H. Choi, J. Jo and Y. W. Lee, *Mater. Lett.*, 2014, **136**, 90–94.
- 730 K. Ali, K.-H. Choi and N. M. Muhammad, *Chem. Vap. Deposition*, 2014, **20**, 380–387.
- 731 T. Hirvikorpi, R. Laine, M. Vähä-Nissi, V. Kilpi, E. Salo, W.-M. Li, S. Lindfors, J. Vartiainen, E. Kenttä, J. Nikkola, A. Harlin and J. Kostamo, *Thin Solid Films*, 2014, **550**, 164–169.
- 732 P. S. Maydannik, T. O. Kääriäinen, K. Lahtinen, D. C. Cameron, M. Söderlund, P. Soininen, P. Johansson, J. Kuusipalo, L. Moro and X. Zeng, *J. Vac. Sci. Technol., A*, 2014, **32**, 051603.
- 733 J. A. McCormick, K. P. Rice, D. F. Paul, A. W. Weimer and S. M. George, *Chem. Vap. Deposition*, 2007, **13**, 491–498.
- 734 K. Sharma, R. A. Hall and S. M. George, *J. Vac. Sci. Technol., A*, 2015, **33**, 01A132.
- 735 D. J. Higgs, J. W. DuMont, K. Sharma and S. M. George, *J. Vac. Sci. Technol., A*, 2018, **36**, 01A117.
- 736 L. F. Hakim, J. Blackson, S. M. George and A. W. Weimer, *Chem. Vap. Deposition*, 2005, **11**, 420–425.
- 737 L. F. Hakim, S. M. George and A. W. Weimer, *Nanotechnology*, 2005, **16**, S375–S381.
- 738 D. M. King, J. A. Spencer, X. Liang, L. F. Hakim and A. W. Weimer, *Surf. Coat. Technol.*, 2007, **201**, 9163–9171.
- 739 X. Liang, K. S. Barrett, Y. B. Jiang and A. W. Weimer, *ACS Appl. Mater. Interfaces*, 2010, **2**, 2248–2253.
- 740 D. M. King, X. Liang and A. W. Weimer, *Powder Technol.*, 2012, **221**, 13–25.
- 741 C. L. Duan, X. Liu, B. Shan and R. Chen, *Rev. Sci. Instrum.*, 2015, **86**, 075101.
- 742 S. Adhikari, S. Selvaraj and D.-H. Kim, *Adv. Mater. Interfaces*, 2018, **5**, 1800581.
- 743 L. F. Hakim, J. H. Blackson and A. W. Weimer, *Chem. Eng. Sci.*, 2007, **62**, 6199–6211.
- 744 D. M. King, X. Liang, C. S. Carney, L. F. Hakim, P. Li and A. W. Weimer, *Adv. Funct. Mater.*, 2008, **18**, 607–615.
- 745 D. M. King, X. Liang, P. Li and A. W. Weimer, *Thin Solid Films*, 2008, **516**, 8517–8523.
- 746 D. M. King, X. Liang, Y. Zhou, C. S. Carney, L. F. Hakim, P. Li and A. W. Weimer, *Powder Technol.*, 2008, **183**, 356–363.
- 747 D. Longrie, D. Deduytsche and C. Detavernier, *J. Vac. Sci. Technol., A*, 2014, **32**, 010802.
- 748 J. R. Wank, S. M. George and A. W. Weimer, *Powder Technol.*, 2004, **142**, 59–69.
- 749 J. R. Wank, S. M. George and A. W. Weimer, *J. Am. Ceram. Soc.*, 2004, **87**, 762–765.
- 750 <https://www.forgenano.com/products/morpheus/>.